MAGNETIZATION DYNAMICS IN ULTRATHIN MAGNETIC FILMS.

by

Oleksandr Mosendz
Bachelor of Science, Kiev Taras Shevchenko University, 2002

A THESIS SUBMITTED IN PARTIAL FULFILLMENT
OF THE REQUIREMENTS FOR THE DEGREE OF
DOCTOR OF PHILOSOPHY
in the Department
of
Physics

SIMON FRASER UNIVERSITY
Spring 2008

APPROVAL

Name: Oleksandr Mosendz

Degree: Doctor of Philosophy

Title of thesis: Magnetization dynamics in ultrathin magnetic films.

Examining Committee: Dr. David Broun, Professor (Chair)

Dr. Bret Heinrich (Senior Supervisor)
Professor, Department of Physics

Dr. Michael R. Scheinfein (Supervisor)
Adjunct Professor, Department of Physics

Dr. Daryl Crozier (Supervisor)
Professor, Department of Physics

Dr. Patricia Mooney (Internal Examiner)
Professor, Department of Physics

Dr. Axel Hoffmann (External Examiner)
Staff Scientist, Argonne National Laboratory

Date Approved: July 30, 2008

Abstract

Ultrathin magnetic multilayer structures are prepared by Molecular Beam Epitaxy (MBE) on GaAs(001) substrates. Growth was monitored and characterized by Reflection High Energy Electron Diffraction (RHEED), Auger Electron Spectroscopy (AES), X-Ray Photoelectron Spectroscopy (XPS) and Scanning Tunneling Microscopy (STM). The Fe/GaAs interface and its influence on the static magnetic properties in magnetic ultrathin films was studied by means of Ferromagnetic Resonance (FMR) and Mossbauer spectroscopy. These studies were performed using the high quality single crystalline Fe(001) films. It will be shown that in ultrathin magnetic films the magnetic properties are governed by the interface and bulk contributions. The static and dynamic magnetic properties of the Fe single and double layers were studied by FMR and Time Resolved Magneto-optic Kerr Effect (TRMOKE) in a wide range of microwave frequencies. Magnetic damping was studied in the Au/Fe/GaAs(001) structures as a function of thickness of the Fe and the capping Au layer, respectively. Spin currents generated by spin pump/spin sink effects were extensively investigated in magnetic Au/Fe/Au/Fe/GaAs(001) double layers. Pure spin current driven dynamics in these magnetic double layers was studied using the TRMOKE technique. Spin accumulation and spin diffusion model was applied to explain the spin momentum propagation in the Au spacer. The spin diffusion length in Au was found of 34 nm at room temperature. The spin pump/spin sink theory was tested for antiparallel driving of the two Fe layers in Au/Fe/Au/Fe/GaAs(001). This condition was achieved via patterning the sample into a coplanar waveguide. Results are in good agreement with simulations based on the spin pump/spin sink model together with diffusive transport of the accumulated spin momentum across the non-magnetic spacer. The Au/Fe/Au/Fe/GaAs(001) structure was used to study the spin pump/spin sink effect in a non-collinear orientation of the magnetic moments. It is shown that only the transverse component of the spin momentum to the static magnetization contributes to non-local dynamics.

To my parents

Acknowledgments

I would like to express my gratitude to my supervisor Prof. Bret Heinrich. The impact of his deep theoretical knowledge and thorough analysis of the experiment on my work is impossible to overestimate. I am very thankful to him for the plenty of scientific discussions, which lead me through my work. His experience and leadership created very friendly and productive atmosphere in our group. World wide collaborations initiated by Prof. Heinrich gave me an outstanding opportunity to work with scientists in Europe and Canada. I greatly appreciate the benefits from the opportunities that were given to me by Prof. Heinrich. It was an honor to work with him.

I would also like to thank Prof. Mike Scheinfein, whom I was working with at the early stages of my studies. He introduced me to the field of magnetism and supported through the whole program.

I want to thank Ken Myrtle for his help with experiments. I really appreciated his analytic approach to the environment. I wish to thank him for his help with solving many technical problems which I faced.

I wish to thank my colleagues at surface science lab for their help. I owe gratitude to Bartek Kardasz, Dr. Georg Woltersdorf, and Prof. John Cochran. I wish to thank my friend and colleague Bartek Kardasz for his big input in all projects discussed in the thesis. Our collaboration was extremely fruitful. Sharing ideas and performing experimental work together with Mr. Kardasz was very important for me.

I would like to thank our collaborators from other institutions for their valuable contribution to this thesis:

Prof. Christian Back at Regensburg University for inviting me to use time and spatially resolved magneto-optic Kerr effect setup. I wish to acknowledge fruitful collaboration with Dr. Georg Woltersdorf which started in Vancouver and lasted for many years.

I gratefully acknowledge Prof. Mark Freeman, Dr. Xiaobin Zhu and Dr. Zhigang Liu from University of Alberta for collaboration on time resolved Kerr effect.

I acknowledge Prof. Jurgen Kirchner, Dr. Marek Przbylski and Dr. Jan Zukrovski from Max Planck Institute in Halle for inviting me to participate in interface structure studies using pulsed laser depositions technique and Mossbauer effect.

I gratefully acknowledge National Research and Engineering Council of Canada and Canadian Institute for Advanced Research for their financial support and productive meetings.

I wish to thank my parents for their care and support during all my studies.

Contents

Approval ii

Abstract iii

Dedication iv

Acknowledgments v

Contents vii

List of Tables x

List of Figures xi

1 Introduction 1

2 Theoretical considerations 6

- 2.1 Magnetization in ultrathin magnetic films 6
  - 2.1.1 Magnetic anisotropies in thin films 6
  - 2.1.2 Landau-Lifshitz-Gilbert equation of motion 10
  - 2.1.3 Ferromagnetic resonance 11
- 2.2 Damping in magnetic ultrathin films 14
  - 2.2.1 Eddy currents 14
  - 2.2.2 Spin-orbit relaxation in metallic ferromagnets 15
  - 2.2.3 Magnetic relaxations at ferromagnet/normal metal interface. Spin pumping. 20
- 2.3 Magneto optical Kerr effect 24

3 Experimental techniques and apparatus 30

- 3.1 Ultra-high vacuum Molecular Beam Epitaxy system 30

3.1.1 Auger Electron Spectroscopy (AES) 31
3.1.2 X-Ray Photoelectron Spectroscopy (XPS) 33
3.1.3 Reflection High Energy Electron Diffraction (RHEED) 35
3.1.4 In-situ Scanning Tunnelling Microscope 36
3.1.5 GaAs substrate preparation 40
3.1.6 Molecular Beam Epitaxy (MBE) 45
3.2 Ferromagnetic resonance technique (FMR) 47
3.2.1 Conventional FMR spectrometer 47
3.2.2 Network analyzer 52
3.2.3 Typical FMR data 55
3.3 Time resolved magneto-optic Kerr effect technique 58
3.3.1 Magnetization detection and depth sensitivity 60
3.3.2 Continuous wave excitation and synchronization 63
3.3.3 Sample patterning and magnetic field configuration 64
3.3.4 Measurements configuration and typical data 65

4 Magnetic properties of ultrathin films 67
4.1 Sample preparation 68
4.2 Studies of static properties of ultrathin magnetic multilayers 71
4.2.1 Magnetic crystalline anisotropies in metallic multilayers 72
4.2.2 Origin of uniaxial magnetic crystalline anisotropy in Fe/GaAs(001) 75
4.2.3 Collinear and non-collinear FMR resonance 78
4.2.4 Ghost FMR resonance 80
4.3 Dynamic properties of magnetic multilayers 80
4.3.1 Intrinsic Gilbert damping 80
4.3.2 Intrinsic non-local damping in magnetic multilayers 83
4.3.3 Extrinsic damping due to long range inhomogeneities 86
4.3.4 Extrinsic damping due to a short range inhomogeneity, two-magnon scattering 92

5 Spin currents in magnetic trilayer structures 103
5.1 Diffusive spin momentum transfer 103
5.2 Exchange of spin momentum in Au/Fe/Ag/Fe/GaAs films 105
5.2.1 Static magnetic properties 105

- 5.2.2 Dynamic magnetic properties 107
- 5.2.3 Spin sink contribution 108
- 5.2.4 Angular dependence of FMR linewidth 110
- 5.3 Phase of spin currents 112
  - 5.3.1 Antiparallel driving experiment 112
  - 5.3.2 Spin sink effect in absorption spectra using antiparallel driving . . 115
- 5.4 Spin currents in non-collinear configuration of magnetic moments 115

6 Spin diffusion length in Au 119

- 6.1 FMR studies on nAu/16Fe/GaAs(001) 119
- 6.2 TRMOKE measurements on double layers 121
  - 6.2.1 Propagation of light in metallic media 122
  - 6.2.2 Radiation due to the Kerr effect 125
  - 6.2.3 Depth sensitivity of MOKE 129
  - 6.2.4 Experimental evidence for the suppression of the direct Kerr signal from the bottom Fe layer 130
  - 6.2.5 Detection of the spin sink driven signal 133
  - 6.2.6 Other possible mechanisms of dynamic coupling and validity analysis 135
  - 6.2.7 The dependence of the spin sink driven signal on the Au spacer thickness 137
- 6.3 Summary and comparison with other measurements 138

7 Conclusions 140

A Sample preparation using patterning 144

- A.1 FMR with antiparallel driving 144
  - A.1.1 Sample patterning for FMR experiment 144
  - A.1.2 Coplanar waveguide in rf circuitry 148
- A.2 Sample patterning for TRMOKE experiments 149
  - A.2.1 Defining pads of the epitaxial sample 149
  - A.2.2 Coplanar waveguide evaporation 149

B Transmission through FM/NM interface 154

- B.1 Diagonalization of transmission and reflection matrices. 155
- B.2 Spin current pumped by $\vec{M}(t)$. 157

Bibliography 159

List of Tables

4.1 Anisotropy parameters for 20Au/16Fe/30Au 74
4.2 Anisotropy parameters for 30Au/16Fe/GaAs 74
4.3 The in-plane uniaxial anisotropy parameter, $K_{u||}$,the in-plane four-fold anisotropy parameter, K_{1eff}, and the effective demagnetizing field $4\pi M_{eff}$ for the listed structures 77

6.1 Optical properties of Au, Fe and GaAs 123

List of Figures

2.1 Coordinate system 7
2.2 Schematic diagram of spin-flip scattering 16
2.3 Model of spin momentum flow in doublelayers 22
2.4 The polar magneto-optical Kerr and Faraday effects 25
2.5 Kerr rotation and ellipticity in magnetic doublelayers 27

3.1 Schematic cartoon of the UHV chamber 32
3.2 Illustration of the Auger electron emission process 33
3.3 Sketch illustrating emissin of photoelectron in XPS 34
3.4 Geometry of RHEED. Ewald sphere concept 37
3.5 Example of RHEED intensity oscillations during film deposition 38
3.6 Schematic diagram of the STM apparatus 39
3.7 STM and RHEED studies of the hydrogen cleaned GaAs surface 40
3.8 STM and RHEED studies of the sputtered GaAs surface 42
3.9 STM and RHEED studies of the 4X6 reconstructed GaAs 43
3.10 Subatomic STM image of the 2X6 reconstructed GaAs 44
3.11 STM studies of meatallic film growth 46
3.12 STM studies of Pd film surface topology at RT and 180° C 46
3.13 RHEED studies of Pd film surface topology at RT and 180° C 47
3.14 Auger studies of interface diffusion 48
3.15 Diagram of an FMR system 49
3.16 A schematic drawing of the cylindrical cavity and sample 50
3.17 Rf magnetic field distribution in the cavity and waveguide 51
3.18 FMR setup using a NA and transmission line 52
3.19 Coplanar transmission line with a magnetic film 53
3.20 Phase correction on the FMR data obtained using the vector NA 54
3.21 Typical in-plane FMR data 57
3.22 Schematic diagram of the TRMOKE apparatus 59

3.23 Illustration of the Kerr signal detection 62
3.24 Sample geometry in TRMOKE experiment 64
3.25 Typical TRMOKE data 66

4.1 RHEED studies of Fe deposition on GaAs 68
4.2 RHEED studies of Au deposition on Fe/GaAs 70
4.3 STM studies of Au deposition on Fe/GaAs 70
4.4 RHEED studies of Fe deposition on Au/Fe/GaAs 71
4.5 FMR peak positions in 20Au/16Fe/30Au/16Fe/GaAs 73
4.6 CEMS spectra for TD and PLD samples 75
4.7 Relative contributions of the CEMS spectral components for TD and PLD samples 76
4.8 FMR peak positions for TD and PLD samples 77
4.9 Collinear and non-collinear branches of FMR 79
4.10 Ghost FMR resonance 81
4.11 Damping in Fe/GaAs ultrathin fims 82
4.12 Non-local damping in magnetic doublelayers 84
4.13 Sample and transmission line 87
4.14 Damping at low frequencies in FMR field sweep mode 88
4.15 Damping at low freuqencies in FMR frequency sweep mode 90
4.16 The rf field distribution around a CTL 91
4.17 Growth studies of Pd grown on an Fe/GaAs(001) template 93
4.18 Growth studies of Au on a Pd/Fe/GaAs(001) template 94
4.19 STM studies of a Au/Pd/Fe/GaAs(001) specimen 95
4.20 ΔH_{FMR} *vs* φ_H for 20Au/**7Fe**/40Au/11Pd/10Fe/GaAs 96
4.21 ΔH_{FMR} *vs* f for 20Au/**7Fe**/40Au/11Pd/10Fe/GaAs 97
4.22 ΔH_{FMR} *vs* f for 20Au/7Fe/40Au/11Pd/**10Fe**/GaAs 98
4.23 Two-magnon scattering path 101

5.1 Spin pump/spin sink effect in standard FMR 106
5.2 Spin sink effect in FMR absorption spectra 109
5.3 ΔH_{FMR} *vs* φ_H in magnetic doublelayers 111
5.4 Rf field in FMR with antiparallel driving 112
5.5 FMR with antiparallel driving 113
5.6 Spin sink effect in FMR with antiparallel driving absorption spectra . . . 116
5.7 Spin sink effect in non-collinear configuration 117

5.8 Spin current flow in non-collinear configuration 118

6.1 ΔH_{FMR} *vs* t_{Au} in Au/16Fe/GaAs 120
6.2 α^{sp} *vs* t_{Au} in Au/16Fe/GaAs 121
6.3 Schematics of light propagation in Au/Fe/Au/Fe/GaAs 123
6.4 Calculated propagation of light in Au/Fe/Au/Fe/GaAs 124
6.5 Magnetic layer as radiating antenna 127
6.6 Kerr signal calculation 128
6.7 Kerr signal from the top and bottom Fe films 128
6.8 Depth resolution of TRMOKE 131
6.9 Experimental evidence of depth selective signal suppression on TRMOKE 132
6.10 f_{res} *vs* H in Au/12Fe/Au/16Fe/GaAs 133
6.11 Pure spin current driven magnetization precession 134
6.12 Exchange coupling in TRMOKE experiment 136
6.13 TRMOKE measurements of δ_{sd} 137

A.1 Patterning sample into CPL: Optical lithography 145
A.2 Patterning sample into CPL: Dry etching 147
A.3 Sample as a part of rf circuitry 148
A.4 Pads of epitaxial film: Optical lithography 150
A.5 Pads of epitaxial film: Dry etching 151
A.6 CPL deposition: Optical lithography 152
A.7 CPL deposition: Liftoff process 153

B.1 Model structure of FM/NM interface 156

Chapter 1

Introduction

Nano-magnetism is developing in a fascinating manner. The ever increasing rate of interest in this field is driven by several factors. Firstly, the use of the Molecular Beam Epitaxy (MBE) technique in magnetism in the early 80's created the possibility to prepare unique magnetic structures. Consequently the 80's and 90's were marked by a number of important discoveries in magnetism: interface anisotropies, the interlayer exchange coupling mechanism, and the Giant Magneto Resistance (GMR) effect [1]. These are perhaps the most important milestones along which the further development of magnetic nanostructures has evolved. The importance of these three effects was instantly recognized by the scientific community. The field of magnetic nanostructures is a new and central area of advanced condensed matter science and has led to a major new developement in electronics called "spintronics". In spintronics the electron spin momentum plays a role equal to the role of the electrical charge. Magnetism has now merged with electronics in a very fundamental manner allowing one to create new technologies for data storage, data transfer, and logic operations. Research on these subjects is, at the present time, probably the most widely worked on in the category of solid state physics. And of course new information always raises new questions, which have yet to be answered. During the course of this thesis work I focused on the investigation and understanding of the basic properties of ultrathin magnetic films. These studies led to a better understanding of spin dynamics which, in an important way, influences further developments in spintronics.

The small lateral dimensions of spintronics devices require the use of magnetic metallic ultrathin film structures, where the magnetic moments across the film are locked together by exchange coupling. This simplifies the description of thin-film magnetic systems. One does not need to worry about spatial variations of the magnetic moment across the film thickness.

The excellent crystalline quality of the magnetic thin films used during the course of this thesis work provided suitable systems for understanding the microscopic mechanisms which determine macroscopic quantities like the magnetization vector, magnetic anisotropy, and magnetic damping. The work in this thesis was based on the following important steps and techniques: (a) Preparation of single-crystalline magnetic single and multi-layer structures on GaAs(001) substrates using the Molecular Beam Epitaxy (MBE) technique; (b) The utilization of vacuum compatible, monolayer-sensitive analysis techniques: RHEED, STM, XPS, and Auger spectroscopy; (c) Ferromagnetic Resonance (FMR) studies using microwave spectrometers and a microwave network analyzer; (d) Development of a sophisticated time (ps), lateral (μm), and depth (nm) resolved Magneto Optical Kerr Effect (TRMOKE) system for probing static and dynamic magnetic properties of the thin-film specimens; (e) SQUID and MOKE systems for static magnetometry; (f) The development of computer codes allowing one to carry out simulations of magnetization dynamics in magnetic single and multilayer systems.

In the limit of ultrathin films the interfaces represent a considerable part of the magnetic structure. It will be shown that the Fe/GaAs(001) interface structure can introduce a unique in-plane uniaxial magnetic anisotropy which in principle should be absent in systems having cubic symmetry. In fact this anisotropy was crucial in a number of experimental studies to be presented in this thesis. A robust in-plane interface uniaxial anisotropy in the Fe/GaAs(001) films allowed one to investigate the magnetic excitations in non-collinear magnetic moment configurations and spin pumping in magnetic double layer Fe/NM/Fe/GaAs(001) structures where it was important to separate the resonance conditions of the two Fe films (NM stands for a normal metal spacer layer).

Magnetic relaxation processes are the object of much of the ongoing studies in spintronics. Magnetic relaxation in metals is perhaps one of the most controversial and least understood subjects of spin dynamics. In this thesis I will show that many controversies arise from extrinsic factors that are often not well identified and understood. Magnetic damping can be influenced by various factors. Some of them are intrinsic and cannot be avoided while others are extrinsic and most likely are caused by either structural or compositional defects. In order to understand these processes one needs to create simple systems where one can isolate and enhance a particular damping mechanism in order to study it in detail. In this thesis six major aspects of spin dynamics were addressed:

(i) The rules which allow one to separate and identify intrinsic and extrinsic contributions to the damping.

(ii) Separation of the interface and bulk contributions to the intrinsic magnetic damping.

(iii) Investigation of spin dynamics in a system containing a self- assembled network of misfit dislocations and their contribution to extrinsic magnetic damping.

(iv) Study of the spin momentum transfer mechanism in magnetic single layers covered by a normal metal.

(v) Examination of spin momentum transfer in magnetic double layers.

(vi) Determination of the spin diffusion length in Au using Fe/Au/Fe(001) structures.

Studies of intrinsic magnetic damping mechanisms required nearly ideal structures. The Au/Fe/GaAs(001), Au/Fe/Au/Fe/GaAs(001) and Au/Fe/Ag/Fe/GaAs(001) magnetic ultrathin structures were prepared using MBE. The small 1.4% lattice mismatch between Fe and GaAs enabled us to prepare high quality crystalline magnetic multilayers on a semiconductor substrate. The lattices of Au[001] and Ag[001] are almost matched to the Fe[001] lattice when rotated by 45^o around the [100] crystallographic axis. The crystalline quality of the deposited structures was monitored by means of *in situ* reflection high energy electron diffraction (RHEED) and scanning tunneling electron microscopy (STM). In addition, cross-sectional transmission electron microscopy (XTEM) images were obtained at the Max Planck Institute in Halle [2]. Patterning of magnetic pixels and coplanar microwave transmission lines for the TRMOKE studies was carried out at the University of Regensburg using their wet lithography facilities.

It will be shown that in magnetic single layers having a high degree of crystalline perfection the magnetic relaxation can be described by the Gilbert damping mechanism. I will demonstrate that the Gilbert damping in ultrathin Au/Fe/GaAs(001) magnetic single layer films consists of both bulk and interface contributions. It will be shown that the deviations from Gilbert damping observed at low microwave frequencies are not due to intrinsic relaxation terms as claimed by some groups, but are of extrinsic origin. They are caused by long range magnetic inhomogeneities. In the magnetic double layers (F1/NM/F2), layers separated by a nonmagnetic spacer layer (NM), there is an additional Gilbert like damping contribution. It arises from dynamic non-local spin transport. At the F1/NM interface spin pumping creates a pure spin current entering the NM spacer layer and this spin current propagates across the NM spacer and becomes absorbed by the NM/F2 interface [3, 4]. One layer acts like a spin pump and the other layer acts like a spin sink. Since this current is not accompanied by a net electric charge flow this mechanism has the potential to lead to a spintronics device having no capacitance. The spin pump/spin sink effect in this thesis was studied under various experimental conditions using symmetric and asymmetric rf magnetic field driving. For the first time it has been successfully demonstrated that one can directly measure the propagation of a spin current across the normal metal spacers using TRMOKE (Time Resolved Magneto-Optic Kerr Effect). It will be shown that the propagation of spin momentum can be described by a diffusion equation, and this can be used to determine the momentum and spin flip relaxation times in Au and thereby enables one to obtain the corresponding spin diffusion length.

Extrinsic contribution to the magnetic damping will be illustrated with the utmost clarity using Au/Fe/Au/Pd/Fe/GaAs(001) structures. The lattice match in these structure is very poor. The Pd lattice is mismatched to the Fe lattice by $\sim$ 4 percent, and this results in a self assembled network of misfit dislocations. It will be shown that this dislocation network leads to strong two- magnon scattering. At low microwave frequencies this two-magnon scattering results in an effective Gilbert damping that exceeds the intrinsic damping by more than one order of magnitude. The desired reversal time of the magnetic moment in spintronics device pixels corresponds to the time domain of low microwave frequencies, the order of 10 GHz, and therefore it is possible to engineer a desirable magnetic relaxation time by means of the extrinsic damping due to the self-assembled network of magnetic defects.

Due to a significant variety of experimental tasks several rf techniques were employed in the study of magnetic properties. The FMR measurements at low microwave frequencies were performed using a network analyzer (NA) technique (1 to 20 GHz). FMR measurements from 9 to 73 GHz were carried out using standard microwave spectrometers and rectangular wavequides. TRMOKE experiments were carried out on a modified system at the University of Regensburg. The modified TRMOKE system allowed one to carry out stroboscopic MOKE studies using a coplanar wavequide operating with a continuous wave (cw) microwave signal that was synchronized with the the train of fs laser pulses: this allowed one to measure the rf magnetization precession in the cw time domain. This technique was used to directly monitor the propagation of spin currents in the Au spacers.

This thesis is organized in the following way: **Chapter 2** provides the theoretical background necessary for the understanding and interpretation of the measured data. **Chapter 3** describes the experimental techniques and equipment that was used to prepare the samples and to carry out the magnetic measurements. In **Chapter 4** the sample growth, static magnetic properties, and dynamic magnetic properties of single and double magnetic layers are discussed. Several aspects of the static properties are addressed: (a) interface and bulk anisotropies, (b) influence of the Fe/GaAs interface on magnetic properties of the Fe layer, and (c) unique static properties of samples characterized by good crystalline quality. Studies of dynamic properties in this chapter cover the following topics: (a) measurements of intrinsic Gilbert damping, (b) analysis of the damping parameter in nearly ideal structures at low microwave frequencies, (c) damping enhancement due to the spin pumping mechanism and (d) extrinsic damping due to short wavelength inhomogeneities. **Chapter 5** describes the FMR experiments that provide a reliable test of the spin pump/spin sink theory in magnetic double layers. The FMR experiments on these double layers were carried out in the following configurations: Section 5.2: a collinear configuration of the magnetic moments in which the two layers are driven in-phase by the rf driving fields. Section 5.3: collinear configuration of the magnetic moments in which the two films are driven by anti-parallel rf magnetic fields. Section 5.4: a non-collinear configuration of the magnetic moments using in-phase rf driving fields. **Chapter 6**: deals with the spin momentum propagation through the Au spacers. Section 6.1 covers FMR experiments on magnetic single layers (Au/Fe/GaAs). The direct observation of pure spin current driven dynamics is presented in Section 6.2. This section concludes with the measurements of the spin diffusion length in Au via direct observation of spin current driven dynamics presented in Subsection 6.2.7. Section 6.3 compares our FMR and TRMOKE measurements with measurements reported by other groups. Conclusions drawn from this thesis work are presented in **Chapter 7**. Additional information on the sample patterning procedure is presented in **Appendix A**. In **Appendix B** the theoretical derivation of spin pumping theory based on the Buttiker formalism is summarized.

Chapter 2

Theoretical considerations

In this chapter a brief review of important theoretical aspects of this work is presented. The magneto-crystalline anisotropies and magnetization equations of motion will be discussed in the limit of ultrathin magnetic films. The rf susceptibility at Ferromagnetic Resonance (FMR) in the presence of magneto-crystalline anisotropies will be derived. Extra emphasis will be put on magnetic damping. Firstly, the origin of intrinsic damping due to the spin orbit interaction will be described. Secondly, non-local damping will be addressed in detail using a time and spin dependent scattering matrix. The interaction of light with a magnetized media will be addressed in order to interpret the time resolved Kerr effect measurements.

2.1 Magnetization in ultrathin magnetic films

The description of the magnetic properties of ultrathin films can be significantly simplified compared to that for bulk materials. Ultrathin layers loose their internal degree of freedom. The exchange coupling in thin ferromagnetic layers that are excited by an rf magnetic field that is uniform in the film plane keeps the magnetic moments across the film nearly parallel and hence the concept of a giant magnetic moment can be applied to the individual layers. Interface and bulk magnetic properties are shared together in ultrathin films allowing one to create unique magnetic systems and materials.

2.1.1 Magnetic anisotropies in thin films

The magnetic anisotropy describes the dependence of the magnetic energy on the direction of the magnetization. There are two main contributions: these are the shape anisotropy and the crystalline anisotropy energy density. The shape anisotropy arises from the dipolar energy in a finite specimen. The crystalline anisotropy is caused by the spin orbit interaction and leads to a magnetic energy density dependent on the orientation of the magnetization with respect to the crystalline axes.

Crystalline anisotropy The magnetic anisotropy energy (MAE) is given by the work (W_{MAE}) needed to rotate the magnetization from an easy direction, corresponding to a minimum energy, to an arbitrary direction. If this rotation is performed at constant temperature, the MAE is given by the change in the free energy F. This is easy to see when one considers that for a closed system (no exchange of particles) $dF = dW - SdT$, S being the entropy; at constant temperature, T, this expression reduces to $dF = dW$. Consequently:

$$F_2 - F_1 = \int_1^2 dW_{MAE} = MAE, \tag{2.1}$$

where 1 and 2 denote the initial and final directions of the magnetization.

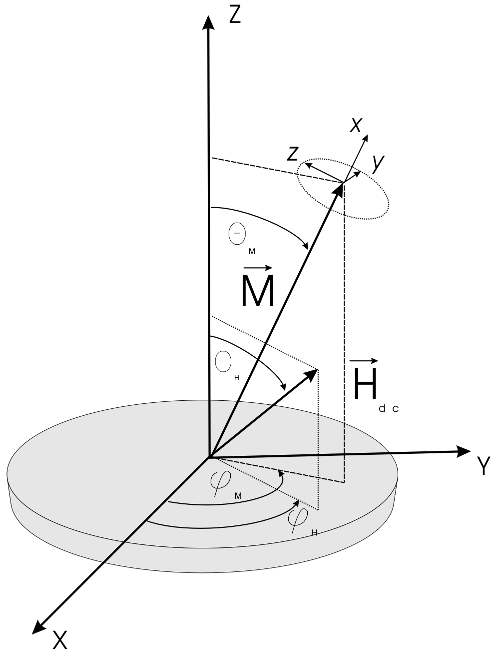

Figure 2.1: The laboratory system of coordinates is described X,Y,Z. $\vec{M}$ and $\vec{H}$ are the magnetization and applied magnetic field, respectively. The x,y,z coordinates are used to describe the magnetization dynamics. The x axis lies parallel with the static magnetization vector $\vec{M}_s$.

The total free energy has to include a contribution from the work done by the force. In magnetism this contribution is called the Zeeman energy. The anisotropy energy plus the Zeeman energy then represents the Gibbs magnetic energy. The static direction of the magnetic moment is determined from the minimization of the Gibbs energy. In a single domain one needs to find the magnetization angles Θ_M and ϕ_M for a given external field $\overrightarrow{H}$. In equilibrium the torque $\vec{M} \times \vec{H}$ due to the external field is balanced by the torque due to the magnetic anisotropy. The direction of the magnetization $\overrightarrow{M}$ can be different from the direction of the external field $\overrightarrow{H}$. This effect is particularly pronounced when the Zeeman energy density is comparable to the anisotropy energy density. When the external field is not oriented along a magnetic easy axis the magnetization points somewhere in between the direction of the easy axis and the direction of the field $\overrightarrow{H}$. This effect is often referred to as "magnetization dragging".

In the theory of FMR one needs an expression for the rf susceptibility. In order to proceed one needs to determine the effective fields arising from the magnetic anisotropy. The anisotropy effective fields, $\overrightarrow{H}_{eff}$, can be derived from variational calculations [5] and is given by

$$\vec{H}_{eff} = -\frac{\partial F}{\partial \vec{M}}, \tag{2.2}$$

The phenomenological expression for F has to satisfy the symmetry of the system [6]. In the following we will limit the discussion to cubic symmetry which is relevant for this thesis. The free energy of a single magnetic domain can be expressed in a power series of the directional cosines of the magnetization vector $\overrightarrow{M}$; $\alpha_i = \frac{\vec{M}}{M} \cdot \hat{e}_i$ (i=X,Y,Z), where the coordinates X,Y,Z are defined by the principle crystallographic axes $< 100 >$,

$$\begin{aligned} \alpha_X &= \sin\Theta_M \cos\varphi_M, \\ \alpha_Y &= \sin\Theta_M \sin\varphi_M, \\ \alpha_Z &= \cos\Theta_M. \end{aligned} \tag{2.3}$$

Ultrathin films of cubic materials grown along the [001] crystallographic direction have in general a tetragonal symmetry. The corresponding free energy per unit volume can be written in the form [6]:

$$F_a^{cub} = -\frac{1}{2}K_1(\alpha_X^4 + \alpha_Y^4) - \frac{1}{2}K_1^{\perp}\alpha_Z^4 - K_u^{\perp}\alpha_Z^2 \;, \tag{2.4}$$

where K_1, $K_1^{\perp}$ are the in-plane and perpendicular four-fold anisotropy parameters; and $K_u^{\perp}$ is the perpendicular uniaxial anisotropy energy density parameter. The four-fold terms in Eq. 2.4 in the absence of tetragonal symmetry ($K_1 = K_1^{\perp}$) lead to pure cubic anisotropy:

$$F_a^{cub} = K_1(\alpha_X^2\alpha_Y^2 + \alpha_X^2\alpha_Z^2 + \alpha_Y^2\alpha_Z^2) \;, \tag{2.5}$$

since

$$\alpha_X^4 + \alpha_Y^4 + \alpha_Z^4 = 1 - 2(\alpha_X^2\alpha_Y^2 + \alpha_X^2\alpha_Z^2 + \alpha_Y^2\alpha_Z^2)\,. \tag{2.6}$$

In the coordinate system of Fig. 2.1 the cubic anisotropy energy term can be written explicitly using relations 2.3:

$$\begin{aligned}F_a^{cub} &= K_1(\sin^2\Theta_M\cos^2\varphi_M\sin^2\Theta_M\sin^2\varphi_M) + K_1(\sin^2\Theta_M\cos^2\varphi_M\cos^2\Theta_M) \\ &\quad + K_1(\sin^2\Theta_M\sin^2\varphi_M\cos^2\Theta_M) \\ &= K_1\sin^2\Theta_M - \frac{1}{8}K_1(\cos 4\varphi_M + 7)\sin^4\Theta_M\end{aligned} \tag{2.7}$$

This equation shows that for $K_1 > 0$ the $< 100 >$ directions are the easy axes while for $K_1 <0$ the $< 111 >$ directions are the easy axes.

Shape anisotropy At each lattice point within a cubic lattice the dipole fields of all other lattice points results in a dipolar field proportional to the saturation magnetization and therefore plays no role in the torque. However this is only true for an infinite system. As soon as surfaces are present, a magnetic pseudo surface charge develops and results in a dipole-dipole interaction energy. In systems with reduced dimensions, such as a thin film, the shape anisotropy might even be the leading term in the overall MAE. For a thin film the shape anisotropy has the form of a uniaxial anisotropy:

$$F_s^{demag} = 2\pi D M^2 \cos^2\Theta_M \ , \tag{2.8}$$

where D is the demagnetizing factor and is very close to 1 for sufficiently thin films. For very thin films only a few atomic layers thick the continuum approximation fails to describe the dipolar shape anisotropy [7, 8, 9]. The discreteness of the atomic moments results in a variation of the dipolar field across the sample particularly in the vicinity of the surface [10, 11]. The dipolar field generated by a given layer decreases exponentially away from its surface with a decay length given by the in-plane lattice spacing. Thus the average value of the total dipolar field at a given lattice site strongly decreases when the thickness of the film is decreased to a few monolayers. For the bcc(001) Fe films this reduction can be written as a reduced demagnetizing factor: $D = 1 - \frac{0.425}{N}$, where N is the number of atomic layers in the film. In fact this contribution acts like a perpendicular uniaxial anisotropy with $K_{\perp,dip} = 0.425\pi M_s^2 a_0$, where a_0 is the lattice spacing parameter.

Surface anisotropy In thin films the presence of the symmetry breaking at the interfaces introduces a uniaxial anisotropy term

$$F_s^{\perp} = -K_u^{\perp}\alpha_Z^2 \tag{2.9}$$

A non-zero uniaxial perpendicular anisotropy can also be induced by vertical lattice distortions and magneto-elasticity energy terms [7]. In a purely cubic lattice the expression for the anisotropy energy contains no quadratic directional cosine terms because any such term would have to appear in the combination $\alpha_X^2 + \alpha_Y^2 + \alpha_Z^2 = 1$. However, any distortion normal to the film surface causes the in-plane and out-of-plane axes to become non-equivalent leading to an anisotropy term $\sim \alpha_Z^2$.

A uniaxial anisotropy energy term can also occur with an axis oriented in an in-plane direction. This can be caused either by preferential interactions due to electronic hybridization at the film-substrate interface or because of a magneto-elastic energy density associated with a uniaxial in-plane shear [12]. Such a term can be described by the uniaxial in-plane anisotropy density

$$F_s^{\|} = -K_u \sin\Theta_M \cos^2(\phi - \delta) \ , \tag{2.10}$$

where K_u is the anisotropy strength and δ is the angle that the uniaxial in-plane anisotropy axis makes with respect to a fiducial direction.

The terms F_s^{demag}, $F_s^{\|}$, and $F_s^{\perp}$ are a consequence of the thin film geometry, lattice strains, and the breaking of the lattice symmetry at the interfaces.

In order to separate the anisotropy into volume and surface contributions one needs to investigate the anisotropy generated effective fields as a function of $1/d$, where d is the film thickness. In this case the anisotropy energy density is given by a constant term and a term proportional to $1/d$. The constant term is determined by the bulk anisotropy parameter, and the slope describes the interface anisotropy parameter.

The magnetic free energy can then be presented in the following form:

$$F = F_a^{cub} + F_s^{demag} + F_s^{\|} + F_s^{\perp}. \tag{2.11}$$

2.1.2 Landau-Lifshitz-Gilbert equation of motion

The motion of the magnetization vector in the effective field $\vec{H}_{eff}$ is described by the Landau-Lifshitz-Gilbert (LLG) equation of motion [7]:

$$\frac{1}{\gamma}\frac{\partial \vec{M}}{\partial t} = -\left[\vec{M} \times \vec{H}_{int}\right] + \frac{\alpha}{\gamma}\left[\vec{M} \times \frac{\partial \vec{n}}{\partial t}\right] \ , \tag{2.12}$$

where $\vec{n}$ is the unit vector in the direction of the magnetization $\vec{M}$, $\gamma = g \mid e \mid /2mc$ is the absolute value of the gyromagnetic ratio, and $\alpha = \frac{G}{\gamma M_s}$ is the dimensionless Gilbert damping parameter. G is the Gilbert parameter in units of inverse seconds. The first term on the right-hand side represents the torque on the magnetization due to the internal field $\vec{H}_{int}$. In the static case $\vec{n}$ has to be parallel with the internal field $\vec{H}_{eff,anis} + \vec{H}_{dc}$, where $\vec{H}_{dc}$ is the applied external field.

The second term represents the Gilbert damping torque [7, 13, 14]. With an increasing damping coefficient α the second term on the right hand side of Eq. 2.12 eventually becomes dominant and $\frac{\partial \vec{M}}{\partial t} \to 0$. For $\alpha \to \infty$ the magnetic system approaches its equilibrium at an infinitely slow rate.

Other forms for the phenomenological damping term can be found in the literature: for example the **Landau Lifshitz (LL) term** is expressed in the following form:

$$-\frac{\lambda}{\gamma M_s^2}(\vec{M} \times [\vec{M} \times \vec{H}_{int}]), \tag{2.13}$$

where λ is the LL damping parameter.

The Gilbert and LL damping terms are identical for small damping, $\alpha \ll 1$. In fact the LL equation can be transformed to the LLG equation by means of the following substitution:

$$\frac{\lambda}{M_s} = \alpha\gamma, \; \gamma = \gamma_{Gilb}\frac{1}{1+\alpha^2}. \tag{2.14}$$

The difference between the LL and Gilbert forms of damping occurs only for large damping, $\alpha \sim 1$. In the LL equation with increasing λ the damping term becomes dominant over the precessional torque $\vec{M} \times \vec{H}_{int}$. One can view it as an increasingly fast relaxation to the lattice. Effectively it means that the system is always in a quasi-equilibrium state. This behavior is unrealistic. In fact the LL damping was derived from general thermodynamic principles only for the limit of weak damping [15, 16]. The magnetization vector should slow down as if it was put in a thick gel, consequently ($\frac{\partial \vec{M}}{\partial t} \to 0$) and therefore the magnetization never reaches equilibrium and indeed the Gilbert relaxation term behaves in this manner.

Equation 2.12 describes both the static and dynamic response of the system.

2.1.3 Ferromagnetic resonance

The dynamic response of a magnetic system can be calculated by applying a small rf magnetic field $\vec{h}_{rf} = \vec{h}\exp^{i\omega t}$, where ω is the circular frequency, and $\vec{h}_{rf}$ is oriented perpendicular to the static magnetization $\overrightarrow{M}_s$. The resulting torque leads to a precessional motion of the magnetization $\overrightarrow{M}$ [17]. In FMR the rf field $\vec{h}$ in ultrathin films is equal to an external driving field created in a microwave cavity assuming that the driving field is symmetric, the same on both sides (top and bottom) of the film. For small precessional angles equation 2.12 can be linearized by looking for solutions in the form:

$$\vec{M} = \vec{M}_s + \vec{m}, \tag{2.15}$$

where $\vec{M}_s$ is the static saturation magnetization and $\vec{m}$ is the rf magnetization component perpendicular to $\vec{M}_s$. Thus the total internal field is

$$\vec{H}_{int} = \vec{H}_{eff} + \vec{H}_{dc} + \vec{h}_{rf}. \tag{2.16}$$

It is convenient to carry out this linearization in the (x,y,z) magnetization coordinate system in which the x axis points along the direction of $\vec{M}_s$ and the y axis lies in the film plane parallel to the rf field $\vec{h}$, see Fig. 2.1. For a small angle of precession $m \ll M_s$. The directional cosines with respect to the X,Y,Z system of coordinates are given by

$$\alpha_X = \frac{M_x}{M}\cos\varphi_M \sin\Theta_M - \frac{M_y}{M}\sin\varphi_M - \frac{M_z}{M}\cos\varphi_M\cos\Theta_M \tag{2.17}$$

$$\alpha_Y = \frac{M_x}{M}\sin\varphi_M \sin\Theta_M + \frac{M_y}{M}\cos\varphi_M - \frac{M_z}{M}\sin\varphi_M\cos\Theta_M \tag{2.18}$$

$$\alpha_Z = \frac{M_x}{M}\cos\Theta_M + \frac{M_z}{M}\sin\Theta_M \tag{2.19}$$

where the magnetization components refer to the magnetization co-ordinate system: x,y,z in Fig. 2.1.

In-plane configuration: The magnetization and external field lie in the film surface, i.e. $\Theta_M = \Theta_H = 90°$. The effective anisotropy field $\vec{H}_{eff}$ must be calculated using equations 2.11 and 2.2 along with the direction cosines given by 2.17, 2.18 and 2.19. The magnetization vector $\vec{M}$ in the (x,y,z) coordinate system can be written for small deviations from equilibrium:

$$\vec{M} = M_s\hat{x} + m_y\hat{y} + m_z\hat{z}. \tag{2.20}$$

where $\hat{x}, \hat{y}, \hat{z}$ are unit vectors. The total external field is

$$\vec{H}_{dc} = H_{dc}\{\cos(\varphi_M - \varphi_H)\hat{x} - \sin(\varphi_M - \varphi_H)\hat{y}\}. \tag{2.21}$$

The anisotropy effective fields were inserted into equation 2.12. Solutions for $\vec{m}$ were found using the following ansatz $\vec{m} = (m_y\hat{y} + m_z\hat{z})\exp^{i\omega t}$. After linearizing the LLG equations, i.e. dropping all higher order terms in m_y, m_z and h, the following coupled system of equations was obtained:

$$i\frac{\omega}{\gamma}m_y + (\mathbf{B_{eff}} + i\alpha\frac{\omega}{\gamma})m_z = 0, \tag{2.22}$$

$$(\mathbf{H_{eff}} + i\alpha\frac{\omega}{\gamma})m_z - i\frac{\omega}{\gamma}m_y = h_{rf}M_s. \tag{2.23}$$

The z component of the LLG equation of motion also includes a large term proportional only to the large effective field components. This term is zero after minimizing the total Gibbs potential. It states that the dc torque is zero in equilibrium. The effective fields $\mathbf{B_{eff}}$ and $\mathbf{H_{eff}}$ are

$$\begin{aligned} \mathbf{B_{eff}} &= H_{dc}\cos(\varphi_M - \varphi_H) + 4\pi M_{eff} + \\ &+\frac{K_1}{2M_s}(3+\cos 4\varphi_M) + \frac{K_u^{\parallel}}{M_s}(1+\cos 2(\varphi_M-\delta)), \end{aligned} \tag{2.24}$$

$$\mathbf{H_{eff}} = H_{dc}\cos(\varphi_M - \varphi_H) + \frac{2K_1}{M_s}\cos 4\varphi_M + \frac{2K_u^{\parallel}}{M_s}\cos 2(\varphi_M-\delta). \tag{2.25}$$

Here δ is an angle f uniaxial axis with respect to the $\langle 100\rangle$ crystallographic direction and the demagnetizing factor $4\pi DM_s$ is grouped together with the perpendicular uniaxial anisotropy contribution:

$$4\pi M_{eff} = 4\pi DM_s - \frac{2K_u^{\perp}}{M_s}. \tag{2.26}$$

The transverse rf susceptibility χ_y can be found from the system of equations 2.22 and 2.23:

$$\chi_y \equiv \chi_y' + i\chi_y'' \equiv \frac{m_y}{h} = \frac{M_s\left(\mathbf{B_{eff}} - i\alpha\frac{\omega}{\gamma}\right)}{\left(\mathbf{B_{eff}} - i\alpha\frac{\omega}{\gamma}\right)\left(\mathbf{H_{eff}} - i\alpha\frac{\omega}{\gamma}\right) - \left(\frac{\omega}{\gamma}\right)^2}, \tag{2.27}$$

where χ_y' and χ_y'' are dispersive and absorbtive parts of the rf susceptibility, respectively. Ferromagnetic resonance occurs when the denominator of the susceptibility function χ_y is at minimum. Neglecting a small damping contribution to the resonance condition,

$$\left(\frac{\omega}{\gamma}\right)^2 = \mathbf{B_{eff}}\mathbf{H_{eff}}\mid_{H_{FMR}} \tag{2.28}$$

Eq. 2.27 shows that the dependence of χ_y'' on the externally applied field can be mathematically represented by a Lorentzian function centered around the FMR field H_{FMR} with a half width at half maximum $\Delta H = \alpha\frac{\omega}{\gamma}$:

$$\chi_y'' = \left(\frac{M_s\mathbf{B_{eff}}}{\mathbf{B_{eff}} + \mathbf{H_{eff}}}\right)_{H=H_{FMR}} \times \frac{\Delta H}{(\Delta H)^2 + (H_{dc} - H_{FMR})^2} \tag{2.29}$$

Perpendicular configuration: This is a special case for the out-of-plane orientation of $\overrightarrow{M_s}$ when the magnetization $\vec{M_s}$ and the external field $\vec{H}$ are strictly parallel with the film normal. Solving Eq. 2.12 for small deviations from equilibrium leads to

$$\left(\frac{\omega}{\gamma}\right)^2 = \left(H_{FMR} - 4\pi M_{eff} + \frac{2K_1^{\perp}}{M_s}\right)\left(H_{FMR} - 4\pi M_{eff} + \frac{2K_1^{\perp}}{M_s} - \frac{2K_u^{\parallel}}{M_s}\right) \tag{2.30}$$

For Gilbert damping and collinear configuration of $\overrightarrow{M}$ and $\overrightarrow{H}$ the FMR linewidth (in the field sweep) is strictly given by $\Delta H = \alpha\frac{\omega}{\gamma}$ independent of the ellipticity of the magnetization precession.

2.2 Damping in magnetic ultrathin films

Phenomenologically magnetic relaxation is described by the second term on the right hand side of Eq. 2.12. The magnetic damping parameter α is usually extracted from the frequency dependence of the FMR linewidth using the following relation:

$$\Delta H = \alpha\frac{\omega}{\gamma} = \frac{G}{\gamma M_s}\frac{\omega}{\gamma}. \tag{2.31}$$

For Gilbert damping ΔH is strictly proportional to the microwave frequency ω and inversely proportional to M_s. There is no explicit dependence on the applied field $\vec{H}$ and any magnetic anisotropies.

Magnetic damping is sample dependent, and therefore does not fully reflect the intrinsic properties of the material. Some processes are, however, unavoidable and are called intrinsic. In ultrathin films the Gilbert damping is caused by spin-orbit interaction and contains both bulk and interface contributions. The interface contribution can not be avoided and is considered to be intrinsic. Effects which are caused by structural defects and other inhomogeneities are, in principle, possible to avoid and are called extrinsic. The smallest damping, which satisfies the linear frequency dependence for the FMR linewidth (cf. Eq. 2.31) is by definition declared to be intrinsic.

Physical concepts, which describe intrinsic damping mechanisms, will be discussed in this section. Extrinsic damping mechanisms are addressed in Section 4.3.

2.2.1 Eddy currents

In metallic films, the magnetic damping can be affected by eddy currents. For thin films where the rf field fully penetrates the film the contribution of eddy currents to the magnetic damping can be evaluated by integrating Maxwells equations across the film thickness d. The resulting effective field has a Gilbert like form with α_{ed} (in Gaussian units) given by

$$\alpha_{ed} = \frac{M_s\gamma}{6}\left(\frac{4\pi}{c}\right)2\sigma d^2 \ , \tag{2.32}$$

where σ is the electrical conductivity and c is the velocity of light in free space. For Fe, the measured intrinsic Gilbert damping parameter is $\alpha_{Fe} \approx 2 \times 10^{-3}$ [18]. The effective eddy current Gilbert parameter becomes comparable to the intrinsic damping in Fe for film thicknesses of 40nm. G_{ed} is proportional to the square of the film thickness and therefore decreases rapidly with decreasing film thickness. In the ultrathin film limit, $d < 10$ nm, [19] eddy currents play no role in damping. For thick films one has to solve the LLG and Maxwells equations self consistently. The role of eddy currents in FMR for thick films has been quantitatively studied in references [20, 21] and is usually referred to as the exchange-conductivity mechanism.

2.2.2 Spin-orbit relaxation in metallic ferromagnets

The theory of Gilbert damping based on spin orbit scattering has been developed since the late sixties. It is of considerable interest these days due to its importance in spintronics applications. This section has been partially adapted from Heinrich's chapter on magnetic relaxations [13].

Spin flip scattering. The original model of relaxation based on spin-orbit interaction was introduced by Heinrich et al. [18]. The relaxation mechanism is caused by the s-d exchange interaction. The interaction of itinerant s-p like electrons with localized d-spins can be obtained from the integration of the s-d exchange energy density functional [22]:

$$H_{sd} = \sum_j \int_V J(\vec{r_j} - \vec{r})\mathbf{S}_{j.d}\mathbf{s}_s(\vec{r})dr^3 \ , \tag{2.33}$$

where $J(\vec{r_j} - \vec{r})$ is the s-d exchange interaction between the s-p electron spin density $\mathbf{s}_s$ and the localized d-electron spin density $\mathbf{S}_{j.d}$ where j is the lattice site. The transverse interaction Hamiltonian is described by three particle collision terms

$$E_{sd} = \left(\frac{2S}{N}\right)^{\frac{1}{2}} \sum_k J(\vec{q}) a_{\vec{k},\uparrow} a^+_{\vec{k}+\vec{q},\downarrow} b_{\vec{q}} + (h.c.) \ , \tag{2.34}$$

where N is the number of atomic sites, a, a^+ are electron annihilation and creation operators respectively, and b is a magnon annihilation operator. ↑ and ↓ correspond to the majority and minority spin electrons. This equation provides a particle representation of the s-d exchange interaction; its schematic representation is shown in Fig. 2.2. This process is Hermitian and would lead on its own only to renormalization of the gyromagnetic parameter γ. No damping would result from these interactions alone because the total angular momentum in the s-d exchange is conserved. In order to account for magnetic relaxation one has to consider incoherent scattering of $(a_{\vec{k},\uparrow} a^+_{\vec{k}+\vec{q},\downarrow})$ electron-hole pairs by thermally excited phonons and magnons. Phenomenologically incoherent scattering can

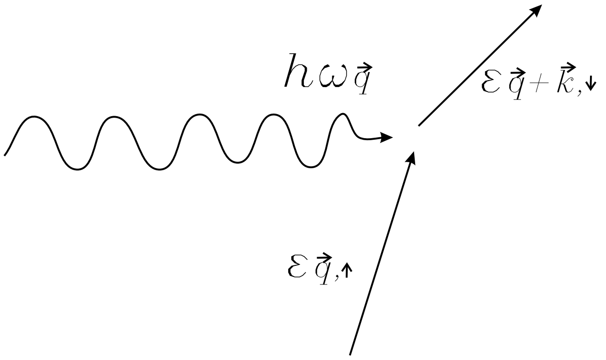

Figure 2.2: Schematic diagram of spin-flip scattering: a magnon having an energy $h\omega_{\vec{q}}$ collides with an itinerant electron having energy $\varepsilon_{\vec{k}}$ and spin $\uparrow$. This results in the annihilation of the magnon and the creation of an electron-hole pair. The hole energy and spin are the same as the initial electron. The excited electron carries the energy $\varepsilon_{\vec{k}+\vec{q}}$ and spin $\downarrow$. Notice that the spin of the electron-hole pair has to flip because the total spin momentum is conserved by the exchange interaction.

be accounted for by assigning a finite life time τ_{eff} for the electron hole pairs. This term modifies the electron hole pair energy:

$$\Delta\varepsilon_{\vec{k},\vec{k}+\vec{q}} = \varepsilon_{\vec{k}+\vec{q},\downarrow} - \varepsilon_{\vec{k},\uparrow} + i\frac{\hbar}{\tau_{eff}} \ , \tag{2.35}$$

where i is the symbol for the imaginary unit. The effective lifetime is described by the spin-flip lifetime τ_{sf}. The spin flip lifetime τ_{sf} is caused by the spin orbit interaction. The electron momentum lifetime τ_m, entering the conductivity, is caused by the electron interaction with phonons and magnons. Usually $\tau_{sf} \gg \tau_m$. The reason is that one needs to invoke the spin-orbit interaction to flip the electron spin during the relaxation of electron hole pairs by phonons. It was shown by Elliot [23] in the 50's that for simple metals

$$\tau_{sf} = \frac{\tau_m}{(g-2)^2} \ , \tag{2.36}$$

where g is the electron spectroscopic g-factor. The deviation of the g-factor from 2, its pure electron value, is caused by the spin-orbit coupling, which is much weaker in normal metals than in ferromagnets. Thus the above formula is not directly applicable to transition metals. In the case of a ferromagnetic metal it is better to calculate τ_{sf} from the spin diffusion length δ_{sd} using the following relation [24, 25, 26]:

$$\delta_{sd} = \left[\frac{\lambda^m_{FM} v_F \tau_{sf}}{6}\right]^{\frac{1}{2}} \ , \tag{2.37}$$

where v_F is the Fermi velocity of the electrons participating in the spin accumulation process. λ_{FM}^m , is calculated using the momentum mean free paths for minority $\lambda_\downarrow$ and majority $\lambda_\uparrow$ electrons:

$$\lambda_{FM}^m = 2\left[\frac{1}{\lambda_\downarrow} + \frac{1}{\lambda_\uparrow}\right]^{-1} = \frac{mv_F}{ne^2\rho^\star}, \tag{2.38}$$

where $\rho^\star = \rho^{DC}(1-\beta^2)$. Here ρ^{DC} is the measured resistivity of the ferromagnet and β is a bulk spin asymmetry coefficient. The calculations based on the theory proposed by Dubois et al. [25] and Piraux et al. [26] resulted in the following parameters: for permalloy (Py): $\tau_{sf}^{Py} = 3\times 10^{-14}$ s and $\tau_{sf}^{Py}/\tau_m^{Py} \simeq 20$. These parameters calculated for Co are: $\tau_{sf}^{Co} = 3.8\times 10^{-12}$ s and $\tau_{sf}^{Co}/\tau_{sf}^{Py} \simeq 300$.

The damping parameter due to spin-flip scattering can be calculated by using the Kubo Green function formalism in the Random Phase Approximation (RPA) [27]. α is usually expressed as an effective damping field:

$$\alpha\frac{\omega}{\gamma} = \frac{2\langle S\rangle}{Ng\mu_B}\sum_k |J(\vec{q})|^2 (n_{\vec{k}+\vec{q},\downarrow} - n_{\vec{k},\uparrow})\delta(\hbar\omega_{\vec{q}} + \varepsilon_{\vec{k},\uparrow} - \varepsilon_{\vec{k}+\vec{q},\downarrow}), \tag{2.39}$$

where the summation is carried out over the states available around the Fermi surface, $\langle S\rangle$ is the reduced spin $M_s(T)/M_s(0)$, and $n_{\vec{k},\uparrow}$ and $n_{\vec{k}+\vec{q},\downarrow}$ are the occupation numbers. The factor $g\mu_B$ was used to convert the relaxation energy into an effective relaxation field and δ stands for Dirac's delta function. The difference in occupation numbers is

$$\Delta n = n_{\vec{k}+\vec{q},\downarrow} - n_{\vec{k},\uparrow} = \delta(\varepsilon_{\vec{k}} - \varepsilon_F)\hbar\omega_{\vec{q}}\,, \tag{2.40}$$

where δ is Dirac's delta function and ε_F is the Fermi energy. This relation shows that the relaxation processes are limited to electrons at the Fermi level. Eq. 2.40 leads to an important conclusion: $\hbar\omega_{\vec{q}} = \hbar\omega$, the energy of the resonant magnons drives the scattering process. The Dirac δ function in Eq. 2.39 broadens into a Lorentzian due to incoherent scattering processes with thermally excited magnons and phonons:

$$\delta(\hbar\omega_{\vec{q}} + \varepsilon_{\vec{k},\uparrow} - \varepsilon_{\vec{k}+\vec{q},\downarrow}) \to \frac{\frac{\hbar}{\tau_{sf}}}{(\hbar\omega_{\vec{q}} + \varepsilon_{\vec{k},\uparrow} - \varepsilon_{\vec{k}+\vec{q},\downarrow})^2 + \left(\frac{\hbar}{\tau_{sf}}\right)^2}. \tag{2.41}$$

This Lorentzian function should be viewed as an expression for the probability of a scattering event. In FMR one usually studies magnon modes that are nearly homogeneous ($\vec{q} \simeq 0$). In that case the difference in the electron energy in a spin-flip processe is dominated by the exchange energy:

$$\varepsilon_{\vec{k}+\vec{q},\downarrow} - \varepsilon_{\vec{k},\uparrow} = 2\langle S\rangle J(0). \tag{2.42}$$

In a unit volume $N\langle S\rangle g\mu_B = M_s(T)$, where T is the absolute temperature. From this point one can show that the damping field is proportional to ω and inversely proportional to M_s. This is the direct finger print of Gilbert damping. The integration over the Fermi surface yields the damping parameter α:

$$\alpha_{sf} = \frac{\chi_{pauli}}{\gamma M_s \tau_{sf}} \ , \tag{2.43}$$

where χ_{pauli} is Pauli's susceptibility for the itinerant electrons. χ_{pauli} can be calculated by integration over the fermi surface k vectors:

$$\chi_{pauli} = \left(\frac{\hbar\gamma}{2\pi}\right)^2 \int k^2 dk \delta(\varepsilon_{\vec{k}} - \varepsilon_F) = \mu_B^2 N(\varepsilon_F), \tag{2.44}$$

where $N(\varepsilon_F)$ is the density of states at the Fermi level.

Scattering without spin flip. In the seventies Kambersky showed that the intrinsic damping in metallic ferromagnets can be treated more generally by using the spin-orbit interaction Hamiltonian [28].

The spin-orbit Hamiltonian corresponding to the transversal spin and angular momentum components can be expressed in a three-particle interaction Hamiltonian

$$H_{so} = \frac{1}{2}\left(\frac{2S}{N}\right)^{\frac{1}{2}} \xi \sum_{\vec{k}} \sum_{\alpha,\alpha',\sigma} \langle\beta|L^+|\alpha\rangle c^+_{\beta,\vec{k}+\vec{q},\sigma} c_{\alpha,\vec{k},\sigma} b_{\vec{q}} + h.c. \ , \tag{2.45}$$

where ξ is the coefficient of the spin-orbit interaction, and $L^+ = L_x + iL_y$ is the right handed component of the transversal atomic site angular momentum $\vec{L}_{a,t}$. $c_{\alpha,\vec{k},\sigma}$ and $c^+_{\beta,\vec{k}+\vec{q},\sigma}$ annihilate and create electrons in the appropriate Bloch states with the spin σ, and $b_{\vec{q}}$ annihilates the spin wave having the wave-vector $\vec{q}$. The indexes α and β represent the projected local orbitals of Bloch states and are used to identify the individual electron bands. For simplicity, no dependence of the matrix elements $\langle\beta|L^+|\alpha\rangle$ on the wave-vectors will be considered. The rf susceptibility can be calculated using the Kubo Greens function formalism in the random phase approximation (RPA) [27]. The effective damping field is given by

$$\alpha\frac{\omega}{\gamma} = \frac{1}{2}\frac{\langle S\rangle^2}{M_s}\xi^2 \left(\frac{1}{2\pi}\right)^3 \int d\vec{k} \langle\beta|L^+|\alpha\rangle\langle\beta|L^-|\alpha\rangle \tag{2.46}$$

$$\times\delta(\varepsilon_{\alpha,\vec{k},\sigma} - \varepsilon_F)\hbar\omega \frac{\frac{\hbar}{\tau_m}}{(\hbar\omega + \varepsilon_{\alpha,\vec{k},\sigma} - \varepsilon_{\beta,\vec{k}+\vec{q},\sigma})^2 + \left(\frac{\hbar}{\tau_m}\right)^2} \ ,$$

where $\langle S\rangle$ is the reduced spin at temperature T. Since no spin flip is present during the scattering, the relaxation time corresponds to the simple momentum relaxation time τ_m

which enters the conductivity. Note, that the effective damping field is proportional to the frequency and inversely proportional to the saturation magnetization as expected for Gilbert damping.

Intraband Transitions, $\alpha = \beta$: the Kambersky model was originally based on the observation that the Fermi surface changes shape with the direction of the magnetization [29]. This model corresponds to **intraband transitions**. This mechanism is relatively easy to describe using a classical picture. As the precession of the magnetization evolves in time and space the Fermi surface also distorts periodically in time and space. This is often referred to as a *breathing Fermi surface.* The ability of electrons to repopulate the changing Fermi surface states is delayed by the finite relaxation time of the electrons and this results in a phase lag between the Fermi surface distortions and the precessing magnetization. This is a typical scenario for frictional damping.

The electron energy balance in the denominator of 2.46 equals $\hbar\omega - (\hbar^2/2m)(2\vec{k}\vec{q} + q^2)$. For low-frequency spin waves such as those generated in (FMR) $q \ll k_F$ can be significantly less than $\frac{\hbar}{\tau_m}$. This limit is satisfied, even in good crystalline structures, for temperatures in excess of cryogenic temperatures and it significantly simplifies the integration over the Fermi surface. After the integration over the Fermi surface the Gilbert damping can be approximated by

$$\alpha_{intraband} = \tau_m \frac{\langle S\rangle^2}{\gamma M_s}\left(\frac{\xi}{\hbar}\right)^2 \sum_\alpha \chi^\alpha_{pauli}\langle\beta|L^+|\alpha\rangle\langle\beta|L^-|\alpha\rangle \ , \tag{2.47}$$

where χ^α_{pauli} are the Pauli susceptibilities of those states which participate in the intraband electron transitions and satisfy the low frequency limit. In this limit, the Gilbert damping is proportional to the relaxation time τ_m and consequently scales with the conductivity.

Interband Transitions, $\alpha \neq \beta$: Interband transitions are accompanied by energy gaps $\Delta\varepsilon_{\alpha\beta}$. The interband transitions are accompanied by dynamic orbital polarization, i.e. changes of the electron wave functions in addition to changes in their energies. The electron hole pair energy can be dominated by these gaps. For gaps that are much larger than the relaxation frequency $\frac{\hbar}{\tau_m}$ the Gilbert damping can be approximated by

$$\alpha_{interband} = \frac{1}{\tau_m}\frac{\langle S\rangle^2}{\gamma M_s}\sum_\alpha \chi^\alpha_{pauli}(\Delta g_\alpha)^2 \ , \tag{2.48}$$

where Δg_α is the deviation of the g-factor from 2, its purely electronic value. This deviation is in agreement with Baberschke's [30] calculation of Δg,

$$\Delta g_\alpha = 4\xi\frac{\sum_\beta\langle\alpha|L_x|\beta\rangle\langle\beta|L_x|\alpha\rangle}{\Delta\varepsilon_{\alpha\beta}}. \tag{2.49}$$

Δg_α determines the contribution of the spin orbit interaction to the spectroscopic splitting factor g. Notice that this is similar to the damping derived for the s-d exchange interaction, see eqs. 2.43 and 2.36. In this approximation, the Gilbert damping scales with resistivity. At temperatures greater than absolute zero, a large distribution of energy gaps modifies the overall temperature dependence. The interband damping can be expected to be dependent on resistivity only at low temperatures. At higher temperatures the relaxation rate $\frac{\hbar}{\tau_m}$ becomes comparable to the energy gaps $\Delta\varepsilon_{\alpha\beta}$, and this results in a gradual saturation of the interband Gilbert damping with increasing temperature.

The above equations for the intrinsic damping are not intended for real calculations. They just show the underlying ideas and parameters that enter into the understanding of the intrinsic damping in metals. This picture is simple and easier to follow than the existing more detailed theory. Complete quantitative calculations using a more sophisticated treatment of noise in the spin orbit interaction can be found in [28] and [31].

2.2.3 Magnetic relaxations at ferromagnet/normal metal interface. Spin pumping.

Magnetic multilayers provide a special case in which dynamic interactions between itinerant electrons and the magnetic moments in ultrathin films offers a new spin scattering mechanism. Non-local spin dynamics in metallic multilayers was first theoretically introduced by Tserkovnyak et al. [3]. This theory is based on a generalization of the Buttiker [32] theory. The derivation of spin dependent transmission through a FM/NM interface is rather complex and is addressed in Appendix B. This theory yields an expression for pure spin currents created at the FM/NM interface. The expectation value of the spin current, see Appendix B, is expressed in the following form:

$$\hat{I}_S^{pump}(t) = \frac{\hbar}{4\pi} A_r \left(\vec{n} \times \frac{\partial \vec{n}}{\partial t}\right) - \frac{\hbar}{4\pi} A_i \frac{\partial \vec{n}}{\partial t} \ , \tag{2.50}$$

where the interface scattering parameters A_r and A_i are given by

$$A_r = \frac{1}{2} \sum_{mn} (|r_{mn,U,\uparrow\uparrow} - r_{mn,U,\downarrow\downarrow}|^2 + |t_{mn,U,\uparrow\uparrow} - t_{mn,U,\downarrow\downarrow}|^2), \tag{2.51}$$

$$A_i = Im \sum_{mn} (r_{mn,U,\uparrow\uparrow} r^*_{mn,U,\downarrow\downarrow} + t_{mn,U,\uparrow\uparrow} t^*_{mn,U,\downarrow\downarrow}) \tag{2.52}$$

Additional Gilbert damping constant. Effectively Eq. 2.50 shows that the ferromagnetic layer pumps magnetic moment density away from the ferromagnet/normal metal interface. According to the spin conservation law the total spin momentum in the system must be conserved:

$$\frac{\partial \vec{S}}{\partial t} = -I_S^{pump} \; , \tag{2.53}$$

where $\vec{S}$ is the total spin momentum in the ferromagnetic film. It is related to the total magnetic moment of the ferromagnet by

$$\vec{M}(t) = \vec{n}(t) M = \gamma \vec{S} \; , \tag{2.54}$$

where $\gamma = \frac{g\mu_B}{\hbar}$ is the gyromagnetic ratio. The effect of spin pumping on the time evolution of the magnetization vector is then given by

$$\frac{\partial \vec{n}(t)}{\partial t} = -\frac{g\mu_B}{\hbar M} \vec{S} \; . \tag{2.55}$$

Using Eq. 2.50 one gets:

$$\frac{\partial \vec{n}(t)}{\partial t} = \alpha' \left(\vec{n} \times \frac{\partial \vec{n}}{\partial t} \right) \; , \tag{2.56}$$

where the additional Gilbert damping α' is given by

$$\alpha' = \frac{g\mu_B A_r}{4\pi M} \; . \tag{2.57}$$

Thus the presence of an interface in the spin dynamics leads to a spin momentum loss, i.e. additional damping which has the same form as the Gilbert damping phenomenology.

Spin pump/spin sink model in doublelayers Tserkovnyak et al. [3] and Heinrich et al. [4] have shown that an interface damping term can be generated by spin current pumping from a ferromagnet (F) into the adjacent NM layers, see Fig. 2.3. The spin current generated by the precessing magnetic moment in the layer F1 at the F1/NM interface causes a dynamic magnetic moment density to accumulate in NM. The direction of the spin current is perpendicular to the F/NM interface. For small precessional angles the pumped spin current is almost entirely transverse to the dc magnetic moment and proportional to the rf transverse magnetization. It is given by

$$\vec{I}_{sp} = \frac{\hbar}{4\pi} Re(2g_{\uparrow\downarrow})[\vec{\mathrm{n}} \times \frac{\partial \vec{\mathrm{n}}}{\partial t}] \; . \tag{2.58}$$

where, $g_{\uparrow\downarrow}$ is the spin mixing conductance in units of e^2/h and is determined by the transmission and reflection coefficients $t^{\uparrow}, t^{\downarrow}, r^{\uparrow}, r^{\downarrow}$ for the majority and minority spins in NM, respectively.

$$g_{\uparrow\downarrow} = \sum_l (1 - 2r_l^{\uparrow} r_l^{\downarrow *} - 2t_l^{\uparrow} t_l^{\downarrow *}) \approx 0.75 n^{\frac{2}{3}} \; , \tag{2.59}$$

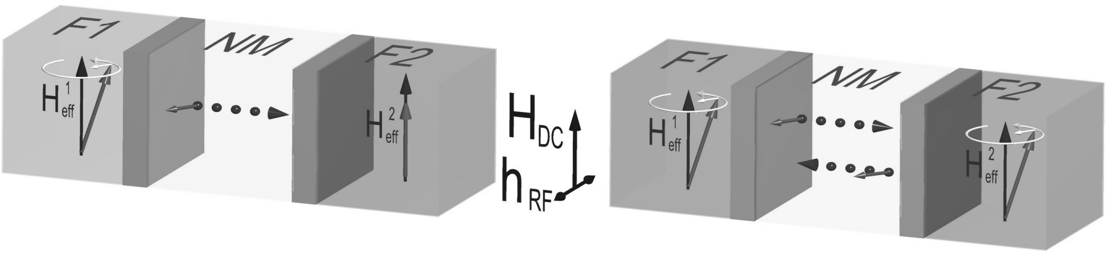

Figure 2.3: A schematic cartoon showing the spin current distribution inside a double layer structure. The left side represents the situation when only one magnetic layer undergoes FMR resonance. The spin momentum is pumped away from the layer resulting in an enhanced magnetic damping parameter. The right figure shows the spin current flow when both magnetic layers are at FMR resonance. The spin pumping process can be compensated by the spin sink effect, and therefore at the FMR peak the magnetic damping in both films drops to a value that is characteristic for Gilbert damping in the single layer films in the absence of the spin pumping effect.

where l is the number of spin channels at the Fermi level impinging on the F/NM interface and n is the density of electrons per spin in the normal metal, NM. The spin current generated at the F1/NM interface leads to an accumulated spin density $\vec{\mathbf{m}}_{NM}$ inside the NM spacer layer. In the spin ballistic limit $\vec{\mathbf{m}}_{NM}$ propagates with the Fermi velocity v_F of itinerant electrons and has equal probability to travel in both the forward and backward directions. The total spin current balance is given by:

$$\vec{I}_{sp} - 0.5 v_F \vec{\mathbf{m}}_{NM} = 0.5 v_F \vec{\mathbf{m}}_{NM} \tag{2.60}$$

In this expression one assumes that the return spin current is entirely absorbed at the F1/NM interface. This is strictly correct for a small precession angle where the spin momentum is perpendicular to the saturation magnetization moment [33, 13] and under these conditions the F1/NM interface acts as an ideal spin sink. Note that only half of the spin current is directed in the forward direction.

In magnetic double layers F1/NM/F2, in which the two static magnetic moments are collinear, the NM/F2 interface acts as an ideal spin sink. The pumped magnetic momentum from the F1/NM interface is fully absorbed at the NM/F2 interface providing an effective spin brake for the precessing magnetic moment in F1. This leads to the loss of spin momentum in the F1 layer. Conservation of the total angular momentum for the F1 layer (see eq. 2.61) leads to an additional damping in the F1 layer, which follows the phenomenology of Gilbert damping; the damping effective field is proportional $\partial\vec{M}/\partial t$. Its contribution scales inversely with the ferromagnetic film thickness [34, 35] and it therefore exhibits the interface nature of this effect, see eq. 2.62.

$$\frac{\partial \vec{S}^{FM}}{\partial t} + \vec{I}_{sp} = 0 \tag{2.61}$$

$$\alpha^{SP} = \frac{G_{sp}}{\gamma} = \frac{g\mu_B}{8\pi} g_{\uparrow\downarrow} \frac{1}{d} , \tag{2.62}$$

where μ_B is the Bohr magneton and d is the thickness of the ferromagnetic layer. An Fe layer can perform both functions; it generates the spin current (spin-pump) and absorbs the spin current (spin-sink) from the adjacent ferromagnetic layer. Evidence for this effect was found in the ferromagnetic resonance (FMR) line broadening observed in magnetic single [36] and double layers [34, 4] and see further references in the review article by Heinrich [13]. In magnetic single layers having a large precession angle the spin accumulation due to spin pumping was also detected by measuring the dc voltage across the FM/NM interface [37].

When the resonance frequencies are equal in both F films then the net transfer of spin momentum across the F1/NM and NM/F2 interfaces can be compensated resulting in zero interface damping [4]. The spin pump/spin sink effect can be included in the LLG equation of motion by the addition of two extra terms. For small precessional angles the magnetization dynamics in the presence of dynamic exchange coupling can be described by the following coupled set of Landau-Lifshitz-Gilbert equations [4]:

$$\begin{aligned} \frac{d\vec{\mathrm{n}}_i}{dt} &= -\mu_0\gamma \left[\vec{\mathrm{n}}_i \times \vec{\mathrm{H}}_{\mathrm{eff}}\right] + \alpha_i \left[\vec{\mathrm{n}}_i \times \frac{d\vec{n}_i}{dt}\right] \\ &+ \alpha_i^{\mathrm{SP}} \left[\vec{\mathrm{n}}_i \times \frac{d\vec{\mathrm{n}}_i}{dt} - \vec{\mathrm{n}}_j \times \frac{d\vec{\mathrm{n}}_j}{dt}\right] , \end{aligned} \tag{2.63}$$

where $\vec{\mathrm{n}}_i$ are the unit vectors along the instantaneous magnetization directions in F1 and F2, $i, j = 1, 2$ and $j \neq i$. The interface damping parameter α in a magnetic double layer when only one layer undergoes FMR is given by

$$\alpha_i^{\mathrm{SP}} = g\mu_B \frac{g_{\uparrow\downarrow}}{\mu_0 M_s} \frac{1}{d_i} , \tag{2.64}$$

where d_i is the film thickness, [38, 4]. Notice that the exchange of spin currents is a symmetric effect and the equation of motion for another layer is obtained by interchanging the indices $i \longleftrightarrow j$ in Eq. 2.63. The third and fourth terms on the right hand side of Eq. 2.63 represent the spin-pump and spin-sink effects, respectively. The third term is generated by spin-pumping in the layer i and the fourth term in eq. 2.63 is the absorbed spin current in the layer i due to spin pumping from the layer j. The signs $(+)$ and $(-)$ in the third and fourth terms in Eq. 2.63 represent the spin current directions.

The mutual exchange of spin currents between F1 and F2 can be viewed as a time dependent interlayer exchange coupling [4, 39]. In contrast to the static interlayer exchange coupling this coupling does not oscillate with the spacer thickness, it is almost independent of the interface roughness, and its range is limited only by the spin diffusion length [4].

2.3 Magneto optical Kerr effect

The magneto-optical Kerr effect was discovered at the end of the 19th century by Kerr [40]. In recent years it has become widely used for magnetization studies of thin films [41, 42]. The technique is based on a small rotation of the polarization plane of the reflected light which can be detected by a polarization vector analyzer. The physical origin of the Kerr effect lies in the spin orbit interaction. The spin orbit interaction contributes to the off -diagonal components of the optical permittivity tensor. This component is proportional to the direction of the instantaneous unit vector $\vec{n}$ parallel to the magnetization vector $\vec{M}$. A generalized dielectric permittivity tensor for a cubic material can be written [43, 44, 45, 46]:

$$\epsilon = \epsilon_0 \begin{pmatrix} 1 & -iQ_V n_z & iQ_V n_y \\ iQ_V n_z & 1 & -iQ_V n_x \\ -iQ_V n_y & -iQ_V n_x & 1 \end{pmatrix} . \tag{2.65}$$

Here Q_V is the Voight optical constant describing the magneto-optical rotation of the polarization plane. It can be rewritten as

$$\vec{D} = \epsilon_0(\vec{E} + iQ_V \vec{n} \times \vec{E}) \tag{2.66}$$

It follows from equation 2.66 that the polarization vector of the light rotates around the magnetization. The rotation of the polarization also occurs for light transmitted through a magnetized media and in this case it is called the Faraday effect [47]. However, the Faraday effect can only be observed in transparent materials. Nevertheless, for a full treatment of Maxwell's equations one needs to include both the transmitted and reflected light waves.

Depending on the mutual orientation of the incident light and the magnetization one can observe the polar, transverse or longitudinal Kerr effects. Only the polar Kerr effect was used in our studies and the discussion will be limited to this case. In a classical picture the origin of the polarization rotation can be understood if one considers the interaction of the electrons with the electric field of incident light. In particular, the motion of the electrons in a harmonic (crystal) potential will be driven by the electric field of the incident light, and the resulting Lorentz force due the extraordinary Hall effect produces a rotation of the optical polarization vector. The resulting force is

$$m\ddot{\mathbf{x}} + m\omega_0^2\mathbf{x} = e\mathbf{E_0}\exp^{i\omega t} + \chi[\dot{\mathbf{x}} \times \mathbf{B}] \ , \tag{2.67}$$

where $\mathbf{x}$ is the electron displacement, ω_0 is the oscillatory frequency of the atomic restoring force, and χ is the Lorentz's force coefficient, and ω is the angular frequency of the light. This electron displacement contributes to the electric polarization vector which contributes to the electric permittivity.

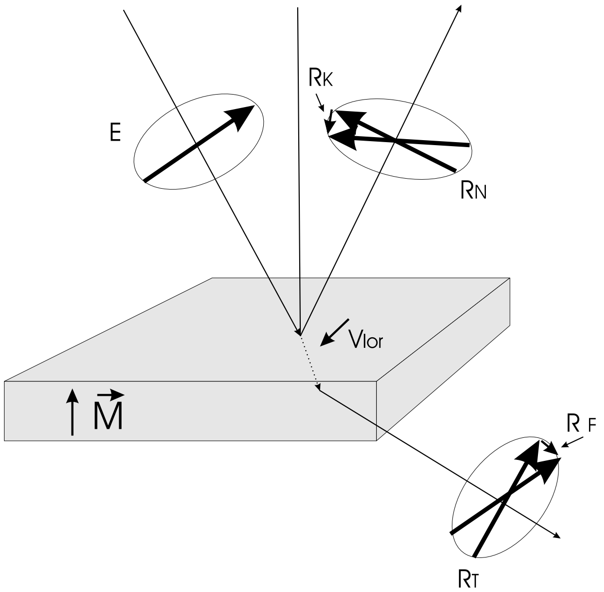

Figure 2.4: The polar magneto-optical Kerr and Faraday effects. R_N and R_T are the usual reflected and transmitted electric field amplitudes. R_F and R_K are generated as a result of the Lorentz force.

Let us assume that the magnetization in a film is oriented perpendicular to the surface, see Fig. 2.4, and the incident light is directed along the surface normal. Then a linearly polarized light beam will induce electron oscillations in the film. The reflected R_N and transmitted R_T light polarizations contain both diagonal and off diagonal components. The Lorentz force, see Eq. 2.67, induces the off diagonal components ϵ of the dielectric polarization vector. The superposition of R_T and R_N with R_F and R_K leads to the magnetization dependent polarization rotation.

The polar Kerr effect is proportional to the projection of the incoming light on the surface normal. For a particular geometry, and for a (001) oriented cubic crystal, the Kerr effect is almost independent of the orientation of the incident electric field vector.

Since the off diagonal elements of the susceptibility tensor ϵ are in general complex numbers the Kerr signal consists of two parts: a Kerr rotation Θ and a Kerr ellipticity ε, see Fig. 2.5(b).

In a multi-layer sample the total magneto-optical signal is a superposition of contributions from the different magnetic layers. For ultrathin films the driving electric field in a given layer has a constant amplitude and consequently the Kerr analysis becomes simplified. For this approximation to be valid the following condition has to be satisfied

$$t \ll \frac{\lambda_m}{abs(4\pi\varepsilon_{FM})^{\frac{1}{2}}} \approx 10nm, \tag{2.68}$$

where λ_m is the wavelength of the light inside the metallic film [48, 49]. Effectively ultrathin means that the profile of the electrical field generated by the incident light wave is not influenced by the presence of the ultrathin FM layers. Thus, if a structure contains several FM layers, the condition for the validity of the ultrathin approximation can be written as

$$\sum_i 4\pi[abs(\epsilon^i_{FM})^{\frac{1}{2}}]t^i \ll \lambda_m. \tag{2.69}$$

In a realistic experimental setup the Kerr signal is detected via comparing the Kerr signal with a reference signal. The ordinary reflected light usually plays the role of the reference signal. In the polar Kerr effect the polarization of the incident beam lies in the plane of the magnetic film due to the normal incidence (s-polarized). This significantly simplifies the data analysis since the simple unrotated portion of the reflected light for an s-polarized incident wave has the same polarization as the incident light wave. This fact in turn implies that the polarization of the additional signal due to the polar Kerr effect is strictly orthogonal in direction to the reference reflected light. This space separation is an essential feature which enables one to shift the time phase of the polar Kerr effect signal with respect to the reference light using a 1/4 wave plate. In magnetic double-layers the time phase of Kerr signals generated in the different layers is intrinsically different due to the different optical paths through the double-film structure. The magnitude of the Kerr signal is much smaller than the magnitude of the reflected light. If the time phase shift of a Kerr signal is $\pi/2$ shifted with respect to the reference light they add in quadrature and the contribution of that MOKE signal to the total light intensity becomes negligible. Using this technique one is able to realize depth resolved Kerr effect measurements.

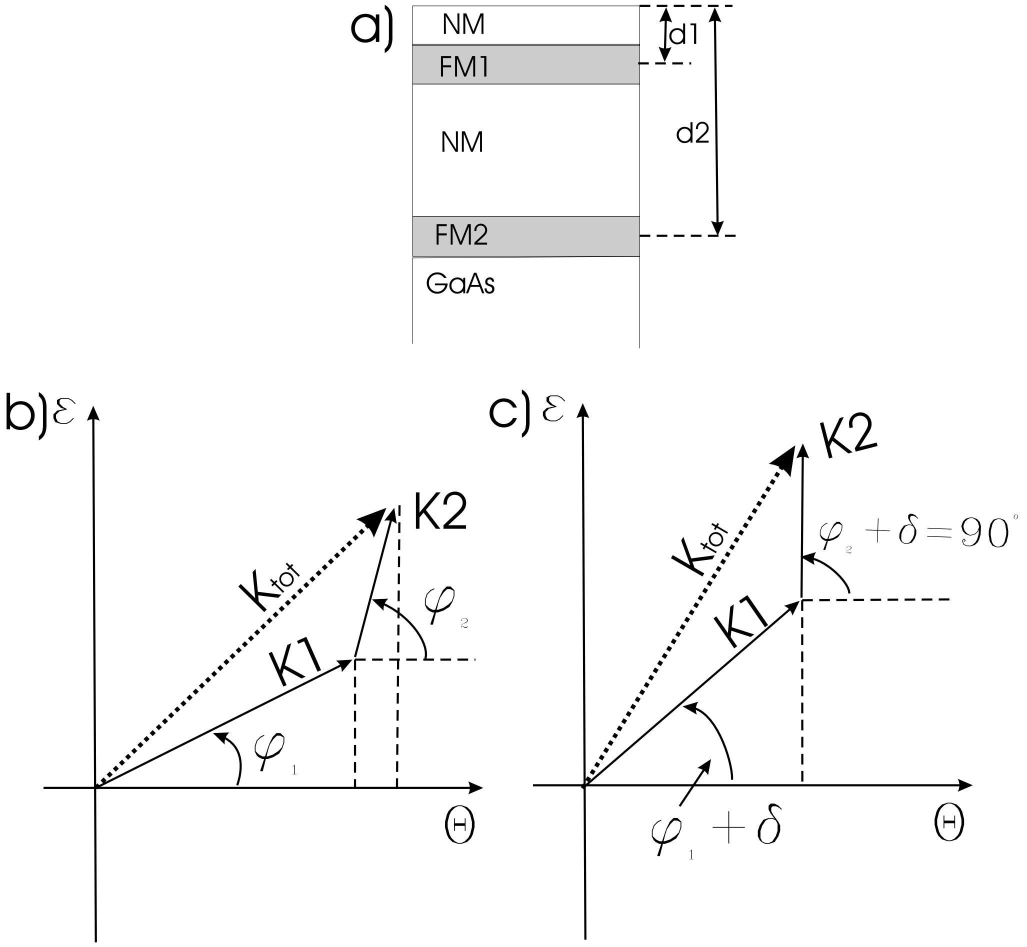

Figure 2.5: (a) shows a magnetic double layer sample composed of two ultrathin ferromagnetic films separated by a non-magnetic spacer layer. (b) - visualization of the Kerr effect in the $\Theta\varepsilon$ plane. The measured Kerr signal for each FM layer is obtained from the projection of the Kerr vector K(i) on the axis of polarization rotation. The magnitude of the detected signal for each layer is determined by the angle φ_i. (c) shows the effect of a 1/4 wave plate. Here a phase shift δ is applied to the phases of the Kerr signal. The phase shift δ is adjusted such that the Kerr signal from the bottom layer, K2, is shifted $\frac{\pi}{2}$ with respect to the reference signal.

I have to point out that this simple argument does not portray the full picture. One has to include the complex nature of the Kerr effect which leads to an elliptical polarization [50, 51, 52, 49].

The complex Kerr effect K can be visualized as a Kerr vector in the complex plane, here called the $\Theta\varepsilon$ plane. The $\Theta\varepsilon$ plane used for an analysis of the depth sensitivity corresponds to a small region in the Cartesian complex plane of polarization around the point representing the polarization of the incident wave [53]. For the structure presented in Fig. 2.5(a) the representation of the polar Kerr effect on the $\Theta\varepsilon$ plane fulfills the following properties (cf 2.5(b)):

- The projection of the Kerr vector on the real axis gives the Kerr rotation Θ, and the projection on the imaginary axis the Kerr ellipticity ε. The length of the Kerr vector corresponds to the Kerr amplitude K and its orientation to the Kerr phase φ.

- For a given multi-layer structure the polar Kerr effect K(i) originating from the ith layer is proportional to the z component of the magnetization $\vec{M}_i$, where the z axis is defined to be normal to the film plane, and the x and y axes both lie in the plane of the film. The additivity of the Kerr effect is represented in Fig. 2.5(b) by the summation of Kerr vectors for the individual FM layers.

- In the case of the polar Kerr effect the experimental setup measures a Kerr signal S, which is the projection of the complex Kerr effect K onto the real axis Θ, see Fig. 2.5(b).

The variation of the Kerr phase φ can be realized by means of a 1/4 wavelength compensator, giving a phase shift δ to the Kerr signal. The 1/4 waveplate is placed in the reflected light beam. For a properly adjusted δ the elliptically polarized Kerr signal will be transformed into linearly polarized light. Note that now the reference reflected light and the Kerr signal do not have orthogonal polarizations in space due to the Kerr signal ellipticity. This means that one should alter the polarization of the incident light together with the Kerr phase shifter in order to obtain a unique situation in which the polarizations of the reflected light and the Kerr induced wave are orthogonal. This technique was first demonstrated by Schaefer et al. on magnetic doublelayers [54]. In doing so one can set the phase of the Kerr signal from one of the layers (cf. 2.5(c)) to be $\pi/2$ shifted with respect to the reference light, i.e. one can make Kerr signal from this layer undetectable. The Kerr signal from the other layer will, however, be still measurable, due to an extra phase shift introduced by the additional path of the light through the non magnetic spacer. This complex situation has been analytically addressed by Hamrle et. al, [55].

Chapter 3

Experimental techniques and apparatus

Experimental work requires a thorough expertise and in-depth understanding of the physical processes which lie behind the equipment operation. Having this expertise one is able to minimize errors and optimize the efficiency of measurements. With the fast progress in technology novel tools are available to experimentalists. Some of them can potentially lead to a new experimental setup, while others can significantly simplify existing experimental procedures. Computerization and automation of the experiments is important and useful. It allows one to optimize and improve the quality of the data collection and analysis. The chapter is organized in the following way: In Section 3.1 the molecular beam epitaxy (MBE) system is highlighted. This includes the characterization, analysis techniques, and ultrathin film preparation. In Sections 3.2 and 3.3 the ferromagnetic resonance (FMR) and magneto-optical Kerr effect (MOKE) for magnetic characterization will be described.

3.1 Ultra-high vacuum Molecular Beam Epitaxy system

The core of the Surface Science Laboratory at Simon Fraser University is an ultra-high vacuum chamber and associated devices (UHV chamber). This chamber is used for sample preparation and characterization. The UHV chamber is split into 4 major subsections: (a) Introduction chamber: this chamber is used for H cleaning of GaAs substrates and sample outgassing. (b) Analysis chamber: this chamber contains an

Ar^+ sputtering source, and apparatus for Auger electron spectroscopy and for X-Ray photoelectron spectroscopy. (c) Growth chamber: this chamber is equipped with 8 thermal sources for metal and oxide deposition, and contains a Reflection High Energy Electron Diffraction (RHEED) setup for growth monitoring. (d) Scanning tunnelling microscopy(STM): this chamber is equipped with a commercial large sample STM/AFM Omicron STM for surface analysis.

The schematic diagram of the MBE system is shown in Fig.3.1. The UHV Chambers are separated by valves 1, 2, 3 and 14. This setup provides for differential pumping and enables one to work independently in every chamber. A sample transfer mechanism between the chambers is realized by using arms 9, 15 and 21. Transfer arm 21 is equipped with azimuthal and polar rotation degrees of freedom which allows one to obtain multiple sample orientations inside the UHV system. This arm is also equipped with a temperature control stage. Ultimate low UHV pressures are achieved by using several pumps. The loadlock is pumped using the turbo pump 8. The intro chamber is pumped by means of a turbo pump 23 and an ion pump 4 which includes a titanium sublimator. The STM chamber is pumped using the ion pump 5. The analysis chamber is pumped using the ion pump 6 and the growth chamber is pumped using the ion pump 7 which includes a titanium sublimator. The samples and STM tips can be stored in UHV in the storage arm 22. The elemental and chemical composition of the epitaxial films were determined by means of Auger Electron Spectroscopy (AES) and X-ray Photoelectron Spectroscopy (XPS).

3.1.1 Auger Electron Spectroscopy (AES)

Auger spectroscopy is employed to monitor the composition of deposited films [56]. The AES technique is surface sensitive, however when combined with an Ar sputtering gun it can be used to measure the composition across the thickness of the sample film structure [57]. The primary electron beam of 3 keV is used to generate Auger electron excitations (see electron gun 13 in figure 3.1). The escape depth of the Auger electrons is dependent on their kinetic energy and does not exceed a few nm; this makes AES a near surface sensitive technique [58, 59]. An Auger process is shown in Fig. 3.2; in this particular case a primary electron ionizes the K shell; the created vacancy in the K-shell is then filled with an electron from the outer shell L', and the released energy $E_K - E_{L'}$ is transferred to an Auger electron. The kinetic energy of the emitted Auger electron is given by the excess energy $E_K - E_{L'} - E_{L''}$, and therefore it is characteristic of the

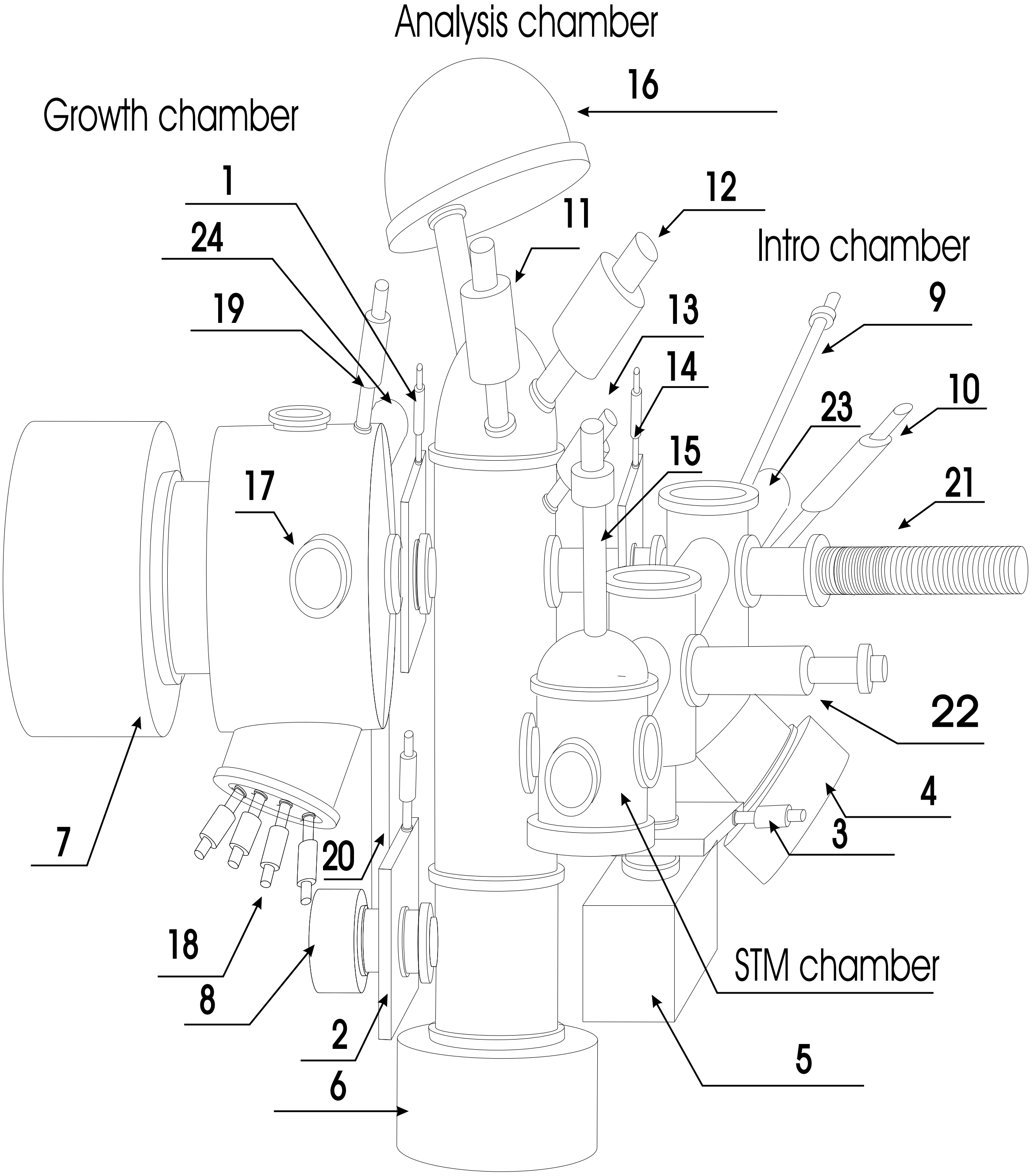

Figure 3.1: UHV chamber. Numbers indicate specific chamber elements, referred to in the text.

individual elements. The emitted electrons are collected by means of the hemispherical analyzer 16, which allows one to obtain electron counts in the energy window ΔE as a function of the kinetic energy E. In a hemispherical analyzer (see item 16 in figure 3.1) the energy window ΔE is constant and is set by the pass energy (usually 140 eV) . The Auger peaks appear on a large electron count background coming from inelastically scattered electrons. The sample composition is determined by calculating the area under the Auger peak for every element and weighting it with the corresponding sensitivity coefficients as provided by the manufacturer [60].

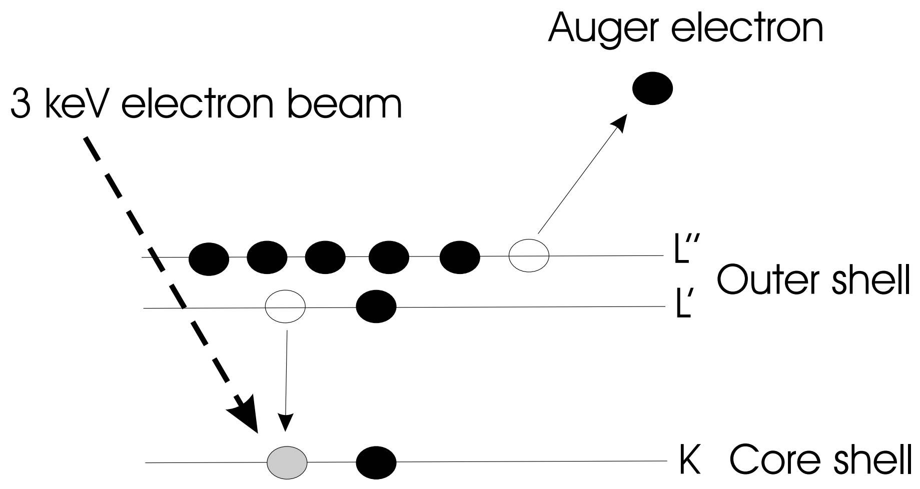

Figure 3.2: Schematic picture of the Auger electron emission process. An outer electron falls into the inner orbital vacancy, and a second electron (Auger electron) is emitted carrying away the excess energy.

3.1.2 X-Ray Photoelectron Spectroscopy (XPS)

The XPS technique allows one to identify the chemical elements and their chemistry (participation of elements in chemical compounds). XPS electrons are excited by irradiating sample with a soft X-Ray beam generated by the X-ray source 11, see figure 3.1. The X-ray source represents an electron gun in combination with Al or Mg targets [61]. When electrons accelerated to 15 keV hit the target the resulting X-Ray beam includes a strong component at an energy specific to the target: MgKα x-rays (1253.6 eV) or AlKα x-rays (1486.6 eV). These photons interact with atoms via the photoelectric effect [56], which is schematically shown in Fig. 3.3. The emitted photoelectrons are analyzed using the hemispherical electron analyzer 16, see Fig. 3.1. The kinetic energy of the emitted electrons is given by:

$$KE = h\nu - BE - \varphi_s \tag{3.1}$$

where $h\nu$ is the energy of the X-ray photon, BE is the binding energy of the atomic orbital from which the electron originates and φ_s is the spectrometer work function. The photoemission electron sometimes results in an Auger process so that Auger electrons are included in a XPS binding energy scan. However the Auger electron energy does not depend on the primary x-ray beam energy thus the binding energy of Auger electrons is changed by switching x-ray targets and can be easily distinguished from photoelectron peaks. This feature is particularly useful in multi-element samples where the Auger and XPS peaks can overlap. Soft X-rays interact weakly with matter and therefore exhibit narrow XPS lines which enable one to resolve small shifts in the binding energy due the chemical environment: this is usually referred to as chemical shifts in the XPS spectra. The penetration depth of soft X-Rays in solids is of the order of microns due to their weak interaction with matter, and this means that the specimen atoms are excited far beyond the surface layer. Nevertheless only photoelectrons generated within a thin layer of 2 to 20 Angstroms [58, 59] from the surface are able to escape the sample without an energy loss due to the electron-electron interactions. This makes XPS a surface sensitive technique.

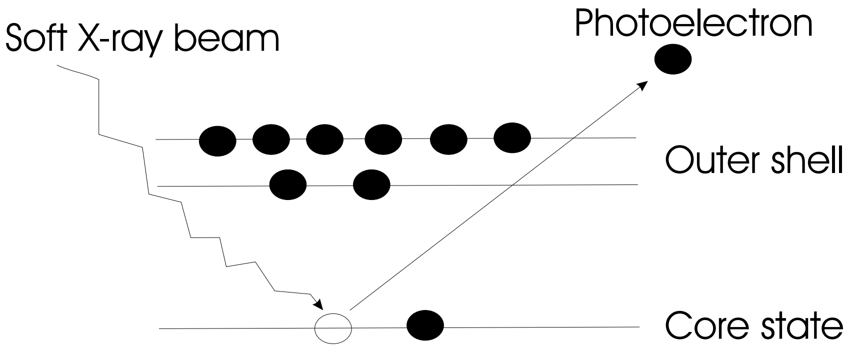

Figure 3.3: XPS schematics. A photoelectron is emitted from the core shell as a result of the interaction between the incident soft X-Ray beam and specimen atoms.

Using Auger and XPS techniques we were able to obtain the composition of samples with an uncertainty of approximately 0.1 monolayer. The high sensitivity of the AES and XPS techniques enabled us to prepare contamination free substrates and to analyze surfactant effects in multi-layers.

3.1.3 Reflection High Energy Electron Diffraction (RHEED)

In order to characterize the crystallographic structure of a specimen one has to obtain the lattice symmetry and analyze the long range coherence between the atoms in the lattice. Reflection High Energy Electron Diffraction (RHEED) is a suitable technique for obtaining this information. It is easily compatible with a UHV setup and can be used to continually monitor the specimen structure and thickness during its preparation. The RHEED system consists of two elements which are located in the growth chamber: the electron gun 24 and photoluminescent screen 17 (see Fig. 3.1). These are positioned such that the 10 keV electron beam impinges at a glancing angle of a few degrees upon the specimen surface during the deposition, and the beams reflected from the specimen hit a photoluminescent screen. A CCD camera was used to monitor the diffraction pattern and its time evolution during the sample growth. A schematic representation of the RHEED system is shown in Fig. 3.4. The energy of the diffracted electrons maintains the energy of the primary incident beam, while their momentum changes. It can be visualized utilizing the concept of the Ewald sphere [62, 63], see figure 3.4. The Ewald sphere is centered on the sample surface with a radius equal to the $\vec{k}_0$ wave-vector of the incident electrons:

$$|\vec{k}_0| = \frac{2\pi}{\lambda} \tag{3.2}$$

where $\vec{k}_0$ is the wave-vector of the incoming beam, and λ is the wavelength of the incident electrons. The diffraction conditions are satisfied for angles such that the rods of the two-dimensional crystal reciprocal lattice intersect Ewald's sphere. Since the glancing primary electrons do not penetrate inside the sample lattice the reciprocal lattice rods are given by the reciprocal space of the surface atoms. The elastic scattering process requires:

$$|\vec{k}_0| = |\vec{k}_d| \tag{3.3}$$

where $\vec{k}_d$ is the wave-vector of the diffracted beam. The directions of the diffracted beams on the Ewald sphere are given by the following equations:

$$\vec{G} = \vec{k}_d - \vec{k}_0 \tag{3.4}$$

where $\vec{G}$ is given by:

$$\vec{G} = \hat{x}n\frac{2\pi}{a} + \hat{y}m\frac{2\pi}{a} + \hat{z}z \tag{3.5}$$

where a is the surface lattice constant for a square surface net, n and m are integers, and z is the perpendicular k-vector chosen to satisfy equation 3.3. As can be seen from equation 3.5 and figure 3.4 many reciprocal lattice rods meet the diffraction condition, however in a real RHEED system one is able to see only the low order diffraction beams at the fluorescent screen, see Fig. 3.4. The RHEED pattern at the detector screen is a projection of only those k vectors which are within the angular range subtended by the detector. The separation between the diffraction beams with the primary beam oriented along the main symmetry azimuths allows one to determine the surface lattice symmetry and spacing. RHEED allows one to monitor the surface structure including surface reconstructions that occur for certain materials [64], see Fig. 3.9b.

The RHEED technique is extremely useful for monitoring the quality of the epitaxial growth as well as the film thickness. During a quasi layer by layer growth (the surface roughness is mainly limited to the top two atomic layers) the intensity of the specular spot, see figure 3.4 oscillates with the film thickness [65]. Each full period of the RHEED intensity oscillations corresponds to the formation of a new atomic layer. The presence of RHEED intensity oscillations is partly a consequence of the interference between electrons scattered from exposed atoms in the top two atomic layers and partly a consequence of diffuse scattering from the oscillating surface roughness. The strongest RHEED oscillations are obtained using an incident angle such that the electrons impinging on the sample surface satisfy the anti-Bragg diffraction condition. This means that electrons reflected from atoms in the top layer and electrons reflected from the exposed atoms in the second layer are out of phase. A full coverage will produce a smooth surface leading to a maximum in the RHEED intensity, whereas a full layer covered by a half layer represents a rough surface leading to a minimum in the RHEED intensity. To obtain well pronounced RHEED oscillations one has to maintain good layer by layer growth. In certain cases more than 40 oscillations were observed, see Fig. 3.5.

3.1.4 In-situ Scanning Tunnelling Microscope

The k space information describing the specimen obtained using RHEED was correlated with the real space specimen images acquired using scanning tunnelling microscopy (STM). An in situ commercial Omicron Large sample STM/AFM chamber [66] is a part of the Surface Science Laboratory UHV system, see figure 3.1. A clever design of the STM/AFM tip mounting stage enables one to replace tips and change the mode of operation from STM to AFM without opening the UHV chamber (AFM stands for Atomic

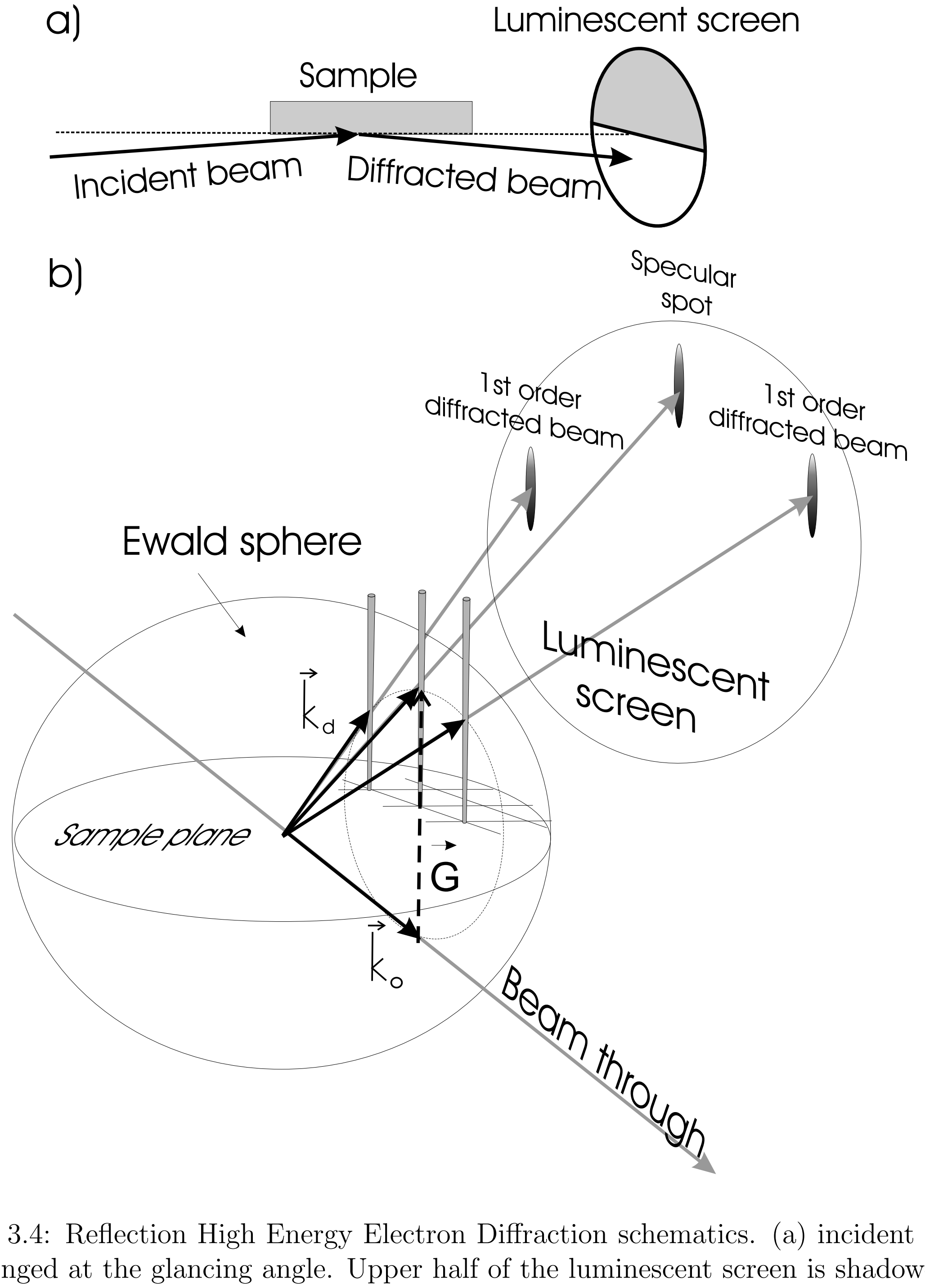

Figure 3.4: Reflection High Energy Electron Diffraction schematics. (a) incident beam is impinged at the glancing angle. Upper half of the luminescent screen is shadowed by sample. Diffracted beam impinges on the lower half of the luminescent screen. (b) The RHEED construction of the Ewald Sphere at the sample surface. The angle of incidence shown in the figure is different from glancing incidence in order to illustrate the Ewald sphere in a cartoon. The radius of the Ewald sphere is equal to the magnitude of the $\vec{k}_0$ vector. The $\vec{k}_d$ vectors, correspond to diffraction beams satisfying the surface lattice symmetry and energy conservation. G vector is the difference between the $\vec{k}_d$ and $\vec{k}_0$ vectors.

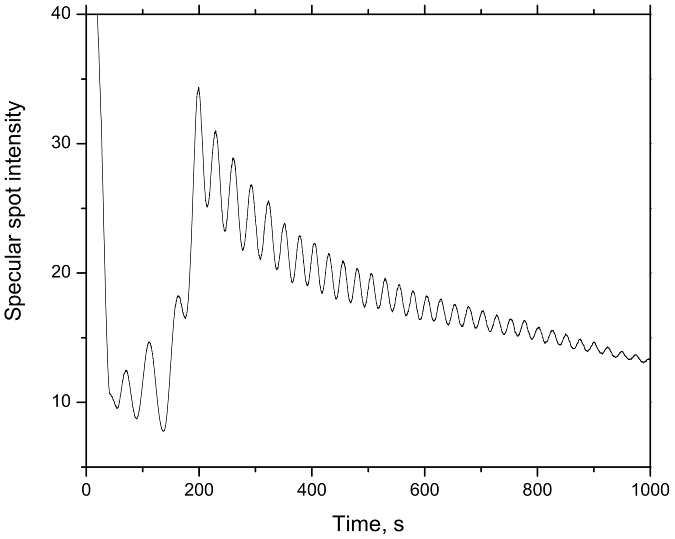

Figure 3.5: Example of RHEED intensity oscillations of Fe grown on GaAs. Steady layer by layer growth was observed.

Force Microscope). Tips and samples are transferred to the STM/AFM stage from the Growth and Analysis chambers using transfer arms 9 and 15, see figure 3.1. The principle of the STM technique is shown in Fig. 3.6. A bias voltage between the sample and tip is set to create hot electrons and to stimulate the tunnelling process. The STM tip is kept at a distance of approximately two nanometers from the sample surface in such a way as to maintain a steady tunnelling current. Fine positioning of the tip relative to the sample surface is achieved using a 3 axis piezoelectric tube. The constant current regime is realized using a commercially available Scala feedback system [67], which controls the voltage operating the z direction of the piezoelectric tube (the STM tip-sample surface distance) according to the detected tunnelling current.

The STM image is obtained via scanning the tip across the surface of the sample and mapping the vertical position of the STM tip on a single graph as a function of the x and y directions. To insure high quality STM images one has to use a stable and reliable STM tip. For our experiments we used etched PtIr commercially available STM tips from the Molecular Imaging company. The STM device enabled us to obtain a subatomic resolution of surface atoms. The STM images were essential for the characterization of the substrate template and film surface roughness and surface reconstructions.

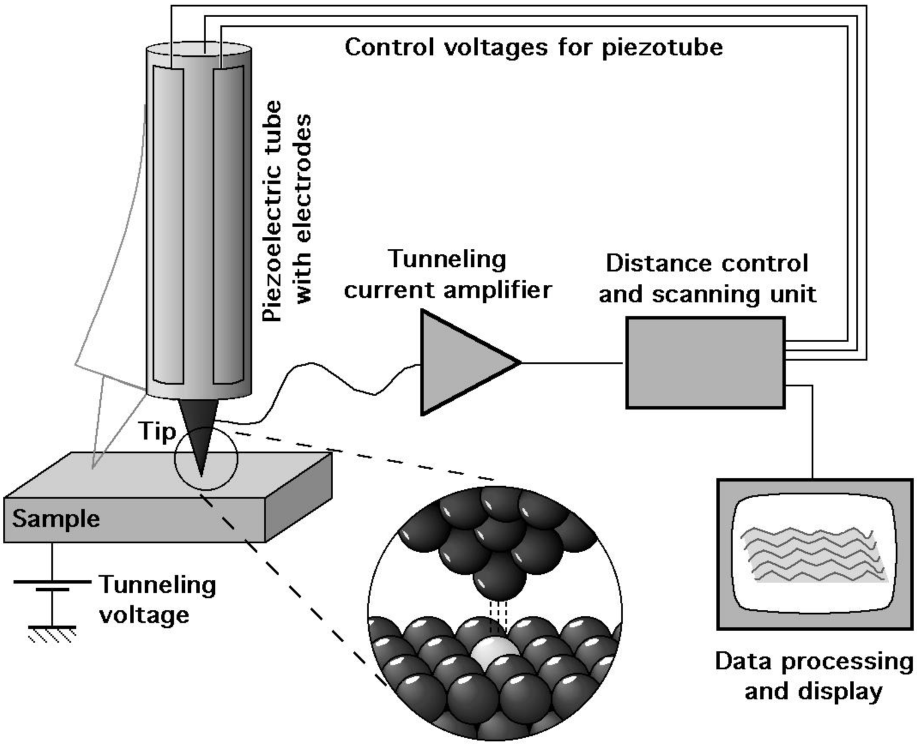

Figure 3.6: A schematic diagram of the STM apparatus. A conducting tip is brought close to the specimen surface to establish a steady tunnelling current. The tip position is adjusted by means of a 3-axis piezoelectric tube. Tunnelling current is recorded as a function of the lateral position of the tip. The surface STM image is reconstructed using a SCALA image acquisition unit.

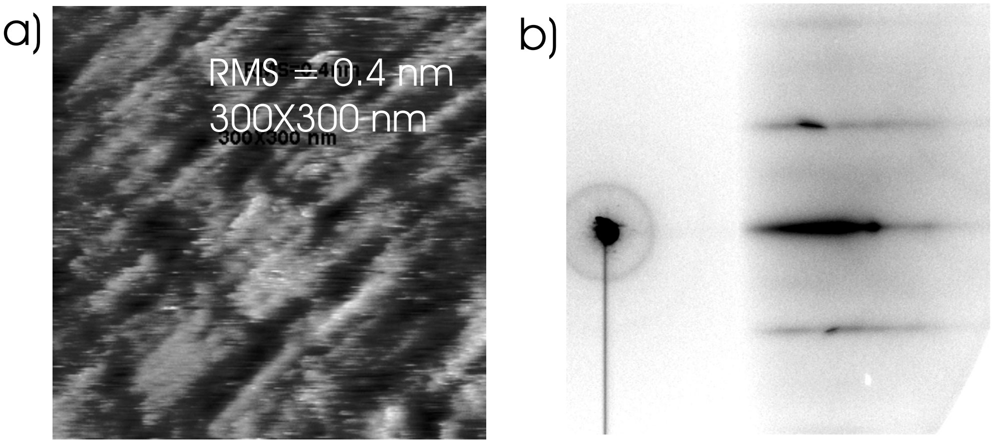

Figure 3.7: (a) STM image of the hydrogen cleaned GaAs substrate surface. Hydrogen cleaning at 400° C results in partial annealing of the substrate, see the relatively large terraces. A terrace step exceeds 1 atomic layer and results in a relatively large RMS surface roughnes. (b) shows a RHEED diffraction pattern with the electron beam oriented along the $[1\bar{1}0]$ crystallographic direction. Shadowed areas between the main diffraction streaks indicate a partial reconstruction of the prepared substrate.

3.1.5 GaAs substrate preparation

Magnetic thin films for our experiments were grown on GaAs single crystal substrates. GaAs substrates were chosen for several reasons: firstly its lattice constant is only 1.4% different from the double lattice constant of bcc Fe, which ensured layer by layer epitaxial growth of Fe on GaAs. Secondly the Fe/GaAs interface creates a strong uniaxial magnetic anisotropy in Fe and this property was used to identify the magnetic signals due to each Fe layer in Fe/NM/Fe/GaAs multi-layers, where NM stands for a non-magnetic metal spacer layer. And finally, GaAs is a semiconductor, which creates an opportunity to integrate magnetic structures into modern semiconductor technology. Commercial epi-ready GaAs wafers produced by American Xtal Technology were found to be a reliable and accessible source of substrates. The sample holder and substrate were exposed to the environment and thus they were contaminated by oxides and carbon. To remove contaminants from the molybdenum sample holder and to ensure that the ultra high vacuum was maintained during the substrate preparation temperature cycling it was enough to outgas the introduced sample at 350° C for 4 hours. Subsequently the following procedure was applied to prepare the GaAs for the Fe deposition:

H^+ cleaning: Non-destructive H^+ cleaning was used to remove contaminants from the GaAs surface. To create a beam of extremely reactive hydrogen atoms we used a commercial OS-Crack Thermal Gas Cracker from Oxford Scientific, see item 10 on figure 3.1. The gas cracker uses electron bombardment to produce intense localized heating of a tungsten capillary. The electrons were accelerated to 1.1 kV with a current of 35 mA to produce a total heating power of 39 W delivered to a small area thereby creating a high power density and producing temperatures in excess of 1500° C. Molecular hydrogen passing through the hot capillary was dissociated into hydrogen atoms, which impinged on a GaAs substrate that was preheated to 400° C. The hydrogen atoms formed stable chemical compounds with oxygen and carbon which were evaporated from the epi-ready GaAs surface. The base pressure in the system during the hydrogen cleaning was set to $5x10^{-7}$ Torr by opening the H_2 leak valve. This pressure may be destructive for the ion pump and thus pumping was carried out using the 500 L turbo pump and the titanium sublimator. After exposure of the sample to the H^+ beam for 30 minutes Auger spectroscopy detected only residual amounts of oxygen and carbon on the GaAs surface (oxygen and carbon line intensities were within the noise level (less then equivalent of 0.1ML) of Auger technique).

H^+ atoms are very reactive and are the lightest possible elements. Due to these factors the H^+ technique quickly removes all contaminants from the GaAs surface without penetrating deeply into the GaAs structure. The disadvantage of this technique is that the temperature of the substrate is elevated to a temperature of 400° C, which causes partial annealing of the GaAs surface. STM and RHEED images of a H^+ treated GaAs surface are shown in figure 3.7. The STM clearly shows quite large terraces, however the RMS roughness is approximately 0.4 nm, which is close to the lattice parameter of GaAs. This is in good agreement with the RHEED image, where we observe a streaky type of picture. This indicates a two dimensional type of surface. The large terraces characteristic of the GaAs surface represent a stable structure. Further annealing of GaAs at 600° C temperature has very little effect on the topography. It is also worth noticing that the GaAs crystallographic structure is not perturbed by the H^+ cleaning technique. As a result one might expect that the required 4X6 reconstruction of the GaAs surface is not easily reached since mobility of the atoms inside the lattice is much less than the mobility of atoms in the disordered state. Moreover there is a possibility for trace amounts of H^+ atoms to remain inside the GaAs.

Ar$^+$ sputtering: In order to remove the residual contaminants and to reshuffle the surface atoms the GaAs substrate was exposed to 3 hours of Ar$^+$ sputtering at room temperature. The Ar$^+$ gun 12, see Fig. 3.1, was used for the Ar ion bombardment of the GaAs. Parameters of the ion beam were set as follows: accelerating voltage equals -650 V with the emission of approximately 25 mA of Ar$^+$. Ar was inserted into the system through a leak valve, and the back-pressure was adjusted to 1x10^{-7} Torr. The Ar pressure in the gun was close to 7.5x10^{-5} Torr. A focused Ar$^+$ beam was rastered across the GaAs surface. Ar is a noble gas with a quite high atomic mass, consequently it is not reactive and was easy to pump out using the 500L turbo pump. The large atomic mass of Ar insures a strong interaction between the Ar ions and the GaAs substrate, and bombardment from a constant position may result in a preferred direction of surface formation. The sample was rotated during the Ar$^+$ bombardment to minimize this effect.

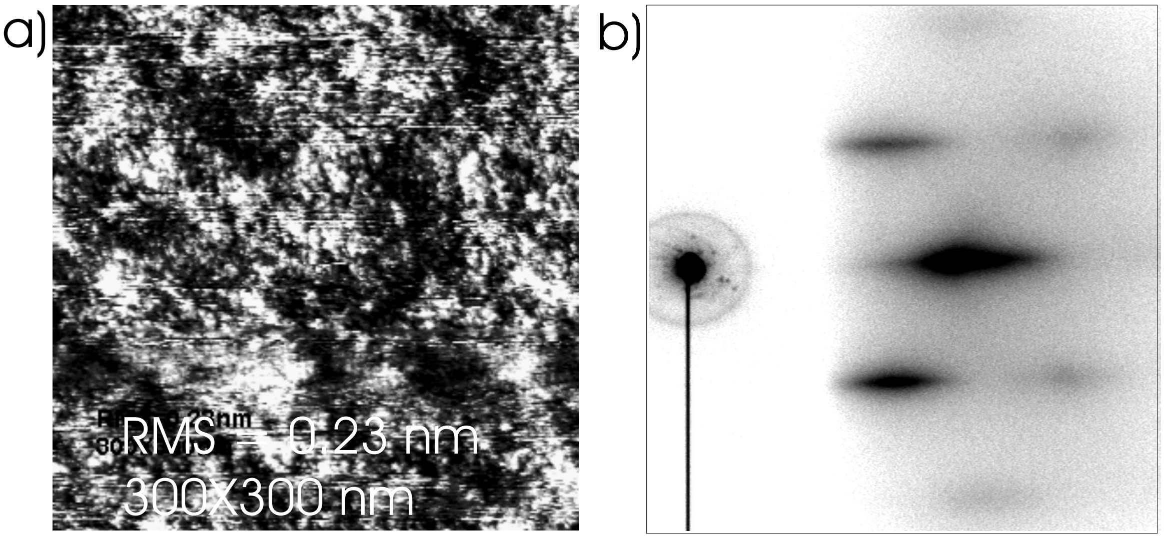

Figure 3.8: (a) An STM image of the sputtered GaAs. The azimuthal rotation applied to the sample during sputtering results in a uniformly rough surface clean of contamination. (b) shows the RHEED diffraction pattern of the same surface. It indicates an unreconstructed three dimensional template.

Auger spectroscopy indicated full removal of contaminants from the GaAs surface. The stoichiometry of the Ga and As was close to that expected for GaAs. The topology of a GaAs surface formed after the Ar$^+$ treatment was studied using STM and RHEED, see Fig. 3.8. The STM image shows a uniformly disordered surface with terraces less than 2 nm wide. The RMS roughness of this image is only 0.23 nm, which insures that sputtering did not lead to the formation of 3 dimensional large scale structures. The RHEED image confirms the small size of the terraces and the three dimensional nature of the surface. A transformation of the RHEED streaks into separate spots observed after H$^+$ cleaning indicates shorter terraces.

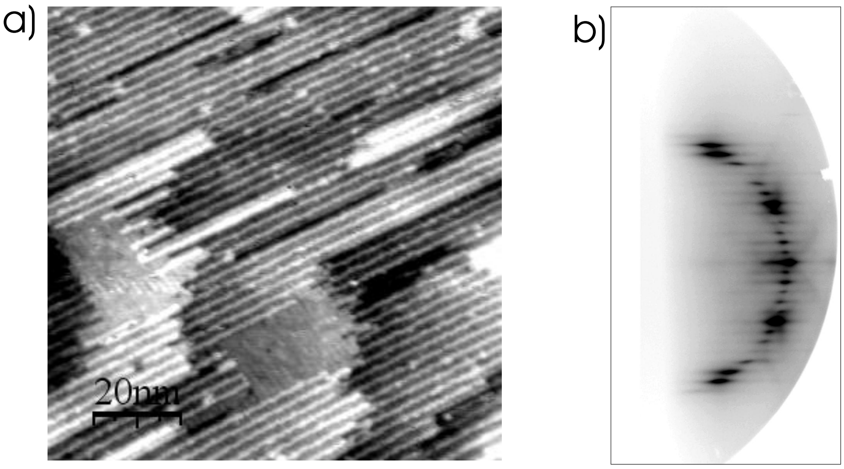

Figure 3.9: (a) An STM image of the reconstructed GaAs substrate. The 4X6 reconstruction is a pseudo reconstruction which consists of As rich 2X6 reconstructed regions with As dimers running along the $[1\bar{1}0]$ direction and Ga rich 4X2 reconstructed regions with Ga dimers running across the [110] direction. Large flat terraces are observed for the reconstructed substrate. (b) The RHEED diffraction pattern observed for an electron beam directed along the $[1\bar{1}0]$ crystallographic direction. The 2X6 reconstruction observed is in good agreement with the STM image.

Annealing: The most suitable template for Fe deposition is a pseudo 4X6 reconstructed GaAs [68]. At the annealing temperature surface atoms become mobile and are free to self-assemble into a structure having a minimum surface energy. Annealing of the GaAs is monitored and characterized using RHEED throughout the whole procedure. The RHEED data enables us to observe surface transformations and provides continuous data for monitoring the surface symmetry. In order to create a 4X6 reconstructed GaAs template having a large terrace size the GaAs is annealed at 600° C. As was shown by Xue [64] and Monchesky [68] the 4X6 reconstruction observed at 600° C is a pseudo reconstruction which consists of 2X6 and 4X2 regions of the reconstructed

GaAs surface. Our RHEED studies with the electron beam directed along the [110] crystallographic direction revealed a pronounced formation of a X4 reconstruction already at 400°C. At temperatures near 600° C a X6 reconstruction becomes clearly visible for the RHEED beam directed along the $[1\bar{1}0]$ crystallographic direction, while a X4 reconstruction along the [110] crystallographic direction remains intense and clearly visible. The RHEED pattern intensities are similar for both reconstructions. This suggests that the surface coverage for these two competing reconstructions is about 50%. However the STM studies, see figure 3.9(a), showed that the 2X6 reconstruction of GaAs occupies about 95% of the GaAs surface. The 4X2 reconstruction is a Ga rich surface state which forms at 400° C. When the annealing temperature reaches 600° C the 2X6 reconstructed As rich surface has a lower surface energy and As is released from the bulk GaAs to form the 2X6 reconstruction. This mechanism of surface formation is stimulated by a preliminary Ar^+ bombardment which creates defects inside the GaAs thereby increasing As mobility.

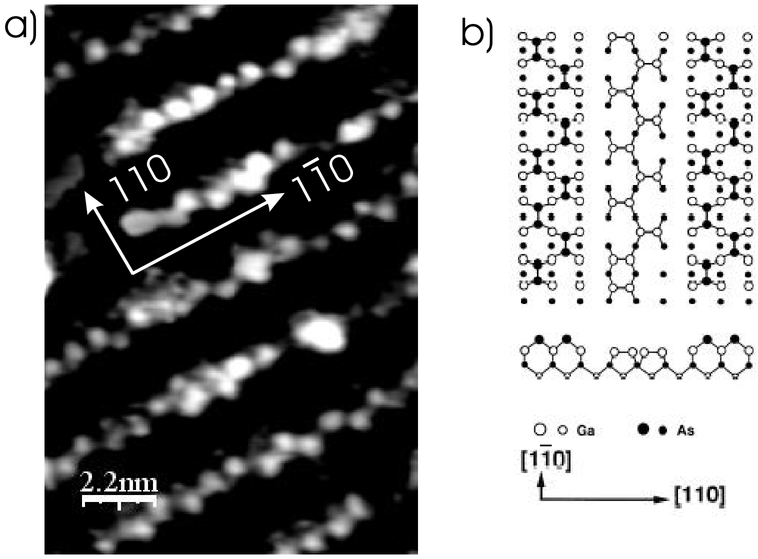

Figure 3.10: (a) A subatomic STM image of the 2X6 region of the reconstructed GaAs substrate. (b) Shows a model of the surface with As dimers running in rows along the $[1\bar{1}0]$ direction. Note the good agreement between the observed reconstruction and the model.

Subatomic resolution STM data, see Fig. 3.10, shows good agreement between the observed image and the model for the 2X6 reconstruction suggested by Biegelsen *et. al.* [69].

3.1.6 Molecular Beam Epitaxy (MBE)

Deposition of ultrathin metallic layers on a GaAs substrate was carried out using the method of molecular beam epitaxy. Resistive heating sources were used for material evaporation, see item 18 in figure 3.1. Precut pieces of high purity Au, Pd and Ag were placed inside individual Alumina (Al_2O_3) or pyrolytic boron nitride crucibles. Each crucible was kept inside a multi-layer tantalum radiation shield and resistively heated by means of tantalum filament having an impedance of $\approx 0.5\ \Omega$ and carrying a current of 30-65 A. The furnace design using a heated crucible is long lasting and provided deposition rates of ≈ 2 ML/min. However slight variations of the temperature inside the crucible resulted in a shading effect from the crucible walls and led consequently to a sub-monolayer gradient of the deposited film thickness across the sample. To avoid inhomogeneity in the magnetic Fe layers a furnace equipped with an Fe plate was used for the Fe deposition.The Fe plate was located above a tantalum filament and formed part of the radiation shield. This design was not sensitive to the shading effect and produced uniform Fe ultrathin films. The growth was monitored by the observation of the RHEED specular spot intensity oscillations, the RHEED diffraction pattern, and STM. The base pressure during the film deposition did not exceed $4\text{x}10^{-10}$ Torr. A layered growth in epitaxial register with the GaAs template was maintained throughout the whole growth. In figure 3.11(a) one can see that only 2 unfilled layers are present in the beginning of the deposition. The same topology is observed for a much thicker and more complicated structure as presented in Fig. 3.11(b).

Terrace size and flatness are dependent on the material, but can be altered by annealing. Due to a considerable mismatch between the Fe and Pd lattices (6%) the Pd forms small (about 2 nm) terraces when grown on the Fe template. For thicknesses above 3 nm of Pd the RMS roughness of the surface dramatically increases and the RHEED diffraction pattern exhibits a three-dimensional type of surface. In the case of three dimensional growth one can increase the atomic mobility and significantly flatten the surface by elevating the temperature of the substrate, see figures 3.12 and 3.13. However, in order to avoid interface diffusion between the layered materials at the elevated temperatures one has to form a room temperature interface. After a deposition of 9 monolayers of material an interface is established and a temperature increase will not change the character of the interface between two layers. Interface diffusion was monitored using Auger spectroscopy as the temperature was gradually increased. The ratio between elements of the underlying layer and the newly deposited 9 monolayers of

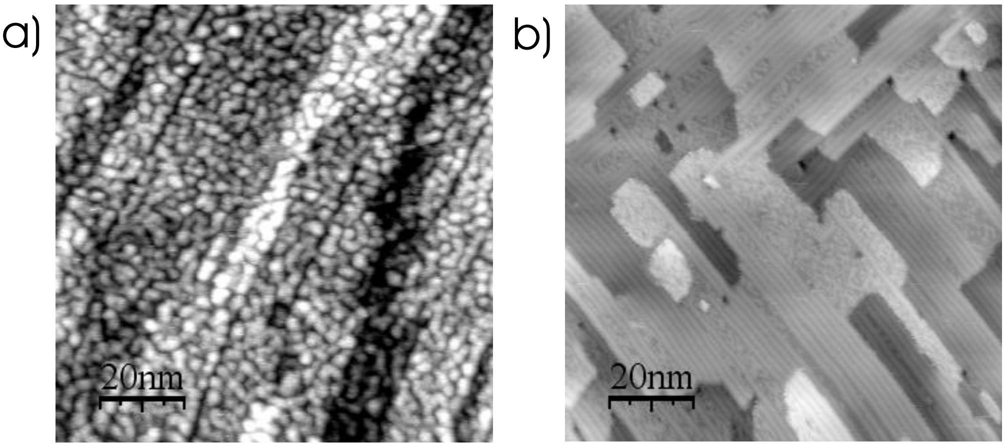

Figure 3.11: STM images showing surface topography. (a) shows the surface after 2 atomic layers of Fe are deposited on GaAs at room temperature, indicating full coverage of the substrate. 3 main shades of the image are induced by terraces of GaAs. (b) shows the surface of a multi-layer Au/Fe/Au/Pd/Fe/GaAs structure. The STM shows that the film is a single crystal and has only two unfilled layers: this indicates a smooth epitaxial growth for all layers.

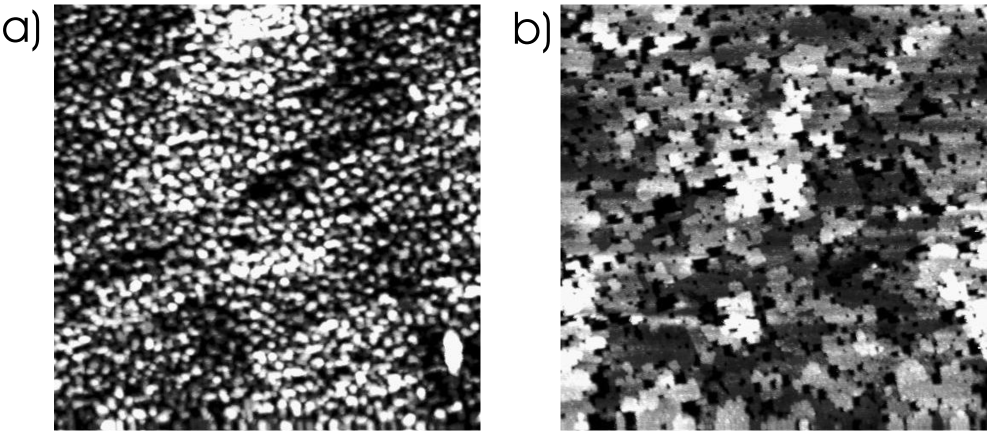

Figure 3.12: An STM image showing the surface topography of a Pd/Fe/GaAs structure. Two cases are addressed: (a) A Pd/Fe/GaAs room temperature growth showing small terraces and significant roughness, and (b) a Pd/Fe/GaAs growth at 180° C that indicates that an elevated temperature growth results in a much smoother surface compared with the room temperature growth.

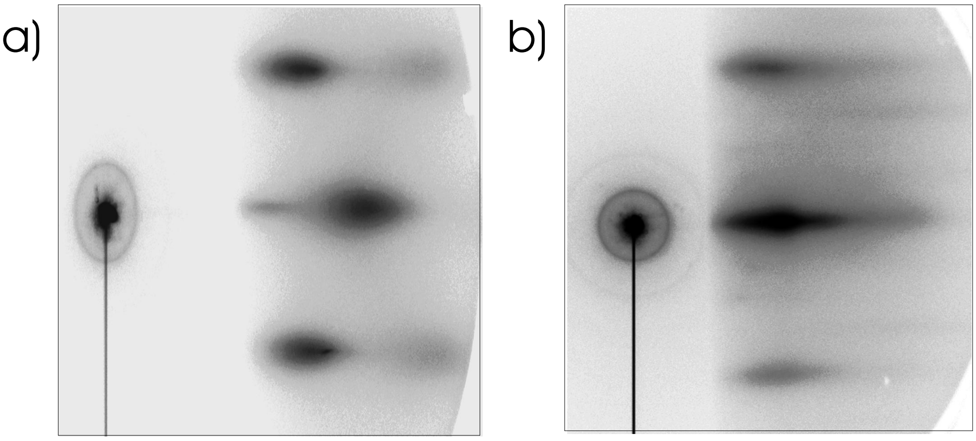

Figure 3.13: A RHEED diffraction pattern for a Pd/Fe/GaAs structure. Two cases are addressed: (a) a room temperature growth and (b) a growth at 180° C.

material were measured, for example see Fig. 3.14. Empirically we concluded that a temperature of 180° C is sufficient for surface flattening and does not stimulate interdiffusion of the atoms between two adjacent layers.

The thickness of the deposited material is measured by means of RHEED specular spot intensity oscillations. An independent measure is also acquired from the precalibrated thickness monitor, see item 19 on Fig. 3.1. Results from these two techniques were very well correlated.

3.2 Ferromagnetic resonance technique (FMR)

Static and dynamic magnetic properties of ultrathin magnetic nano structures were studied using ferromagnetic resonance (FMR) over a wide range of frequencies. Standard FMR spectrometers were used at frequencies of 10, 14, 24, 36 and 74 GHz. A Network Analyzer system was used over the frequency range from 50 MHz to 40 GHz.

3.2.1 Conventional FMR spectrometer

Major components and parts of a standard FMR spectrometer are shown in Fig. 3.15. Gunn diode oscillators and reflex klystrons were used as microwave sources. A Gunn diode oscillator, also known as a transferred electron device (TED), is based on a high-frequency diode used in microwave electronics. Three semiconductor layers are employed

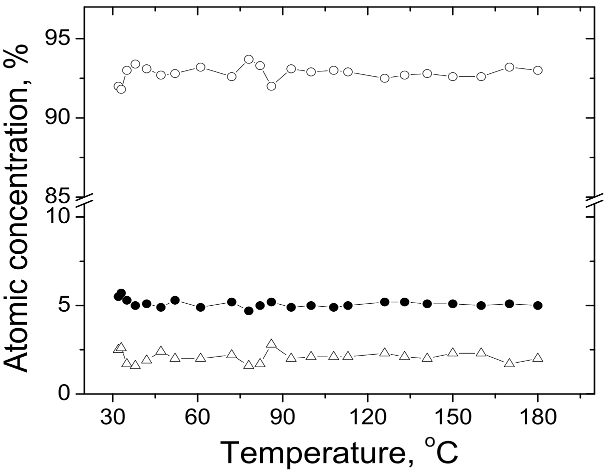

Figure 3.14: Sample surface composition ratio as a function of temperature for 9Pd/16Fe/GaAs. The composition ratio is calculated from Auger peak to peak intensities for As (△), Pd (○) and Fe (●). The graph shows that no interdiffusion is observed for temperatures less than 180° C.

in the Gunn diode: two layers are heavily n-doped and are attached to the two device terminals, and a thin layer of lightly doped material is inserted between them. When a voltage is applied to the device, the electrical gradient will be largest across the thin middle layer. Eventually, this layer starts to conduct, reducing the gradient across it and this results in decreased conduction. This means that a Gunn diode exhibits a region of negative differential resistance. The negative differential resistance combined with the timing properties of the intermediate layer allows one to generate rf power by applying a suitable direct current through the device. The oscillation frequency is determined mainly by the properties of the thin middle layer, but can be adjusted by external factors. Gunn diodes are commonly employed in the 10's of GHz range of frequencies.

In a reflex klystron, an electron beam generated by an electron gun passes through a single microwave resonant cavity. After passing through the resonant cavity the electrons are reflected by a negatively charged reflector electrode and pass back through the cavity and are eventually collected. The electron beam is velocity modulated by electric fields in the cavity on the first pass through the cavity. As a result the electrons form bunches in the drift space between the reflector and the cavity. The voltage on the reflector must be adjusted so that the bunching is at a maximum as the electron beam re-enters the resonant cavity, thus ensuring a maximum energy transfer from the electron beam

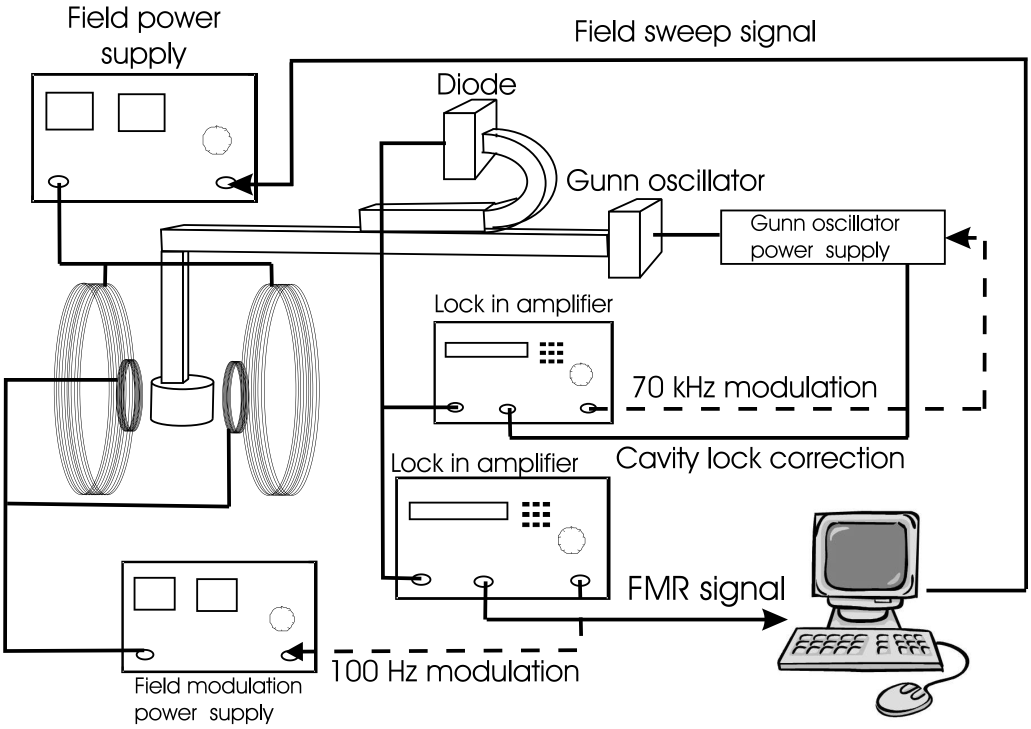

Figure 3.15: A schematic diagram of a typical FMR system used in our experiments.

to the rf oscillations in the cavity. This maximum of energy transfer from the electron bunches to the microwave field in the cavity occurs at a cavity resonant frequency. The microwave frequency was measured using a calibrated cavity frequency meter. The microwave absorption at a constant microwave frequency was monitored as an external magnetic field was swept over a suitable interval. The external dc magnetic field was generated using a Varian 3800 electromagnet. The magnetic field strength was measured using a Hall probe calibrated by comparison with the nuclear magnetic resonance of protons in H_2O. The external field could be rotated to make an arbitrary angle with respect to the sample axes with a precision of 0.1°. A microwave cavity was used to enhance the rf driving field on the sample. The geometry of the waveguide and microwave cavity is shown in figures 3.16 and 3.17. The microwave frequency was varied slightly so that the cavity remained on resonance as the specimen absorption varied during the measurement. This was achieved by applying an additional voltage modulation at 70 kHz on the Gunn diode (or klystron) power supply. This slightly modulates the output microwave frequency. De-tuning of the cavity resulted in a 70 kHz error signal at the detection diode. The error signal was rectified by a lock-in amplifier and the resulting dc output voltage was fed back to the control circuitry of the microwave source in such a way as to keep the microwave cavity always on resonance. To enhance the FMR signal to noise ratio the external field was modulated at 100 Hz applied using a separate set of coils inside the main magnet. The FMR signal was then detected by means of a lock-in amplifier operating at 100 Hz. The output signal from the lock-in amplifier was proportional to the magnetic field derivative of the absorption signal. Typical data for the derivative of the FMR absorbtion is shown in Fig. 3.21(a). The two modulation frequencies are well separated and do not interfere with each other during the measurements.

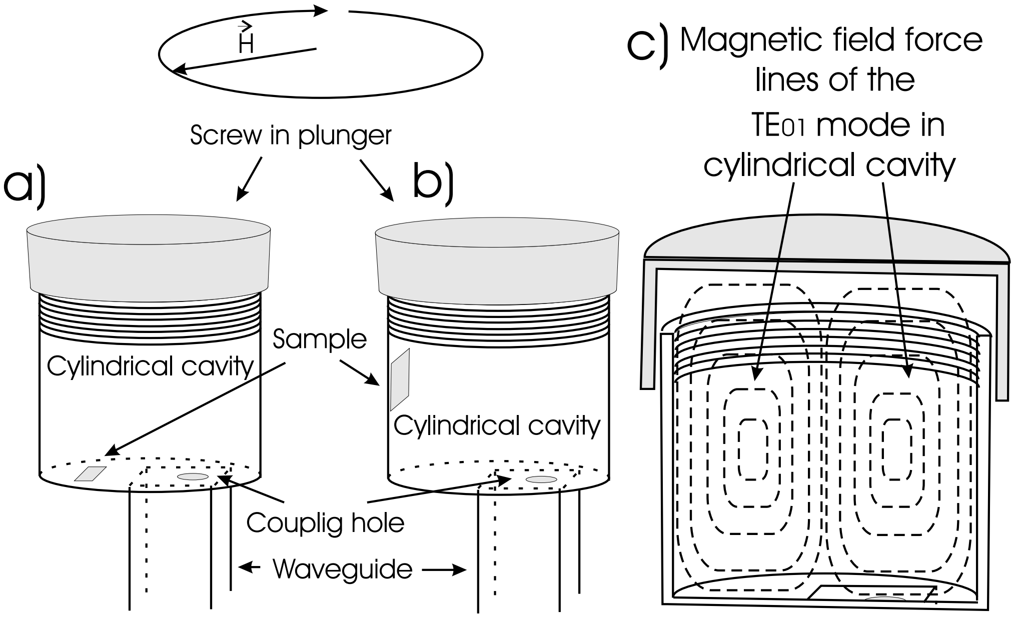

Figure 3.16: A schematic drawing of the cylindrical cavity and sample. (a) shows the sample position for in-plane FMR measurements; (b) shows the sample position for the out of plane FMR measurements; $\vec{H}$ displays the external field direction, which can be rotated in the plane of the cavity base. If the sample is mounted on the wall of the cavity as shown in (b) the magnetization can be tilted out of the film plane; for a particular angle the applied field is oriented perpendicular to the film plane. (c) Force lines of the rf magnetic field inside the cavity of the TE_{01} cavity mode are shown with dashed elliptical lines.

The cavity geometry is specifically designed for each frequency range. The field intensity in the cavity is significantly increased compared to the field strength in the waveguide, see Fig. 3.17. The cylindrical cavity TE_{01} mode, see Fig. 3.17(c) is very suitable for FMR measurements because the cavity quality factor, Q, does not depend on the quality of the electrical contact between the tuning plunger and the cylindrical wall, see Fig. 3.16. The TM_{01} mode is frequency degenerate with the TE_{01} mode [70]. However in the TM_{01} mode rf currents flow between the tuning plunger and the cylindrical wall of the cavity. Consequently this mode can be eliminated by using a poor electrical contact between the plunger and the cylindrical wall. One can design a cylindrical cavity for which the TE_{01} mode is the only dominant resonant mode that provides a large rf magnetic field to drive FMR in ultrathin metallic films, see Fig. 3.16. The coupling between the cavity and the microwave track is established via a coupling hole between the waveguide and the resonant cavity, see Figs. 3.16 and 3.17. The size of the coupling hole is adjusted to obtain sub-critical coupling. This means that the reflected microwave power decreases when the coupling is increased. Optimum sensitivity is achieved when the reflected power at resonance is approximately equal to half the incoming power.

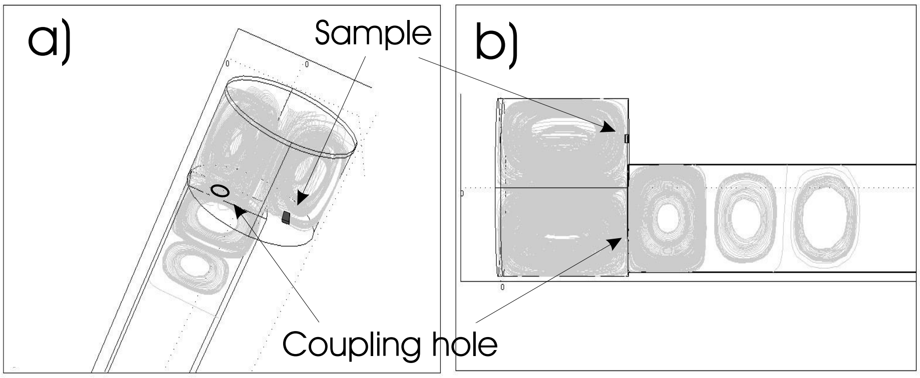

Figure 3.17: FEMLAB simulations for the magnetic field distribution in the cavity and waveguide. Only the dominant TE_{01} resonant mode for a cylindrical cavity is considered. The degenerate TM_{01} mode is suppressed by breaking the electrical contact between the cavity walls and the cavity base opposite to the waveguide connection. In an experiment this configuration is realized by a poor contact between the cavity walls and the tuning plunger. The elliptical lines in the figure illustrate the rf magnetic lines of force. The magnetic field strength inside the cavity is significantly enhanced. Partial leakage of the cavity microwave power back into the waveguide is observed due to the presence of the coupling hole.

Both the in-plane and out of plane FMR measurements were carried out using an FMR spectrometer as illustrated in Fig. 3.15. The FMR data acquired in the out of plane configuration (i.e. the magnetization is inclined with respect to the film surface), required the sample plane to be rotated by 90 degrees with respect to the cavity base, see Fig. 3.16(b).

Standard FMR spectrometer measurements are reliable, however they require major adjustments when the microwave frequency range is changed. A separate microwave source, microwave parts, and microwave cavity are required for each frequency band.

3.2.2 Network analyzer

The complications associated with the use of microwave cavities can be avoided by switching to a Network analyzer system using a coplanar waveguide. In this case the vector Network Analyzer (NA) operating in transmission mode provides the microwave power and measures the transmitted microwave field, see Fig. 3.18(a). The vector network analyzer compares the incident signal that leaves the analyzer with either the signal that is transmitted through the test device or the signal that is reflected from the device input. Since it is difficult to measure the total current and voltage at higher frequencies the so-called S-parameters are used instead. These parameters can be used to determine common parameters such as gain, loss, and reflection coefficients. The number of S-parameters for a given device is equal to the square of the number of ports. In our

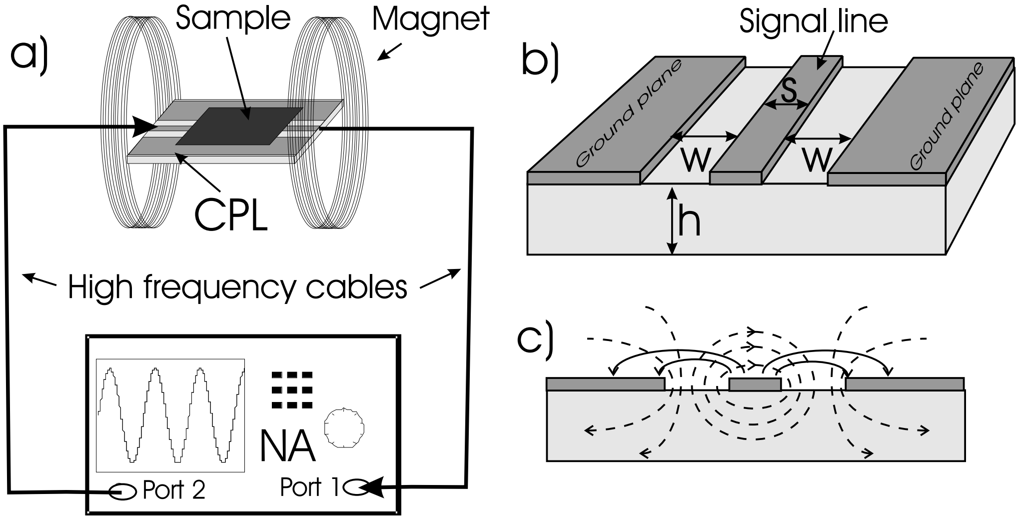

Figure 3.18: FMR setup using a Network Analyzer (NA) and transmission line. (a) Shows the transmission line with the sample above it connected to output and input ports of the NA. The transmission coefficient S21 was measured: S21 is a measure of the power emerging from Port 1 as a result of applying an rf stimulus to Port 2. In (b) a schematic drawing of the coplanar transmission line is shown. Metallic structures (Au in our case) were deposited on a GaAs semi-insulating substrate. The central signal line of width s is separated by air gaps of width w from the ground planes. The ratio between s and w determines the impedance of the coplanar waveguide. (c) shows the rf field distribution around the conductors of the coplanar transmission line: dashed lines show the magnetic field force lines, and the solid lines show the electric field force lines.

measurements, a two-port device has four S-parameters. The numbering convention for the S-parameters is that the first number following the S is the port at which energy emerges from the NA, and the second number is the port at which energy enters the NA. Forward S-parameters are determined by measuring the magnitude and phase of the incident, reflected, and transmitted signals when the output is terminated by the characteristic impedance of the test system. In the case of a simple two-port network, S11 is equivalent to the input complex reflection coefficient, while S21 is the forward complex transmission coefficient, i.e. S21 is a measure of the power emerging from Port 1 as a result of applying an rf stimulus to Port 2.

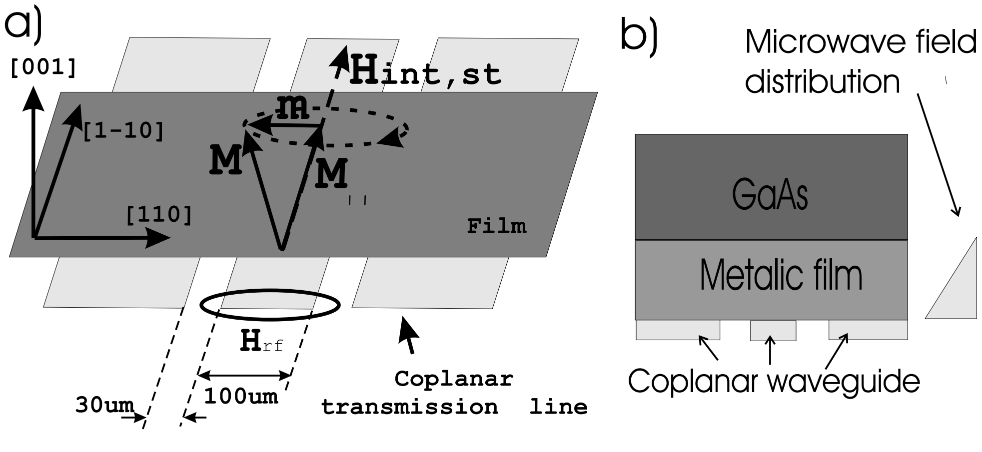

Figure 3.19: (a) A schematic drawing illustrating the configuration of a coplanar transmission line with a magnetic film used to measure FMR in the film. The magnetization M precesses with a small rf magnetization component m (m$\ll$M$_s$). The time independent component M$_{||}$ is parallel to the static internal field Hint,st, (M$\simeq$M$_s$). A typical force line of the rf magnetic field is shown by the solid ellipse. The precessional motion of the film magnetization was predominantly driven by the in-plane rf magnetic field component. (b) A sketch of the magnetic sample position with respect to the coplanar waveguide and rf magnetic field distribution inside the sample. The impedance mismatch between the metallic magnetic film and the semi-insulating GaAs substrate leads to a triangular distribution of the rf field inside the metallic film: the field is strongest at the metal/vacuum interface and it decays linearly to a small value at the metal/semiconductor interface. The strength of the field at the metal/semiconductor interface is given by Maxwell's equations and the boundary conditions required to satisfy the impedance mismatch.

A coplanar waveguide, see Fig. 3.18(b), is used as a coupling mechanism between the microwave source and the sample. The coplanar waveguide must have a characteristic impedance of 50 Ohms in order to match standard commercially available rf devices. The dielectric constant of any insulating material, the thickness (h), the width of the signal line (s), and the distance between signal line and ground conductors (w) are the major parameters that have to be taken into account when preparing a coplanar transmission line. We used optical lithography to pattern Au coplanar transmission lines on a semi-insulating GaAs substrate. The microwave transmission through a patterned transmission line was reasonably flat and the microwave power loss did not exceed 20 dBm for frequencies below 20 GHz. Commercially available low insertion loss probes from Picoprobe were used to couple the high frequency coaxial cables to the transmission line. The rf electromagnetic fields around the signal line is shown in figure 3.18(c). The samples to be measured were placed on the transmission line with their metallic layers facing the transmission line and the GaAs specimen substrate was covered by a metallic plate which significantly decreased the field dependent rf background signal. The sample and transmission line configuration is shown in Fig. 3.19(a). The magnetic films were

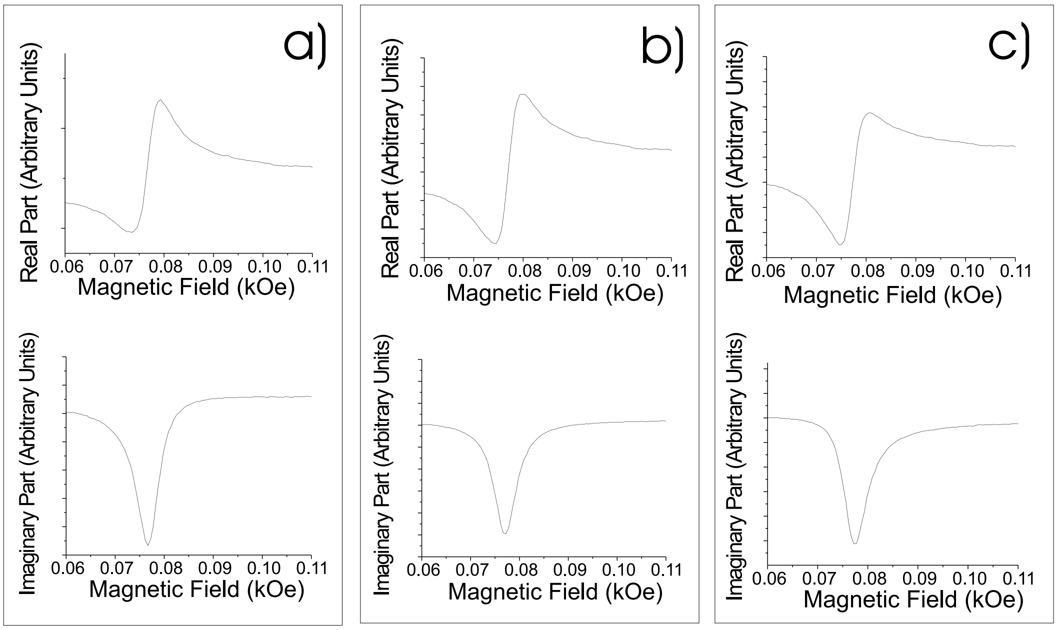

Figure 3.20: An example of the phase correction performed on the S21 data obtained using the vector NA. The measured signal was transformed by rotating the system of coordinates used by the NA. The rotation angle determines the phase between the stimulus signal and the signal emerging from the measuring port. Three angles of rotation are considered in the figure: (a) -15°, (b) 0°, and (c) +15°. Figures (a) and (c) clearly correspond to a signal that is an admixture of the real and imaginary parts of the rf susceptibility. In (b) the phase angle is such that the absorption and dispersion signals correspond separately to the imaginary and the real part, respectively, of the transmission S21 coefficient.

driven most effectively by the rf magnetic field generated by the signal conductor. This field is parallel to the film surface.

The rf field was inhomogeneous across the film thickness decreasing with increasing depth inside the metallic film, see figure 3.19b. This effect is caused by the impedance mismatch between the metallic film and the GaAs semi-insulating substrate. The FMR data were taken using a constant selected microwave frequency and sweeping the external magnetic field. The NA functions as a lock-in amplifier operating at variable microwave frequencies that allows one to collect two microwave signals having their phases separated by 90 degrees. The phase of the rf signal, S21, is dependent on a number of external parameters such as loading of the waveguide, length of the connecting cables, etc. However, postprocessing of the measured signals by rotating the NA system of coordinates allows one to clearly identify the real and imaginary parts of the rf magnetic susceptibility, see figure 3.20.

The Network Analyzer can be also used for FMR measurements in which the frequency is varied while holding the applied magnetic field constant. In that case the microwave absorbtion is monitored as a function of frequency. The data so obtained are strongly dependent on the transmission properties of the microwave track and one needs to correct the data for the frequency dependence of the track (background signal). The background signal is obtained by carrying out an equivalent frequency sweep in a high magnetic field such that the sample susceptibility has little or no field dependence. Unfortunately the system components are not completely independent of the applied magnetic field and consequently this correction turned out to be only partly satisfactory. Hence most of the measurements reported in this thesis were carried out in the field sweep mode while maintaining a constant frequency.

3.2.3 Typical FMR data

FMR analyses were carried out using that signal which is proportional to the imaginary part of the in-plane rf susceptibility. There are two important parameters: the FMR absorption peak position and the FMR absorption peak linewidth. The peak position provides information about internal fields, effective magnetization, and g-factor. The linewidth provides information about the magnetic damping. The angular dependence of the FMR peak position was used to determine the magnetic crystalline anisotropies. The FMR linewidths were used to determine magnetic damping parameters. The measured FMR signals generally included an unknown phase shift which resulted in an admixture of the real part $\chi^{'}$ with the imaginary part $\chi^{''}$ of the rf susceptibility, see Eq. 3.7. It is important to realize that the NA records the data along two axes that are shifted in phase by $\pi/2$. Therefore for the network analyzer the separation of the signals proportional to $\chi^{'}$ and $\chi^{''}$ was achieved by a suitable rotation of the NA system of coordinates, see Fig. 3.20. The peak position and linewidth were extracted by fitting imaginary part of the data with the following function (see Eq. 2.29):

$$\chi'' \sim \frac{\Delta H}{\Delta H^2 + (H - H_{FMR})^2} \tag{3.6}$$

where ΔH is the half width at half maximum, H_{FMR} is the external field at which FMR occurs and H is the value of the external field.

For conventional FMR measurements using standard microwave spectrometers the interpretation of FMR is carried out in a simpler way. One assumes a certain admixture of the $\chi^{'}$ and $\chi^{''}$ signals. The fitting function is modified by using a mixing angle φ in the set of fitting parameters. The mixed (asymmetric) FMR absorption function is described by equation 3.7 (see Eq. 2.27).

$$\chi'' cos\varphi + \chi' sin\varphi \sim \frac{\Delta H cos\varphi + (H - H_{FMR}) sin\varphi}{\Delta H^2 + (H - H_{FMR})^2} \tag{3.7}$$

where χ' is the dispersive part of the susceptibility. To take into account the low frequency modulation of the external field one has to fit the FMR data to the derivative of the above function 3.8

$$\frac{d(\chi'' cos\varphi + \chi' sin\varphi)}{dH} \sim -\frac{2\Delta H cos\varphi (H - H_{FMR})}{\{\Delta H^2 + (H - H_{FMR})^2\}^2} - \frac{(\Delta H^2 - (H - H_{FMR})^2) sin\varphi}{\{\Delta H^2 + (H - H_{FMR})^2\}^2} \tag{3.8}$$

Typical FMR spectra from a magnetic double layer is presented in figure 3.21. In this example two separate resonances are observed due to the fact that the specimen consisted of two magnetic layers having difference magnetic properties and separated by a non-magnetic spacer layer.

Intensities of the resonance absorption spectra are proportional to the saturation magnetization, magnetic film thickness and driving rf field amplitude. For FMR data obtained using a conventional microwave system (see Fig. 3.15) the FMR linewidth affects the strength of the measured signal since it is the derivative of the absorption signal that is measured. To obtain a quantitative measure of the intensity for this case one has to carry out a double integration of the field derivative of the absorption. The intensity so obtained is directly proportional to the total magnetic moment ($M_s d$) of the specimen. One can therefore carry out measurement of the thin film magnetization by comparing the strength of the FMR resonance for the thin film with the strength of the FMR resonance observed using a film sufficiently thick that $4\pi M_s$ attains the bulk value. In this way one can investigate the influence of thickness and the proximity of other metals on the magnetization [71, 8]. However this technique is very sensitive to the rf driving field and to the coupling of the cavity to the microwave track, and therefore these parameters must be accurately measured.

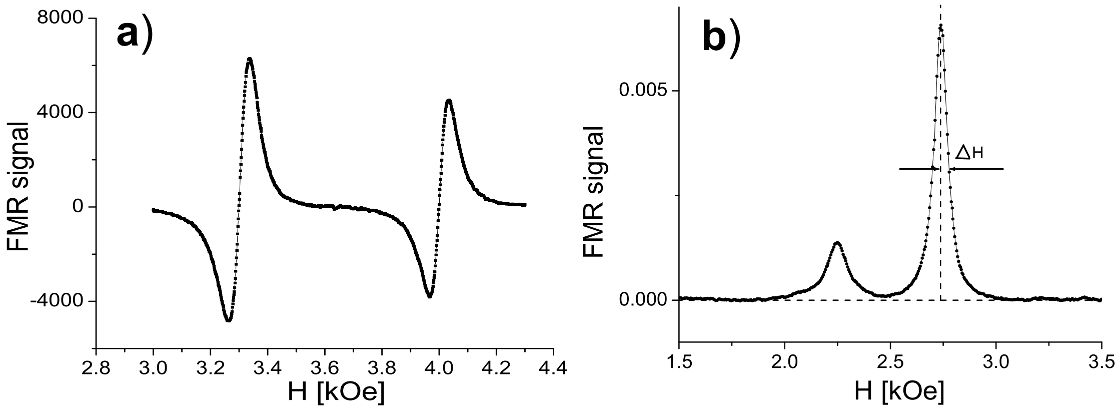

Figure 3.21: Typical in-plane FMR data for a magnetic doublelayer. The different magnetic properties of the two magnetic layers results in different FMR resonance conditions for the two films, i.e. FMR resonance occurs at different applied magnetic field values. (a) Conventional FMR spectrometer measurements at 24.4GHz on 20Au/16Fe/15Au/14Fe/GaAs sample, showing the derivative with respect to the field of the absorbtion spectrum. (b) The phase corrected imaginary part of the S21 transmission coefficient obtained using a Network Analyzer on a 30Au/40Fe/15Au/14Fe/GaAs sample at 15 GHz. Pure Lorentzian absorption lines are observed for both magnetic layers.

For network FMR analyzer data a direct correlation of the intensity of the fitted spectra with the film thickness is complicated by the non-uniform driving magnetic field in the two layers, see Fig. 3.19b. The difference in driving amplitudes influences the intensity of each absorption peak. The value of the driving field even varies across a given magnetic film thickness, and this makes an analysis based upon the rf driving in a film a very convoluted problem. Thus no saturation magnetization and film thickness analysis was performed on the NA data.

3.3 Time resolved magneto-optic Kerr effect technique

Magneto-Optical Kerr Effect (MOKE) is another useful way to probe the magnetic properties of ultrathin magnetic thin films. The off-diagonal components of the dielectric permittivity tensor affect the polarization vector of the reflected light by creating a small polarization component oriented perpendicular to the incident beam polarization. The amplitude of this orthogonal reflected component is proportional to the magnetization density inside the studied film. This results in a rotation of the total polarization vector. The studies reported in this thesis were carried out using the polar Kerr effect in which the primary linearly polarized light beam falls at perpendicular incidence upon the thin film specimen.

In the polar effect the MOKE polarization rotation is proportional to the magnetization component perpendicular to the film surface. In general the MOKE signal is shifted in phase with respect to the primary reflected beam. Thus the final polarization vector can be described in general by a rotation angle θ of the polarization axes and an ellipticity ε. Detailed quantitative analysis and its implications for MOKE experiments on magnetic doublelayers is presented in Chapters 2 and 6. In order to obtain information about the magnetic dynamic properties of thin films it is vital to probe the nonequilibrium behavior of the magnetization on a picosecond time scale. The time resolved magneto-optic Kerr effect technique (TRMOKE) was employed in our studies. The TRMOKE technique was used for several reasons: (a) studies on magnetic doublelayer structures of the form F2/NM/F1/GaAs required observation of the magnetization precession in both the top F2 layer and the bottom F1 layer. Modification of the original system, described in Section 3.3.1, allowed us to carry out depth resolved TRMOKE measurements and thereby isolate the Kerr signals induced in each of the two ferromagnetic layers. (b) In our TRMOKE setup it was possible to use a continuous wave rf excitation of the magnetic specimen which was phaselocked to the laser repetition rate. It will be shown in Section 3.3.2 how the continuous phase-locked wave excitation was realized in our experimental setup. I have to point out that the interpretation of the experimental data was based on the fact that a steady precession (not a transient precession) of the magnetization was generated. (c) The interaction of light with the magnetized media occurs on a timescale of femtoseconds [72]. On a picosecond timescale, which was used in our experiments, the magnitude of the Kerr rotation is a reproducible and steady quantity. These TRMOKE features were essential for the present thesis work.

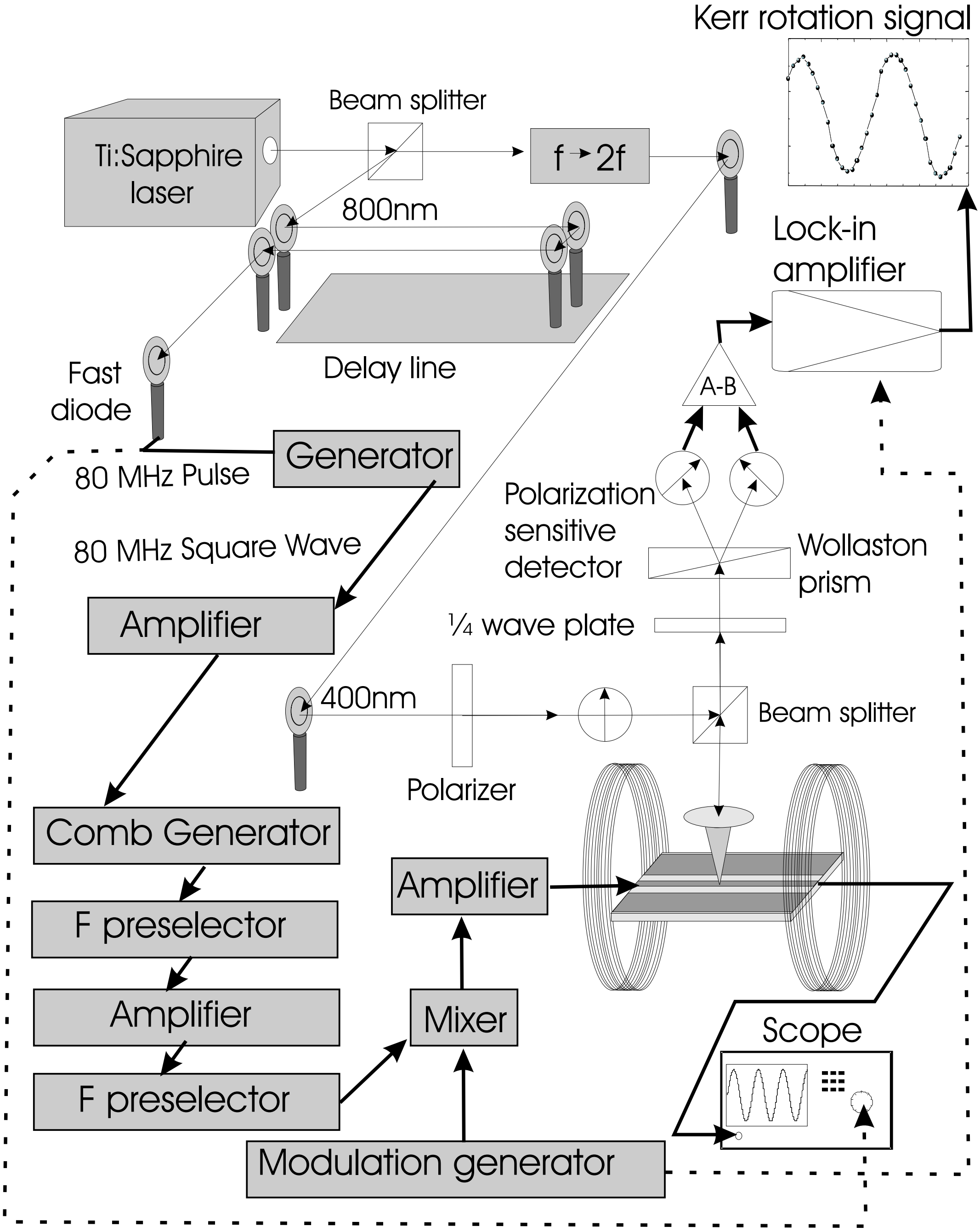

Figure 3.22: A schematic diagram of the TRMOKE apparatus. Optical detection sytem is discussed in Subsection 3.3.1. Microwave excitation description is given in Subsection 3.3.2.

A schematic diagramm of the TRMOKE system employed in my studies is shown in figure 3.22. In this system pulsed light from a mode-locked Ti:Sapphire laser (10 Watt output power) was used for both synchronizing the rf sample excitation and probing the magnetization precession; a detailed review of this technique can be found in chapter 6 of reference [73]. The angle of incidence of the incident laser beam was $\pi/2$ (perpendicular to the surface). The change in polarization of the reflected light was monitored as a function of the delay time between the rf pumping signal (magnetic excitation) and the probing beam. Using this technique one was able to observe the rf out of plane magnetization component with a picosecond time resolution. The time delay with this resolution between the pump signal phase and the probe pulse was achieved by means of an optical delay line. Our TRMOKE provided also a spatial resolution of 200 nm. This was achieved by employing the objective lens of an optical microscope to focus the laser spot size down to 200 nm. A high spatial resolution was required in order to carry out experiments on small specimens. Spatial scans were carried out by moving the sample using a high precision capacitive piezo stage.

During the course of this work a number of important modifications were made to the excitation method (we used comb generator to create continuous rf excitation) and to the signal acquisition (we used 1/4 wave plate to carry out depth resolved measurements) to suit our experiments. In the next few paragraphs I will describe the detection and magnetic excitation techniques, and finally the sample preparation procedure. The 7 ps risetime laser pulse generated by a Ti:Sapphire laser having an 800 nm optical wavelength and a repetition rate of 80 MHz was split into two beams. One beam was used as a probe while the other beam was used to generate a continuous wave rf excitation signal.

3.3.1 Magnetization detection and depth sensitivity

The light probe beam was frequency doubled to a wavelength of $\lambda = 400$ nm and subsequently linearly polarized using a plate polarizer. After the probe beam was reflected from the sample, the time dependence of the magnetization component Mz, the component perpendicular to the specimen plane, was carried out by means of an optical polarization vector analysis in an optical bridge, see figure 3.23. The polarization rotation induced by the magnetization component Mz was detected by splitting the reflected beam into two beams having mutually orthogonal linear polarizations as shown in figure 3.23(a). This was achieved by passing the reflected beam through a Wollaston prism. The orientation of the Wollaston prism was adjusted, in the absence of a MOKE signal, to bring the difference between the DC voltages on the two photodiodes in the optical bridge to zero. The output of each photodiode was approximately 2 V. The probing beam was attenuated in order to prevent overheating of the sample. In the absence of a specimen magnetization precession (excitation) the reflected beam polarization was constant leading to a time independent signal, see figure 3.23(b). On the other hand when a continuous wave rf excitation was applied to the sample, see figure 3.22, the output of the optical bridge provided a signal proportional to Mz, the instantaneous magnetization component perpendicular to the film surface. The rf microwave power was modulated by means of mixing the output from a 2.3 kHz generator with the rf driver. This modulation of the rf driver signal resulted in an ac 2.3 kHz MOKE signal, see figure 3.23(c). This MOKE signal was then detected by means of a lock-in amplifier operating at 2.3 kHz.

The measured MOKE signal is always significantly smaller than the reference signal. The MOKE polarization vector is perpendicular to the primary beam polarization vector. The MOKE polarization can be split into a pure rotation (in phase with the reference polarization) and an elliptical polarization ($\pi/2$ shifted from the reference polarization). The output of the optical bridge is insensitive to the elliptical polarization because it is in quadrature with the reference polarization. One is able to detect the pure rotational part of the polarization vector only because it adds or subtracts from the reference polarization inside the Wollaston prism. In that case the output from the detection diodes is linearly proportional to the MOKE signal. The phase of the Kerr polarization with respect to the reference polarization can be adjusted using a 1/4 wavelength plate, see Figure 2.5. This is a crucial feature for the study of magnetic double layer structures separated by a non-magnetic metal spacer, F1/NM/F2. One can adjust the 1/4 wavelength plate such that the MOKE polarization of a particular F layer has the elliptical MOKE component phase shifted by $\pi/2$. In that case this particular layer does not contribute to the MOKE signal. For thick NM spacers the phase of the MOKE polarization is significantly different for the F1 and F2 layers due to the different optical paths inside the film, see [55]. This means that the other ferromagnetic layer can have an appreciable optical in-phase rotational component to the MOKE polarization and thus contribute to the MOKE signal. This allows one to attain depth resolution in the MOKE studies. This depth resolution feature of MOKE was first demonstrated by Schaefer et al. [54]. For thick NM spacers the MOKE signal from the bottom F layer (grown on GaAs) is also significantly attenuated due to the short penetration depth of the laser beam in metallic films ($\approx$ 60 nm).

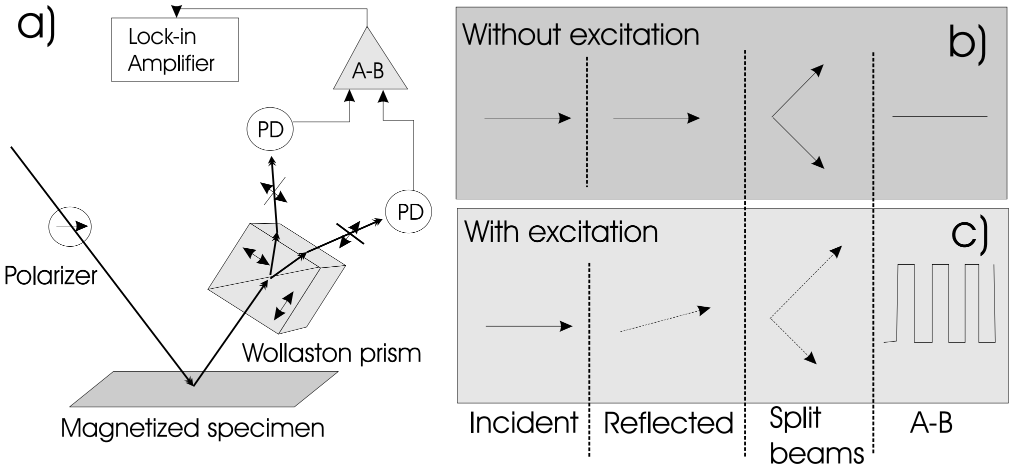

Figure 3.23: Kerr signal detection. (a) shows the detection system based on an optical bridge: light reflected from the magnetized specimen is split by the Wollaston prism into two beams having orthogonal polarizations. The intensities of the two beams are measured separately using photodiodes. The difference between the intensities of these orthogonally polarized beams is measured using a lock-in amplifier at the 2.3 kHz frequency of the microwave power modulation. The angle of incidence shown in the figure is different from normal incidence in order to illustrate the optical components in a cartoon: in a real experimental setup the incident beam is normal to the sample surface. Diagrams (b) and (c) schematically show how the detection system responds to the specimen magnetization in the presence of the rf excitation and in the absence of the rf excitation. The direction of the arrows shows the beam polarizations and the arrow lengths show the intensity of light having this polarization. The reader should follow the detection system schematics aided by columns separated by the dashed vertical lines: Incident light - the same polarization of the incident beam in both cases; Reflected light - without excitation the polarization is the same as the incident light, but in the presence of the rf driving signal the polarization of the reflected beam is rotated due to the polar Kerr effect; Split beams - without the rf excitation both beams have same intensity with orthogonal polarizations after passing through the Wollaston prism. With rf excitation the intensities of the two orthogonal beams are different due to the Kerr rotation of the polarization. A-B - the difference in voltage detected by the photodiodes is constant and equal to zero without rf excitation, but when a modulated rf excitation is applied to the magnetic specimen the intensity difference oscillates at the 2.3 kHz frequency of the rf power modulation.

3.3.2 Continuous wave excitation and synchronization

In order to generate magnetic excitations in the ferromagnetic thin film specimens a continuous wave (cw) rf magnetic field was used having a selected microwave frequency with its phase synchronized to the light pulse repetition rate. This was achieved in several steps, see figure 3.22. Firstly a part of the 800 nm laser pulse was sent through an optical delay line allowing one to measure the MOKE signal with a ps time resolution, see figure 3.22. Secondly this laser pulse was fed into a fast photodiode, see figure 3.22. The fast photodiode created voltage pulses at the 80 MHz frequency of the laser repetition rate. These voltage pulses were converted to an 80 MHz square wave voltage signal by employing a HP8082 pulse generator. The 80 MHz square wave signal was amplified to a 27 dBm power level (about 0.5 W) and subsequently a Picosecond Pulse labs Comb generator, model LPN 7110, was used to generate multiple 80 MHz harmonics. The LPN 7110 output provided us with a wide band of microwave frequencies accessible for the measurements: we were able to choose any frequency in the 3 to 20 GHz range which was a multiple of 80 MHz. The comb generator functioned as a frequency multiplier allowing one to phase-lock its output to the laser beam pulses. The LPN 7110 is based on monolithic Non-Linear-Transmission-Line (NLTL) circuit technology. The NLTL is a synthetic transmission line in which Schottky varactor diodes are distributed along a high impedance transmission line, and their lumped capacitance is a part of the transmission line. The capacitance of a reverse biased Schottky diode is a nonlinear function of the voltage such that the capacitance at low reverse bias is much greater than the capacitance at high reverse bias. The signal on this synthetic transmission line propagates with a velocity that is voltage dependent. A large step signal which changes from a small to a large voltage will be compressed in time since the initial low voltage portion of the step travels down the line slower than the higher voltage portion of the step. Consequently, the higher voltage portion of the waveform "catches up" with the lower voltage portion of the step, resulting in "edge compression", increasing the sharpness of the low-to-high transition edge. This behavior is similar to an ocean wave getting steeper and steeper as it approaches the shore, when the trough of the wave is slowed by interaction with the ocean floor, while the crest continues at a higher velocity, until the wave "breaks". This process of edge steepening allows one to obtain high intensities in the microwave range of frequencies. The rf frequency (closest harmonic) of interest was then filtered out using a YIG bandpass filter. Finally, the isolated harmonic was amplified to the desired power level. The selected rf signal was then amplitude modulated using a HP11720 modulator at 2.3 kHz frequency driven by a Voltcraft FG1617 signal generator. The

2.3 kHz frequency signal was used also as the reference signal for the lock-in amplifier employed in the detection of the MOKE signal.

3.3.3 Sample patterning and magnetic field configuration

The sample to be studied was deposited in proximity of the central conductor of a co-planar transmission line. The configuration used for the TRMOKE measurements is shown in figure 3.24(a). The samples were prepared using the MBE technique. Epitaxial specimen pads from the initially continuous deposited thin film structure were defined by optical lithography and dry etching. After this step a 2 micron thick ion-bombarded photoresist was left on the top of the epitaxial structure. Subsequently a 200 nm thick Au coplanar wave guide on the same wafer was prepared by means of optical lithography, thermal evaporation, and a lift off processes. At first glance it appears that one can see some epitaxial specimen pads though the 200 nm Au layer. In between an epitaxial pad and the 200 nm Au conductor there was still the 2 micron thick photoresist. During the lift-off process this photoresist dissolves and the Au layer on top of the epitaxial structure tears off at the edges. Separation between the epitaxial pad and the waveguide

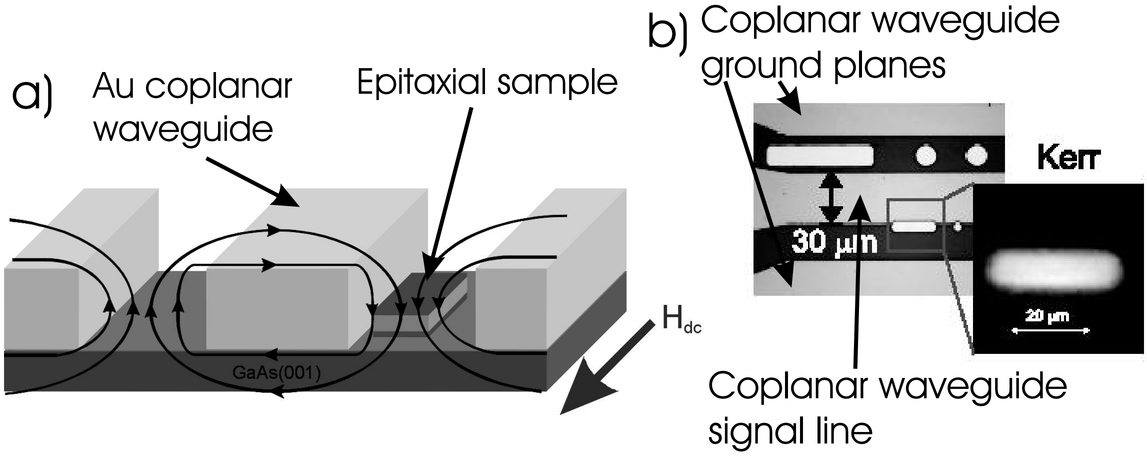

Figure 3.24: (a) A schematic diagram shows the sample position with respect to the coplanar waveguide (for details see Appendix A.2). The solid elliptical lines show the cw rf driving field force lines. The sample magnetization precesses around the dc magnetic field direction driven by the out of plane rf field, which is constant across the sample structure. The TRMOKE probe beam is incident on the open face of the epitaxial pad. (b) An optical micrograph of a real sample prepared for measurements. The inset shows a spatially resolved MOKE signal measured on an epitaxial specimen pad. The uniform color code on the epitaxial pad indicates that the sample is excited uniformly and that dipolar fields due to the pad edges are negligible.

was assured by evaporating the Au under an angle of 15 degrees with respect to the surface normal (shadow effect). The epitaxial layer structure was located in the gap between the signal conductor and the ground conductors of the coplanar waveguide, see figure 3.24(a). A detailed description of the sample patterning procedure is given in the Appendix A.2.

Microwave magnetic field force lines are illustrated by means of the solid lines drawn around the signal line of the coplanar transmission waveguide, see Fig. 3.24(a). For this configuration the rf-magnetic field is out-of-plane and in phase across the whole sample structure. A magnetic dc-field was applied parallel to the waveguide using an externally controlled electromagnet. DC magnetic fields between zero and 1.2 kOe were used during the experiment. An optical micrograph and the lateral scan Kerr signal at FMR across an 25×8 μm^2 epitaxial island is shown in figure 3.24(b). From the uniformity of the magnetic signal it is evident that the dipolar fields were weak for this geometry.

3.3.4 Measurements configuration and typical data

A continuous applied rf magnetization field generates a steady state precession of the magnetization. For a given setting of the delay time the MOKE signal is constant, see figure 3.25(a). The MOKE signal at the given delay time is proportional to the transverse rf susceptibility χ, see figure 3.25(a). The measured signal E_m consists of 2 parts:

$$E_m \sim \chi' cos\phi + \chi'' sin\phi \tag{3.9}$$

where χ' and χ'' are the dispersive and absorption parts of the rf susceptibility component perpendicular to the film surface. ϕ is the phase angle between the driving rf magnetic field and the probing optical pulse. By proper selection of the delay line position one is able to isolate these two parts of the rf susceptibility and observe them separately. If the probing beam is in phase with the rf driving field one observes the dispersive part $\chi^{'}$. By shifting the delay by the time corresponding to a $\pi/2$ phase shift one observes χ''. Thus by fixing the delay time and sweeping the external DC magnetic field one is able to measure the in-phase and out of phase components of the transverse rf susceptibility over a wide range of magnetic fields including the field corresponding to FMR. Typical data obtained in this way are shown in figure 3.25(b). The measured χ'' as a function of the external field can be fit with equation 3.6 and this allows one to extract the magnetic parameters of the sample. It is extremely important to have the phase ϕ of the driving rf field locked to the pulse repetition rate. Small drifts in the phase result in a changing admixture of the real and imaginary parts of the susceptibility within one field scan, and

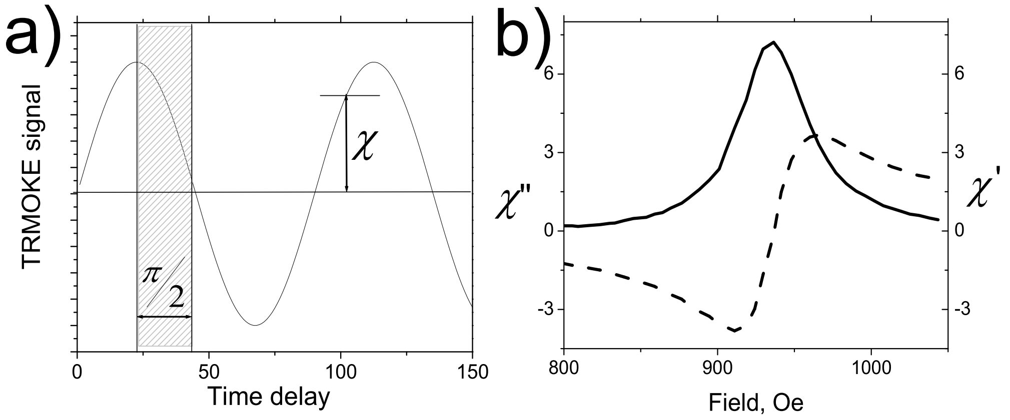

Figure 3.25: (a) A schematic diagram of the MOKE signal as a function of the time delay between the MOKE probe pulse and the optical pulse, which generates the rf magnetic field. (b) The experimentally observed TRMOKE signal for a 9.3 GHz continuous rf excitation at a fixed delay time as a function of the applied dc field for a 10 atomic layer Fe film. The solid line shows the absorption part of the susceptibility χ'', and the dashed line shows the dispersive part of susceptibility χ'.

this phase drift results in serious distortions of the FMR Lorentzian lineshape 3.6 and consequently introduces errors in the data analysis.

Chapter 4

Magnetic properties of ultrathin films

Nano magnetism is developing in a fascinating manner. The ever increasing rate of interest in this field is driven by several factors. Firstly, the use of the Molecular Beam Epitaxy (MBE) technique in the growth of magnetic films in the early 80's created the possibility of preparing unique magnetic structures. Consequently the 80's and 90's were marked by a number of important discoveries in magnetism; interface anisotropies, interlayer exchange coupling, and the Giant Magneto Resistance (GMR) [1, 74, 75, 76] effect are perhaps the most important milestones along which the further development of magnetic nanostructures has evolved. The importance of these three effects was instantly recognized by the scientific community. The field of magnetic nanostructures is a new and central area of advanced condensed matter science which has led to a major new direction in electronics called "spintronics". In spintronics the electron spin momentum plays an equal role with the electrical charge. Magnetism has now merged with electronics in a very fundamental manner allowing one to create new technologies for data storage, data transfer, and logic operations. In order to create a spintronics device one has to understand and control magnetization dynamics in the nano-second time regime and beyond. This requires an understanding and control of the magnetic relaxation processes in nanostructures. Magnetic relaxation processes are a central part of ongoing studies in spintronics. Magnetic relaxation in metals is perhaps one of the least understood areas of magnetism. It has led to lively discussions and various and sometimes controversial interpretations. In this chapter I will show that many controversies arise from extrinsic factors which are often not well identified and understood. Magnetic damping is a complicated subject which is affected by various factors. Some of these factors are intrinsic and cannot be avoided in the system while others are extrinsic and most likely are caused either by structural or compositional defects. In order to understand these processes one needs to create simple systems in which one can isolate and enhance a particular type of damping mechanism thereby allowing one to study it in detail. For this reason sample preparation and characterization becomes an essential part of such studies. By preparing suitable magnetic multilayer structures one is able to control the static and dynamic magnetic properties. The following chapter is organized as follows: The sample growth will be addressed in Section 4.1. Static properties will be discussed in Section 4.2. Studies of magnetic damping mechanisms will be shown in Section 4.3. The experimental data for this Chapter were obtained using ultrathin Au/Fe(001), Au/Fe/Au/Fe(001) and Au/Fe/Au/Pd/Fe(001) film structures grown on 4x6 reconstructed GaAs(001) templates.

4.1 Sample preparation

MBE allows one to prepare high quality crystalline epitaxial films. Crystalline films require that the film surface lattice be reasonably matched to the substrate surface lattice. Crystalline Fe films were grown on GaAs(001) templates at room temperature (RT). The

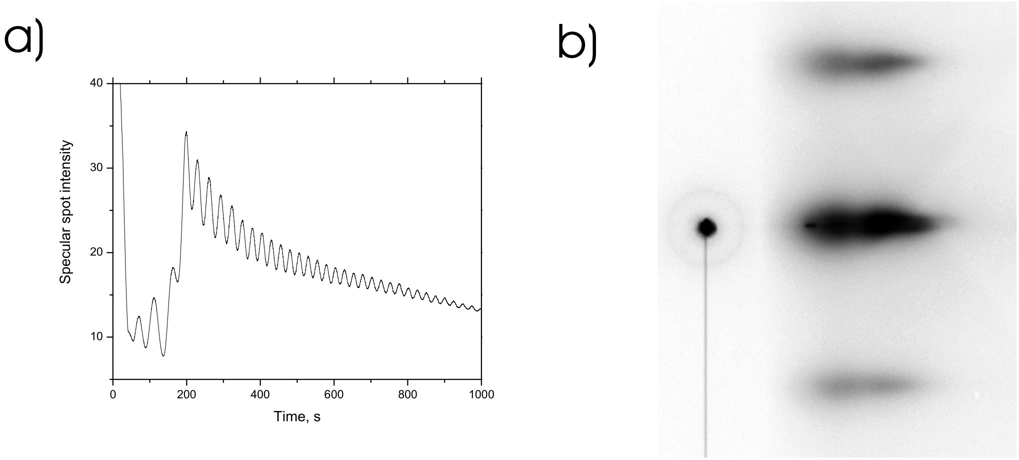

Figure 4.1: (a) RHEED specular spot intensity oscillations for Fe grown on GaAs(001). The recovery of the specular spot intensity after reaching three atomic layers indicates that a continuous film was formed at this point. (b)The RHEED diffraction pattern with the electron beam oriented along the $[1\bar{1}0]$ crystallographic direction of Fe. The split streaks indicate that the atomic terraces were only several nm wide.

lattice mismatch between the Fe (bcc crystal with lattice parameter 2.87 $\mathring{A}$) and GaAs (001) (zinc-blend crystal with lattice parameter 5.64 $\mathring{A}$) is 1.4% (here one has to consider that the Fe(001) surface mesh has a lattice constant that is only 1.4% smaller than the size of the half unit cell of the GaAs(001) surface mesh). The growth of Fe was checked by monitoring RHEED patterns and specular spot intensity oscillations. A continuous film was formed after depositing the equivalent of three atomic layers of Fe. The deposition of the equivalent of three atomic layers resulted in well defined RHEED patterns and strong RHEED intensity oscillations, see figures 4.1(a) and 4.1(b). The observed separation between RHEED streaks has shown that the Fe film grew in its bcc single crystal structure (in fact Fe formed bct single crystal due to strain induced Fe/GaAs interface). The diffraction streaks, see figure 4.1(b), were split indicating that the atomic terraces were several nm across. Strong RHEED intensity oscillations indicated that the growth proceeded in a pseudo layer by layer growth where the top surface consisted of a maximum of two incomplete atomic layers. The Fe surface topography was studied by means of *in-situ* STM. A typical STM image of an Fe film grown on a GaAs(001) substrate is shown in figure 3.11(a). The STM images confirm that the terrace size is of the order of 3-5 nm. The atomic terraces are relatively small but the surface roughness is confined mainly to one atomic layer. The mean surface roughness was found to be 0.19 nm. *Ex situ* magnetic studies required a Au cap layer to protect the Fe film from ambient conditions. Au was chosen for the following reasons: Firstly, the fcc Au crystal (001) mesh has a very close lattice match with the Fe mesh when rotated by 45 degrees, i.e. the [100] direction of Au(001) (fcc crystal with lattice constant 4.09 $\mathring{A}$) is parallel with the [110] direction of Fe(001); the lattice mismatch is 0.5%. Secondly, Au is a nobel metal that creates a lasting protection (up to 1 year) from ambient conditions. The RHEED specular spot intensity oscillations of Au grown on the Fe/GaAs(001) template are shown in figure 4.2(a). The RHEED diffraction patterns shown in figures 4.2(b) and (c) indicate that the deposited film is in a single crystal epitaxial form. However, apart from the main streaks characteristic for the Au surface mesh additional diffraction streaks were observed corresponding to the half lattice distance as a result of the formation of a 2x2 surface reconstruction. This 2x2 reconstruction on the Au film surface was formed because As atoms act as a surfactant. Our Auger spectroscopy studies showed that the equivalent of $\approx$0.4 atomic layers of As were present on the Au surface. The 2X2 surface reconstruction is confirmed by the atomic resolution STM images of the Au/Fe/GaAs(001) surface, see figure 4.3(b). In figure 4.3(a) a larger area of the Au surface is shown (100x80 nm^2). Au atomic terraces of the order of 10-20 nm are clearly

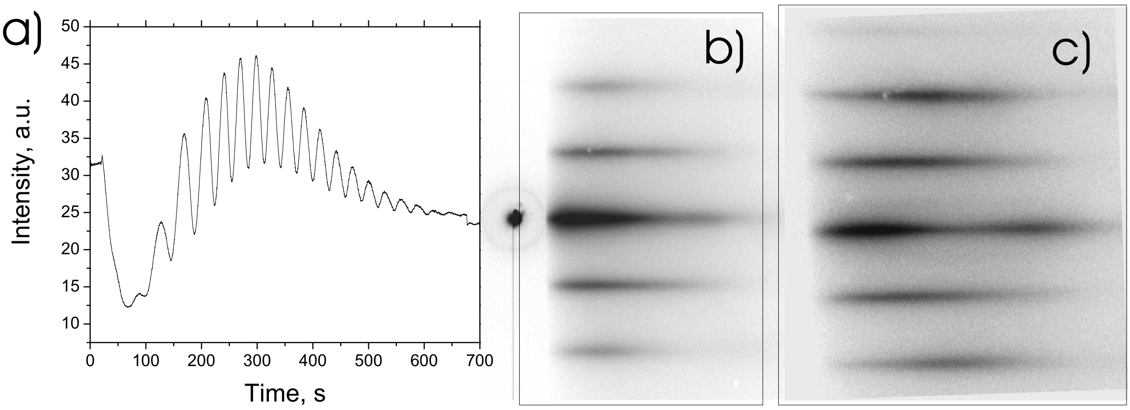

Figure 4.2: Deposition of Au on the Fe/GaAs(001) template. (a) Intensity oscillations of the RHEED specular spot indicate a well defined layer by layer growth. The intensity of the specular spot recovers at the 3rd oscillation, which shows that a continuous film of Au is formed after two atomic layers are deposited. (b)The RHEED diffraction pattern for the electron beam directed along the [100] crystallographic direction of Au. The RHEED image shows that the surface displays a 2X2 reconstruction due to As atoms that float to the surface. (c)The RHEED diffraction pattern for the electron beam directed along the [110] crystallographic direction of Au. Only streaks characteristic of the Au lattice spacing are observed along this direction. Image here is scaled and real spacing between streaks in (c) is larger than in (b) by a factor of 1.45.

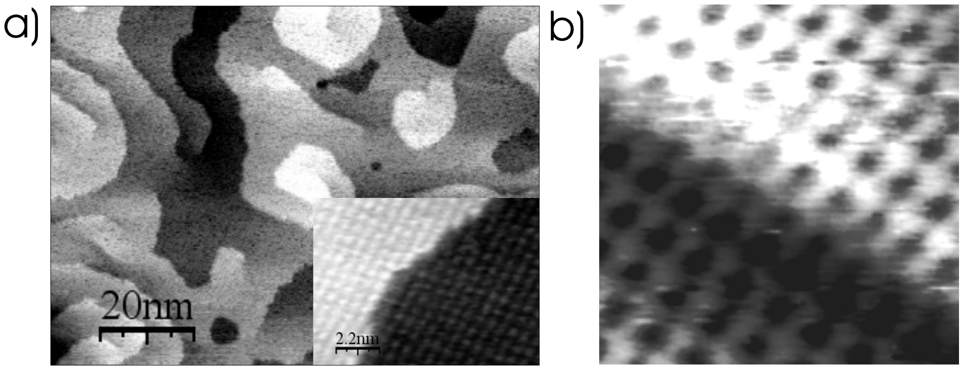

Figure 4.3: (a)A 100X80 nm^2 STM image of the Au/Fe/GaAs surface. The rounded terrace shapes indicates the presence of surfactant As. The presence of surfactant As is confirmed by the atomic resolution STM image of the same surface, see the inset and (b). (b) A 5X5nm^2 area picked from inside (a). The atomic resolution of the Au surface indicates that the overall periodic surface mesh is doubled from that of the Au bulk lattice spacing. The reconstruction is continuous across the whole surface area and is not perturbed by the atomic terraces.

visible. Au/Fe/GaAs(001) templates were used to prepare Fe/Au/Fe/GaAs(001) magnetic double layers. The growth of Fe on Au(001) was monitored by means of RHEED specular spot intensity oscillations, see figure 4.4(a). The RHEED diffraction pattern, see figure 4.4(b), showed that the Fe/Au/Fe/GaAs(001) magnetic double layer remained a single crystal epitaxial film.

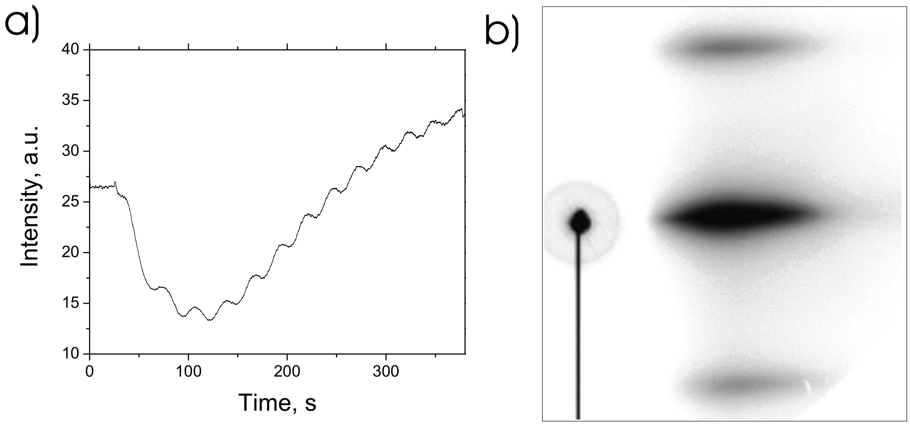

Figure 4.4: The growth of Fe on a Au/Fe/GaAs(001) template. The RHEED specular spot intensity oscillations shown in (a) indicate epitaxial crystalline growth of Fe on Au/Fe/GaAs(001). (b) The RHEED diffraction pattern of the Fe surface on the Fe/Au/Fe/GaAs(001) film. The top Fe layer formed a two dimensional epitaxial crystalline surface.

4.2 Studies of static properties of ultrathin magnetic multilayers

The static properties of ultrathin magnetic films are significantly different from those in bulk materials. The main reason for these differences lies in the interfaces. The presence of interfaces changes the energetics of the system and needs to be taken into account. In fact, the magnetic properties of ultrathin films can be treated more simply than is the case for bulk materials. In ultrathin films one can ignore spatial variations of the magnetization across the film thickness. Interface atomic moments and bulk atomic moments (a few ML below the interface) are locked together by the exchange interaction. In this respect ultrathin films behave like giant magnetic molecules. This means that the interface magnetic properties are shared together with the bulk magnetic properties resulting in a typical $1/d$ contribution to the magnetic anisotropies and their effective fields where d is the film thickness [77, 7]. Ultrathin magnetic films represent a good approximation to two dimensional systems.

4.2.1 Magnetic crystalline anisotropies in metallic multilayers

Single crystalline Fe films prepared by means of MBE possess well defined magnetic crystalline anisotropies. Magnetic anisotropies have been studied by means of Ferromagnetic Resonance (FMR) [77, 7]. The presence of interfaces breaks the symmetry of the lattice. This becomes particularly evident for the cubic lattice where the spin orbit contribution to the bulk magnetic energy is significantly decreased by quenching of the electron orbital momentum. The decreased symmetry at the interface introduces a large uniaxial perpendicular surface anisotropy having its axis perpendicular to the film surface. For a saturated film the effective demagnetizing field $4\pi M_{eff}$ is given by

$$4\pi M_{eff} = 4\pi M_s - \frac{2K_u^{\perp}}{M_s d} \, , \tag{4.1}$$

where $K_u^{\perp}$ is the uniaxial perpendicular interface anisotropy and d is the film thickness. $4\pi M_{eff}$ can be widely varied by changing the film thickness. For a positive value of $4\pi M_{eff}$, and ignoring any bulk magnetic anisotropy, the resonance field H_{res} is less than ω/γ for the parallel configuration, that is when the applied magnetic field and the static magnetization lie in the plane of the film. The resonance field can be easily shifted several kOe simply by changing the film thickness.

The in-plane magnetic anisotropies also include interface terms. For a square template this includes the in-plane interface four fold anisotropy. There should be no intrinsic in-plane uniaxial anisotropy. However iron films grown on a 4x6 reconstructed GaAs(001) template have an in-plane uniaxial anisotropy with the hard axis along the $[1\bar{1}0]$ direction, see [34, 78]. The origin of the uniaxial anisotropy is undetermined at the present time and has been discussed by many groups, see the review by Wastlbauer [12]. There are two mechanisms which, in principle, can explain the uniaxial anisotropy: (a) The GaAs(001) template has a uniaxial symmetry due to dangling bonds associated with the 2X6 reconstructed surface having As dimers running along the $[1\bar{1}0]_{GaAs}$ direction. The anisotropy can be explained by the coupling of the interface Fe electronic structure to the substrate dangling bonds (sp^3 like bonding) [79]. (b) The second mechanism that can explain the uniaxial anisotropy mechanism is a magneto-elastic term caused by the Fe/GaAs lattice mismatch and which leads to a shear type of lattice distortion of the Fe.

It was shown by Moosbuhler [80] that, in fact, the uniaxial anisotropy does not depend on the reconstruction of the GaAs substrate. This suggests that the electronic structure at the interface is not important for the underlying mechanism. In our studies discussed in Section 4.2.2, I will present structural and magnetic studies of the Fe/GaAs interface which indicate that the uniaxial anisotropy is caused by elastic strain.

The in-plane magnetic anisotropies further shift the resonance field. With the external field **H** oriented along the easy magnetic axis the resonance field is shifted towards lower values of **H**. On the contrary when **H** is aligned along the hard magnetic axis H_{res} is shifted to higher values. The angular dependence of the FMR field for a 20Au/16Fe/30Au film is shown in figure 4.5(a). The contribution of the four-fold magnetic anisotropy to the variation of the resonance field is shown by the dotted line. It is noticeable that the two hard axes are not exactly equivalent. The simple four-fold angular dependence is altered by the presence of a weak uniaxial anisotropy having the easy axis oriented along the $[1\bar{1}0]$ Fe crystallographic direction; its contribution is shown by

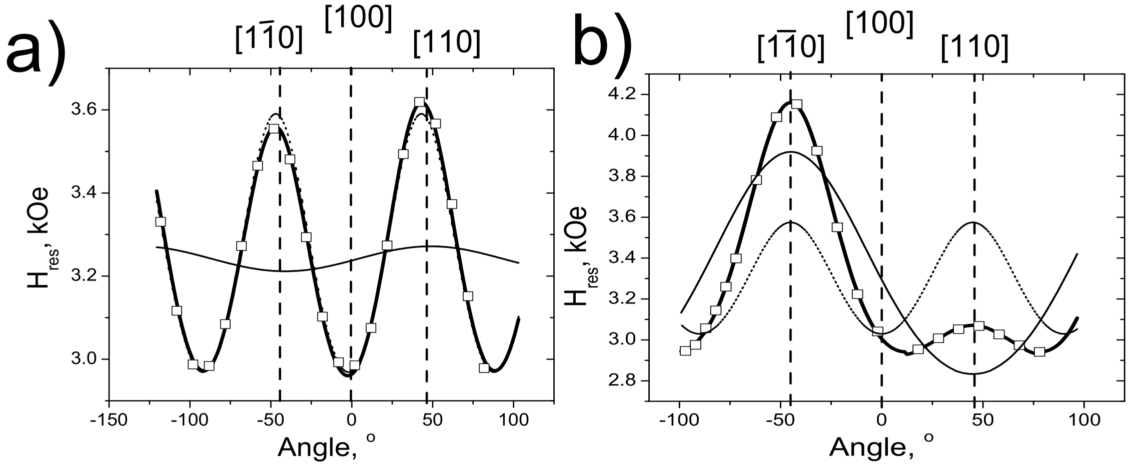

Figure 4.5: The angular dependence of the resonant FMR peak magnetic field for the 20Au/16Fe/30Au/16Fe/GaAs structure. The magnetic field was rotated in the plane of the film. The measurements were carried out at 24 GHz. Angles are relative to [100] crystallographic direction of GaAs. (a) 20Au/16Fe/30Au. (b) 30Au/16Fe/GaAs(001). The data are shown by the open squares. The contributions of the four-fold and uniaxial magnetic anisotropies are shown using the dotted and thin solid lines, respectively. A self consistent fit to the data using the in-plane and perpendicular anisotropies is shown using the thick solid lines (See the text for a list of magnetic parameters). Clearly the Fe film grown on the GaAs(001) template is characterized by different magnetic crystalline anisotropies than that grown on the 30Au(001) film. Dashed vertical lines indicate major crystallographic directions.

the thin solid line. The experimental data shown by the open squares are well described by the presence of the above two anisotropies. A computer fit to the experimental data is shown by the thick solid line and was obtained using a self consistent calculation of H_{res} as a function of the angle of the applied field with respected to the [100] axis. The direction of the static magnetization M_s in the given external field was obtained by minimizing the total magnetic energy. The magnetic parameters which were used to fit the 20Au/16Fe/30Au film are as follows: g=2.09, $4\pi M_s = 21.5$ kOe, and anisotropy parameters listed in Table 4.1 The in-plane four-fold anisotropy K_1 has the easy axes along the Fe $\langle 100\rangle$ crystallographic directions and the in-plane uniaxial anisotropy K_u has the easy axis oriented along the $[1\bar{1}0]$ Fe direction. The static magnetic properties of the 16Fe layer grown on GaAs(001) and covered by the 30Au layer are significantly different from the iron layer in the 20Au/16Fe/30Au specimen. From figure 4.5(b) it is obvious that a strong uniaxial magnetic anisotropy having the hard magnetic axis along the $[1\bar{1}0]$ crystallographic direction dominates the four-fold in-plane anisotropy. The following magnetic parameters were used to fit the observed resonant field angular data for the Fe layer in the 30Au/16Fe/GaAs specimen: g=2.09, $4\pi M_s = 21.5$ kOe, and anisotropy parameters listed in Table 4.2 For the Fe film grown directly on GaAs substrate four-fold anisotropy K_1 has the easy axes along the Fe $\langle 100\rangle$ crystallographic directions, and the in-plane uniaxial anisotropy K_u has the hard axis directed along the $[1\bar{1}0]$ Fe crystallographic direction. The uniaxial in-plane anisotropy in the Au/Fe/GaAs(001) samples is inversely proportional to the Fe layer thickness [34], this suggests its interface origin.

Sample	K_1	K_u	$4\pi M_{eff}$
20Au/16Fe/30Au	2.97x10^5 erg/cm^3	2.75x10^4 erg/cm^3	17.5 kOe

Table 4.1: Anisotropy parameters for 20Au/16Fe/30Au

Sample	K_1	K_u	$4\pi M_{eff}$
30Au/16Fe/GaAs	2.61x10^5 erg/cm^3	-5.02x10^5 erg/cm^3	16.85 kOe

Table 4.2: Anisotropy parameters for 30Au/16Fe/GaAs

4.2.2 Origin of uniaxial magnetic crystalline anisotropy in Fe/GaAs(001)

The uniaxial anisotropy parameter K_u in Au/Fe/GaAs is caused by the Fe/GaAs(001) interface [34]. The structural and chemical properties of the GaAs/Fe(001) interface is widely discussed [81, 82], but not yet fully understood. In order to understand the effect of the chemical environment of Fe at the interface with GaAs and its influence on the magnetic properties we deposited the Fe films using the pulsed laser deposition technique (PLD) and compared the resulting films with thermally deposited (TD) films. The equivalent of two atomic layers of ^{57}Fe was used as a probe layer for Conversion Electron Mössbauer Spectroscopy (CEMS); further details are discussed in [83]. The following samples were prepared using the TD and PLD depositions: GaAs/2^{57}Fe$_{PLD}$/8Fe$_{PLD}$/20Au(001), GaAs/2^{57}Fe$_{TD}$/8Fe$_{TD}$/20Au(001).

Mössbauer studies: The magnetic states of the Fe atoms at the GaAs/Fe interface were identified using the CEMS technique at room temperature (RT). The spectra are shown in Fig. 4.6. 10-11 Mössbauer components were required to account for the measured spectra.

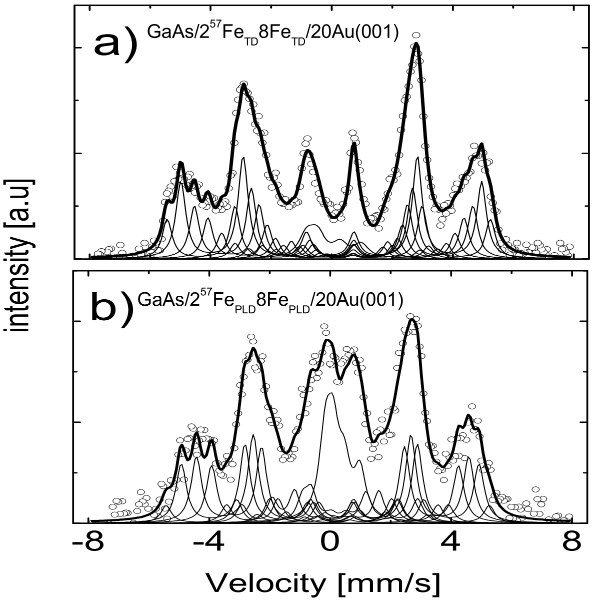

Figure 4.6: Conversion electron Mössbauer spectra (CEMS) for, (a) thermally deposited (TD) and (b) Pulsed Laser Deposition (PLD) samples. The thin solid lines represent individual hyperfine field components corresponding to the different chemical environments of the Fe atoms. The thick solid line represents the overall fit to the data.

The relative contributions of the spectral components and the corresponding hyperfine fields (H_f) are summarized in the Fig. 4.7. The Mössbauer spectra were collected at the University of Krakow in collaboration with Mark Przybylski and Jan Zukrovski. From the CEMS spectra one is able to extract the relative contributions of the hyperfine fields (H_f). The results are summarized in Fig. 4.7. The Mössbauer spectra for the TD and PLD films exhibit a broad hyperfine field distribution for the ^{57}Fe probe layer grown directly on the GaAs(001) template, see Fig. 4.6(b). The model used to fit the CEMS data assumed that the hyperfine field was reduced by 23 kOe with the substitution of one of the nearest neighbors of Fe by either a Ga or an As atom (further details can be found in [83]).

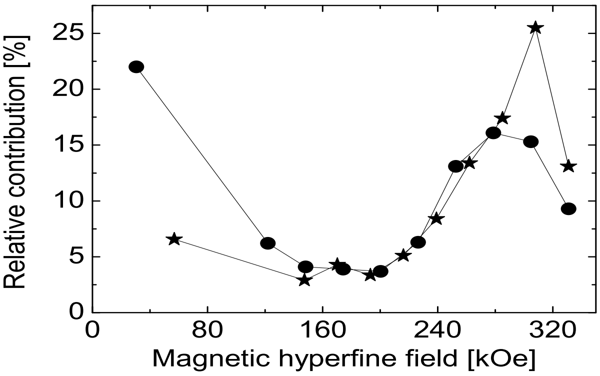

Figure 4.7: Relative contributions of the spectral components vs. the corresponding magnetic hyperfine fields from the data reported in Fig 4.6. The (•) and (⋆) represent the PLD, and TD samples, respectively.

The main difference between the PLD and TD prepared samples was observed at the lowest and highest hyperfine fields. A particularly large contribution at the lowest hyperfine field was observed for the PLD sample. The low hyperfine field contributions are attributed to an extensive incorporation of the Fe atoms into the GaAs lattice. The overall deposition rate for both techniques was approximately 2ML/min. In the case of the thermal deposition the molecular beam was continuous and composed of atoms having a low thermal energy. The TD Fe atoms do not significantly disturb the GaAs lattice because of their insufficient thermal energy. On the other hand the PLD Fe atoms were extracted from an Fe disk target by means of short but high energy laser pulses. The short laser pulses heat the rotating Fe target to plasma temperatures so that the Fe atoms were extracted in short explosion-like cycles. The bunches of Fe atoms released from the target possessed a higher kinetic energy than those deposited by TD, and thus the PLD Fe atoms landing on the GaAs could be incorporated more deeply into the GaAs template.

FMR studies of the TD and PLD films: The magnetic properties of the TD and PLD Fe films were studied by means of FMR. The angular dependence of the FMR peak position as a function of the direction of the applied external magnetic field is shown in Fig. 4.8. The static magnetic properties for the two methods of deposition were significantly different, see table 4.3. The large in-plane uniaxial magnetic crystalline anisotropy observed in the TD sample was observed to be significantly smaller in the

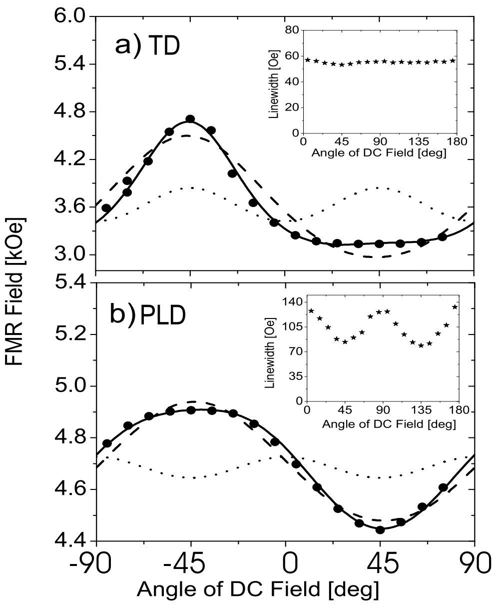

Figure 4.8: The in-plane angular dependence (0° corresponds to [100] crystallographic axis) of the FMR field (f=24 GHz) for GaAs(001)/10Fe/20Au(001) samples prepared by (a) TD and (b) PLD. The dashed and dotted lines are the calculated resonance field contributions from $K_{u||}$ and K_{1eff}, respectively. The solid line represents the overall fit. The insets show the corresponding angular dependence of the FMR linewidth.

Sample	$K_{1,eff}$ [10^5 erg/cm^3]	$K_{U,II}$ [10^5 erg/cm^3]	$4\pi M_{eff}$ [kG]
GaAs/**2^{57}Fe$_{TD}$**8Fe$_{TD}$/20Au(001)	2.02	-7.01	14.74
GaAs/**2^{57}Fe$_{PLD}$**8Fe$_{PLD}$/20Au(001	**-0.43**	-2.25	9.60

Table 4.3: The in-plane uniaxial anisotropy parameter, $K_{u||}$,the in-plane four-fold anisotropy parameter, K_{1eff}, and the effective demagnetizing field $4\pi M_{eff}$ for the listed structures

PLD sample. The interface four-fold anisotropy in the PLD sample (negative with respect to the bulk parameter K_1) was increased in magnitude and resulted in a negative overall K_{1eff} even for a 10ML thick Fe film. The FMR results show that the modified interface structure of the deposited films plays a crucial role in determining the magnetic properties.

Correlation between the structural and magnetic properties: CEMS has shown that the magnetic state of Fe at the GaAs(001) interface is very sensitive to the deposition technique. Fe films prepared by pulsed laser deposition exhibit a more intermixed interface than those prepared by thermal deposition. Consequently the Fe interface lattice in the PLD films can be expected to be clamped more strongly to the bcc GaAs(001) lattice than that in the TD films. Gordon and Crozier [82, 84, 85] recently reported the presence of interface lattice shear at the GaAs/Fe(001) interface. This suggests that the in-plane interface uniaxial anisotropy can be explained by a magneto-elastic term which includes the lattice shear [86, 87]. This term has its uniaxial anisotropy oriented along the in-plane lattice diagonal ([110]) as was observed in Fe films grown on GaAs(001). A significant decrease in the in-plane interface uniaxial anisotropy in the PLD films could then be caused by hard lattice clamping of the Fe interface atoms to the cubic GaAs(001) lattice positions. Consequently the lattice interface shear would be decreased which would most likely result in the observed decrease of the in-plane uniaxial anisotropy. It can be argued that the clamping of the Fe interface atoms to the cubic atomic positions of the GaAs lattice in the PLD samples could result in a decrease in the in-plane uniaxial anisotropy and an increase in the interface four-fold anisotropy.

4.2.3 Collinear and non-collinear FMR resonance

For the in-plane FMR measurements on the 20Au/16Fe/30Au/16Fe/GaAs structure with the dc field applied along the Fe $[1\bar{1}0]$ crystallographic axis the resonance conditions in the saturated state are given by

$$\left(\frac{\omega}{\gamma}\right)^2 = \left(H + 4\pi M_{eff} + \frac{K_1}{M_s} \pm \frac{2|K_u|}{M_s}\right) \cdot \left(H - \frac{2K_1}{M_s} \pm \frac{2|K_u|}{M_s}\right) \, , \tag{4.2}$$

where the upper and lower signs corresponds to the top 16 ML Fe film (surrounded by Au) and the bottom 16 ML Fe film (facing the GaAs). This is a consequence of different uniaxial easy axis direction for 16Fe layer grown on GaAs and 16Fe layer grown on 30Au/16Fe/GaAs. The resonance frequencies as a function of the applied field along the hard magnetic axis ($[1\bar{1}0]$) for the 20Au/16Fe/30Au/16Fe/GaAs(001)specimen are shown

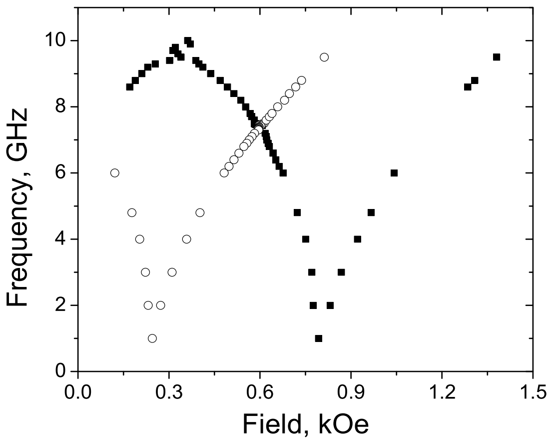

Figure 4.9: The resonant frequencies observed for a 20Au/16Fe/30Au/16Fe/GaAs(001) specimen as a function of the field (fvsH) applied along [1$\bar{1}$0]. The (■) corresponds to the bottom Fe film that faces the GaAs substrate. The (○) corresponds to the 16Fe top 16Fe film that is surrounded by Au. The well-defined cusps correspond to the fields required to reach saturation, H_{sat}. $H_{sat} = \pm 2 \mid K_u \mid /M_s + 2K_1/M_s$, where the plus and minus signs correspond to the bottom 16Fe and top 16Fe, respectively.

in Fig. 4.9. Clearly, a second branch of the FMR peak position curve was observable for fields less than the saturation field value. This branch corresponds to a non-collinear orientation of the magnetic moments in the 16 ML Fe layers with respect to the external applied field. The applied magnetic field was oriented along the hard magnetic axis in both Fe layers. The bottom Fe film (Au/Fe/GaAs(001)) has its uniaxial magnetic hard axis aligned along [1$\bar{1}$0] due to a strong in-plane interface anisotropy at the Fe/GaAs interface. The four-fold in-plane anisotropy has its magnetic hard axes along $\langle 110 \rangle$ which further enhances the strength of the [1$\bar{1}$0] hard axis. This leads to a unique behavior of the FMR branch (fvsH, f$_{res}$ as a function of H) in the non-collinear configuration (M$_s$ not parallel to H) in the film facing the GaAs. The competition between the in-plane uniaxial and cubic anisotropies results in three FMR peaks as a function of the applied field in the 6-9.3 GHz range of microwave frequencies [88]. These are reduced to two resonant peaks at the critical frequency f$_{cr}$ where the slope of the fvsH curve goes to zero. At this frequency the non-collinear resonance peak occurs at the critical field H$_{cr}$ = 0.33 kOe. The second resonant peak occurs at H = 1.35 kOe and corresponds to collinear FMR in which the static magnetization is parallel with the applied magnetic field, see Fig.4.9.

4.2.4 Ghost FMR resonance

For frequencies greater than the critical frequency one expects to see only one FMR peak corresponding to the collinear configuration in which the static magnetization and the applied field are parallel. Surprisingly an additional FMR peak was observed in the non-collinear configuration, see Fig. 4.10(a) and (b). Its intensity rapidly decreased and the linewidth rapidly increased with increasing microwave frequency, $f > f_{cr}$. This peak can be explained as a "ghost resonance" (GR) which was driven purely by the magnetic losses. The GR peak persisted for frequencies $\sim$ 1 GHz greater than the critical frequency. The GR peak behavior is in agreement with simulations taking into account the Landau-Lifshitz-Gilbert (L.L.G.) equation of motion for the non-collinear configuration and including magnetic losses, see Fig. 4.10(c). For zero magnetic damping ($\alpha = 0$) the GR peak entirely disappears. The frequency range in which this peak persists increases with increasing damping. The magnetic response (χ'') at [H_{cr}, f_{cr}] is spread out in the H and f plane (for $f > f_{cr}$) due to magnetic losses [89]. The field sweep passes along the profile of the susceptibility peak $\chi''(H, \omega)$ in the low-field tail. Consequently the GR peak remains nearly constant in field as the frequency increases but its width rapidly increases and its intensity rapidly decreases as the frequency increases.

4.3 Dynamic properties of magnetic multilayers

Dynamic magnetic measurements allow one to study magnetic excitations and magnetic damping, see Eq. 2.31.

4.3.1 Intrinsic Gilbert damping

Magnetic single crystalline ultrathin films provide ideal candidates for extracting intrinsic magnetic relaxations. A set of six 20Au/nFe/GaAs(001) samples, n = 8, 10, 13, 16, 20, 25, and 30, was prepared for the study of the intrinsic magnetic damping. The integers represent the numbers of atomic layers. The FMR linewidth (ΔH) in these samples scaled linearly with the microwave frequency with no appreciable zero frequency offset in the in-plane and perpendicular FMR configurations. This behavior is characteristic for Gilbert damping described by eq. 2.12 and describe α in equation 2.31. The results displayed in Fig. 4.11 show that there is a very weak angular dependence of the damping in all samples. However the damping parameter α is comprised of two contributions. One part is a constant independent of the film thickness and corresponds to the bulk Gilbert

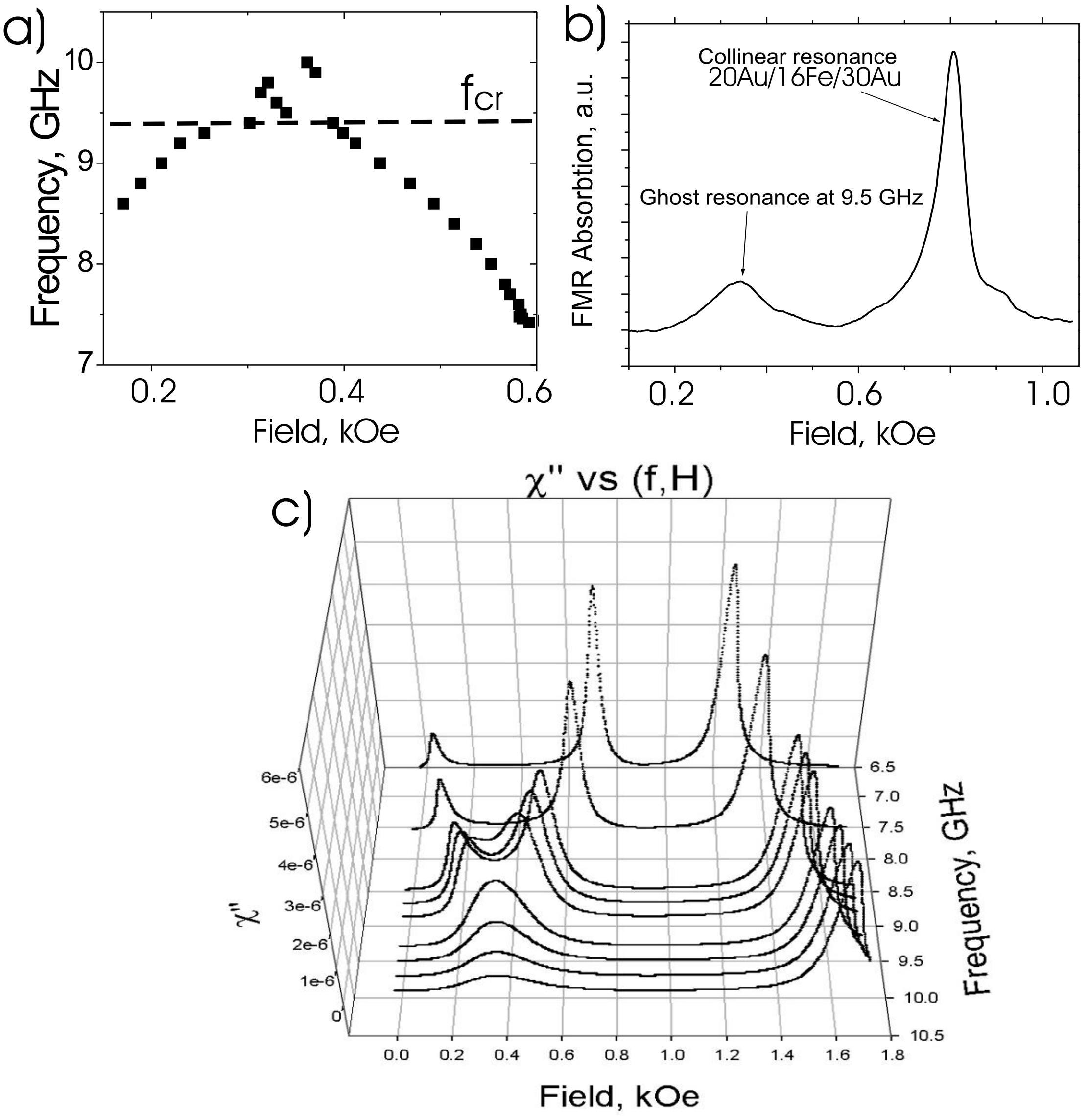

Figure 4.10: (a) An additional FMR resonance is observed for frequencies greater than the critical frequency $f_{cr} = 9.3$ GHz and persists for ≈ 1 GHz. (b) The imaginary part of the in-plane rf susceptibility $\chi''(H, \omega)$ for a frequency of 9.5 GHz, a frequency greater than the critical value of $f_{cr} = 9.3$ GHz, as a function of the magnetic field applied along the hard magnetic axis for the Fe layer in 30Au/16Fe/GaAs(001). Clearly an additional FMR absorbtion peak is observed at the critical field H_{cr} =0.33 kOe. (c) A theoretical simulations of the magnetic response (χ'') for the Fe film adjacent to the GaAs substrate as a function of frequency and applied magnetic field. Fortran code for simulations was developed in our lab as a part of thesis work (program is called: biexchange noncollinear). The magnetic response at [H_{cr}, f_{cr}] is spread out in the H-f plane (for $f > f_{cr}$) due to magnetic losses. The peak corresponding to the non-collinear configuration does not disappear immediately, but rather decays rapidly due to the lossy tail of the $\chi''(H, \omega)$ susceptibility.

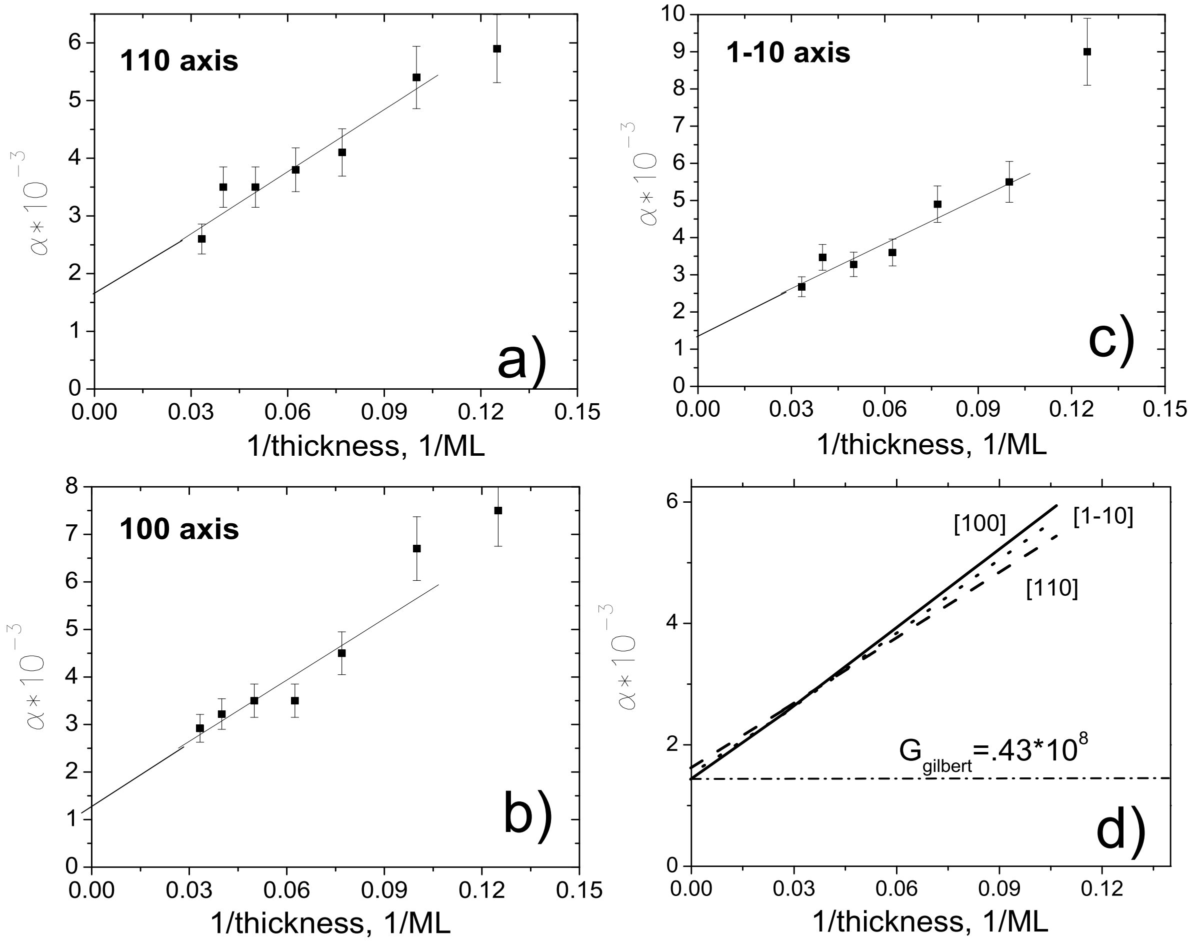

Figure 4.11: Thickness dependence of the magnetic damping parameter α in 20Au/nFe(001)GaAs(001) single Fe layers, where n = 8, 10, 13, 16, 20, 25, and 30. The bullet ■ points in (a), (b), and (c) correspond to experimentally observed values of α with the magnetization oriented along the [110], [100] and $[1\bar{1}0]$ axes. The solid lines represent linear fits of the α parameter as a function of $1/d$. Figure (d) shows the resulting fits for the major 3 crystallographic axes. The horizontal dash-doted line shows the extrapolated value of α corresponding to the bulk Fe limit.

damping. A second part is inversely proportional to the film thickness and originates at the film interfaces. The bulk damping is caused by noise in the spin orbit interaction. The bulk value is $\alpha_b = 1.3\text{x}10^{-3}$, and the correspoding relaxation rate is G $= 0.43\text{x}10^{8}\text{s}^{-1}$, see Fig. 4.11(d). Note that the interface damping is significant; at a film thickness of 10 atomic layers it surpasses the bulk damping by a factor of 2.5, see Fig. 4.11(d). Interface damping is attributed to the interface electron band structure. Safonov and Bertram [90] pointed out that lattice point defects can lead also to an additional Gilbert like damping. A large background in RHEED for the thinnest samples indicates that lattice point defects were present and these defects likely play a role in magnetic damping. In fact the thinnest sample we studied was 20Au/8Fe/GaAs and the resulting damping parameter α deviated from the general trend observed for the other samples. This was especially pronounced for the magnetization oriented along the $[1\bar{1}0]$ crystallographic direction, see Fig. 4.11(c). Since lattice defects played a significant role in this sample its damping parameter was not included in fitting the data.

4.3.2 Intrinsic non-local damping in magnetic multilayers

Magnetic multilayers provide new opportunities to study phenomena where the interaction between the itinerant electrons and magnetic moments can lead to unprecedented and exciting effects. Fert [1] and Gruenberg showed that the electrical resistance of a magnetic double layer depends on the relative orientation of the magnetic moments in the two layers. Berger [91, 92, 93] and Slonczewki [94, 95] pointed out that the inverse process can also take place. That is, the direction of the current flow perpendicular to the interfaces can change the relative orientation of the magnetic moments in magnetic double layers (parallel or antiparallel). This switching effect was experimentally realized in point contact experiments [96, 97] and in experiments on nano-pillars [98, 99]. Slonczewski [94] has shown that the flow of spin momentum that is carried by a current directed perpendicular to the interfaces of a magnetic double layer system NM/F1/NM/F2/NM results in Landau Lifschitz like torques acting on the layers F1 and F2 and these torques change direction when the current direction is reversed. Here NM stands for normal metal and F1,2 stand for the ferromagnetic films. If the magnetization in F2 is fixed in direction (hard magnetic layer) then the magnetization in F1 is allowed to rotate (free magnetic layer). High current densities lead to spin torques sufficient to overcome the intrinsic damping torques and lead to spin instabilities and to switching phenomena [95]. Spin instabilities in turn can lead to the phase coherent emission of microwaves in the presence of a dc magnetic field. This phenomenon was first observed by the Cornell and NIST groups [100, 101].

Testing the spin pump/spin sink model Brataas et al. [102] have generalized the theory of peristaltic charge pumping [103] by including a spin dependent scattering potential. Peristaltic charge pumping is based on the quantum mechanical scattering matrix approach introduced by Landauer and Buttiker [104]. In magnetic multilayers an additional source of Gilbert damping arises from dynamic non-local spin transport, as discussed in Section 2.2.3. The spin pump contribution to magnetic damping was studied in a 20Au/16Fe/15Au/14Fe/GaAs magnetic bilayer structure, see Fig. 4.12.

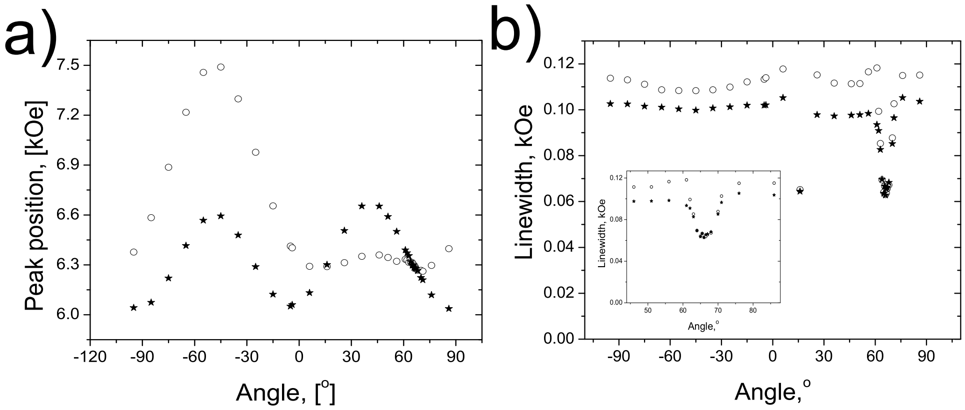

Figure 4.12: FMR results measured at 36 GHz on a 20Au/16Fe/15Au/14Fe/GaAs(001) specimen. The $\star$ and $\circ$ points correspond to the **16Fe** and **14Fe** films, respectively. (a) shows resonant peak position as function of the external field angle. The interface uniaxial anisotropy at the Fe/GaAs interface separates the 16Fe and 14Fe resonance conditions, except for two regions where an accidental crossover occurs. (b) FMR linewidth as a function of the angle between the dc field and the $[100]_{GaAs}$ axis. When the FMR fields were different the FMR linewidths were observed to be larger than the linewidths observed in single layer structures. At the accidental crossovers the FMR linewidths dropped to a value expected for single ferromagnetic layer films. The inset shows a magnified part around the crossover point at (65°), where the data points were measured every 0.5° degrees.

The accumulated spin density in the NM is transported by itinerant electrons. The motion of the itinerant electrons in the NM is affected by momentum scattering (leading to resistance) and spin flip scattering (leading to loss of spin momentum). Spin flip scattering in a cubic NM is caused by weak spin orbit coupling. This means that most momentum scattering events are not accompanied by spin flip event [23]. Consequently the accumulated spin density can penetrate through a relatively thick NM spacer. A ballistic spin regime is achieved when the spin mean free path in the NM metal becomes significantly larger than the NM film thickness. This limit will be addressed in the next paragraph. Diffusive spin transport is discussed in detail in Chapters 5 and 6.

The thickness of the Au spacer was 3 nm which satisfies ballistic spin transport criteria, see revision by Bass et.al. [105]. The angular dependence of the FMR peak position for the 20Au/16Fe/15Au/14Fe/GaAs specimen is shown in Fig. 4.12(a). The interface uniaxial in-plane anisotropy at the 14Fe/GaAs interface separates the FMR peak positions of the two magnetic layers over a wide range of angles of the applied external field. Fig. 4.12(b) shows the FMR linewidth for the **16Fe** and **14Fe** layers as a function of the angle of the applied external field with respect to the $[100]_{GaAs}$ axis. The experimentally measured FMR linewidths, ΔH, for fields far removed from the peak position crossing are 97 Oe and 112 Oe respectively. The intrinsic Gilbert damping parameter for **16Fe** and **14Fe** is expected to be $\alpha \approx 4.5 \times 10^{-3}$, see Fig. 4.11, which corresponds to $\Delta H = 55$ Oe at 36 GHz. Thus a significant enhancement of the damping was observed and is due to the spin pumping mechanism. This situation corresponds to Fig. 2.3(a). The FMR peak positions for the **16Fe** and **14Fe** films cross each other at the angle of $\approx 65^o$, see Fig. 4.12(a). At this cross-over angle both films are in the resonance precession mode, which corresponds to the reduced linewidth shown in Fig. 2.3(b). At cross-over the spin pumping contribution is cancelled by the spin-sink contribution. The FMR linewidth of both magnetic films drops to 62 Oe, see the inset to Fig. 4.12(b). This FMR linewidth is nearly the same as that observed for bulk Fe, and which is due to intrinsic Gilbert damping. For angles far removed from the crossover angle the spin-sink contributions were negligible and the interface spin-pumping contributions caused increased FMR linewidths compared with intrinsic damping linewidths. Notice that in the vicinity of the crossover angle the FMR linewidth can be increased even more than the value corresponding to simple addition of the interface and bulk Gilbert dampings mechanisms. This is caused by the changing phase of the rf precession for fields near the FMR resonance field and will be discussed in detail in Chapter 5 of this thesis. Simulations using eqs 2.63 have shown that this additional increase in linewidth for fields near the resonance field always happens in the thinner ferromagnetic layer in a ferromagnetic bilayer structure [4, 13].

4.3.3 Extrinsic damping due to long range inhomogeneities

Several groups have reported an enhancement of the magnetic damping at microwave frequencies less than 10 GHz [106, 107, 108] using co-planar transmission lines. These results were unusual because they did not agree with the Gilbert damping mechanism. However, the interpretation of these results required a critical review. Particularly, the role of sample homogeneity and the homogeneity of the microwave rf field in a coplanar transmission line must be included in the analysis of the FMR measurements. We have addressed this question by using high quality crystalline double layer Fe(001) films. We used a Network Analyzer (NA) together with a coplanar transmission line to extend our FMR studies to low microwave frequencies.

A magnetic double layer 30Au/40Fe/14Au/14Fe/GaAs(001) was grown using Molecular Beam Epitaxy. The integers represent the number of atomic monolayers in each film. FMR measurements were carried out using two different systems. (1) A standard FMR spectrometer, using a klystron and microwave waveguides operating at frequencies of 10, 24, 36 and 73 GHz, and (2) a network analyzer operating from 1 GHz to 24 GHz. The network analyzer (NA) was attached to a coplanar transmission line (CTL) with width and separation of conductors equal to 800 and 150 μm, respectively: see Fig. 4.13. A relatively wide central conductor, 800 μm, provided a reasonably uniform magnetic driving field. NA was used in two modes: (a) A constant microwave frequency f and an applied field sweep; and (b) a constant applied field H and a microwave frequency sweep, f. The sample was placed across the CTL with the film side down and facing the transmission line, see Fig. 4.13. The main FMR studies were carried out on the top 40 ML Fe layer with the external magnetic field applied along the GaAs [110] direction. The $[110]_{GaAs}$ axis is a hard direction for the cubic magnetic anisotropy for Fe films grown on a Au(001) template. In this configuration the **14Fe** layer in the 30Au/40Fe/14Au/14Fe/GaAs(001) specimen is oriented along an easy axis of the total magnetic anisotropy and consequently the FMR resonance fields in the H sweep, and the frequencies in the f sweep, are well separated. The absorption lines for the two films were clearly separated for frequencies ranging from 1 to 74 GHz.

The magnetic properties of a **40Fe** film grown on a Au(001) template and covered by Au were very nearly the same as those of bulk Fe. The four fold effective anisotropy field was $\frac{2K_1}{M_s} = 460$ Oe; the in-plane uniaxial anisotropy field was small, $\frac{2K_u}{M_s} = 30$ Oe with the easy magnetic axis directed along the $[1\bar{1}0]$ axis, and the effective perpendicular demagnetizing field $4\pi M_{eff} = 20.1$ kG.

Along the hard magnetic axis, the leading anisotropy field in the second bracket of

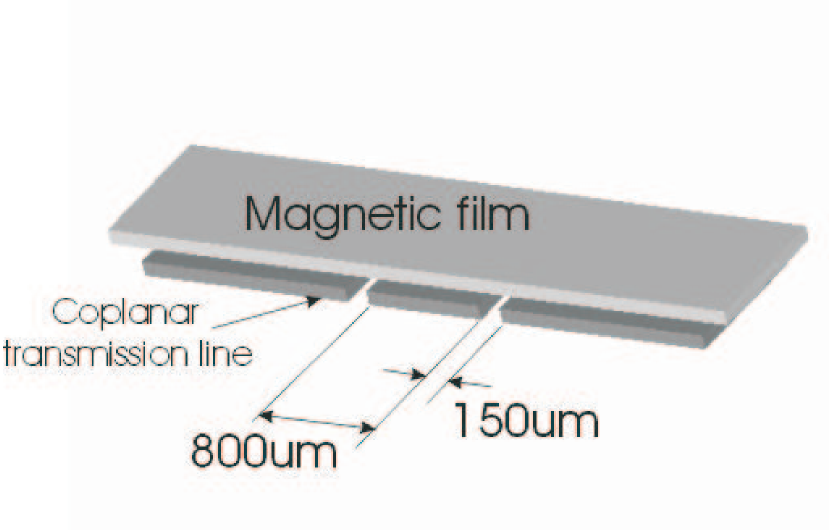

Figure 4.13: A schematic diagram of a coplanar waveguide (CPL) having an 800 μm central conductor and with a magnetic sample inserted above the transmission line. Only the part of CPL covered by sample is shown (cf. 3.18.

Eq. 4.2 is negative and one was able to asymptotically reach zero resonance frequency by approaching the critical magnetic field at which the **40Fe** film was completely saturated. The resonance frequency as a function of the applied field directed along the [110] crystallographic direction for a 20Au/40Fe/30Au/GaAs(001) specimen is shown in Fig. 4.14(a). Well defined f vs H cusps around the saturation field is clearly visible. In order to reach low resonant frequencies one has to orient the field as close to the hard axis as possible. The small misalignment of 1° would not allow one to reach a frequency lower than 5 GHz. The **40Fe** film FMR resonance itself was used in order to determine the best alignment of the applied field with the hard axis. One can indeed see a sharp cusp with a minimum frequency approaching 1 GHz. The FMR peak positions are in good agreement with the calculations, see the solid line in Fig. 4.14(a).

Inhomogeneity contribution to the FMR linewidth in the field sweep mode

The frequency dependence of $\Delta H(f)$ for the field and magnetization oriented along the [110] direction is shown in Fig. 4.14(b). Clearly the $\Delta H(f)$ (obtained using field sweeps) is chiefly described by Gilbert damping with $\alpha = 0.0045$. $\Delta H(f)$ is given by

$$\begin{aligned}\Delta H &= \alpha\left(\frac{\omega}{\gamma}\right) \qquad (4.3)\\ &= \alpha\sqrt{\left(H + 4\pi M_{eff} + \frac{K_1}{M_s} \pm \frac{2\mid K_u\mid}{M_s}\right)\cdot\left(H - \frac{2K_1}{M_s} \pm \frac{2\mid K_u\mid}{M_s}\right)},\end{aligned}$$

where ± corresponds to top and bottom films respectively. After subtracting the spin pumping contribution, $\alpha_{sp} = 0.0016$, the bulk Gilbert damping in the **40Fe** film was found to be $\alpha_b = 0.0029$ which is only 10 percent higher than the damping parameter found for the best Fe bulk samples. The small zero frequency offset shown in

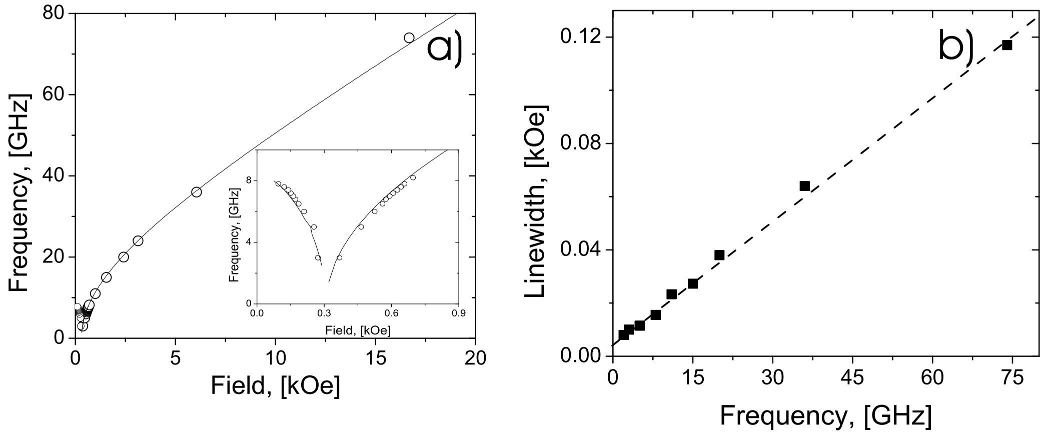

Figure 4.14: FMR measurements on 20Au/40Fe/30Au/GaAs(001) using the field sweep mode with the external field oriented along the [110] crystallographic direction. (a) ∘ show the experimentally obtained resonance frequency vs applied magnetic field. Solid lines shows results of simulations using the following parameters: g = 2.09, $\frac{2K_1}{M_s} = 460$ Oe; $\frac{2K_u}{M_s} = 30$ Oe with the easy magnetic axis directed along the $[1\bar{1}0]$ axis, the effective perpendicular demagnetizing field $4\pi M_{eff} = 20.1$ kG, and saturation magnetization $4\pi M_{eff} = 21.5$ kG. (b) The FMR linewidth as a function of the frequency showing a small zero frequency offset. The zero frequency offset can be attributed to inhomogeneous internal fields, ΔH_{inh}=4 Oe.

Fig. 4.14(b)is due to the presence of long wavelength magnetic inhomogeneities [109]. This frequency dependent $\Delta H(f)$ was interpreted using a Gilbert damping parameter α and a width ΔH_{inh} corresponding to a Lorentian distribution of internal magnetic fields:

$$\Delta H_{inh} = \frac{1}{1 + \left(\frac{H_{inh}}{\Delta H_{inh}}\right)^2}\ , \tag{4.4}$$

Variations in the internal field lead to various resonance conditions in different parts of the sample. It is worthwhile to point out that even at low microwave frequencies the observed FMR signal exhibited a Lorentian lineshape. For long wavelength inhomogeneities the FMR resonance can be described as a superposition of local FMR lines. This leads to an additional contribution to the FMR linewidth. The inhomogeneous field contribution can be accounted for by summing up over multiple FMR absorption lines using a suitable Lorentian width ΔH_{inh} for a distribution of internal fields. A good fit to the measured data is shown by the dashed line in Fig. 4.14(b) using $\alpha = 0.0044$ and $\Delta H_{inh} = 4$ Oe. In fact this contribution to ΔH can just be caused by a distribution of dipolar fields due to an inhomogeneous rf field in the coplanar transmission line structure, see Fig. 4.16. The inhomogeneous rf field leads to an inhomogeneous rf magnetization distribution which results in an inhomogeneous rf dipolar field, equivalent to an internal anisotropy field, and results in a shift of the resonance condition.

At low microwave frequencies the shift in the FMR field due to small inhomogeneties is independent of the microwave frequency. In that case the slope of ΔH vs. frequency is proportional to the Gilbert damping, and the zero frequency offset, $\Delta H(0)$ is determined by the strength of magnetic inhomogeneities. When the zero frequency offset becomes comparable to the intrinsic ΔH the convolution of multiple FMR lines effectively decreases the slope of ΔH as a function of microwave frequency.

Inhomogeneity contribution to the FMR linewidth in the frequency sweep mode The Network Analyzer (NA)is a unique tool which provides an opportunity to select any frequency in the range 50 MHz to 40 GHz, and to determine the microwave transmission coefficients at that frequency with a sample attached to the microwave transmission line. The sample was placed across the Coplanar Transmission Line (CTL) with the film facing the transmission line, see Fig. 4.13. The NA was operated in the S21 transmission mode and essentially functioned as a lock-in amplifier operating at variable microwave frequencies. One collects two microwave signals which have their phases separated by 90 degrees. This allowed one to measure both the in phase and out of phase rf susceptibility of the measured film. Frequency variations of the transmitted microwave signal (background signal) were significantly decreased by covering samples with a metallic plate. This had a negligible effect on the FMR lineshape. Fig. 4.15(b) shows the frequency dependence of the frequency linewidth. The intrinsic frequency linewidth is given by:

$$\left(\frac{\Delta\omega}{\gamma}\right)_{int} = \alpha\left(2H + 4\pi M_{eff} + \frac{4K_u}{M_s} - \frac{K_1}{M_s}\right) \tag{4.5}$$

where α in the **40Fe** film consists of two parts; (1) Gilbert damping α =0.0029 and (2) spin-pumping interface Gilbert damping of 0.0016. The total damping parameter is then $\alpha_{tot} = 0.0045$ [4]. This contribution is shown by the circular points in Fig. 4.15(b). The FMR frequency linewidth slowly decreases its value with increasing resonance frequency. However, at low frequencies there is a clear turn up in the measured $\Delta\omega/\gamma$ (shown by the star points) indicating the presence of inhomogeneities in the effective internal fields. The maximum linewidth was observed at the bottom of the cusp corresponding to minimum frequency. It is not likely that the intrinsic Gilbert damping changes from high to low frequencies. The FMR linewidth ΔH for frequencies greater than 10 GHz is well described by Gilbert damping, and therefore it would be rather surprising to find some new type of relaxation process at frequencies less than 10 GHz. One should realize that going to low microwave frequencies causes the resonance fields to attain small values where one is able to see more readily the presence of long wavelength magnetic inhomogeneities. Such long wavelength inhomogeneities lead to a superposition of FMR lines and consequently to an increase in the FMR linewidth. One possible source of magnetic inhomogeneities could be a spread of magnetic anisotropies. A deviation of the anisotropy field from the mean value leads to a frequency shift given by:

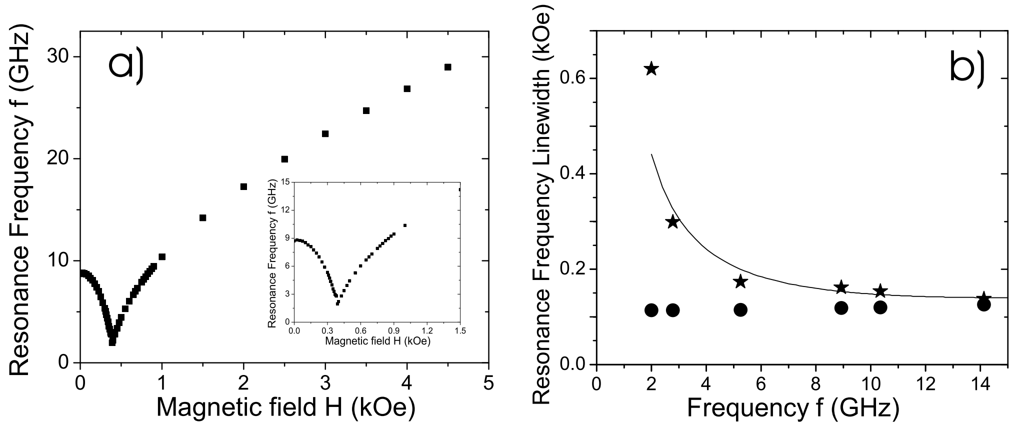

Figure 4.15: FMR results using a 20Au/**40Fe**/30Au/16Fe/GaAs(100) specimen measured in the frequency sweep mode. The magnetic field is directed along the [110] crystallographic direction. (a) Resonance frequency vs applied magnetic field. (b) FMR linewidth (see Eq.(4.5) as a function of the microwave frequency showing the line broadening at low frequencies. The solid stars corresponds to the measured data, the solid circles correspond to the expected Gilbert damping contribution, which was calculated using Eq. 4.5 and α=0.0045. The solid line was calculated from the total frequency linewidth using Eqs. 4.5 and 4.6 with the following parameters: g = 2.09, $\frac{2K_1}{M_s}$ = 460 Oe; $\frac{2K_u}{M_s}$ = 30 Oe with the easy magnetic axis directed along the [1$\bar{1}$0] axis, the effective perpendicular demagnetizing field $4\pi M_{eff}$ = 20.1 kG, and saturation magnetization $4\pi M_{eff}$ = 21.5 kG.and assuming an inhomogeneous field contribution characterized by a spread of | ΔH_{inh}|=7 Oe.

$$\left(\frac{\Delta\omega}{\gamma}\right)_{ext,anis} = \Delta H_{inh}\frac{2H + 4\pi M_{eff} + \frac{4K_u}{M_s} - \frac{4K_1}{M_s}}{\frac{\omega}{\gamma}} \tag{4.6}$$

Therefore a spread $\Delta H_{inh} = \frac{\Delta K_1}{M_s}$ leads to an extrinsic frequency linewidth. The extrinsic and intrinsic linewidths add in quadrature [110]:

$$\left(\frac{\Delta\omega}{\gamma}\right)_{tot} = \left(\frac{\Delta\omega}{\gamma}\right)_{int} \left(1 + \left\{\frac{\Delta\omega_{ext,anis}}{\Delta\omega_{int}}\right\}^2\right)^{\frac{1}{2}} \tag{4.7}$$

The solid line in Fig. 4.15(b) is the calculated total linewidth, which takes into account sample inhomogeneities. Using the average deviation $\Delta\text{H}_{inh} = 7$ Oe provides a good fit to the experimental data. The solid line in Fig. 4.15(b) describes well the experimental data except at the lowest frequency. Since the internal field at this frequency is only 50 Oe, the required additional increase in the frequency linewidth could indicate that the crystalline orientation of Fe along the film surface has some small angular deviations in the alignment with respect to the GaAs(001) mesh. This would result in an incomplete saturation and consequently to an additional FMR line broadening.

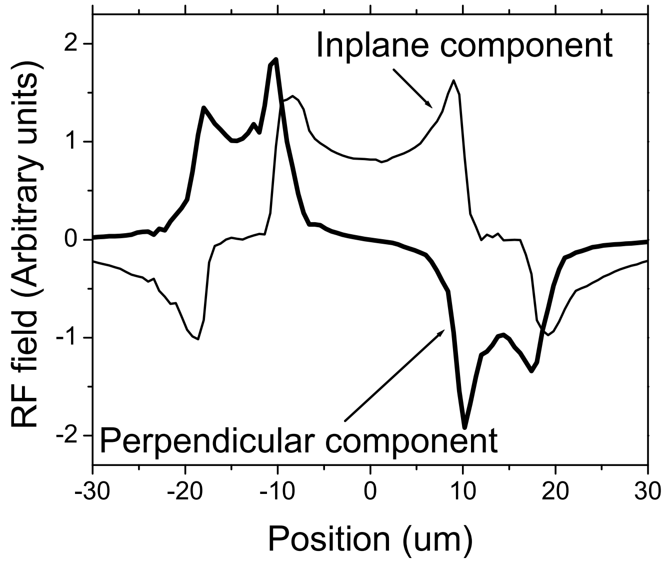

Figure 4.16: The rf field distribution around the central conductor in a coplanar transmission line (CTL). The physical dimensions of the CTL in this simulation are smaller than those used in our experiments. In order to simulate the effect of a thin film sample on the rf field distribution the transmission line dimensions had to be scaled down to accommodate the vertical spatial grid used for the computer simulations.

An additional source of FMR line broadening is associated with the NA technique. Inhomogeneous rf fields around the transmission line conductors , see Fig. 4.16, lead to an inhomogeneous distribution of the rf magnetization which can give rise to rf dipolar fields with a resultent shift of the NA-FMR peak position and an additional FMR linewidth. This was pointed out by Counil et al. [111] for the first time. The frequency shift due to the dipolar field of a magnon having a wave vector $\overrightarrow{k}$ perpendicular to $\overrightarrow{M}_s$ is

$$\left(\frac{\Delta\omega}{\gamma}\right)_{dip} = 2\pi M_s k d \left(\frac{4\pi M_{eff} + \frac{3K_1}{M_s}}{\frac{\omega}{\gamma}}\right) \tag{4.8}$$

where d is the thickness of the film.

The distribution profile of the rf field across a CTL transmission line covered by a metallic film and a thick conducting plate was calculated using Ansoft microwave software. A crude estimate of the average k wave number corresponding to our coplanar transmission line dimensions is 7x10^{-2} cm^{-1} and corresponds to an average dipolar field of 4 Oe. This is equivalent in terms of $|\Delta H_{inh}|$ to 2 Oe, and therefore a true contribution from the cubic anisotropy inhomogeneity to $|\Delta H_{inh}|$ would be only 5 Oe. This suggests that the main part of the extrinsic frequency FMR linewidth arises from variations of the anisotropy field due to long range sample inhomogeneity. Note that this contributes to the damping only about one percent of its mean value.

For an ideal sample without defects and homogeneously driven the frequency dependence of ΔH can be calculated from Eq. 4.5. It is almost linear and has a zero-frequency offset, which can be readily obtained from Eq. 4.5. However, in the case of small long range static sample inhomogeneities the frequency dependence of ΔH exhibits a singular behavior at low frequencies that can be explained using Eq. 4.6.

4.3.4 Extrinsic damping due to a short range inhomogeneity, two-magnon scattering

In this section we shall demonstrate that short range inhomogeneities can strongly affect the spin dynamics. The resonance linewidth in Au/Pd/Fe/GaAs(001) multilayers exhibited a strong extrinsic contribution [112]. The Pd(001) in-plane lattice constant has a large 4.4% mismatch with respect to the Fe(001) template, even when the Pd[110] and the Fe[100] axes are parallel. Au grows over Pd with the in-plane cubic axes parallel to each other ([100]Au || [100]Pd). The Pd and Au lattice spacings are mismatched by 4.5%. The presence of Pd in crystalline Au/Pd/Fe(001) multilayers provides a large lattice strain which for Pd film thicknesses greater than a critical value is relieved by the formation of misfit dislocations. Pd/Fe/GaAs(001) structures [112] are accompanied by a network of misfit dislocations which for sufficiently thick Pd layers can propagate right through the underlying Fe layer. The results in this section are presented using a magnetic double layer 20Au/7Fe/40Au/11Pd/10Fe/GaAs(001)
together with a reference sample 20Au/7Fe/40Au/10Fe/GaAs(001).

The **7Fe** film in the case of the 20Au/7Fe/40Au/11Pd/10Fe/GaAs(001) specimen is grown on a template containing dislocations, which form at the Pd/Fe interface. The misfit dislocation network propagates right through the **7Fe** film resulting in a significant contribution to extrinsic damping.

The RHEED patterns corresponding to Pd growth on an Fe/GaAs(001) template is shown in figure 4.17. Approximate layer by layer growth is confirmed by the RHEED specular spot intensity oscillations and the RHEED diffraction patterns.

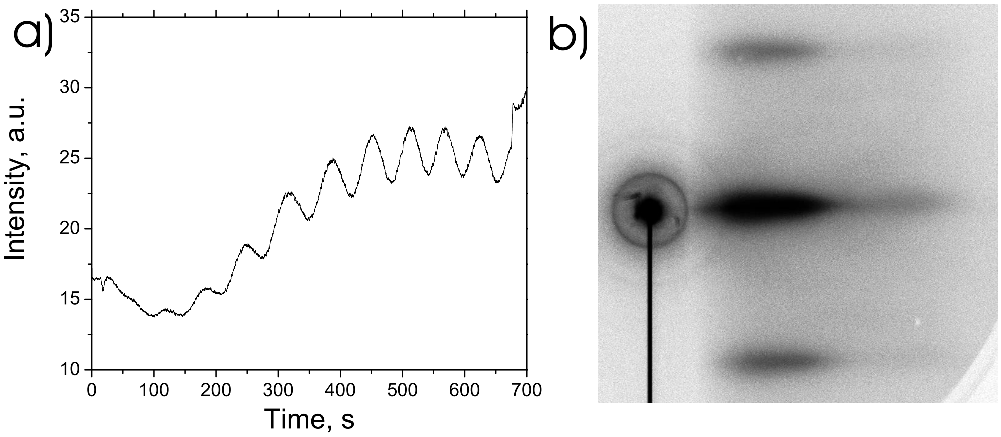

Figure 4.17: Growth studies of Pd grown on an Fe/GaAs(001) template. (a) shows RHEED specular spot intensity oscillations indicating quasi layer by layer growth. (b) The Pd RHEED diffraction pattern. The electron beam was oriented along the $[1\bar{1}0]$ crystallographic direction. The Pd film is in the form of a single crystal, however a Pd film grown at room temperature tends to develop small asperities, see nonuniform RHEED intensity features along the streaks. Such asperities are also found in STM images (cf. 3.12(a)).

Epitaxial deposition of Au on Pd/Fe/GaAs(001) was monitored using RHEED specular spot intensity oscillations, see Fig. 4.18(a). The RHEED pattern observed for the Au(001) layer in 40Au/11Pd/10Fe/GaAs(001) developed fan-out streaks when the primary electron beam was oriented along the [100] Au directions (see Fig. 4.18(b)). The low intensity middle streaks correspond to a 2X2 reconstruction. It has been shown by Pukite [113, 114] that the presence of fan out streaks is related to surface clustering involving a rectangular symmetry. Pukite's interpretation allows one to make the following conclusions: The presence of RHEED fan-out streaks with 90^o symmetry is due to the formation of a rectangular network of surface line defects. For the RHEED electron beam oriented at 45^o with respect to the direction of the line defects the fan-out streak pattern was symmetric and reached a maximum intensity; when the electron beam was oriented along the line defects (for angles 0^o and 90^o) only simple straight streaks were present, see Fig. 4.18(c). The rectangular network of line defects on the surface was caused by the nucleation and glide of misfit dislocation half-loops entering the crystal surface during the film growth in order to compensate for the lattice mismatch (see details in reference [2]).

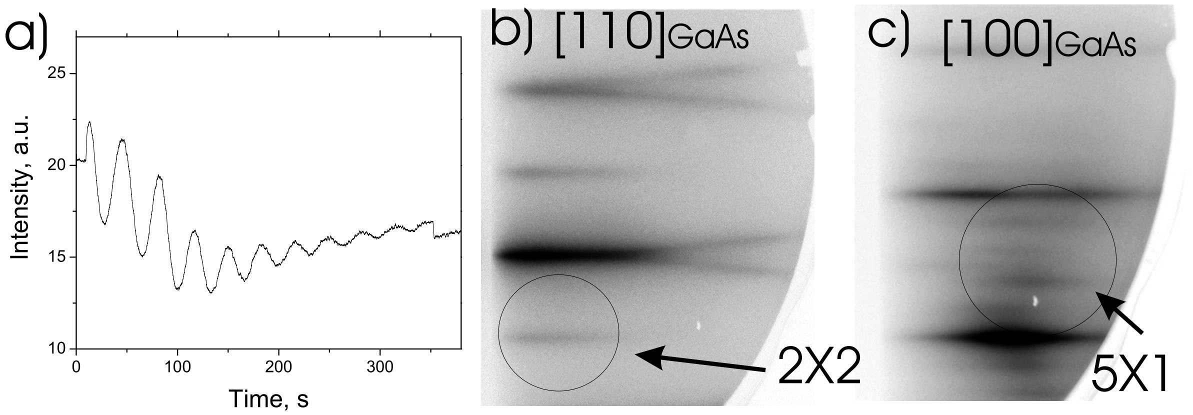

Figure 4.18: Growth studies of Au on a Pd/Fe/GaAs(001) template. (a) shows the RHEED specular spot intensity oscillations that indicate a quasi layer by layer growth. (b) The RHEED diffraction pattern for Pd(001). The electron beam was oriented along the $[1\bar{1}0]$ crystallographic direction of the GaAs(001) substrate. The split RHEED streaks indicate that the surface contains rectangular inhomogeneities having a periodicity much larger than the lattice spacing. A X2 reconstruction of the Au surface is observed along the $[1\bar{1}0]$ direction of the GaAs(001) substrate. (c) The RHEED diffraction pattern obtained with the electron beam oriented along the [100] crystallographic direction of the GaAs(001) substrate. Strong X5 reconstruction was observed in this case.

From the RHEED patterns shown in Fig. 4.18 it can be concluded that the surface of the 40Au/11Pd/10Fe/GaAs(001) structure consists of a network of line defects that are oriented along the $\langle 110\rangle$ crystallographic directions of the Au(001). The presence of line defects is further confirmed by STM studies, see Fig. 4.19(b). The line defects oriented along the $\langle 110\rangle_{Au}$ crystallographic directions in this 300X300 nm^2 image are indicated by the white arrows. Fig. 4.19(a) shows a magnified image of the 40Au/11Pd/10Fe/GaAs(001) surface. This surface is qualitatively different from that of the Au/Fe/GaAs(001) surface shown in Fig. 4.3. One can see that round terraces are substituted by rectangular terraces. Subatomic resolution images, see inset in Fig. 4.19(a), indicate that the Au surface exhibits a 5X1 reconstruction, contrary to the 2X2 Au reconstruction observed for the Au/Fe/GaAs(001) surface. The 5X1 Au reconstruction is confirmed by the RHEED diffraction pattern, shown in Fig. 4.18(c). However a part of the Au/Pd/Fe/GaAs(001) surface shows structures characteristic of the 2X2 Au reconstruction. The 5X1 reconstruction is typical of a clean Au(001) surface. This suggests that the surfactant As is segregated into the 2X2 reconstructed areas leaving the rest of the Au/Pd/Fe/GaAs(001) surface clear of As.

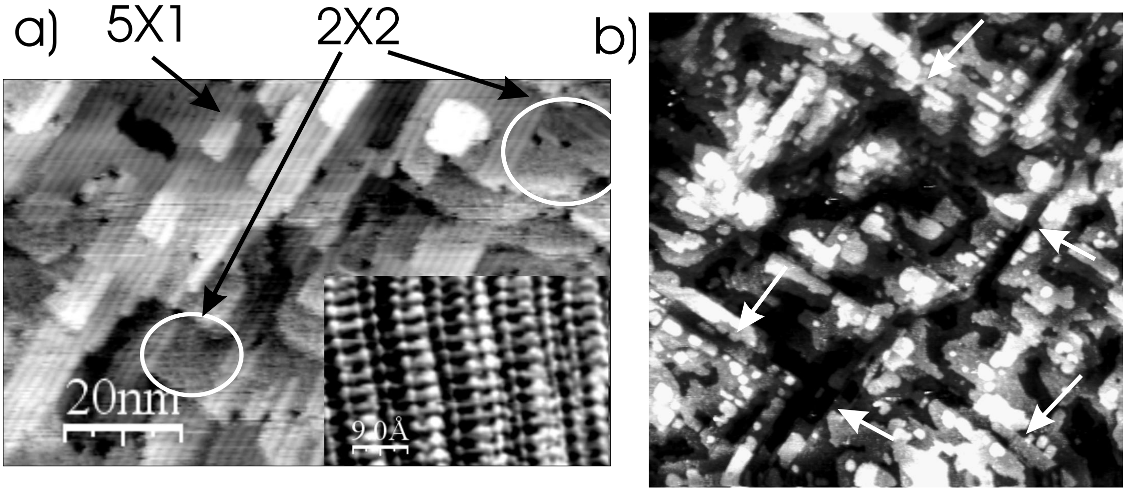

Figure 4.19: STM studies of a Au/Pd/Fe/GaAs(001) specimen. (a) A high resolution STM image showing that the Au surface consists of two different areas: 5X1 reconstructed areas have no surfactant As and occupying 80% of the surface plus 2X2 reconstructed areas covered by surfactant As atoms. The inset shows a subatomic resolution of the 5X1 reconstructed surface. (b) A 300X300 nm STM image of the same surface. On this scale one can observe linear defects propagating in perpendicular directions ($\langle 110\rangle_{Au}$ or $\langle 100\rangle_{GaAs}$); these are marked by the white arrows. These defects are attributed to glide planes of misfit dislocations originating in the Pd layer due to the Pd/Fe and Au/Pd lattice mismatches.

The magnetic anisotropies observed for the **7Fe** and **10Fe** layers in the 20Au/7Fe/40Au/11Pd/10Fe/GaAs(001) and reference 20Au/7Fe/40Au/10Fe/GaAs samples were similar. A striking difference was observed in the magnetic damping between the sample containing the Pd layer and the sample containing no Pd. The Fe layers in the 20Au/7Fe/40Au/10Fe/GaAs reference sample exhibited only Gilbert damping enhanced by the spin-pump/spin-sink mechanism. The FMR linewidth in the 20Au/7Fe/40Au/11Pd/10Fe/GaAs sample was different qualitatively and quantitatively. In this sample the FMR linewidth for the **7Fe** layer was strongly dependent on the angle between the magnetization and the crystallographic [100]Fe axes, and showed a distinct four-fold symmetry, see Fig. 4.20(a). The minima in ΔH were observed when the applied magnetic field was oriented along the $\langle 110\rangle$ crystallographic directions in the Fe, and the maxima in ΔH were observed when the field was oriented along the $\langle 100\rangle$ crystallographic directions of Fe.

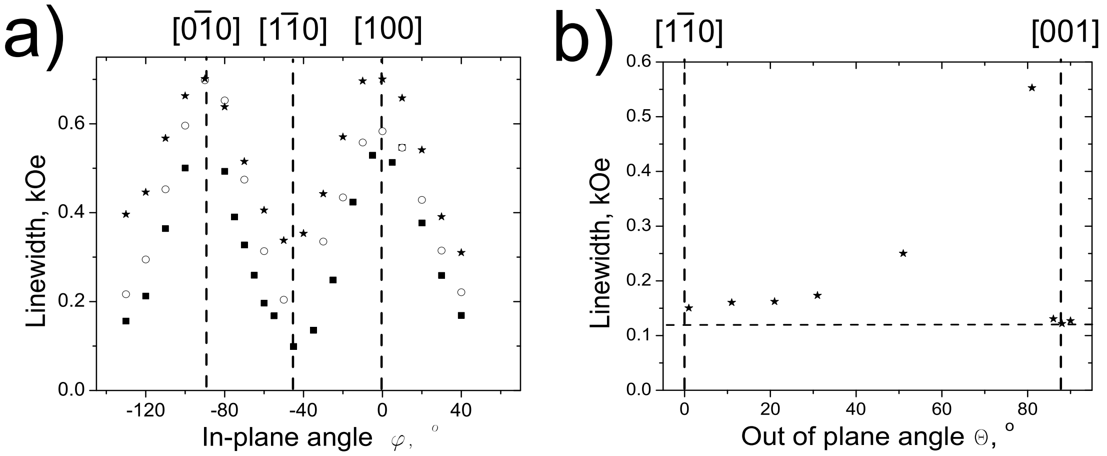

Figure 4.20: (a) In plane angular dependence of the FMR linewidth observed for the **7Fe** film in the 20Au/7Fe/40Au/11Pd/10Fe/GaAs structure. The FMR linewidth at 24 GHz (■), 36 GHz ($\circ$), and 74 GHz ($\star$). A large sinusoidal like angular dependence on the magnetic field orientation was observed. The narrowest lines occurred when the magnetic field was oriented along the $\langle 110\rangle$ directions of the Fe and the widest lines were observed when the field was directed along the $\langle 100\rangle$ crystallographic directions of Fe. (b) Out of plane angular dependence of the FMR linewidth at 24 Ghz. The angle θ was measured between the applied magnetic field and the film surface. The angle θ =0° corresponds to the in-plane[110] crystallographic direction. The angle θ =90° corresponds to the perpendicular direction. The external field was rotated in the (110) plane. Note that the FMR linewidth for the perpendicular orientation of the magnetic field is slightly narrower than that for the in-plane orientation of the magnetic field. Vertical dashed lines indicate major crystallographic directions.

The dependence of the FMR linewidth on the angle θ between the dc magnetic field and the sample normal is shown in Fig. 4.20(b). The data in Fig. 4.20(b) show that the damping decreases significantly in the vicinity of the perpendicular configuration. In fact, the measured ΔH in the perpendicular configuration at 10 and 24 GHz was given exactly by the intrinsic damping. The intrinsic values were obtained from the measurements on the reference sample. All these features indicate that the sample 20Au/7Fe/40Au/11Pd/10Fe/GaAs(001) was affected by a strong extrinsic damping that can be described by an angular dependent two magnon scattering mechanism (see page 99).

Interestingly the narrowest linewidth ΔH in the in-plane FMR configuration at 24 GHz was only 10 Oe wider than the linewidth observed for the perpendicular configuration. This means that the part of the extrinsic damping independent of angle was small compared with the angular dependent part which exhibited a maximum linewidth of 420 Oe of extrinsic damping.

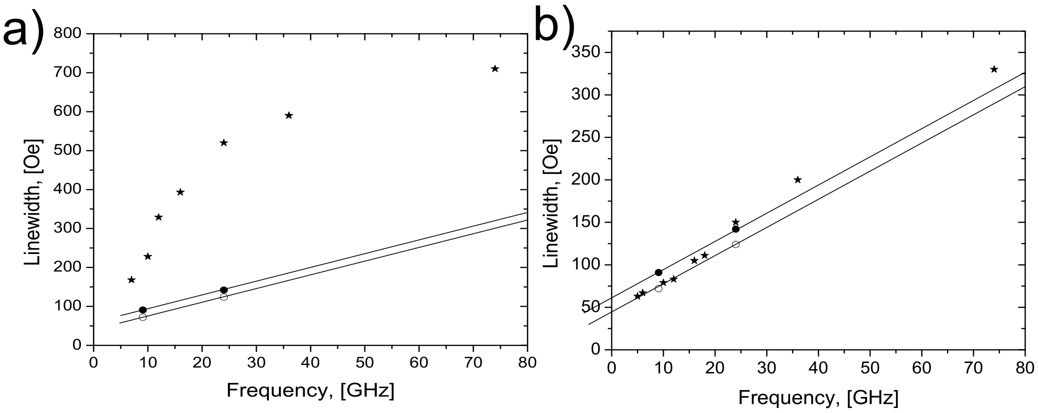

Figure 4.21: Frequency dependence of the in-plane FMR linewidth in the **7Fe** film located in the 20Au/7Fe/40Au/11Pd/10Fe/GaAs(001) structure. (a) The magnetization oriented along the [100] crystallographic axis. The data points are shown using a $\star$. A clear deviation from linear behavior is observed for frequencies greater than 24 GHz.The $\bullet$ points correspond to the linewidths at 10 and at24 GHz when the magnetic field is directed along the film normal. The $\circ$ points show the in-plane FMR linewidth measured in the **7Fe** film located in the reference 20Au/7Fe/40Au/10Fe/GaAs(001) sample (free of extrinsic damping). (b) The magnetizatization oriented along the [110] crystallographic direction. A linear dependence on frequency is observed with a zero frequency offset which can be attributed to long wavelength inhomogeneities in the **7Fe** film. The $\bullet$ points show the perpendicular FMR linewidths at 10 and 24 GHz. The $\circ$ points show the in-plane FMR linewidth measured in the **7Fe** film located in the reference 20Au/7Fe/40Au/10Fe/GaAs(001) sample. Linewidth measurements on the 20Au/7Fe/40Au/10Fe/GaAs(001) sample have shown that there is little or no extrinsic contribution.

The FMR linewidth also varied with the microwave frequency in a very profound way. The frequency dependence of the FMR linewidth, $\Delta H(f)$, when the magnetic field was directed along the $[100]_{Fe}$ and $[110]_{Fe}$ directions is shown in Fig. 4.21. When the field was directed along the $[110]_{Fe}$ direction (see Fig. 4.21(b)), the FMR linewidth was nearly linearly dependent on the microwave frequency over the interval 10 to 73 GHz, but was accompanied by a zero frequency offset $\Delta H(0) = 50$ Oe. This appreciable zero frequency offset can be explained by long range inhomogeneities in the very thin **7Fe** layer, as discussed in section 4.3.3. Small variations in the film thickness change the interface anisotropy fields. A simple estimate shows that variations in the thickness of the **7Fe** as small as 0.1 atomic layer can explain the observed zero frequency offset. However, the slope of the $\Delta H(f)$ vs frequency variation is nearly equal to the intrinsic

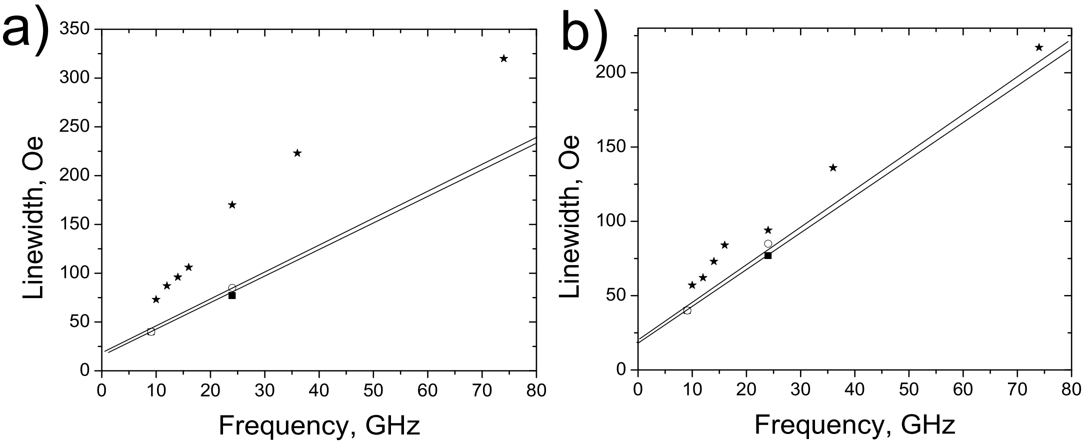

Figure 4.22: Frequency dependence of the FMR linewidth observed for the **10Fe** film. This film was grown on GaAs(001) as a part of the 20Au/7Fe/40Au/11Pd/10Fe/GaAs(001) structure. (a) The measured in-plane FMR linewidth as a function of frequency with the magnetization oriented along the [100] crystallographic axis. The data are shown by the $\star$ symbols. A clear deviation from linear behavior is observed for frequencies greater than 24 GHz. The strength of the non-Gilbert contribution to the FMR linewidth is much weaker than that observed in the **7Fe** film, compare with Fig. 4.21. (b) FMR linewidth vs frequency with the magnetization directed along the [110] crystallographic direction. The data points follow a linear dependence on the microwave frequency with a zero frequency offset that can be attributed to sample inhomogeneities. In both graphs the results of measurements on the reference sample are shown. The ■ symbols show the FMR linewidth in the perpendicular orientation for 10 and 24 GHz. The $\circ$ symbols show the in-plane FMR linewidths measured for the **10Fe** film when the magnetic field was directed along the [100] and [110] crystallographic directions: the **10Fe** film was located in the reference 20Au/7Fe/40Au/10Fe/GaAs(001) sample which was free of misfit dislocation defects and extrinsic damping.

Gilbert damping (including spin-pumping) obtained for the reference sample which has little or no extrinsic damping: see the $\circ$ on the same graph. The $\Delta H(f)$ dependence was quite different when the field was oriented along the $[100]_{Fe}$ orientation, see Fig. 4.21(a). $\Delta H(f)$ can not be described by a simple linear function of the frequency. However, the slope of $\Delta H(f)$ for frequencies greater than 36 GHz is nearly equal to the slope expected for intrinsic Gilbert damping. But the extrapolation of this slope to zero frequency results in an appreciable offset of $\Delta H(0) = 480$ Oe. For frequencies less than 36 GHz the frequency dependence of $\Delta H(f)$ shows a clear concave curvature. For frequencies less than 20 GHz $\Delta H(f)$ can be approximated by a linear dependence on the frequency corresponding to an effective damping parameter α_{eff} almost 10 times larger than that observed for the reference sample.

Extrinsic damping was also present in the **10Fe** layer located in the 20Au/7Fe/40Au/11Pd/10Fe/GaAs(001) structure but it was significantly weaker than that observed in the **7Fe** film grown directly on Au/Pd/Fe/GaAs. Otherwise the main characteristic features were maintained, see Fig.4.22. The formation of magnetic defects was not fully developed in the **10Fe** layer. Previous studies have shown that the full strength of this extrinsic damping is achieved by means of a thick Pd cover layer (more than 130 atomic layers) or by a combination of a thin Pd layer (more than 9 atomic layers) covered by a thick Au layer (more than 70 atomic layers); e.g. 90Au/9Pd/16Fe/GaAs(001) or 200Pd/30Fe/GaAs(001) [112]. In our studies a thinner combination of Au/Pd layers was used. This implies that the strain induced in the 20Au/7Fe/40Au/11Pd/10Fe/GaAs film was not sufficient to enable full propagation of misfit dislocation glide planes through the **10Fe** layer. On the other hand the **7Fe** layer deposited on the Pd template incorporated the dislocation network immediately.

Two-magnon scattering The extrinsic contribution to the FMR linewidth described above can be explained by a two magnon scattering mechanism. A uniform magnon, $q = 0$, driven by the rf field at FMR scatters into a $q \neq 0$ magnon. Energy conservation requires that the scattered magnon have the same energy as the uniform resonant magnon. However momentum conservation, conservation of the q wave vector, is not required due to the loss of translational invariance. The two-magnon scattering mechanism was proposed in the 1960's to explain extrinsic FMR line broadening in YIG spheres [115]. The same mechanism was successfully used to describe the extrinsic damping mechanism in ferrites [116, 117, 118, 119, 120] and in metallic films [121].

The two magnon scattering matrix is proportional to components of the Fourier transform of magnetic inhomogeneities

$$A(q) = \int \Delta U(r) \exp^{-iqr} dr \tag{4.9}$$

where $\Delta U(r)$ stands symbolically for variations of the local magnetic anisotropy energy. In ultrathin films the magnon q vectors are confined to the film plane (i.e. $q = q_{\|}$).

Recently, Arias and Mills [122] introduced a theory of two-magnon scattering that applies to ultrathin films. For an in-plane magnetization oriented along the external field direction, and neglecting magnetocrystalline anisotropies, the spin wave manifold has the form:

$$\left(\frac{\omega_q}{\gamma}\right)^2 = [H + 4\pi M_{eff} - 2\pi M_s qd + Dq^2] \times [H + 2\pi M_s qd \sin^2 \psi_{\vec{q}} + Dq^2], \tag{4.10}$$

where q is the wavevector of the scattered magnon , $\psi_{\vec{q}}$ is the angle between the magnetization direction and the spin-wave wavevector $\vec{q}$, and $D = \frac{2A}{M_s}$ is the exchange stiffness parameter. The FMR mode corresponds to q =0. The third term of the first bracket on the left hand side of eq. 4.10 is negative and proportional to q, and therefore it lowers the resonance frequency for magnons with $q > 0$. For large q vectors, the fourth term in the same bracket increases the magnon energy and is due to the exchange field, and the magnon dispersion curve crosses the energy of the homogeneous precession of the magnetization at a magnon wave vector $q_{deg}(\psi_{\vec{q}})$. This means that the homogenous FMR mode is degenerate with the $q_{deg}(\psi_{\vec{q}})$ mode and can be involved in two-magnon scattering. A mathematical analysis of the spin-wave manifold shows that q of the degenerate mode decreases with increasing $\psi_{\vec{q}}$ and disappears for a critical $\psi_{\vec{q}cr}$. In the two dimensional plane (q_x, q_y) the degenerate modes form lobes, see Fig. 4.23. A more general theory which includes out of plane orientations of the magnetization can be found in [112] and results in the conclusion that there are no degenerate modes when the film magnetization is oriented normal to the film plane (the perpendicular FMR configuration) .

The Arias and Mills theory is based on a Green's response function formalism using a continuous distribution of the magnetization [123]. It shows that two magnon scattering enters the denominator of the transverse rf susceptibility as an additional energy term R:

$$\chi'' = \frac{M_s B}{B_{eff} H - \left(\frac{\omega_{q=0}}{\gamma}\right)^2 + i(H + B)\alpha\frac{\omega_{q=0}}{\gamma} + R}, \tag{4.11}$$

where $B_{eff} = H + 4\pi M_{eff}$. The anisotropy terms are for simplicity neglected. The real part, Re(R), leads to a shift in the FMR field and the imaginary part Im(R) provides additional damping. Both contributions must satisfy the symmetry of the magnetic defects. The static properties measured using FMR can have a frequency dependent part due to the presence of the term Re(R). For samples subject to extrinsic damping the static and dynamic measurements do not, in principle, have to provide equal magnetic anisotropies, however differences are usually small especially at low microwave frequencies.

The strength of the two-magnon scattering varies as the static magnetization changes its orientation with respect to the in-plane crystallographic axes and is given by the imaginary part of R, Im(R). The imaginary part of the two-magnon contribution to the susceptibility is proportional to the square of the Fourier components that describe the magnetic scattering potential:

$$Im(R) \sim 2 \int_{-\psi_{\vec{q}cr}}^{\psi_{\vec{q}cr}} I(q_0, \varphi_q, \varphi_M) \frac{q_0 d\psi_q}{\frac{\partial\omega(q_0,\psi_q)}{\partial q}}, \tag{4.12}$$

where φ_q is the angle between the spin-wave wavevector q and the magnetization vector, φ_M is the angle between the dc magnetization and the [100] crystallographic axis, and $I(q_0, \varphi_q, \varphi_M)$ is the square of the strength of the two-magnon scattering potential.

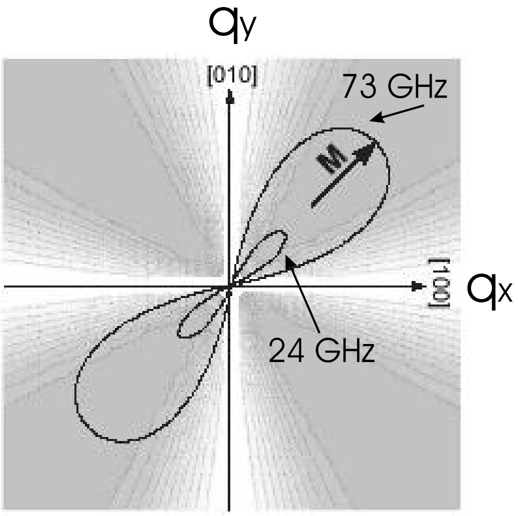

Figure 4.23: The solid lines represent the variation at 24 and 73 GHz of the magnon wave-vectors calculated from Eq. 4.10 for the case in which the applied magnetic field and the magnetization are directed along the Fe[110] crystallographic direction. These two-magnon scattering lobes are superimposed on the magnetic scattering intensity shown using shades of grey as a background and obtained from Eq. 4.13. The white color represents the strongest scattering intensity and grey - the weakest scattering intensity. Note that the orientation of the lobes (magnetization) affects the angular dependence of the FMR linewidth caused by the misfit dislocation network. Integration over the constant frequency lobes when the lobes are oriented along the [110]Fe directions yields a weaker two magnon scattering contribution than when the lobes are oriented along the [100]Fe directions.

Features of the experimental linewidth can be well reproduced by assuming that $I(q_0, \varphi_q, \varphi_M)$ has the following form:

$$I(q_0, \varphi_q, \varphi_M) \sim \cos^2(2\varphi_M) cos^4(2\varphi_q), \tag{4.13}$$

where the first term represents the magnetic symmetry of the defects and the second term represents the lattice defect symmetry. The lattice line defects result in local uniaxial magnetic anisotropies having the anisotropy axes parallel to the dislocation lines. This means that the two-magnon scattering intensity has an explicit dependence on the direction of the magnetization with respect to the symmetry axes of the magnetic defects. Since these symmetry axes are parallel with the crystallographic axes this term satisfies the requirements of the lattice symmetry. It is important to realize that the local uniaxial anisotropy contribution vanishes when the magnetization is oriented 45^o away from its axis. The dislocation glide planes propagate along the $< 100 >$ directions of the Fe. Two magnon scattering is absent in this case when the magnetization is parallel to the $< 110 >$ directions. The Fourier components of the scattering intensity are the product of two parts. One part is explicitly dependent on the angle φ_M between the magnetization and the crystallographic axes, and the second part is purely structural and depends explicitly on the distribution of the lattice defects with respect to the crystallographic axes. One can then represent the contribution of two magnon scattering to the damping as a walking path along the lobes in the orography of the Fourier components of the scattering intensities. Lindner et al. [124] observed an anisotropic extrinsic damping (measured along the [100] and [110] axes) for FeV superlattices. They used the Arrias-Mills theory to interpret their results. They were, in this way, able to understand the frequency dependent FMR linewith. Since the Arrias-Mills theory is isotropic they postulated an additional angular term $\cos^2(2\varphi_M)$, see 4.13. The origin of their proposed angular dependence is unknown but it is perhaps related to atomic steps on the film surfaces. However no explicit structural details were discussed.

Chapter 5

Spin currents in magnetic trilayer structures

The purpose of this chapter is to extend the study of spin pump/sink effects in magnetic multilayers to the case of a thick normal metal spacer, NM. The chapter will cover the following topics: (a) Diffusion of spin momentum across the NM layer. (b) Exchange of spin momentum in Au/Fe/Ag/Fe/GaAs(001) structures (c) Interference and the phase of spin currents. (d) Spin currents in non-collinear configurations of the Fe magnetic moments.

5.1 Diffusive spin momentum transfer

In magnetic F1/NM/F2 double layer structures the spin current generated at the F1/NM interface leads to an accumulated spin density $\vec{\mathbf{m}}_{NM}$ inside the NM spacer layer. Propagation of the spin momentum density across the NM spacer then leads to a dynamic exchange coupling between the magnetic layers. For thick NM layers one has to include a relaxation process that removes the magnetic angular momentum from the spin current. This is, in principle, a nontrivial problem. At this point one is able to treat quantitatively only the spin ballistic and spin diffuse limits. In reality the experimental studies have been carried out continuously for cases ranging from the ballistic to the diffuse limits. Theorists are presently working on the formulation of non-local spin dependent Boltzmann's equations. This theory is not yet available. In this thesis a pragmatic approach was taken. Diffusion equations with the appropriate boundary conditions will be used to describe the NM measurements from the ballistic to the purely diffuse limits.

The accumulated magnetic momentum density $\vec{\mathrm{m}}_{NM}$, created by spin current $\vec{\mathrm{j}}_m$ (at

F1/NM interface), in the NM is described by a diffusion equation:

$$i\omega\,\vec{\mathrm{m}}_{NM} = D\frac{\partial^2\vec{\mathrm{m}}_{NM}}{\partial x^2} - \frac{1}{\tau_{sf}}\vec{\mathrm{m}}_{NM}\ , \tag{5.1}$$

where ω is the angular frequency, τ_{sf} is the spin flip relaxation time, x is the coordinate in the direction perpendicular to the interface, $D = v_F^2\tau_m/3$ is the diffusion coefficient, and τ_m is the electron momentum relaxation time constant [125]. The diffusion Eq. 5.1 determines the spin diffusion length δ_{sd} in the NM. For $1/\tau_{sf} \gg \omega$ δ_{sd} is given by

$$\delta_{sd} = (D\tau_{sf})^{0.5}\ . \tag{5.2}$$

The solution of Eq. 5.1 requires boundary conditions. For the F/NM (spinpumping) interface the boundary condition is [125]

$$\vec{\mathrm{j}}_m - 0.5v_F\vec{\mathrm{m}}_{NM} = -D\frac{\partial\vec{\mathrm{m}}_{NM}}{\partial x}\ . \tag{5.3}$$

where v_F is the Fermi velocity For the outer interface, in a single F/NM magnetic layer structure, a free magnetic moment condition (full spin current reflection) was used.

$$\frac{\partial\vec{\mathrm{m}}_{NM}}{\partial x} = 0\ . \tag{5.4}$$

For a magnetic F1/NM/F2 double layer structure the boundary condition at the F1/NM interface is equivalent to Eq. 5.3. The boundary condition at the NM/F2 (spin sink) interface is [125]

$$-\frac{\partial\vec{\mathrm{m}}_{NM}}{\partial x} = 0.5v_F\vec{\mathrm{m}}_{NM}\ . \tag{5.5}$$

The boundary conditions of Eq. 5.5 are valid for the case when the layer F2 is off resonance and therefore contributes negligibly to spin pumping. The coefficient 0.5 corresponds to the effective transmission coefficient from the NM to the F layers and is given by Eq. (13) in [125]. The right hand side of Eq. 5.5 represents the magnetic current flowing from the NM into F2 and acts as a driving torque for the magnetic moment in F2. When both layers are in resonance the boundary condition 5.5 is modified by the spin current created at the F2/NM interface:

$$-\frac{\partial\vec{\mathrm{m}}_{NM}}{\partial x} = 0.5v_F\vec{\mathrm{m}}^1_{NM} - 0.5v_F\vec{\mathrm{m}}^2_{NM}\ . \tag{5.6}$$

where $\vec{\mathrm{m}}^1_{NM}$ and $\vec{\mathrm{m}}^2_{NM}$ are the accumulated magnetic momentum densities due to spin currents created at F1/NM and F2/NM, respectively.

5.2 Exchange of spin momentum in Au/Fe/Ag/Fe/GaAs films

The accumulated spin density in the NM is transported by itinerant electrons. The motion of the itinerant electrons in the NM is affected by momentum scattering (leading to resistance) and spin flip scattering (leading to loss of spin momentum). The momentum scattering also leads to diffusion. The spin flip scattering in cubic normal metals is caused by a weak spin orbit coupling. This means that only some momentum scattering is accompanied by a spin flip event [23] and therefore $\tau_{sf} \gg \tau_m$. The spin diffusion length δ_{sp} determines the length scale for spin momentum decay. For spacers significantly thinner than δ_{sp} the loss of spin momentum is negligible and the spin current propagation can be considered to be nearly in the spin ballistic regime. The spin diffusion length in Ag at RT is expected to be $\approx$ 150 nm in single crystalline Ag [126]. The role of spin currents on the interface Gilbert damping was investigated using a 20Au/12Fe/300Ag/16Fe/GaAs(001) structure, where the integers represent the number of atomic layers. The thickness of the Ag spacer in this structure was approximately 60 nm and therefore the spin current in this structure was expected to be only weakly affected by spin diffusion.

5.2.1 Static magnetic properties

The magnetic anisotropies for the 20Au/12Fe/300Ag/16Fe/GaAs(001) structure were obtained by means of standard FMR measurements [77]. The in-plane FMR measurements at 24 GHz as a function of the angle of the dc magnetic field, see Fig. 5.1(a), resulted in the following magnetic parameters: **The bottom 16Fe** layer grown on GaAs(001): an in-plane uniaxial anisotropy energy $K_u =$ -4.45x10^5 erg/cm^3 with the hard magnetic axis along the $[1\bar{1}0]$ crystallographic orientation of the GaAs(001), an in-plane four fold anisotropy energy K_1 = 2.65x10^5 erg/cm^3; and an effective demagnetizing field $4\pi M_{eff}$= 15.96 kG. **The top 12Fe** film grown on the Ag(001) layer: K_1 = 3.67x10^5 erg/cm^3, $K_u =$ 8.3x10^3 erg/cm^3 with the easy magnetic axis along the $[1\bar{1}0]_{GaAs}$, and $4\pi M_{eff}$ = 14.65 kG. The **16Fe** layer has a large in-plane uniaxial magnetic crystalline anisotropy. The interface uniaxial anisotropy in the 16Fe/GaAs(001) layer is inversely proportional to the Fe layer thickness [34]. This interface uniaxial anisotropy separated the resonance fields for the **16Fe** and **12Fe** layers except for a narrow angular region of the in-plane applied field where an accidental crossover of the resonance fields occurred.

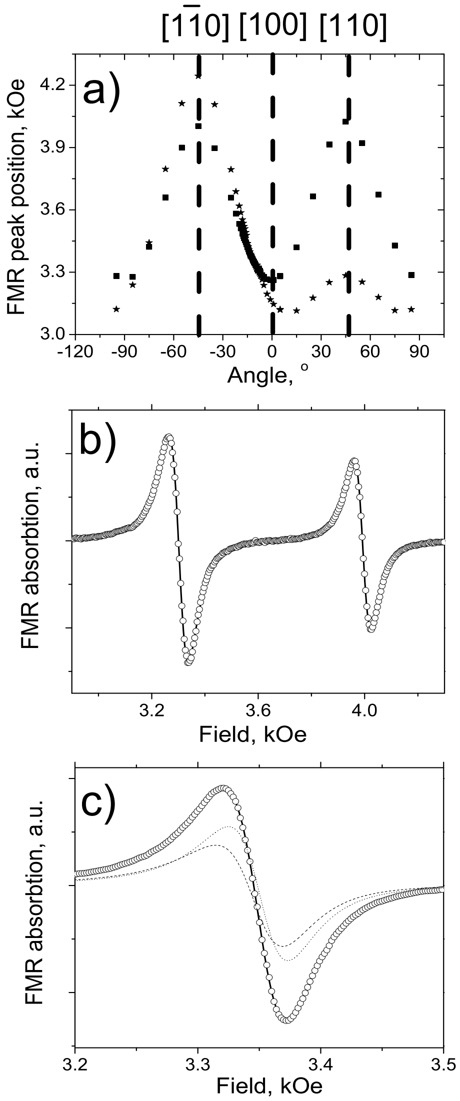

Figure 5.1: FMR studies at 24 GHz using a 20Au/**12Fe**/300Ag/**16Fe**/GaAs(001) specimen. The sample is inserted into a microwave cavity which provides parallel and symmetric driving rf fields for the **12Fe** and the **16Fe** films. (a) The FMR peak position as a function of the angle of the in-plane magnetic field with respect to the [100] crystallographic axis of GaAs. The ■ and $\star$ points correspond to **12Fe** and **16Fe**, respectively. Dashed verical lines indicate major crystallogrphic direcions of GaAs (b)The FMR signal with the external field oriented along the [110] axis. The FMR signals of the two layers are well separated in magnetic field strength. (c) The FMR signal at the accidental crossover of the **12Fe** and **16Fe** FMR fields. The dashed and dotted lines represent fits of the individual film resonances to the field derivatives of Lorentzian lines. The resulting full fit of the data with the sum of two Lorentzian derivatives is shown by the solid line.

5.2.2 Dynamic magnetic properties

The role of spin diffusion in the 20Au/12Fe/300Ag/16Fe/GaAs(001) specimen was tested by means of 20Au/5Ag/16Fe/GaAs(001) and 20Au/300Ag/16Fe/GaAs(001) samples. The magnetic damping parameter α of the **16Fe** film in the 20Au/5Ag/**16Fe**/GaAs(001) was mainly due to intrinsic bulk Gilbert damping. FMR measurements at 24 GHz resulted in $\alpha = 4.5\text{x}10^{-3}$ (ΔH = 37 Oe). The FMR linewidth in the 20Au/300Ag/16Fe/GaAs specimen was increased to ΔH = 45 Oe showing already a spin momentum loss in the Ag spacer due to spin diffusion. Self consistent solution of Eqs. 2.63 and 5.1 allowed one to estimate the diffusion parameters. The following parameters were required to fit the FMR linewidths for the above sample: $\tau_{sf} = 60\text{x}10^{-14}$ s, $\tau_m = 5\text{x}10^{-14}$ s and the spin diffusion length $\delta_{sd} = 150$ nm. The spin mixing conductance $g_{\uparrow\downarrow} = 2.4 \times 10^{15}$ was taken from Fe/Au/Fe/GaAs(001) studies [34]. The mixing conductance $g_{\uparrow\downarrow}$ is given by the the number of transverse spin channels l. Since the Fermi surfaces in Au and Ag are very similar one can assume that $g_{\uparrow\downarrow}$ in Ag and Au are almost the same.

The same set of parameters was able to explain the FMR linewidth, ΔH = 64 Oe, for the **16Fe** film in the magnetic 20Au/12Fe/300Ag/16Fe/GaAs(001) double layer structure when the FMR resonances were well separated, see Fig. 5.1(b). Surprisingly the **16Fe** layer exhibited a larger FMR linewidth than the **12Fe** film (ΔH = 55 Oe). This seemingly contradicts the $1/d$ dependence of the spin pumping contribution. However the total FMR linewidth is given by the sum of the bulk Gilbert and interface spin pumping contributions. The spin pumping contribution is a symmetric effect for the two Fe films and thus should scale with thickness like $1/d$. In order to explain the FMR linewidth in **12Fe** one has to assume that the intrinsic Gilbert damping in **12Fe** is smaller than that in **16Fe**. In the **12Fe** layer the bulk Gilbert damping parameter $\alpha = 2.5 \times 10^{-3}$. While for the **16Fe** film the Gilbert damping parameter $\alpha = 4.5 \times 10^{-3}$. This result is not unexpected considering our recent studies of the intrinsic Gilbert damping in single **Fe** layer structures (20Au/n**Fe**/GaAs(001)). In these structures the spin pumping contribution was negligible compared to the intrinsic Gilbert damping. We found that the Gilbert damping in these Fe films makes a significant $1/d$ contribution to the FMR linewidth, see Section 4.3. In this case the observed $1/d$ dependence is not due to spin pumping but is caused by spin orbit relaxation processes confined to the Fe/GaAs interface. The smaller damping observed for Fe films grown on the Ag template indicated that the intrinsic $1/d$ contribution to the Gilbert damping is much smaller than that found for Fe grown on a GaAs(001) substrate. It is interesting to note that a small value of the intrinsic Gilbert damping was also found in Fe ultrathin films grown on a

Ag single crystal template [127].

Fig. 5.1(b) shows the FMR signal for FMR peaks that are well separated in magnetic field (external field is applied along $[110]_{GaAs}$ direction). Fig. 5.1(c) shows the FMR signal at an accidental crossover of the FMR fields, see Fig. 5.1(a). At the crossover field the spin pumping contributions to the magnetic damping are nearly cancelled out by the spin-sink contributions; the FMR linewidths drop to 17 Oe and 14 Oe for **16Fe** and **12Fe**, respectively.

5.2.3 Spin sink contribution

The spin pump/spin sink effect leads to a redistribution of the rf magnetic moments inside magnetic double layers. The spin pump effect leads to a loss of spin momentum while the spin sink effect leads to a gain of spin momentum. E.g. the spin momentum received by the layer F1 in a F1/NM/F2 structure can be treated like an extra driving field which is proportional to the time derivative of the rf magnetization vector in the F2 layer. The spin sink driving is significantly enhanced when the F2 layer undergoes an FMR resonance. When the FMR fields of the two layers were well separated the contribution of the spin sink effect was non-observable. The spin sink contribution is small and it is completely overshadowed by the torque due to the rf driving field. It is only in the vicinity of the FMR crossover field that the spin sink contribution to the FMR linewidth can be significant.

Figure 5.2 shows the FMR spectrum of the 20Au/**12Fe**/300Ag/**16Fe**/GaAs(001) sample for fields near (but not at) the field corresponding to the crossover of the FMR resonance fields. A computer simulated FMR line is shown by the solid curve in Fig. 5.2(a). It includes the spin pump/spin sink effect and the resulting line is in a reasonable agreement with the experimentally observed FMR line, see Fig. 5.2(b). From these simulations one is able to obtain the contributions from the individual layers, and these are indicated by the dashed and dotted lines in Fig. 5.2(a). Note that the individual contributions are not simple symmetric derivatives of a Lorentzian absorption peak. For the top 12Fe layer one can observe a bump at the resonance position corresponding to the 16Fe layer and for the 16Fe layer one observes a dip at the position corresponding to the resonance position for the top 12Fe layer. The shape of these additional absorption features (dip and bump) follows the double derivative of the magnetization $\frac{\partial^2 \vec{M}}{\partial t \partial H}$, where the time derivative comes from the spin sink contribution. In fact the spin sink contribution leads to a wide and asymmetric

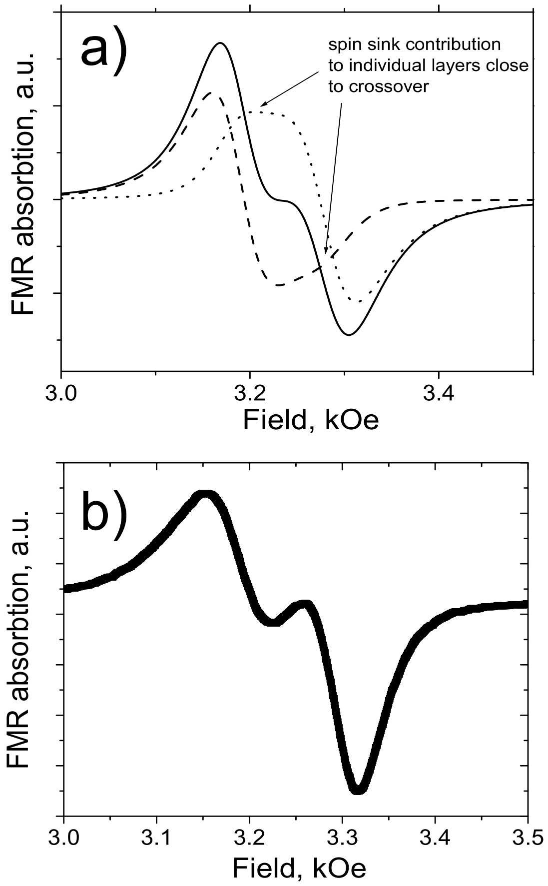

Figure 5.2: 24 GHz FMR absorbtion spectra near the applied field corresponding to an accidental crossover of the two FMR peak positions for the 20Au/**12Fe**/300Ag/**16Fe**/GaAs(001) sample. (a) Computer simulations of the FMR absorption lines. The total FMR absorption line is shown by the solid curve, the dashed line shows the contribution from the top 12Fe layer and the dotted line shows the contribution from the bottom 16Fe layer. The individual lines have an asymmetrical shape due to off resonance driving by the spin sink mechanism. In the vicinity of the crossover the spin sink contribution resulted in a widening of the FMR line. In (b) the experimentally observed FMR absorption line is shown for applied fields near the FMR crossover field.

absorbtion line, which includes an admixture of the absorption and dispersion parts of the rf susceptibility.

In the following the data analyses were carried out using an admixture of the absorptive and dispersive parts of the rf susceptibility. The data were fit using the sum of two admixed resonance lines representing the two Fe layers in a magnetic double layer structure.

5.2.4 Angular dependence of FMR linewidth

In Fig. 5.3(a) the angular dependence of the FMR linewidth is shown for the 12Fe film and the 16Fe film in the 20Au/**12Fe**/300Ag/**16Fe**/GaAs(001) sample. Only a narrow angular range in the vicinity of the FMR crossover is shown. The experimental absorption line for each angle of the external applied field was treated as a superposition of two asymmetric Lorentzians. Far away from the crossover the FMR linewidth was enhanced by the spin pump mechanism. At the crossover the FMR linewidth of both layers dropped due to a compensation of the spin pump contribution by the spin sink contribution. Furthermore, very close to the crossover field the FMR linewidth of the 16Fe film (notice, it reveals a wider line than that of the 12Fe film) increases before it drops to its minimum value. This is again due to off resonance spin sink contributions. Simulations shown in Fig. 5.3(b) reproduce fairly well all characteristic features of the experimental data. One can notice that the experimental linewidth is somewhat larger than the linewidth calculated using the simulations. This can be attributed to an additional small contribution from two magnon scattering, which is present for certain angles of the applied field in the samples with thick spacer layers. Two magnon scattering was not included in the simulations. The intrinsic damping and the strength of the spin pump/sink mechanism were obtained from the narrowest FMR lines, thus avoiding the two magnon contribution, for FMR fields far away from the crossover.

In figure 5.3(c) an analysis of the calculated FMR lines were carried out differently. The analyses were carried out assuming that each line consisted of two parts. One part represents the derivative of the main symmetric Lorentzian peak driven by the rf field. The second part represents the derivative of the satellite dispersion-like Lorentzian resonance peak driven by the spin sink mechanism (cf. 5.2). With this procedure one was able to obtain a perfect fit to the calculated FMR lines, see Fig. 5.3(c). No widening of the FMR absorption line was observed very close to the crossover, compare Fig. 5.3 (a) and (c). Not surprisingly adding the spin sink contribution represented the overall

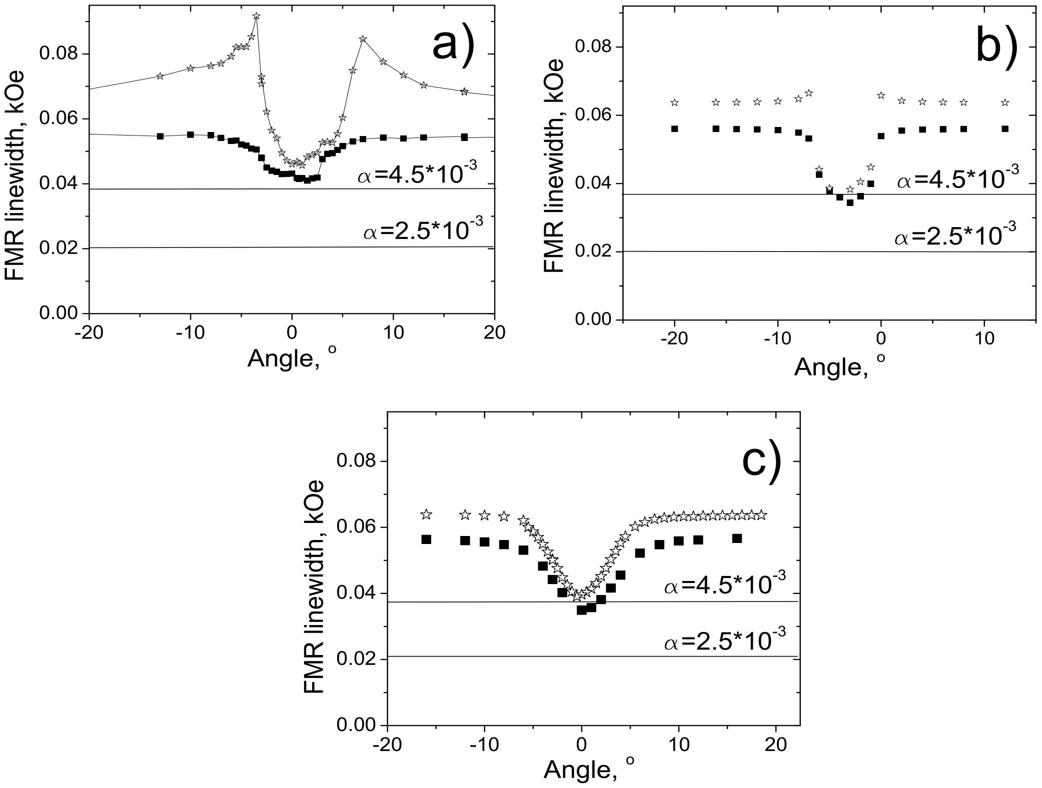

Figure 5.3: (a) FMR linewidth at 24 GHz as a function of the angle of the applied external field in a narrow angular range around angle corresponding to the accidental crossover of the FMR peak positions for the 20Au/**12Fe**/300Ag/**16Fe**/GaAs(001) sample. $\star$ and ■ show the experimental linewidths for the 16Fe film and the 12Fe film, respectively. The FMR absorption lines narrowed significantly at the crossover angle. The FMR linewidth for the 16Fe film decreased by an amount corresponding to the spin pump contribution. At the crossover angle the spin pump contribution is compensated by the spin sink contribution. The FMR linewidth for the 12Fe layer decreased by less than its spin pump contribution. The solid horizontal lines show the FMR linewidths corresponding to intrinsic Gilbert damping. (b) Simulations of FMR linewidths using spin pump/spin sink theory. The FMR linewidth is shown in a narrow angular range around the crossover angle. Computer simulations and the experimental data were fit using two Lorentzian resonances which included an admixture of the absorptive and dispersive parts of the Lorentzian resonance peak. (c) Theoretical linewidths calculated as a function of the angle around the angle corresponding to FMR crossover. The fitting of the calculated FMR line was carried out assuming that each line consisted of the main symmetric Lorentzian peak corresponding to the main resonance driven by the rf field and a satellite dispersion-like Lorentzian peak which was driven by the spin sink mechanism (cf. 5.2). Notice that no increase in the FMR linewidth is observed. This is a more physical way to interpret the data. Simulations were carried out using a theory which self-consistently accounted for spin relaxation and spin diffusion processes together with spin pump/spin sink mechanism. The following relaxation parameters were required to fit the FMR linewidths for the above simulations: $\tau_{sf} = 60\mathrm{x}10^{-14}$ s, $\tau_m = 5\mathrm{x}10^{-14}$ s and the spin mixing conductance $g_{\uparrow\downarrow} = 2.4 \times 10^{15}$. The corresponding spin diffusion length in Ag was found to be $\delta_{sd} = 150$ nm.

behavior of the rf susceptibility very well for angles near the crossover angle.

5.3 Phase of spin currents

The spin pump and spin sink contributions are dependent on the phase of the rf precession [128]. One can check this point by using antiparallel rf driving fields as shown in Fig. 5.4. This is a particularly interesting limit because one expects that the spin pump and spin sink contributions should add at each interface compared with symmetric rf driving for which they should subtract.

5.3.1 Antiparallel driving experiment

Antiparallel driving can be achieved by using the sample as part of a transmission line. For a thick spacer the rf magnetic fields in the ultrathin 12Fe and 16Fe films are antiparallel, see Fig. 5.4. A 20Au/12Fe/250Ag/16Fe/GaAs(001) structure was patterned onto a co-planar transmission line having a 30 μm thick central conductor. The waveguide was patterned from a continuous 20Au/12Fe/250Ag/16Fe film using optical lithography. A detailed description of the patterning procedure can be found in Appendix A.1. Subsequently Argon ion bombardment was used to remove the rest of the metallic film from the semi insulating GaAs substrate. Microwave power sent through this co-planar wavequide created nearly antiparallel rf magnetic fields in the 12Fe and 16Fe layers. This led to a π phase shift of the corresponding spin currents generated by the spin pumping. This produced a pronounced effect at angles and fields near those corresponding to an accidental crossover of the two resonance fields.

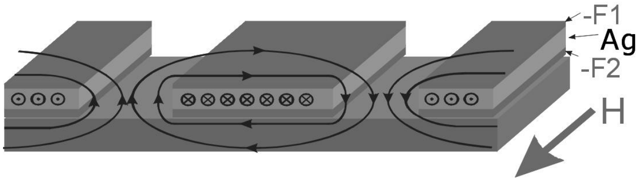

Figure 5.4: Schematic configuration of the FMR experiment using antiparallel rf magnetic field driving. The co-planar transmission line was patterned from a 20Au/12Fe/250Ag/16Fe(001) film grown on a GaAs(001) wafer. Patterning was carried out using optical lithography. The elliptical lines show the direction of the *rf* driving fields.

The patterned co-planar wavequide was positioned inside a dc magnet whose magnetic field was allowed to rotate in the film plane. The angular dependence of the FMR

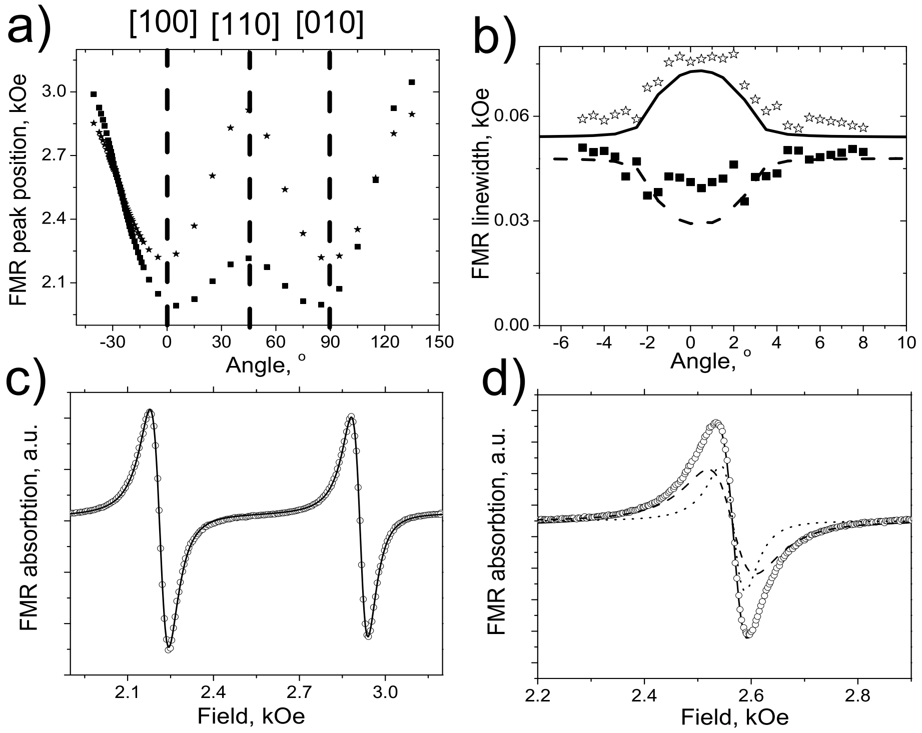

Figure 5.5: Antiparallel rf magnetic field driving. FMR studies at 20 GHz using a 20Au/**12Fe**/250Ag/**16Fe**/GaAs(001) specimen. The sample was a part of a coplanar transmission line which provided antiparallel rf driving fields for the 12Fe and 16Fe films.(a) FMR fields in 20Au/12Fe/250Ag/16Fe/GaAs as a function of the angle of the in-plane magnetic field with respect to the $[100]_{GaAs}$ crystallographic axis. The ■ and $\star$ points correspond to 16Fe and 12Fe, respectively. (b)The FMR linewidth as a function of the angle of the applied external field in a narrow range around the angle corresponding to an accidental crossover of the two FMR peak positions observed for the 20Au/**12Fe**/250Ag/**16Fe**/GaAs(001) sample. The 0° corresponds to the angle where the accidental crossover occurs. The $\star$ and ■ show experimental linewidths observed for the 16Fe film and the 12Fe film respectively. At the crossover the narrower FMR line followed the 12Fe layer and the ■ points. Solid and dashed lines show the linewidth obtained from simulations which self-consistently accounted for spin relaxation and spin diffusion processes together with the spin pump/spin sink mechanisms. The following relaxation parameters were required to fit the FMR linewidths: $\tau_{sf} = 60\text{x}10^{-14}$ s, $\tau_m = 5\text{x}10^{-14}$ s and the spin mixing conductance $g_{\uparrow\downarrow} = 2.4 \times 10^{15}$. The corresponding spin diffusion length in Ag was found to be $\delta_{sd} = 150$ nm. (c) The FMR signal with the external field applied along the $[110]_{GaAs}$ axis. In this case the FMR fields are separated by a large margin. (d) The FMR signal at an accidental crossover of the resonance fields. The dashed and dotted lines were obtained by fitting the data with the field derivatives of two Lorentzian lines. The solid line shows the fit obtained using Eq. 3.8.

was obtained by measuring the microwave transmission signal using a special microwave setup: a network analyzer was used as a frequency generator whose output signal was sent through a sample that was patterned onto a transmission line. A regular diode was used to analyze the microwave transmission signal. This setup provided an especially large signal to noise ratio due to a large filling factor achieved by patterning the sample onto the transmission line, see Appendix A.1. The results of FMR measurements at 20 GHz are shown in Fig. 5.5(a). Fig. 5.5(c) shows the FMR signal for the case in which the resonance fields for the 16Fe film and the 12Fe film were well separated (external field is applied along $[110]_{GaAs}$ direction). The FMR linewidths of 56 Oe and 50 Oe were obtained for the 16Fe film and the 12Fe film, respectively. The static and dynamic magnetic parameters were in good agreement with those obtained from the parallel rf driving measurements using a microwave cavity. The FMR signal at an accidental crossover is shown in Fig. 5.5(d). Intuitively one would expect that at the crossover the change in the phase of the spin sink contribution would lead to an increase of the FMR linewidths for both Fe layers. However, the experimental data showed that there was no obvious increase of the FMR linewidth at the accidental crossover. Fitting of the data was carried out using two Lorentzian lines with an admixture of the absorptive and dispersive parts of a Lorentzian resonance response. The two Lorentzian lines required two different linewidths, see Fig. 5.5(b). At the crossover the wide Lorentzian line (ΔH = 76 Oe) contributed to $\sim$ 85% and the narrow Lorentzian line (ΔH = 40 Oe) to 15% of the total intensity, respectively. Theoretical simulations, using the same magnetic parameters and with the same data processing as in experiment, resulted in a similar angular dependence of the FMR linewidths, see the solid and dashed lines (theory) and the data points (from experiment) in Fig. 5.5(b). The observed angular dependence of the FMR linewidth around the angle corresponding to accidental crossover of the resonance conditions under antiparallel driving of the two magnetic layers is shown in Fig. 5.5(b). Solid and dashed lines represent the results of the simulations and are in good qualitative agreement with the experimental data. However, theoretical calculations showed that the intensity of the narrow line decreased to approximately 1% of the total intensity at the crossover while in experiment this contribution dropped to only 15% of the total intensity. This discrepancy may be caused by a small misalignment of the external field with the crystallographic axes, which would detune the FMR signals of the two films at an accidental crossover. One has to realize that at the crossover the magnetization is not parallel with the dc field and consequently the spin pump/spin sink contributions do not correspond to a collinear geometry. The other possible reason for the discrepancy may be related to the microwave field distribution around the signal line of the coplanar waveguide. It is possible that we do not exactly obtain the condition of antiparallel rf driving due to the different interfaces involved: GaAs on one side of the signal line and air on the other side.

5.3.2 Spin sink effect in absorption spectra using antiparallel driving

The phase of the spin current modifies the FMR absorbtion line. This effect is again mainly visible in the vicinity of an accidental FMR resonance crossover, see Fig. 5.6. Antiparallel driving changes the sign of the spin sink contribution compared to that obtained for the case of parallel driving, see Fig. 5.2. This means that a "dip" is replaced by a "bump" and visa versa in the observed spectra. Visually it results in an additional wiggle between two resonances (cf 5.6(b)).

It is important to realize, that by performing measurements with parallel and antiparallel rf driving fields at the same frequency one is able, in principle, to isolate the spin sink driven signal. By subtracting the normalized absorption spectra for these two cases one obtains the double of the signal induced purely by the spin sink mechanism.

5.4 Spin currents in non-collinear configuration of magnetic moments

In magnetic double layers Au/Fe/Au/Fe/GaAs(001) the anisotropies in the top and bottom Fe films are different due to a large in-plane uniaxial interface anisotropy at the Fe/GaAs interface. This question was addressed in Section 4.2.3. The studies reported in this section were carried out on a 20Au/16Fe/30Au/16Fe/GaAs(001) structure. The resonant frequencies as a function of the applied field along the hard magnetic axes ($[1\bar{1}0]_{GaAs}$) are plotted in Fig. 4.9. The collinear branch of the top 16Fe layer crosses the non-collinear branch of the bottom 16Fe layer at $\sim$ 600 Oe (7.3 GHz), see Fig. 4.9 and the inset in Fig. 5.7. The direction of the noncollinear magnetization (bottom 16Fe layer) was tilted away from the external field by $\approx 30^o$ [89, 109]. It follows that the magnetic moments are also inclined from each other by $\approx 30^o$. In that case the spin current generated by the top 16Fe film was not entirely transverse to the magnetization of the bottom 16Fe layer and visa versa. The transverse components of the spin currents are absorbed at the FM/NM interface, as was shown in studies using a collinear configuration

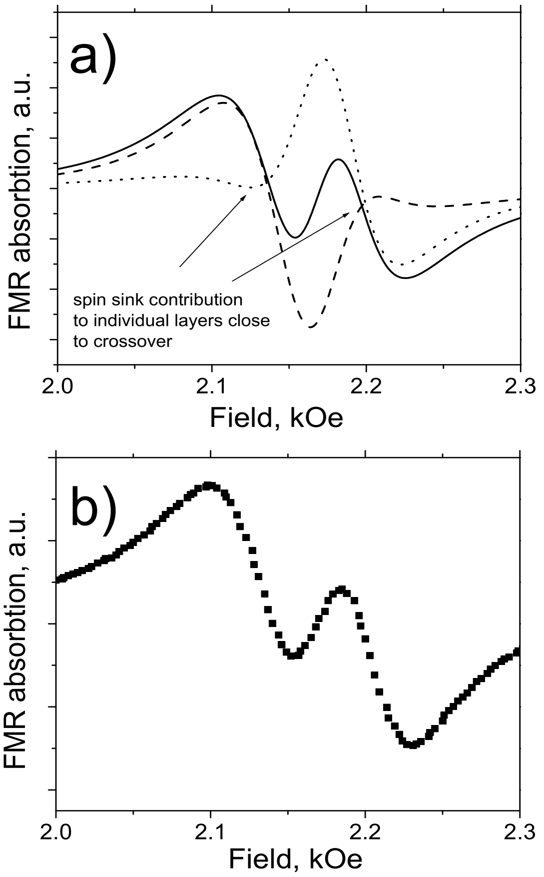

Figure 5.6: Antiparallel rf driving fields: FMR absorption spectra for conditions corresponding to a near accidental crossover of the FMR fields for the case of a 20Au/**12Fe**/250Ag/**16Fe**/GaAs(001) sample. (a) Simulated FMR absorption lines at 20GHz. The total FMR absorption is shown by the solid line; the dashed line shows the contribution from the top 12Fe layer and the dotted line shows the contribution from the bottom 16Fe layer. The individual lines have an asymmetric shape due to off-resonance driving by the spin sink mechanism. The spin sink contribution has the opposite sign from that in the case of homogeneous driving, shown in Fig. 5.2. (b) The FMR signal observed for antiparallel driving. The applied field is oriented near the angle corresponding to an accidental crossover of the two FMR fields. The spin sink contribution leads to the two narrowed and slightly separated lines resulting in an additional wiggle in the middle of the FMR signal. The agreement between theory and the data is good in the vicinity of the crossover; it is not as good exactly at the crossover.

of the magnetic moments. In the following paragraph we will investigate what happens to the parallel component of the spin current, when it reaches the other layer.

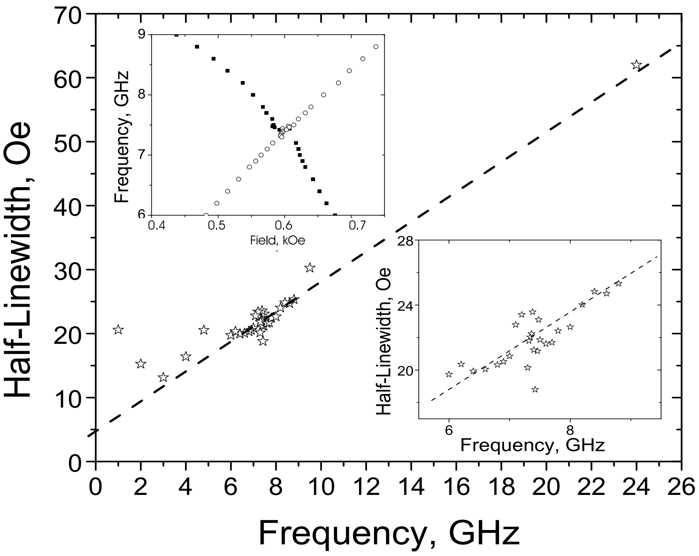

Figure 5.7: The frequency dependence of the FMR linewidth. The ($\star$) corresponds to the top **16Fe** film in a 20Au/16Fe/30Au/16Fe/GaAs structure. The applied field was oriented along the $[1\bar{1}0]_{GaAs}$ direction. The upper inset shows a magnified region of f *vs* H for fields near the crossover. The lower inset magnifies the region of ΔH *vs* f for frequencies near the crossover.

The frequency dependence of the FMR linewidth ($\Delta H(f)$) for the top 16Fe is shown in Fig. 5.7 with the field oriented along the $[1\bar{1}0]_{GaAs}$ axis. The linewidth is a linear function of frequency except for microwave frequencies less than 3 GHz; this discrepancy can be explained by long range inhomogeneities. At the crossover of resonance frequencies one expects that the spin-pumping contribution to ΔH should decrease (perhaps even removed) by exchanging spin currents between the two films [4]. The spin-pumping contribution to ΔH for the top 16Fe at 7.3 GHz is expected to be 8 to 9 Oe. The observed drop in ΔH, see Fig. 5.7, is almost a factor of two smaller than that value. However one should realize that this drop in ΔH happened in a non-collinear configuration of the magnetic moments. Only the spin current momentum component generated by the bottom 16Fe layer which is perpendicular to the saturation magnetization of the top layer is expected to be fully absorbed at the 16Fe/30Au interface. In a non-collinear configuration the parallel component of the spin momentum can be partially reflected. The total spin current passing through the top 16Fe/30Au interface consists of four contributions, see Fig. 5.8: (a) The spin current $\vec{j}_1^{out}$ pumped away from the top 16Fe/30Au interface towards the bottom 30Au/16Fe interface. (b) The spin current $\vec{j}_2^{in}$ received

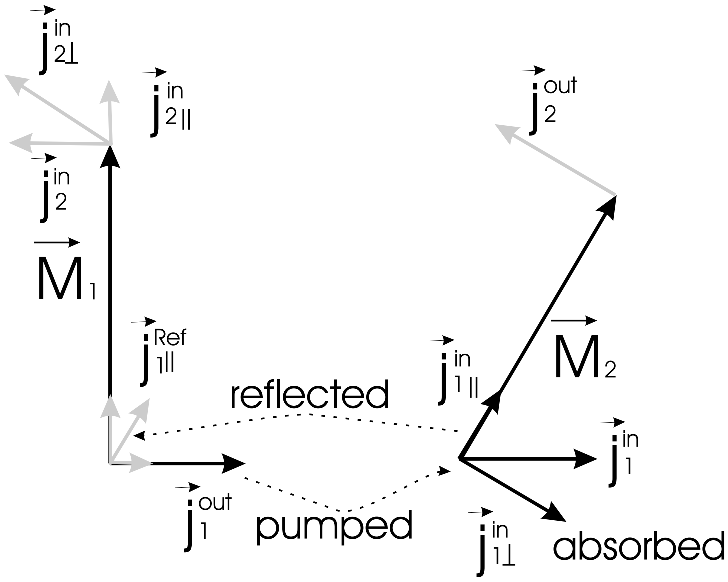

Figure 5.8: Schematic drawing showing the propagation and absorbtion of spin currents in the case of a non-collinear configuration of the magnetic moments $\vec{M}_1$ and $\vec{M}_2$. The precessing magnetic moment $\vec{M}_1$ generates a spin current $\vec{j}_1^{out}$. When $\vec{j}_1^{out}$ reaches the other layer the spin current momentum component can be decomposed into a component parallel to $\vec{M}_2$ $\vec{j}_{1\|}^{in}$ and a component perpendicular to $\vec{M}_2$ $\vec{j}_{1\perp}^{in}$. The current $\vec{j}_{1\perp}^{in}$ is absorbed at layer 2. The component $\vec{j}_{1\|}^{in}$, which is parallel to the magnetization $\vec{M}_2$ can be partially reflected and subsequently reach again layer 1 where it can be partly absorbed and partly reflected leading to multiple scattering events

from the bottom 30Au/16Fe interface. (c) The spin current $\vec{j}_{1\|}^{ref}$ reflected from the bottom 30Au/16Fe interface. (d) The spin current received after multiple reflections. Spin current computer simulations were carried out using the self-consistent exchange of spin momentum assuming that the perpendicular component of the incoming current was fully absorbed. The simulations have shown that in this case the decrease in the FMR linewidth was only 2 Oe, a value that is in good agreement with the experimental data. This means that only the component of the pumped magnetic moment that is perpendicular to the static magnetization contributes to a spin sink. The contribution of the reflected parallel component to the non-local dynamics is reduced by a factor of $\sin^2\theta$, where $\theta \approx 30^o$ is the angle between the static magnetizations of the two Fe layers, and hence was too small to be determined.

Chapter 6

Spin diffusion length in Au

The spin diffusion regime in the transport of spin momentum requires the use of a NM spacer having a thickness comparable to the spin diffusion length.

Two studies were carried out using: (a) Ferromagnetic Resonance (FMR) on Au/Fe/GaAs(001) structures. In this case one measures an increase in the interface Gilbert damping as a function of the Au overlayer thickness [126]. Similar experiments were carried out by Mizukami *et. al.* [129] on polycrystalline Cu/permalloy/Cu/Pt films. (b) Time, spatial and depth resolved Kerr effect studies on Au/Fe1/Au/Fe2/GaAs(001) structures. In this case one investigates the precession of the top Fe1 layer induced by spin currents generated at the bottom layer Fe2. The Fe1 serves as a spin momentum detector (probe) and Fe2 serves as a spin current generator.

6.1 FMR studies on nAu/16Fe/GaAs(001)

In these studies a series of samples with n = 20, 80, 150, 200, 250, 300 were prepared. The integers represent the number of atomic layers in the Au and Fe films. FMR studies were carried out using standard microwave spectrometers at 10, 24, 36 and 73 GHz, see the details in [77]. For Gilbert damping ΔH is strictly linearly dependent on the microwave angular frequency ω, $\Delta H = \alpha\frac{\omega}{\gamma}$. α is extracted from the slope of the curve of ΔH vs ω. In Au/Fe/GaAs(001) structures the Gilbert damping increases initially with increasing thickness of the Au. The spin pumped momentum becomes increasingly attenuated with increasing Au thickness due to a spin relaxation mechanism which can be described in the form of $\frac{1}{\tau_{sf}}\vec{\mathrm{m}}_{NM}$. Spin momentum scattering in the Au consequently leads to a loss of spin momentum from the Fe layer, and thus to an increased interface Gilbert damping parameter α_{sp}. This increase eventually saturates when the Au layer thickness becomes larger than the spin diffusion length δ_{sp}, see Fig. 6.1. For $d_{NM} \ll \delta_{sd}$ the FMR linewidth ΔH is given almost entirely by the intrinsic Gilbert damping in the Fe layer. However, notice that the increase in interface Gilbert damping depends linearly on the Au layer thickness for small thicknesses, therefore in principle there is no real zero thickness contribution to ΔH from spin pumping: the spin pumping contribution can be made negligibly small compared with the bulk intrinsic damping. The equations of motion 2.63 and 5.1 with the boundary conditions 5.3 and 5.4 were solved self-consistently and used for fitting the measured Gilbert damping coefficient α to a function of the Au layer thickness, see Fig. 6.2. Assuming a Fermi velocity υ_F =1.4x10^8 cm/s the curve fitting resulted in the following parameters: α^{intr} =3.5x10^{-3}, $\widetilde{g}_{\uparrow\downarrow}$ =2.4x10^{15} cm^{-2}, τ_m =1.2x10^{-14} s, τ_{sf} =15x10^{-14} s. It is interesting to note that in this fitting procedure the τ_{sp} and τ_m have unique values because the saturated value of α^{sp} is proportional to $(\tau_{sf}/\tau_m)^{0.5}$ while the approach to saturation scales with (δ_{sd}) which is proportional to $(\tau_m\tau_{sf})^{0.5}$ [130]. The electron relaxation time parameters resulted in a spin diffusion length δ_{sd} = 34 nm.

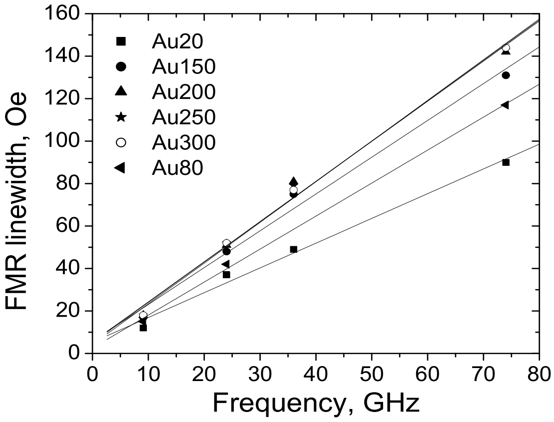

Figure 6.1: FMR linewidth vs frequency as a function of the thickness of the Au capping layer in Au/Fe/GaAs(001) structures. The solid lines represent linear fits to the frequency dependence of the FMR linewidth. The integers in the figure legend represent the number of atomic layers in the Au capping layers.

The spin flip relaxation time τ_{sf} is expected to be larger than the electron momentum relaxation time τ_m. In our samples τ_{sf} is larger than τ_m by a factor of 12.

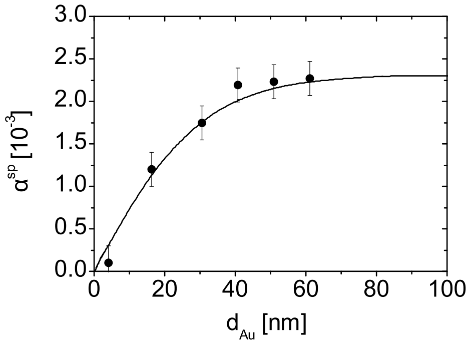

Figure 6.2: The additional Fe damping parameter in Au/**16Fe**/GaAs(001) structures as a function of the thickness of the capping Au layer. The solid line is a theoretical fit to the data using the parameters $\widetilde{g}_{\uparrow\downarrow}$ =2.4x10^{15} cm^{-2}, τ_m =1.2x10^{-14} s, τ_{sf} =15x10^{-14} s, and assuming that the Fermi velocity υ_F =1.4x10^8 cm/s.

6.2 TRMOKE measurements on double layers

TRMOKE studies were carried out using double layer Au/Fe2/Au/Fe1/GaAs(001) magnetic structures. In double layer magnetic structures one can directly study the magnetic excitation induced by the spin sink current. The accumulated spin density which was created by the **Fe1** layer was transported across the Au spacer to the NM/F2 interface. This interface acts as spin sink and the absorbed spin torque excites a precessional motion of the magnetic moment in the probe **Fe2** layer. The magnetization precession in the **Fe2** layer was monitored using the time (∼ 1 ps) and spatially (∼ 300 nm) resolved magneto-optical Kerr effect (TRMOKE) combined with a continuous wave (cw) *rf*-driving field, see Section 2.3.

In order to study the propagation of spin currents it was necessary to acquire the dynamic MOKE signal only from the top **12Fe** layer. This is not a simple problem because the penetration depth of the 400 nm wavelength laser beam is of the order of 100nm which is larger than the spin diffusion length. However, as pointed out in sections 2.3 and 3.3 it is possible to suppress the MOKE signal from the bottom **16Fe** through the use of a rotatable 1/4 wave plate compensator.

In the next few paragraphs a detailed calculation of the light propagation and Kerr signal generation in multilayer samples will be presented.

6.2.1 Propagation of light in metallic media

The following analysis and discussion will be limited to magnetic 20Au/12Fe/nAu/16Fe/GaAs(001) double layers, where integers denote the number of atomic layers and n was set to 150 and 300 atomic layers. A schematic picture of the propagation of light in a magnetic trilayer structure is illustrated in Fig. 6.3. Mathematically the electromagnetic wave inside the layer i of the metallic film can be treated as a superposition of forward and backward waves. The electric field components for the i layer for the forward and backward waves are denoted by e_i^+ and e_i^-, respectively, see Fig. 6.3. The thickness of the GaAs substrate is set to infinity and thus only the forward wave is considered in the GaAs. At an arbitrary position z' (z' is negative) measured from the right interface of the layer i the total electric field is given by a superposition of the forward and backward waves,

$$e_i(z')\exp^{-i\omega t} = (e_i^+ \exp^{-ik_i z'} + e_i^- \exp^{ik_i z'})\exp^{-i\omega t}, \tag{6.1}$$

where ω is the angular frequency of the incident light and k_i is the complex k wave vector inside the layer i,

$$k_i = k_0\sqrt{\epsilon_{i,d}}, \tag{6.2}$$

and $k_0 = \frac{2\pi}{\lambda}$ is the amplitude of the wave vector in vacuum. The distribution of the electromagnetic waves inside the magnetic double layer is, in a very good approximation, determined by the diagonal permittivity components. The magneto-optical Kerr effect can be treated as a small perturbation. Let us assume that the electric field of the incident light, at the wavelength $\lambda = 400$ nm (as used in the real experiment), is linearly polarized along the x direction with the amplitude $e_i = 1$.

Boundary conditions require the continuity of the in-plane e and h field components [131]. The ratio of the transversal components of the magnetic h and electric e fields are given by the characteristic impedance,

$$h_i = \pm\frac{e_i}{Z_i}, \tag{6.3}$$

where ± corresponds to the forward and backward waves, respectively. Z_i is the characteristic transversal impedance given by

$$Z_i = Z_0\sqrt{\frac{1}{\epsilon_i}}, \tag{6.4}$$

where Z_0=377 Ω is the characteristic impedance of free space. At the interface $i/i-1$ the boundary condition for the e field is

$$e_i^+ + e_i^- = e_{i-1}^+ \exp^{-ik_{i-1}d_{i-1}} + e_{i-1}^- \exp^{ik_{i-1}d_{i-1}} \tag{6.5}$$

and for the h field it is

$$\frac{e_i^+}{Z_i} - \frac{e_i^-}{Z_i} = \frac{e_{i-1}^+ \exp^{-ik_{i-1}d_{i-1}}}{Z_{i-1}} - \frac{e_{i-1}^- \exp^{ik_{i-1}d_{i-1}}}{Z_{i-1}} \tag{6.6}$$

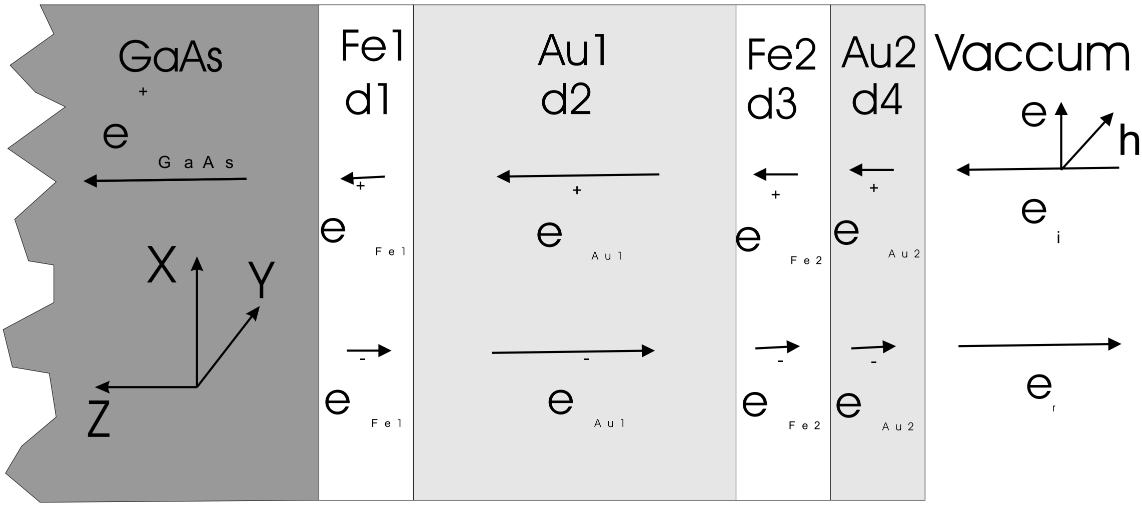

Figure 6.3: A schematic picture of the interface boundaries and propagation of electromagnetic waves in a multilayer sample. The complex amplitudes of the electric field for the layer i and for the forward and backward waves are denoted by e_i^+ and e_i^- respectively.

The diagonal components of the permittivity tensor for a cubic crystal, $\epsilon_{i,d}$, are given by the square of the refractive index $N_i = n - ik$ [132],

$$\epsilon_{i,d} = \epsilon_0[(n^2 - k^2) - i(2nk)] \tag{6.7}$$

For the free space wavelength $\lambda = 400$ nm the following optical parameters were used [133, 134]:

Material	n	k
Au	1.54	1.8
Fe	1.8	3.06
GaAs	4.373	2.14
Vacuum	1	0

Table 6.1: Optical properties of Au, Fe and GaAs

There are 10 unknown electric field components e_i. There are 5 interfaces each having two boundary conditions, leading to 10 equations. The above linear set of equations allows one to calculate the electric fields e_i (10 components) everywhere inside the structure. A Fortran code was used to solve this 10X10 system of linear equations. The distribution of the electric fields inside the 20Au/12Fe/150Au/16Fe/GaAs and 20Au/12Fe/300Au/16Fe/GaAs structures is shown in Fig. 6.4, where the integers represent the number of atomic layers. The amplitude of the electric field inside the

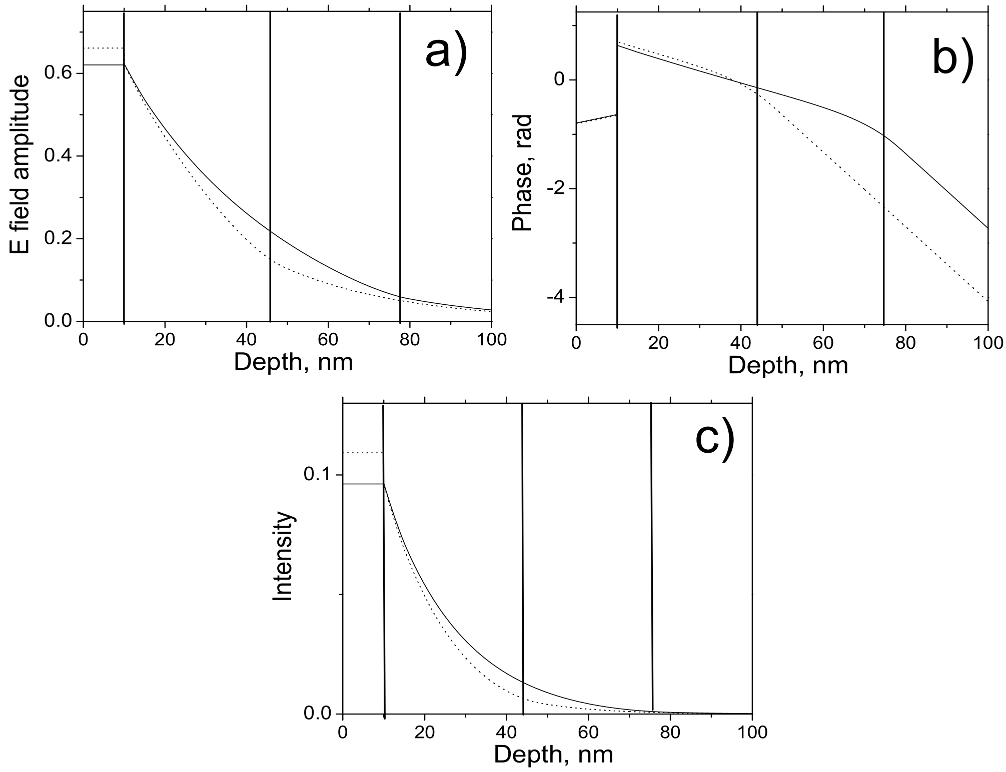

Figure 6.4: Calculation of the propagation of light (λ ~400 nm in free space)in a multilayer metallic/semiconductor structure and for perpendicular incidence. (a) shows the amplitude of the electric field inside the structure. (b) shows the position dependence of the phase of the electric field. (c) shows the position dependence of the electric field intensity. The dotted and solid lines show the results for the 20Au/12Fe/150Au/16Fe/GaAs and 20Au/12Fe/300Au/16Fe/GaAs structures, respectively. The left solid vertical line (at 10 nm) shows the vacuum/metal (vacuum/20Au) interface. The middle solid vertical lines (at $\approx$ 46 nm) show the metal/GaAs (16Fe/GaAs) interface for the 20Au/12Fe/150Au/16Fe/GaAs structure and the right solid vertical line (at $\approx$ 78 nm) shows the metal/GaAs (16Fe/GaAs) interface for the 20Au/12Fe/300Au/16Fe/GaAs structure

structure is strongly attenuated, see Fig. 6.4(a). The electric field intensity is calculated using Poynting vector [135]. In a propagating sinusoidal electromagnetic plane wave of a fixed frequency, the Poynting vector oscillates, always pointing in the direction of propagation. The time-averaged magnitude of the Poynting vector is given with Eq. 6.8 and is shown in Fig. 6.4(c). One can see that a 400 nm light wave is almost entirely attenuated at the metal/GaAs interface for a 300Au thick spacer.

$$A_i(z') = \frac{\varepsilon_0 c}{2} e_i(z') * e_i^*(z'), \tag{6.8}$$

where e_i^* is the complex conjugate of the component e_i and c is the speed of light in free space. Interestingly one observes a more rapid decay of the light intensity inside the film having a thinner Au spacer. This can be understood to be the consequence of the considerable impedance mismatch at the metal/GaAs interface.

Thus the ferromagnetic layers at different depths are exposed to a nontrivial distribution of the electric field of the light.

6.2.2 Radiation due to the Kerr effect

At normal incidence of the incident light wave the interaction of the light with the magnetized media leads to the radiation of light waves having a polarization perpendicular to the polarization of the incident light. Mathematically this radiation can be treated by using a two step process.

Firstly, the off diagonal components of the permittivity ϵ create an electric $\overrightarrow{D}$ component having a polarization perpendicular to the incident electric vector. The thickness of the magnetic layer is much smaller than the decay length of light inside the metal thus one can assume that the component of the electric field inside the magnetic layer j has a constant amplitude and phase and is given by

$$e_j = e_j^+ + e_j^-, \tag{6.9}$$

The vector of the driving electric field inside the layer j is given by

$$\vec{E}_i = \begin{pmatrix} e_j \\ 0 \\ 0 \end{pmatrix}. \tag{6.10}$$

The $\overrightarrow{D}_j$ field induced by the off diagonal components of ϵ inside the magnetic layer j

can be calculated using matrix multiplication

$$\vec{D}_j = \epsilon_0 \begin{pmatrix} 0 & -\epsilon_{xy} & 0 \\ \epsilon_{xy} & 0 & 0 \\ 0 & 0 & 0 \end{pmatrix} \begin{pmatrix} e_j \\ 0 \\ 0 \end{pmatrix} = \epsilon_0 \begin{pmatrix} 0 \\ \epsilon_{xy} e_j \\ 0 \end{pmatrix}. \tag{6.11}$$

where ε_0 and ε_{xy} are the permittivity of free space and the relative permittivity of the media, respectively.

The induced $\overrightarrow{D}$ which is polarized along the y direction can be viewed as acting like a radiating antenna [136], see Fig.6.5. The propagation of waves by a radiating antenna is treated in the same manner as in section 6.2.1. Let us assume that the layer F1 (next to the GaAs) is a radiating antenna. Continuity of e and h fields at the interfaces which do not belong to the layer F1 are the same as in the previous calculation. However at the interfaces of the Fe1 layer the situation is different. The induced D and e electric fields having a polarization along the y axis are constant across the F1 film and Maxwell's equations lead to the following boundary condition:

$$e'(GaAs)_{GaAs/Fe1} = e'(Au1)_{Fe1/Au1}. \tag{6.12}$$

where $e'(GaAs)_{GaAs/Fe1}$ and $e'(Au1)_{Fe1/Au1}$ are the electric fields at the GaAs/Fe1 interface on the GaAs side and the Fe1 side, respectively. One has also to satisfy the Maxwell equation

$$curl\vec{H} = \frac{\partial \vec{D}}{\partial t}. \tag{6.13}$$

Applying Stoke's theorem along the dashed integration path shown in Fig. 6.5a results in a discontinuity of the h fields at the boundaries of the layer Fe1,

$$h^+_{Fe1} - h^-_{Fe1} = \epsilon_0 \epsilon_{xy} e_{Fe1} d_1 \omega, \tag{6.14}$$

where + and - superscripts denote the right and left interface respectively. The right hand side of Eq.6.14 generates light waves inside and outside of the sample. It leads to a MOKE signal outside of the sample. The off diagonal components ϵ_{xy} in Fe were studied in the late 60's by Krinchik and Artem'ev [137, 138]. The real and imaginary parts of ϵ_{xy} were measured for a wide range of wavelengths. At a wavelength of 400 nm $\epsilon_{xy} = 0.12 + 0.11i$.

The Kerr signal generation and the wave propagation was calculated by solving a 9X9 system of linear coupled equations. Fig. 6.6 shows the Kerr signal generated by the 16Fe layer grown on GaAs(001). For comparison two thicknesses of the Au spacer layer y

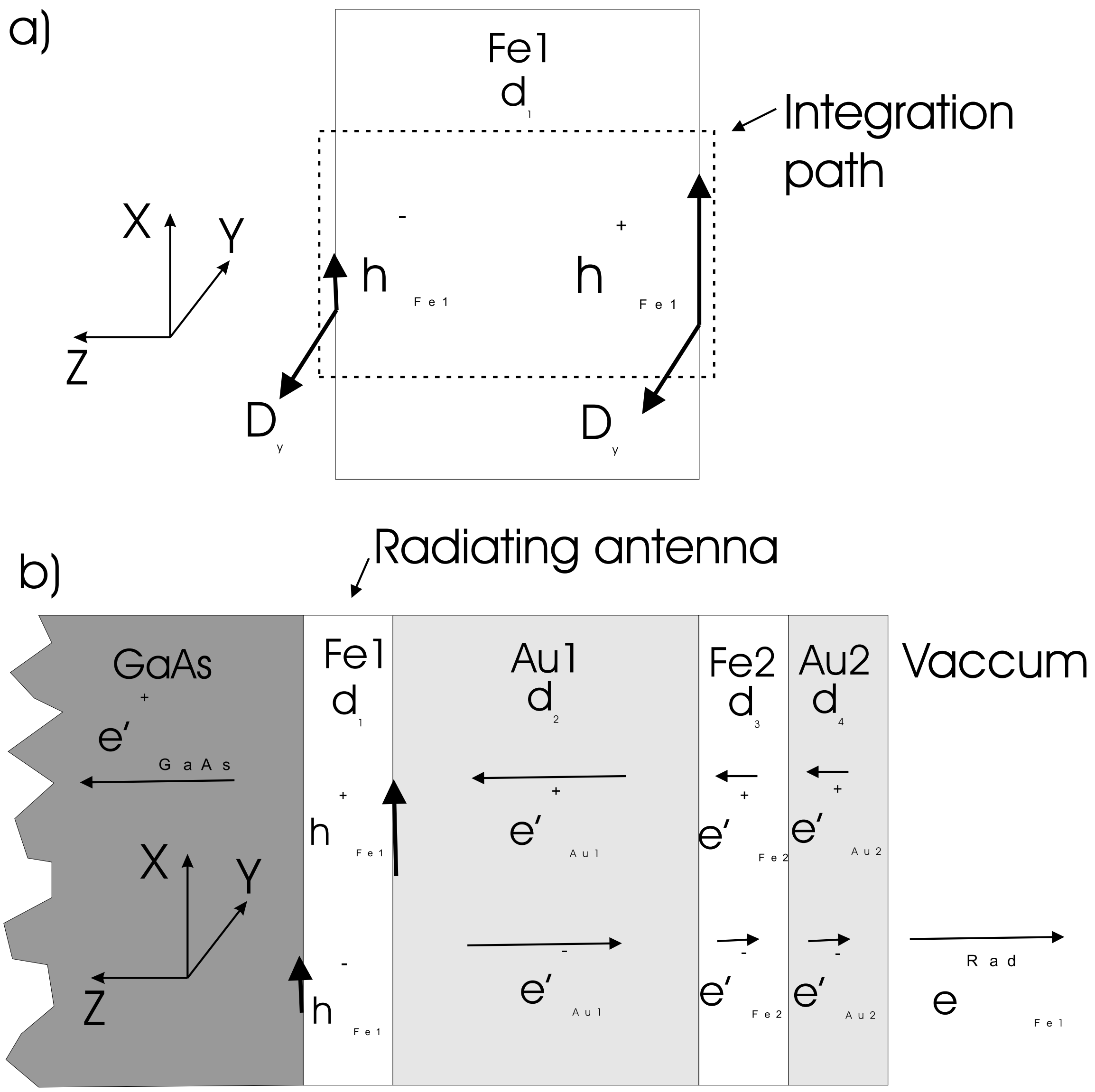

Figure 6.5: (a) The $\vec{D}$ vector created by the Kerr effect leads to electromagnetic waves having a discontinuity in the h field at the ferromagnetic layer interfaces. The dashed line shows the integration path for Stoke's theorem applied to the magnetic field h. (b) The $\vec{D}$ vector can be treated like a radiating antenna setting up its own electromagnetic waves. The e fields are polarized along the y axis and the h field is polarized along the x axis. Propagation of these waves in a multilayer structure is shown by the solid arrows. The complex amplitudes of the electric field of each electromagnetic wave inside the metallic film for the i layer for the forward and backward waves are denoted by $e`^{+}_{i}$ and $e`^{-}_{i}$ respectively.

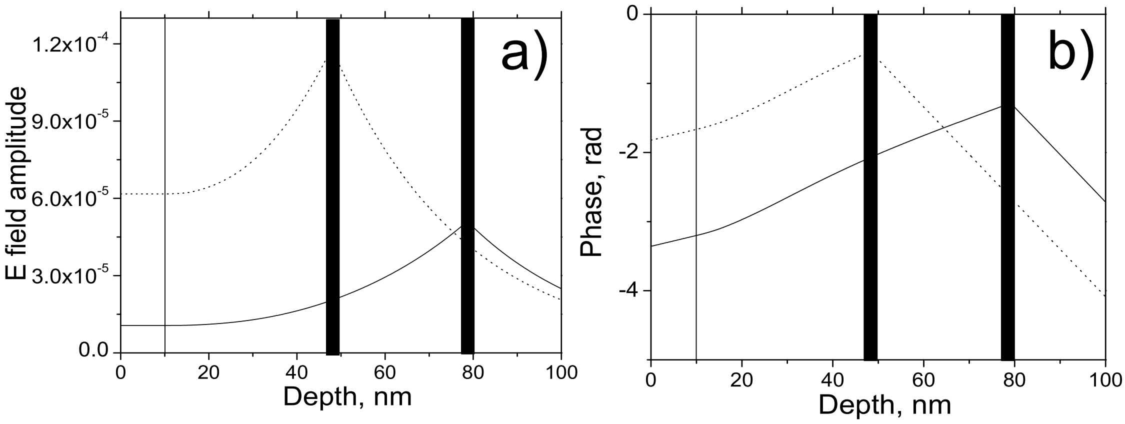

Figure 6.6: Calculation of the electric field corresponding to the Kerr effect generated by the 16Fe film inside the 20Au/12Fe/Au/16Fe/GaAs structure. Figure (a) shows the electric field amplitude and (b) shows the phase of the electric field component. The calculations were carried out for Au spacers 150 atomic layers thick (shown by the dotted line) and 300 atomic layers thick (shown by the solid line). The thick black vertical lines indicate the position of the 16Fe layer. The thin vertical black line at 10 nm indicates the interface between the sample and vacuum.

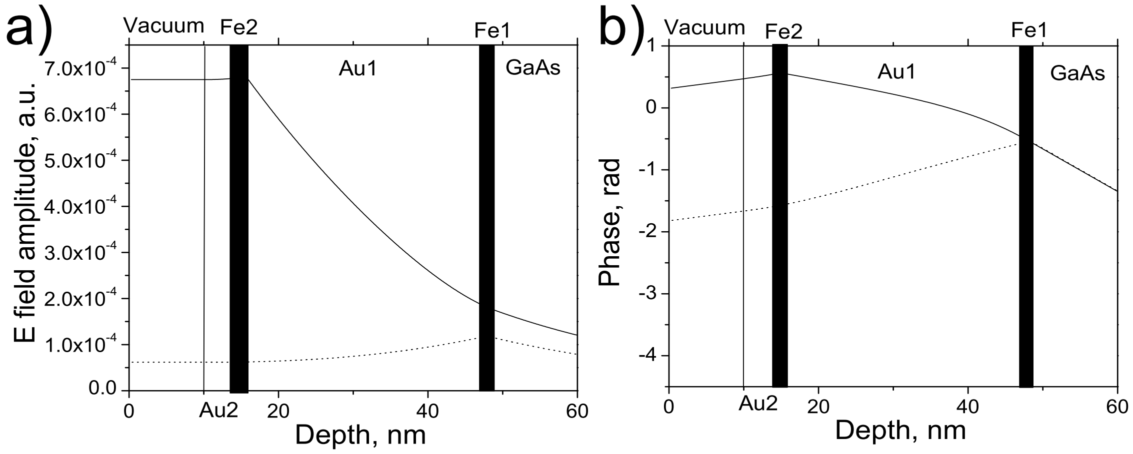

Figure 6.7: Calculation of the electric field generated in the 20Au/12Fe/150Au/16Fe/GaAs magnetic double layer by the Kerr effect. The dotted line shows the Kerr signal created by the 16Fe layer grown on GaAs, and the solid line shows the Kerr signal generated by the top 12Fe layer. The black vertical lines indicate the positions of the two Fe layers. The thin vertical solid line indicates the vacuum/metallic film interface. (a)is a plot of the electric field amplitudes and (b) is a plot of the electric field phase.

were considered: 150 atomic layers and 300 atomic layers. The amplitude and phase as a function of distance inside the 20Au/12Fe/nAu/16Fe/GaAs structure are shown in Fig. 6.6. The thick vertical black lines indicate the 16Fe film position and the vertical thin line indicates the vacuum/metal interface. Notice that the amplitude of the Kerr signal at the **16Fe** layer for the 300Au spacer layer is only about one third as large as that for the 150Au spacer layer. This result is due to the attenuation of the incident light inside the Au spacer layer, see Fig. 6.4. At the vacuum/metal interface this difference is even more pronounced and becomes as large as a factor of 5. The phase difference for the two Kerr signals at the vacuum/metal interface is ≈ 1.5 rad, see Fig. 6.6(b), this is an important parameter for depth resolved MOKE studies.

Similar calculations were carried out for the Kerr electric field generated in the top **12Fe** layer. In this case the light had to propagate only through the thin 20 atomic layer cap before it reached the vacuum/Au interface cf. Fig.(6.3). The **12Fe** layer is exposed to $\approx 90\%$ of the amplitude of the incident electric field (cf. Fig.6.4). The induced $\vec{D}$ in the Fe2 layer was obviously larger than that for the **Fe1** layer grown on GaAs. Calculations for a 20Au/**12Fe**/150Au/16Fe/GaAs structure are shown in Fig. 6.7. The amplitude of the Kerr electric field generated in **12Fe** is ≈ 7 times larger than that generated in **16Fe**. The phases of the Kerr signals from the top and bottom layers differ by 2 radians. The difference between the two Kerr signals can be explained by the extra optical path through an additional 30 nm of Au.

6.2.3 Depth sensitivity of MOKE

The Kerr effect signal (e_j^{kerr}, cf. Fig.6.5) from the j magnetic layer is detected by mixing it with a reference signal using the projection of the reference and Kerr polarizations into a direction selected by an analyzer. The reflected light wave electric field e_r is usually used as a reference signal, see Fig. 6.3. In fact, usually the Kerr signal is detected by means of a diode having an output proportional to the square of the total electric field component,

$$A \sim (e_r + e_j^{kerr})(e_r^* + e_j^{kerr*}). \tag{6.15}$$

The first order term gives

$$A \sim (e_r e_j^{kerr*} + e_j^{kerr} e_r^*). \tag{6.16}$$

Assuming a phase shift ϕ of the Kerr signal with respect to the reflected signal one can rewrite Eq. 6.16 in the following form:

$$A \sim \mid e^{kerr} \mid \cdot \mid e^r \mid \ \cos(\phi), \tag{6.17}$$

Notice that for $\phi = 90^\circ$ the detected Kerr intensity is zero. Using a rotatable compensator, the phase of the Kerr amplitude can be adjusted relative to the reference light signal. In this way the Kerr signal from selected depth zones can be made invisible if the Kerr phase is adjusted to be out of phase with respect to the reference reflected light. This kind of depth selective Kerr signal detection has been demonstrated using Fe/Cr/Fe sandwich samples [54].

Depth selectivity was employed on 20Au/12Fe/Au/16Fe/GaAs structures. In Fig. 6.8 the ratio of the Kerr signals from the top **12Fe** and bottom **16Fe** layers, $(\frac{A_{12Fe}}{A_{16Fe}})$, is shown as a function of the phase shift adjusted by means of a phase compensator. When the phase difference between the reference and Kerr signals from the bottom 16Fe layer is $\frac{\pi}{2}$ (phase shift ≈ 2.7 rad for 20Au/12Fe/150Au/16Fe/GaAs, see graphs 6.8(a), (b) and (c), and the phase shift is ≈ 1 rad for 20Au/12Fe/300Au/16Fe/GaAs, see graphs 6.8(d), (e) and (f)) then one can detect only the signal from the top **12Fe** layer (ratio $\frac{A_{12Fe}}{A_{16Fe}} \rightarrow \pm\infty$). The $\pm$ sign is associated with the sign of the Kerr signal contributions to the reference signal: when $\frac{\pi}{2} < \phi < \frac{3\pi}{2}$ then the detected Kerr signal has a sign opposite to that when $\frac{-\pi}{2} < \phi < \frac{\pi}{2}$. The same argument applies in the opposite direction: if the phase difference between the reference and Kerr signals from the top **12Fe** layer is $\frac{\pi}{2}$ (phase shift ≈ 0.5 rad for 20Au/12Fe/150Au/16Fe/GaAs, see graphs 6.8(a), (b) and (c) and phase shift ≈ 0.7 rad for 20Au/12Fe/300Au/16Fe/GaAs, see graphs 6.8(d), (e) and (f)) then one can detect only the signal from the bottom **16Fe** layer (ratio $\frac{A_{12Fe}}{A_{16Fe}} \rightarrow 0$).

The ratio of detected Kerr amplitudes is plotted for 20Au/12Fe/150Au/16Fe/GaAs and 20Au/12Fe/300Au/16Fe/GaAs structures in Fig. 6.8. It is evident that for double layer structures having different thicknesses of the Au spacer layer the conditions for eliminating a particular Kerr signal are different. Thus in TRMOKE measurements the phase shift has to be adjusted to the required value for each thickness of the Au spacer.

6.2.4 Experimental evidence for the suppression of the direct Kerr signal from the bottom Fe layer

The amplitude of a residual Kerr signal due to the bottom **16Fe** layer was observed to be $\approx 10\%$ of the signal from the **12Fe** for a wide range of phase shifts induced by the 1/4 wavelength plate even for a 200ML Au spacer (40nm). This residual signal can dominate the spin sink driven signal. The depth selectivity of the Kerr effect allowed one to suppress the residual signal from the bottom **16Fe** to a level less than that due

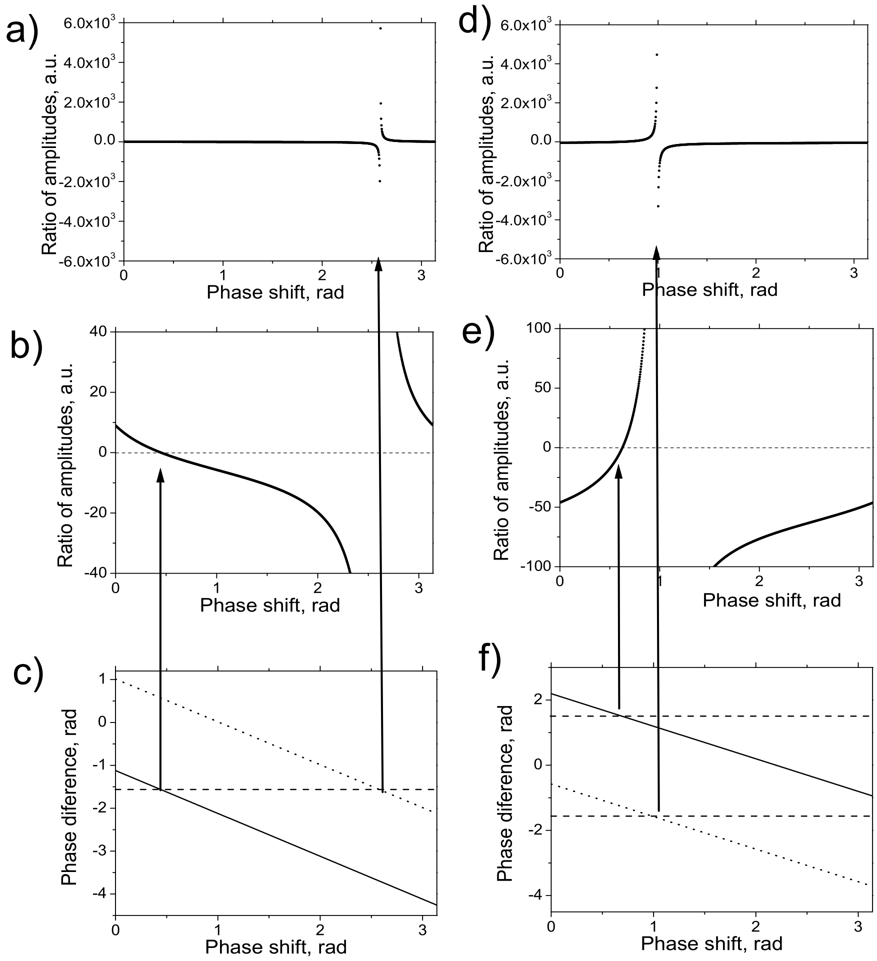

Figure 6.8: The calculated ratio of the Kerr signals created by the 12Fe and 16Fe films ($\frac{A_{12Fe}}{A_{16Fe}}$) as a function of the phase shift provided by a phase compensator: the x-axis is the phase shift induced by the compensator. (a), (b) and (c) are calculated for 20Au/12Fe/150Au/16Fe/GaAs specimen. (a) shows that one is able to isolate one or the other layer by adjusting the phase of the Kerr signal. (b) is a magnified version of the ratio shown in (a). In (c) the total phase of the Kerr signal with respect to the reference signal is plotted as a function of the compensator phase shift for the **16Fe** (dotted line) and **12Fe** (solid line) films. (d), (e) and (f) are calculated for the 20Au/12Fe/300Au/16Fe/GaAs specimen. (d) and (e) show that the spacer thickness changes the phase shift required to isolate the Kerr signal from either the top or the bottom layer. In (f) the same as part (c) but for a 300 atomic layer Au spacer.

to the spin current induced signal.

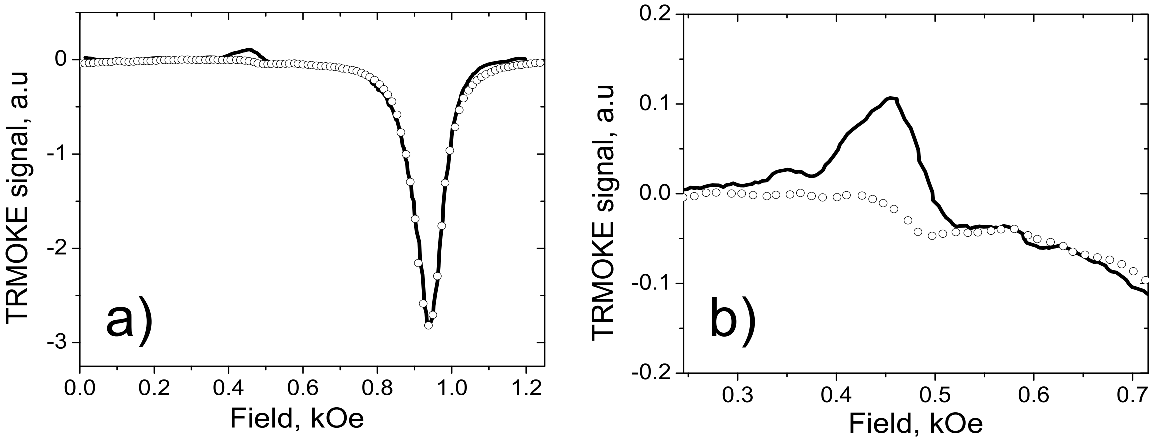

Figure 6.9: The TRMOKE signal for a 20Au/12Fe/200Au/16Fe/GaAs specimen at F=10.3 GHz. (a) The solid line shows the measured signal for an arbitrary position of the phase compensator. The line defined by ◦ points shows the measured signal when the compensator was adjusted so that there was a phase shift of $\pi/2$ between the reference signal and the signal from the bottom **16Fe** layer. (b) A magnified part of the field region shown in part (a) where one can observe the contribution from the spin current induced rf precession. This signal occurs at the FMR field for the **16Fe** layer (cf. 6.10). Notice that the direct signal from the 16Fe (the solid black line) has a different line shape than that corresponding to the spin current induced signal. The residual signal from the **16Fe** has a lineshape similar to that of the main FMR peak for the **12Fe** film at 0.95 kOe. The main peak is $\sim \chi''$. The lineshape of the spin pump induced peak is $\sim \chi'$ and is out of phase with the main FMR peak $\sim \chi''$. The data indicate clearly that the direct Kerr signal from the bottom **16Fe** layer can be fully suppressed by adjusting the $\lambda/4$ plate compensator.

A careful adjustment of the 1/4 wave-plate allowed one to set the phase of the Kerr polarization from the bottom layer to be shifted in phase by $\frac{\pi}{2}$ with respect to the reference beam polarization, see Fig. 6.9. For this case the bottom layer provided a negligible Kerr effect signal. This technique was successfully used in domain imaging in Fe/Cr/Fe multilayers using a Kerr microscope by Schäfer et al. in [139]. In the next subsection it will be shown that the remaining signal at the resonance condition of the bottom **16Fe** (cf. 6.10) layer was generated in the top **12Fe** due to additional driving caused by the spin sink effect.

6.2.5 Detection of the spin sink driven signal

TRMOKE measurements were carried out on a 20Au/12Fe/200Au/16Fe/GaAs(001) magnetic double layer. The difference in magnetic crystalline anisotropies for the top (**12Fe**) and bottom (**16Fe**) films was used to separate their FMR peaks. The in-plane angular dependence at 24 GHz resulted in the following magnetic parameters: **16Fe** grown on GaAs(001): In-plane uniaxial anisotropy parameter K_u = -4.45X10^5 erg/cm^3 with the hard magnetic axis along the [1$\bar{1}$0] crystallographic orientation of GaAs(001), the in-plane four fold anisotropy parameter K_1 = 2.67X10^5 erg/cm^3; and the effective demagnetizing field $4\pi M_{eff}$ = 16.94 kG. **12Fe** film grown on the Au(001) layer: K_1 = 2.49X10^5 erg/cm^3, K_u = 8.63X10^3 erg/cm^3 with the easy magnetic axis along [1$\bar{1}$0] of the GaAs(001), and $4\pi M_{eff}$ = 16.41 kG. The top **12Fe** layer has a small uniaxial in-plane anisotropy, which is almost negligible compared with the other anisotropy fields. For the in-plane FMR measurements with the dc field applied along the $[110]_{GaAs}$ crystallographic axis and neglecting the small in-plane uniaxial anisotropy for the top layer the resonance conditions for the saturated state are given by

$$\left(\frac{\omega}{\gamma}\right)^2 = \left(H + 4\pi M_{eff} + \frac{K_1}{M_s}\right) \cdot \left(H - \frac{2K_1}{M_s} \pm \frac{2\mid K_u\mid}{M_s}\right) , \qquad (6.18)$$

where ± corresponds to the bottom **16Fe** and top **12Fe** films respectively. The FMR peak positions at 10.3 GHz, presented in Fig. 6.10, are at 0.57 kOe and 1 kOe for the bottom **16Fe** and top **12Fe** films, respectively.

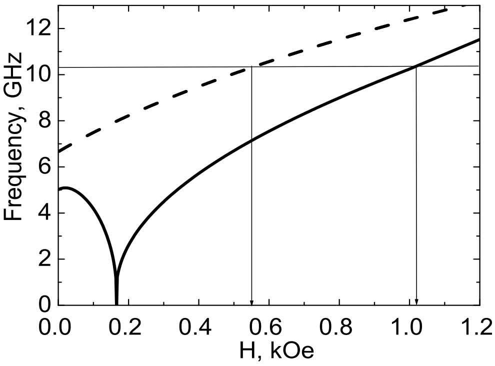

Figure 6.10: Calculated resonant frequencies using eq 6.18 for the top **12Fe** film (solid line) and the bottom **16Fe** film (dashed line) as a function of the applied magnetic field. The field was applied along the $[110]_{GaAs}$ crystallographic direction. At 10.3 GHz the FMR peak positions were separated by ≈450 Oe.

In the field sweep one can observe, apart from the main FMR signal, a magnetization precession induced by spin currents generated by the bottom **16Fe** layer. The induced signal has an FMR-like behavior because the accumulated magnetic moment in the Au spacer follows the FMR response of the bottom **16Fe** layer. The spin current driven signal is proportional to $\frac{d\vec{m}_j}{dt}$. It follows that the direct FMR signal is phase shifted by $\pi/2$ from the spin current induced signal [140]. This means that the χ' susceptibility corresponding to the top FMR signal is accompanied by a spin sink signal component $\sim \chi''$ of the bottom layer FMR and *vice versa*. This feature was used to distinguish between the signal generated in the **12Fe** film by the direct FMR response and the response created by the spin sink effect, see Fig. 6.9. In fact, the 1/4 wave-plate was adjusted in position such that no trace of the direct FMR signal from the **16Fe** was noticeable.

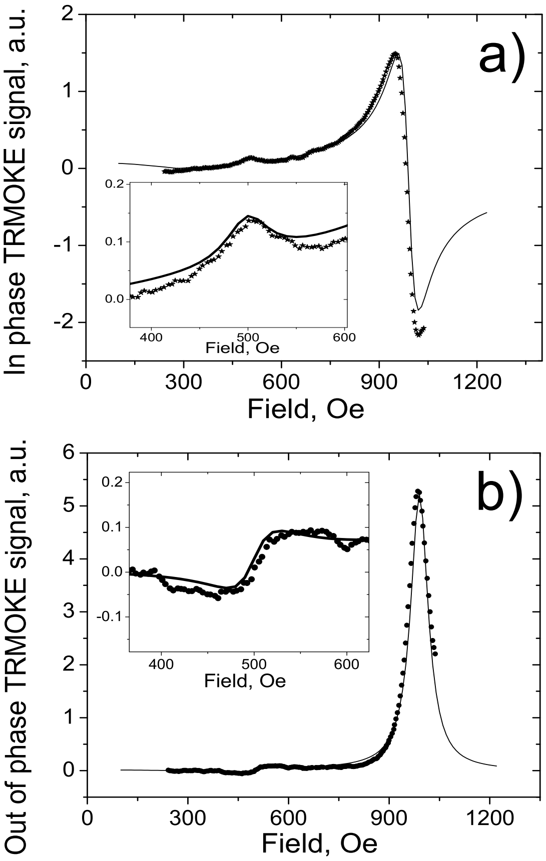

Figure 6.11: TRMOKE field scans at 10.3GHz for a 20Au/12Fe/200Au/16Fe/GaAs sample. (a) shows χ' the susceptibility component which is in phase with the *rf* driving field. (*b*) shows the susceptibility component χ'' which is phase shifted by $\frac{\pi}{2}$ with respect to the *rf* driving field. The insets show magnified signals which were driven by the spin sink mechanism. The solid lines show the results of computer simulations using Eq. 5.1 with the boundary conditions 5.3 and 5.5.

The TRMOKE experiments were carried out at 10.3 GHz. At this frequency the resonance fields for both magnetic films can be calculated using Eq. 6.18. These fields were separated by $\approx$ 450 Oe . The results for the χ' and χ'' signals for the 20Au/12Fe/200Au/16Fe/GaAs sample are shown in Fig. 6.11. In addition to the main FMR signal, one can clearly observe the spin sink induced signal in the tail of the main FMR signal. The field of the spin sink induced signal agrees perfectly with the FMR field of the bottom **16Fe** layer. The FMR fields were calculated from Eq. 6.18. The top **12Fe** layer was driven by the spin current generated by the bottom **16Fe**, see Eq. 2.63, which is proportional to the time derivative of the *rf*-magnetization of the **16Fe** layer. Therefore the spin pump driving torque is phase shifted by $\pi/2$ with respect to the rf magnetization of the top **12Fe** layer. Consequently, the spin sink induced precession resulted in a typical "dispersion wiggle" for the real part of the **12Fe**-susceptibility χ' and a "dip" for the imaginary part of the **12Fe**-susceptibility. The solid lines show computer fits of the data using equations 2.63 and 5.1 with the boundary conditions 5.3 and 5.5 using the following parameters for the Au spacer layer: τ_m =1.2x10^{-14} s and τ_{sf} =15x10^{-14} s. These fitting parameters are very close to those obtained from the FMR measurements on Au/Fe/GaAs(001)samples. Ballistic spin transport would create a signal approximately three times larger than that observed even for the thinnest Au spacer for this series of samples.

6.2.6 Other possible mechanisms of dynamic coupling and validity analysis

One can not exclude a priori other known mechanisms that lead to the coupling of two films in a magnetic double layer. First of all a possible residual static exchange coupling should be addressed. The exchange coupling is proportional to the rf magnetization components. This means this form of coupling would again result in a signal in the **12Fe** at the FMR field for the **16Fe** film having a lineshape similar to the main FMR signal for the **12Fe** film, see Fig. 6.12. Computer simulations for weak exchange ferromagnetic and exchange antiferromagnetic couplings are shown in Fig. 6.12. The exchange couplings were adjusted to obtain signals having a strength similar to those observed in the measurements. Clearly these simulations show that the exchange coupling is not able to explain the signals created by spin pumping. In addition the exchange coupling fields are very weak. Direct exchange coupling can be entirely excluded because the Au spacers are too thick. Even a long wavelength oscillatory coupling is effectively averaged out by the interface roughness for Au spacers thicker than 3 nm.

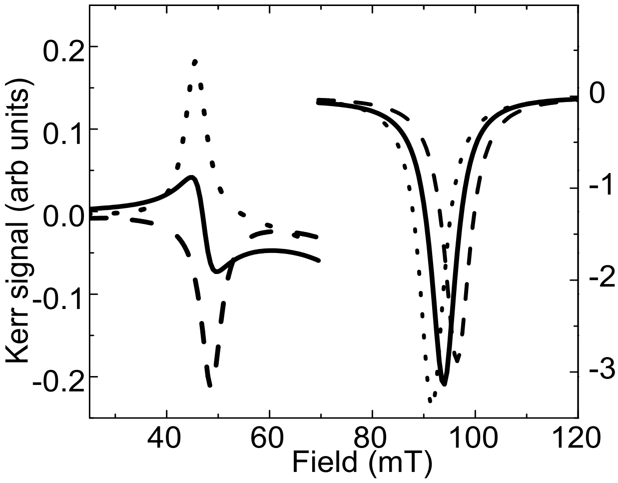

Figure 6.12: Computer simulations assuming three different coupling mechanisms, which can affect the TRMOKE data: a spin pump/sink driven signal (solid line); a residual ferromagnetic coupling (dashed line); and a residual antiferomagnetic coupling (dotted line). These simulations clearly indicate that only the spin pump/sink mechanism can explain the measured data.

Dipolar coupling is another mechanism which may lead to the observed effect. Dipolar fields are proportional to the rf magnetization components. An inhomogeneous magnetization in a finite sized sample can lead to dipolar fields. In an ultrathin film the dipolar field is given by $\mu_0 H_D \sim \frac{1}{2} q t_F \mu_0 M_S \sin\phi$, where q is the wave number of the inhomogeneous rf-magnetization, t_F is the thickness of the ferromagnetic film, and ϕ is the cone angle of the rf-precession. The q wave number is given by $q = \pi/\lambda$, where λ is an appropriate wavelength of the inhomogeneous rf-magnetization and is related to the sample's lateral geometry. Using the conservative numbers $\phi = 0.5°$, $t_F = 2$ nm and $\lambda = 5$ μm results in $H_D = 1 \times 10^{-3}$ Oe. Considering that the excitation field due to spin pumping is 5 Oe it is obvious that the driving field due to dipolar coupling is at least two orders of magnitude weaker than the driving field caused by spin pumping. In addition, the dipolar coupling is proportional to the magnetization and would generate the wrong lineshape - a lineshape that has been previously discussed.

Therefore one can firmly conclude that the signals measured at the **16Fe** film resonance in Figs. 6.11(a) and (b) is a sole consequence of the spin current generated by the **16Fe** film and absorbed in the **12Fe** film.

6.2.7 The dependence of the spin sink driven signal on the Au spacer thickness

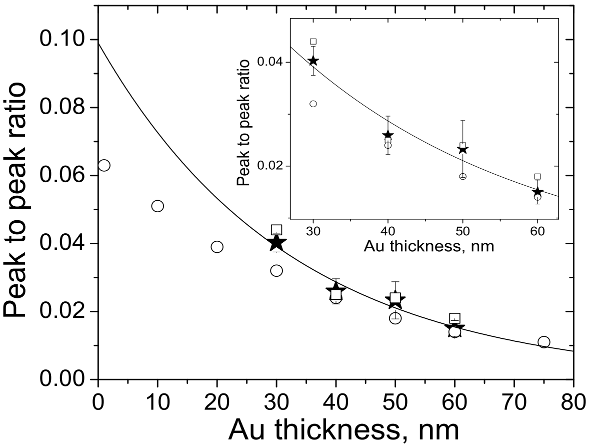

Figure 6.13: The ⋆ points show the ratio of the spin pump induced signal in the **12Fe** film when the **16Fe** film is driven at resonance to the main FMR signal when the **12Fe** film is driven at resonance as a function of the Au spacer layer thickness. The solid line shows a fit of the experimental data to a simple exponential decay. The ○ points show the results of computer simulations assuming a perfect alignment of the magnetic moments with the external field. The □ points show the results of computer simulations which takes into account the dragging of the magnetic moment in the **12Fe** film behind the applied field. The inset shows an expanded region of this graph.

The spin current induced dynamics was studied as a function of the Au spacer layer thickness, see Fig. 6.13. TRMOKE measurements were carried out on 20Au/12Fe/nAu/16Fe/GaAs(001) magnetic double layers, where n=150, 200, 250, 300 is the number of atomic layers. The the spin current induced signal decreased with increasing spacer thickness. A simple exponential fit provides a good description of the data, however it leads to an unrealistically strong contribution in the limit of small thicknesses corresponding to the regime of ballistic spin transport. Spin diffusion theory using perfect alignment between the static magnetic moments and the applied dc field resulted in a less than desirable fit, see the points ○ in Fig. 6.13. A good fit was obtained by including non-collinearity between the magnetic moment in the top **12Fe** layer and the applied field. The bottom layer was oriented parallel with the field along the in-plane easy axis. The applied field in the top layer was applied along the hard axis and consequently the direction of its magnetic moment dragged behind the direction of the applied field and was not collinear with the magnetic moment of the **16Fe** layer. A misalignment of the magnetic moment with respect to the direction of the dc field within 10° resulted in a change in the amplitudes of the main and satellite peaks [128]. The full fit including a misalignment of the magnetic moment in the top **12Fe** layer, see the ☐ points in Fig. 6.13, resulted in a good fit to the data using the following spin diffusion parameters for all thicknesses of the Au spacer: spin flip relaxation time ($\tau_{sf} = 15\text{x}10^{-14}$ s), electron relaxation time ($\tau_m = 1.2\text{x}10^{-14}$ s), and spin diffusion length ($\delta_{sd} = 34$ nm)

6.3 Summary and comparison with other measurements

Pure spin current induced dynamics in magnetic films was investigated using the TRMOKE technique. The propagation of accumulated spin momentum density was studied in magnetic single films and in structures containing two ferromagnetic layers separated by a Au spacer layer. In the Au thickness range investigated the propagation of a spin current was found to satisfy the diffusion equation. Computer simulations which were based on the spin diffusion theory provided nearly perfect agreement with the experimental data using the following spin diffusion parameters: spin flip relaxation time ($\tau_{sf} = 15\text{x}10^{-14}$ s), electron relaxation time ($\tau_m = 1.2\text{x}10^{-14}$ s) and spin diffusion length ($\delta_{sd} = 34$ nm) at room temperature.

τ_{sf} and τ_m were adjusted to explain the FMR and TRMOKE data. The electron relaxation time τ_m can be obtained independently from the expression for the electric conductivity in Au, σ_{Au}:

$$\sigma_{Au} = \frac{ne^2\tau_m}{m}, \tag{6.19}$$

where $n = 5.9\text{x}10^{28}\ m^{-3}$ is the charge carrier density per unit volume, $e = -1.6\text{x}10^{-19}$ C is the electron charge and $m = 9.11\text{x}10^{-31}$ kg is the mass of the electron. $\sigma_{Au} = 0.44\text{x}10^{8}\ (\Omega m)^{-1}$ is obtained from the literature [133]. This set of parameters results in $\tau_m = 2.3\text{x}10^{-14}\ s$, which is almost twice the value $\tau_m = 1.2\text{x}10^{-14}$ s obtained from our experiments. Monchesky *et. al.* [68] pointed out that in thin Au films the conductivity decreases with decreasing thickness due to interface scattering. First principles density functional calculations and Boltzman's equations were successfully employed to explain this thickness dependence. In the range of 20 to 30 nm of Au the average value of the conductivity is $\sigma_{Au} = 0.3\text{x}10^{8}\ (\Omega m)^{-1}$. Using equation 6.19 and the thickness adjusted σ_{Au} we get $\tau_m = 1.6\text{x}10^{-14}$: this value is in good agreement with the result obtained from the magnetic measurements.

Values of the diffussion length in Au, δ_{sd}, obtained from the existing literature are found to be in the range of 10 nm to 170 nm at low temperatures [105]. This wide spread in the data indicates that the measuring techniques and sample preparation played an important role in these studies. Since our samples have a superior crystalline quality and spin pumping is not accompanied by a net charge transport it was desirable to investigate the propagation of spin currents using techniques developed in our Lab. The value of the spin diffusion length in Au obtained from our experiments using FMR and TRMOKE finds partial agreement with non-local measurements performed by other groups. Kurt *et. al.* [141] studied the spin diffusion length by using Current-Perpendicular-to-Plane Giant Magneto Resistance (CPP GMR) measurements on polycrystalline Au/Cu spacers. They obtained $\delta_{sd} = 35$ nm at 4.2 K, for a Au layer thickness in the range 1 to 20 nm. Extrapolation of these data to room temperature should result in a value smaller than that measured in our studies. The decrease in the spin diffusion length in their experiments compared with our result may be explained by an additional electron scattering at the grain boundaries of the polycrystalline Au/Cu spacer. Our results find almost perfect agreement with Au spin diffusion measurements performed in lateral spin valves by Ji *et. al.* [142]. The authors report $\delta_{sd} = 64$ nm at 10 K. Their recent work on Co/Cu/Co lateral spin valves [143] indicate that in Cu δ_{sd} measured at room temperature is approximately a factor two smaller than the 10 K value. Extrapolation of this result to Au yields $\delta_{sd} = 32$ nm at room temperature, a value that is very similar to our results.

Chapter 7

Conclusions

Very good quality crystalline epitaxial metallic multi-layers possessing well defined interfaces were prepared using the molecular beam epitaxy (MBE) technique to deposit metal films on semi-insulating GaAs substrates. Growth of the single crystalline films was monitored using reflection high energy electron diffraction (RHEED). RHEED provides a reciprocal space transform of the epitaxial surfaces. The reciprocal space patterns were correlated with real space subatomic resolution images obtained by means of a scanning tunnelling microscope (STM).

Structural properties of the Fe/GaAs(001) interface were studied by means of Mossbauer Electron Conversion Spectroscopy using two atomic layers of ^{57}Fe deposited either at the Fe/GaAs(001) interface or deeper in the Fe film. Samples in these studies were prepared using MBE thermal deposition (TD) and pulsed laser deposition (PLD). The PLD deposition resulted in a substantial incorporation of Fe atoms into the GaAs lattice wheras the TD films exhibited only a moderate intermixing of Fe with GaAs. The magnetic properties observed in these Au/Fe/GaAs(001) structures were investigated by means of ferromagnetic resonance (FMR). The in-plane uniaxial anisotropy at the Fe/GaAs(001) interface was significantly smaller in the films grown by PLD compared with those grown using TD. In the PLD films the Fe interface lattice structure was robustly pinned to the cubic symmetry of the GaAs lattice while the interface Fe structure in the TD films followed more closely the uniaxial interface symmetry of As dimers on the GaAs(001) surface template. Recent EXAFS studies have shown that the uniaxial symmetry of the 4x6 reconstructed GaAs template leads to an interface shear. Based on the results of Mossbauer spectroscopy and magnetic studies one can argue that the Fe interface uniaxial anisotropy at the GaAs(001) interface is caused by interface lattice shear in the Fe. The interface lattice shear results in a uniaxial anisotropy having its axis along the in-plane lattice mesh diagonal, the [1-10] crystallographic direction, due to the magneto-elastic term in the magnetic free energy [144, 87, 145]:

$$F_{me} = \left(\frac{B_2 \epsilon_6}{2}\right) \sin(2\varphi), \tag{7.1}$$

where $B_2 = 7.62\text{x}10^6$ Jm^{-3} is the magnetoelastic parameter [146], ϵ_6 is the in-plane shear component, and φ is the angle between the magnetization direction and the [100] crystallographic direction.

Strong in-plane uniaxial anisotropy in the Fe/GaAs(001) films allowed one to investigate the magnetic excitations in configurations in which the magnetization was not collinear with the applied magnetic field. Applying the external field along the magnetic hard axis $[1\bar{1}0]$ enabled one to observe magnetic soft modes. Competing in plane uniaxial and four-fold anisotropies resulted in two resonant modes when the film magnetic moment was not collinear with respect to the applied magnetic field. Three FMR resonance modes were observed in a certain range of microwave frequencies with the external field oriented along the hard $[1\bar{1}0]$ magnetic axis. One mode corresponded to a very low frequency and the good crystalline quality of the Fe films brought this resonant frequency to a low of 1GHz. The non-collinear branch of the FMR peaks had a bell like shape, with the critical frequency corresponding to a confluence of two non-collinear modes. For frequencies greater than the critical frequency a “ghost” resonant mode was observed. This mode was driven purely by magnetic losses. Its intensity was observed to decrease exponentially with increasing frequency.

Spin dynamics studies using FMR led to several important results: (a) The FMR linewidth in high quality Fe crystalline films is linearly dependent on the microwave frequency. A Zero-frequency offset (in the FMR field sweep mode) at low microwave frequencies is caused by long range magnetic inhomogeneities. The intrinsic magnetic damping in ultrathin films can be described by the Gilbert phenomenology and is caused by noise in the spin orbit interaction. (b) Gilbert damping is due to contributions from both the bulk and the interface. The interface anisotropy term scales inversely with film thickness indicating that the interface electronic energy bands contribute significantly to the intrinsic Gilbert damping. Bulk Gilbert damping in the Fe films was found to be comparable to that observed in the best bulk Fe samples prepared by chemical vapor deposition. The bulk Gilbert damping parameters were α=1.3x10^{-3} and G=0.4x10^8s^{-1}, respectively. This again testifies to the excellent crystalline quality of Fe films prepared by means of MBE. (c) A precessing magnetization in Fe/NM structures acts like a peristaltic spin pump that generates a spin current propagating perpendicular to the

Fe/NM interface. (d) Au/Fe/GaAs(001) thin film structures allowed one to investigate the spin relaxation mechanism. The spin current propagating in the Au layer becomes progressively attenuated with an increasing Au layer thickness: this attenuation is due to a spin relaxation mechanism in Au. The variation of the measured FMR linewidth as a function the Au layer thickness was interpreted using diffusion equations of motion. A fit of the experimental data to the diffusion equation allowed one to uniquely determine the momentum and spin flip relaxation times τ_m =1.2x10^{-14} s, τ_{sf} =15x10^{-14} s. This value for the spin flip relaxation time leads to a spin diffusion length of 35 nm in Au. The above value for τ_m is in a good agreement with values deduced from DC conductivity measurements. Measurements of the spin diffusion length in Au obtained by the Argonne group using lateral spin valves resulted in a very similar value of spin diffusion length δ_{sd} in Au.

Ultrathin crystalline Fe either grown on, or covered by, a lattice of mismatched crystalline layers triggers a self assembled network of misfit dislocation. A Pd square lattice is almost 4.5 percent larger than that of the square lattice presented by an Fe(001)film. The resulting lattice strain leads to a self-assembled network of misfit dislocations. FMR studies on 20Au/7Fe/40Au/11Pd/10Fe/GaAs structures have shown that misfit dislocation glide planes create a network of uniaxial anisotropies having their uniaxial axes oriented along the lines of misfit dislocations. FMR measurements showed that these anisotropies lead to a robust extrinsic damping which can be ascribed to a two magnon scattering mechanism. Magnetic damping in 20Au/7Fe/40Au/11Pd/10Fe/GaAs(001) exhibited all the classical features of two magnon scattering: (a) The FMR linewidth had an in-plane angular dependence that followed the symmetry of the uniaxial anisotropies induced by the misfit dislocation network. The effective damping was enhanced when the magnetization was oriented along the $< 100 >$ crystalline axes of the Fe(001) film, the directions of the uniaxial anisotropies, whereas an enhanced linewidth was almost absent when the magnetization was oriented along the $< 110 >$ crystallographic axes. (b) Once the magnetic moment was inclined at an angle larger than 45 degrees away from the film plane the contribution of the two magnon scattering disappeared. (c) At low enough microwave frequencies the FMR linewidth was linear in microwave frequency and showed an enhanced Gilbert-like damping which surpassed the intrinsic damping by almost two orders of magnitude. All these features were present with the utmost clarity and could be used as working criteria to distinguish between intrinsic and extrinsic contributions to the magnetic damping.

The spin pump/spin sink mechanism was extensively studied using magnetic double layer structures. The redistribution of the spin momentum leads to an additional interface damping which phenomenologically behaves like Gilbert damping. The role of spin current interference was tested by using an asymmetric rf driving magnetic field that was achieved by patterning the Au/Fe/Au/Fe(001) structure onto a co-planar microwave transmission line. By changing the phase of the spin currents one was able to observe off-resonance driving due to the spin sink mechanism in standard FMR absorption spectra.

The propagation of light in magnetic double layers was formulated using Maxwell's equations with the incident light impinging on the film surface parallel with the surface normal. The magneto-optical effect is the consequence of the optical Lorentz force acting on atomic electrons and results in off diagonal elements of the cubic electric permittivity tensor for a coordinate system coincident with the cubic crystalline axes. The induced electric vector D generates light waves having a polarization vector oriented perpendicular to the incidence light polarization vector: this is the origin of the Kerr effect. The magnetic layers act like radiation antennas [136]. It has been shown that one can achieve excellent depth selectivity by using a phase compensator. This means that by a proper choice of phase compensation one can select a Kerr signal that originates from either the top or the bottom magnetic layer. The depth, time, and spatially resolved magneto-optical Kerr effect (TRMOKE) technique was used to directly detect the spin current driven spin dynamics in magnetic Au/Fe1/Au/Fe2/GaAs(001) double layers. Spin pumping of the magnetic moment in Fe2 created an accumulated spin density and spin current in the Au spacer. The spin current propagated across the Au spacer and was absorbed due to the spin sink effect at the Au/Fe1 interface. The spin sink effect resulted in a precessional motion of the magnetic moment in Fe1. The Fe1 layer served as a spin detector (probe). Depth resolved TRMOKE allowed one to detect the spin current induced precessional motion of the magnetic moment in the probe layer Fe1 with a ps time resolution. The spin current induced dynamics was investigated as a function of the Au spacer thickness. The theory of the spin induced dynamics was formulated by using the diffuse equation of motion for the spin accumulated moment in the Au spacer. The best fit to the experimental data was obtained using the spin diffusion length in Au of 35 nm, which is in perfect agreement with the spin diffusion length deduced from FMR studies on single Fe layers. TRMOKE and spin pumping are unique tools that allow one to study the spin diffusion in normal metals without passing a DC current through the structure under study.

Appendix A

Sample preparation using patterning

In this Appendix a detailed patterning procedure is described. Patterning was used to prepare the samples for FMR studies using antiparallel rf driving and TRMOKE measurements.

A.1 FMR with antiparallel driving

FMR experiments with antiparallel rf driving were carried out on a coplanar transmission line which was patterned from a continuous 20Au/12Fe/250Ag/16Fe(001) film grown on a GaAs(001) substrate. The GaAs wafer covered with the 20Au/12Fe/250Ag/16Fe(001) film and all subsequent modifications will be further referred to as the Sample. Two main steps were involved in patterning: (a) - optical lithography, (b) - dry etching.

A.1.1 Sample patterning for FMR experiment

Optical lithography: Optical lithography is a process used in microfabrication to selectively remove parts of a thin film. It uses light to transfer a geometric pattern from a photomask to a light-sensitive chemical (photoresist) on the substrate. The sample, see Fig. A.1(a), was cleaned in acetone using an ultrasound mixer. The residual contaminants and acetone were removed from the film surface by a subsequent rinse with propanol. A thick layer of negative photoresist (Calriont AZ 5214E) was spun on the Sample surface, see Fig. A.1(b). The following spinning parameters were used: speed - 3000 rpm, and time - 40 sec. The photoresist was hardened by baking for 60 seconds at 90 ° C. This prebaking was also used to drive off excess solvent. After

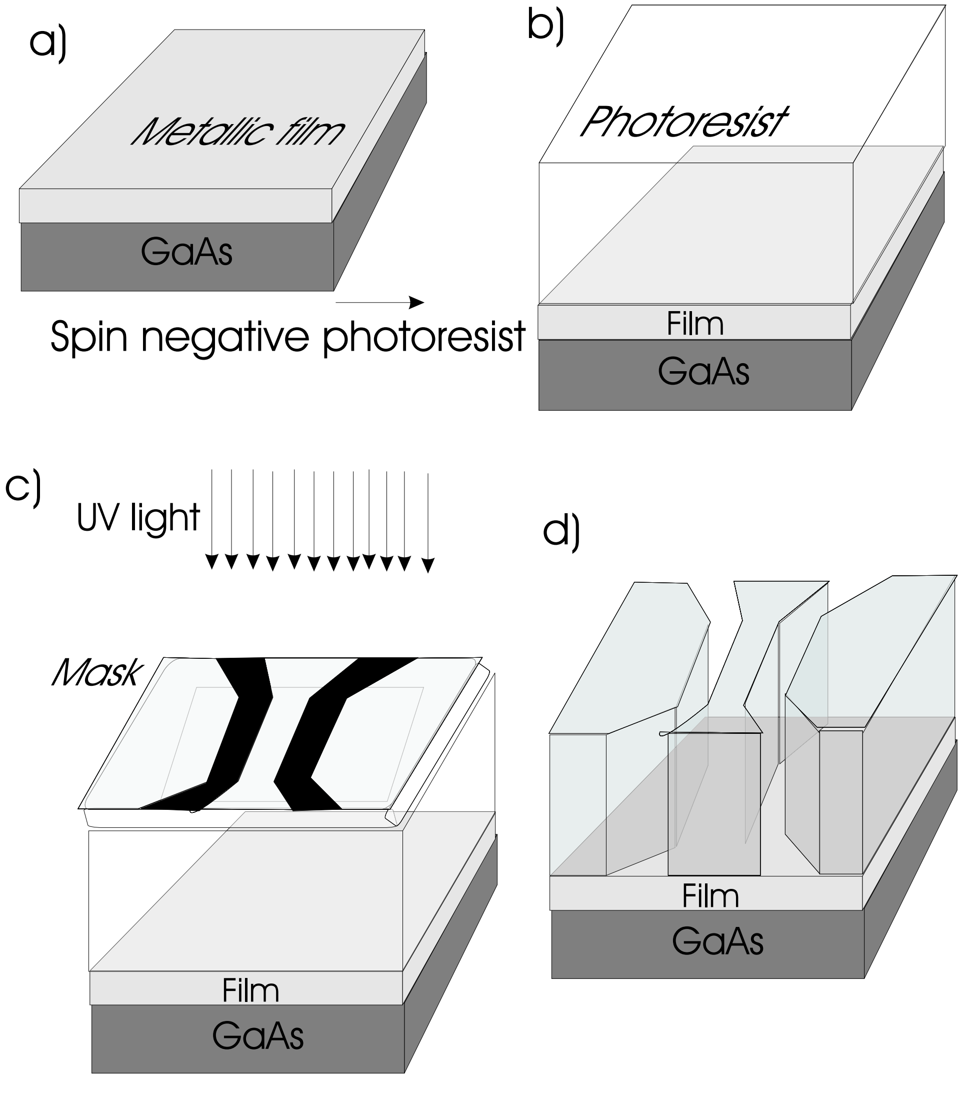

Figure A.1: Defining the waveguide geometry using optical lithography. In (a) the starting point is shown: an epitaxial film is deposited on a GaAs substrate; this will be referred to as the Sample. (b) shows the Sample covered by a thick continuous layer of negative photoresist. In (c) a shadow mask with an image of the coplanar waveguide is aligned along the desired Sample orientation. The width of the central conductor was 30 μm. UV light illuminated the negative photoresist through the shadow mask.The negative photoresist was rendered impervious to the developer in regions exposed to UV light. (d) shows the resulting photoresist structure after the Sample was developed and cleaned with acetone. The soluble regions of the photoresist are removed.

prebaking, the photoresist is exposed to a pattern of intense light. Optical lithography typically uses ultraviolet light. Negative photoresist becomes chemically more stable when exposed to the light. This chemical change allows the unexposed photoresist to be removed by a special solution, called the ”developer” by analogy with a photographic developer. The Sample covered by photoresist was put into a mask aligner. The mask was aligned using an optical microscope so that the axis of the coplanar waveguide was parallel with the [110] axis of the GaAs(001). The alignment was not important for the FMR measurements, but was useful for Sample cleavage. Subsequently the photoresist was exposed to UV light through the mask for 7 seconds, see Fig. A.1(c). The Sample was removed from the mask aligner and baked for 90 seconds at 120 ° C. The hard bake solidifies the remaining photoresist to make a more durable protective layer. After that the Sample was put back into the aligner, the optical lithography was checked and the Sample (without mask) was exposed for 37 seconds to mercury UV light. The patterned photoresist was developed for 80 seconds in Clariont AZ 351B developer in an ultrasound mixer. Subsequently the wafer was rinsed with acetone and propanol to remove the remains of the photoresist and developer. The resulting optical lithography pattern was checked by means of an optical microscope. The optical lithography steps are shown in a cartoon, see Fig. A.1.

Dry etching: The dry etching procedure is similar to Ar ion sputtering, however it involves a much higher Ar ion flow rate. The Sample with the structured photoresist was exposed to heavy Ar ion bombardment (beam current 5 mA) for 8 minutes, see Fig. A.2(a). Ar ion sputtering leads to sample heating. To avoid heat damage to the epitaxial structure dry etching was performed in 4 cycles. Each cycle contained 2 minutes of dry etching followed by 30 seconds of sample cooling. In regions where the Sample was not covered by photoresist the epitaxial film was removed from the GaAs by the dry etching; see Fig. A.2(b). The areas of epitaxial film covered by the photoresist were not affected by the dry etching, since the bombarding Ar atoms were stopped in the thick layer of photoresist above the epitaxial film. The Sample was subsequently cleaned in acetone for 3 minutes to remove all contaminants.

The remaining photoresist containing the implanted Ar atoms had a non-uniform thickness across the sample. This variation was caused by a non ideal distribution of the photoresist during the spinning cycle: the photoresist exhibits a uniform thickness in the middle of the Sample but becomes thicker at the edges. The edges of the wafer with the thick layer of photoresist were removed using a diamond saw.

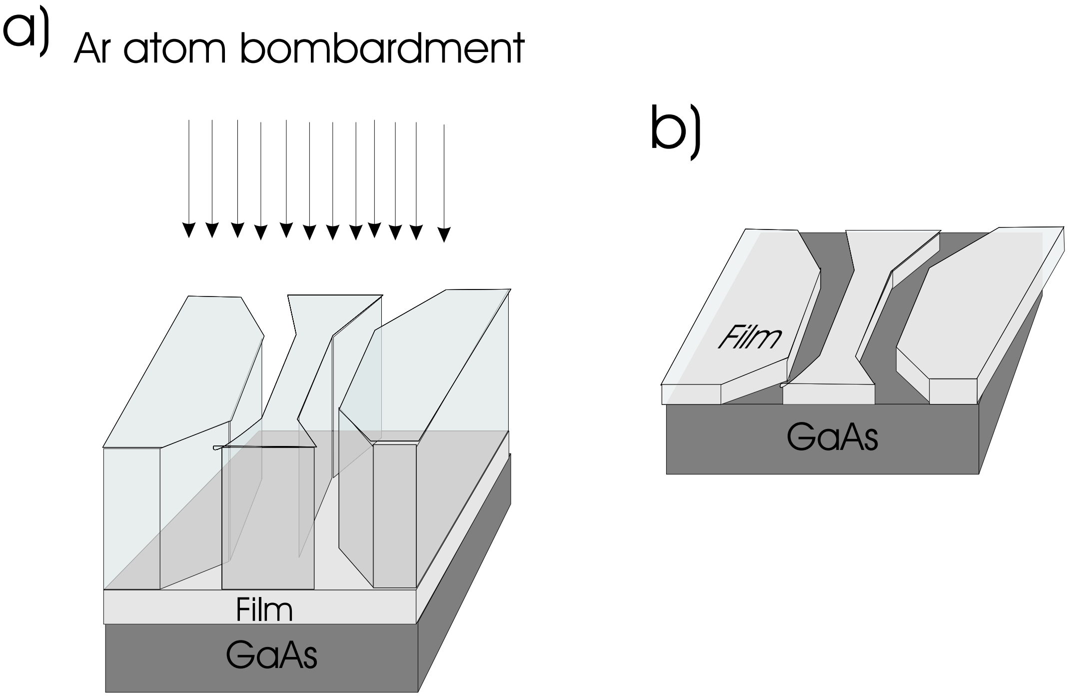

Figure A.2: (a) - The lithographically defined waveguide in photoresist is exposed to Ar ion bombardment. (b) shows the resulting coplanar waveguide defined by the dry etching and optical lithography. The regions of the epitaxial film exposed to Ar ion bombardment were sputtered away, this provides electrical isolation between the signal line and the ground conductors of the coplanar waveguide.

A.1.2 Coplanar waveguide in rf circuitry

The coplanar waveguide with 30 μm central conductor and 15 μm gap between central conductor and ground planes (see s and w in Fig. 3.18(b) has a characteristic impedance close to 50 Ω. This assures that no major reflections of a propagating microwave signal occur at the coplanar waveguide. The coplanar waveguide was connected with the rf circuitry in the following way (cf. Fig. A.3)): SMA rf frequency compatible connectors (flat transmission for frequencies $<$ 26 GHz) were connected to a wide (mm size) coplanar waveguide that was located on a predesigned PCB board. A groove was made in the PCB board to accommodate the Sample with the co-planar waveguide, see Fig.A.3. The depth of the groove was 400 μm, which corresponds to the thickness of the GaAs wafer that carried the Sample. The Sample was glued into the groove. The Sample coplanar waveguide was connected with the coplanar transmission line on the PCB board using Au wire bonds.

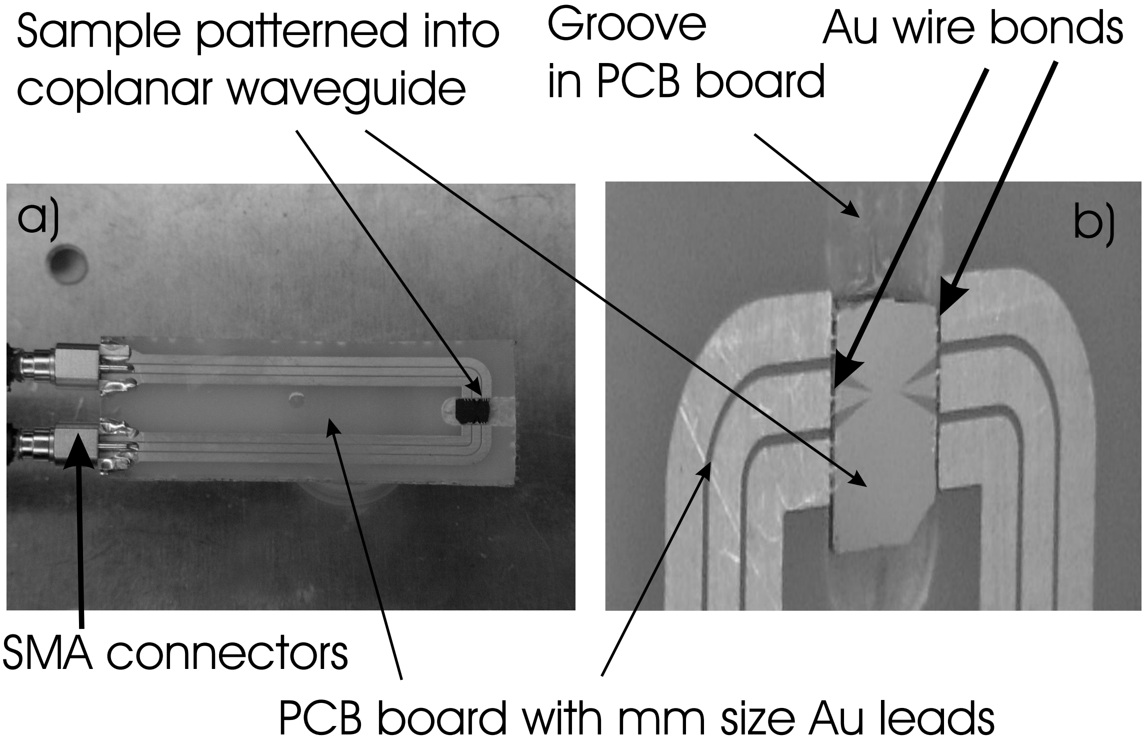

Figure A.3: (a) - shows the PCB board with the Sample incorporated in it. Rf frequency compatible SMA connectors are attached to the mm size Au leads. (b) shows a magnified area of (a). The Sample on the patterned coplanar waveguide is attached to the Au conductors of the PCB board by means of Au wire bonding.

A.2 Sample patterning for TRMOKE experiments

The microwave transmission line and samples defined on the μm scale required for the TRMOKE experiment were made using a two step lithography process. Firstly, the pads of the epitaxial sample were defined. Secondly, a coplanar waveguide was deposited beside the epitaxial pads without making an electrical contact to them. Subsequently the Sample with patterned coplanar waveguide and pads was incorporated into the rf circuitry in the way that was discussed in Section A.1.2.

A.2.1 Defining pads of the epitaxial sample

In the TRMOKE experiments epitaxial samples consisting of thin films of Fe and Au were epitaxially grown on a GaAs(001) substrate. The structure of these films was 20Au/12Fe/nAu/16Fe/GaAs, where the integers represent the number of atomic layers and n = 150, 200, 250 and 300. The pads of epitaxial magnetic double layers were defined using optical lithography. A continuous epitaxial film, see Fig. A.4(a), was cleaned with acetone to remove major contaminants. A layer of positive photoresist was spun on top of the epitaxial film, see Fig. A.4(b). Positive photoresist, the most common type, becomes chemically less stable when exposed to UV light. The Sample was put into the mask aligner. The desired epitaxial pads, see Fig. A.4(c), were oriented along the [110] direction of GaAs(001). This orientation was required for the TRMOKE experiment in order to separate the FMR resonance conditions of the top and bottom magnetic layers of the 20Au/12Fe/nAu/16Fe/GaAs structure. UV light exposure and subsequent developing resulted in the pattern shown in Fig. A.4(d). Here the continuous epitaxial film is free of photoresist except for the μm size regions required for the specimen (pads).

The prepared Sample was exposed to an intensive Ar ion bombardment, see Fig. A.5(a). Dry etching removed the epitaxial film from the GaAs substrate, except for the regions covered by the photoresist, see Fig. A.5(b). The sample now consists of the GaAs wafer carrying μm size pads of epitaxial film covered by a thick layer of photoresist.

A.2.2 Coplanar waveguide evaporation

A 200 nm thick Au coplanar waveguide was placed beside the epitaxial pads using a thermal evaporation and liftoff procedure: the GaAs wafer carrying the epitaxial pads (cf A.6(a)) was preheated to 90 degrees on a hotplate to reduce water contamination of

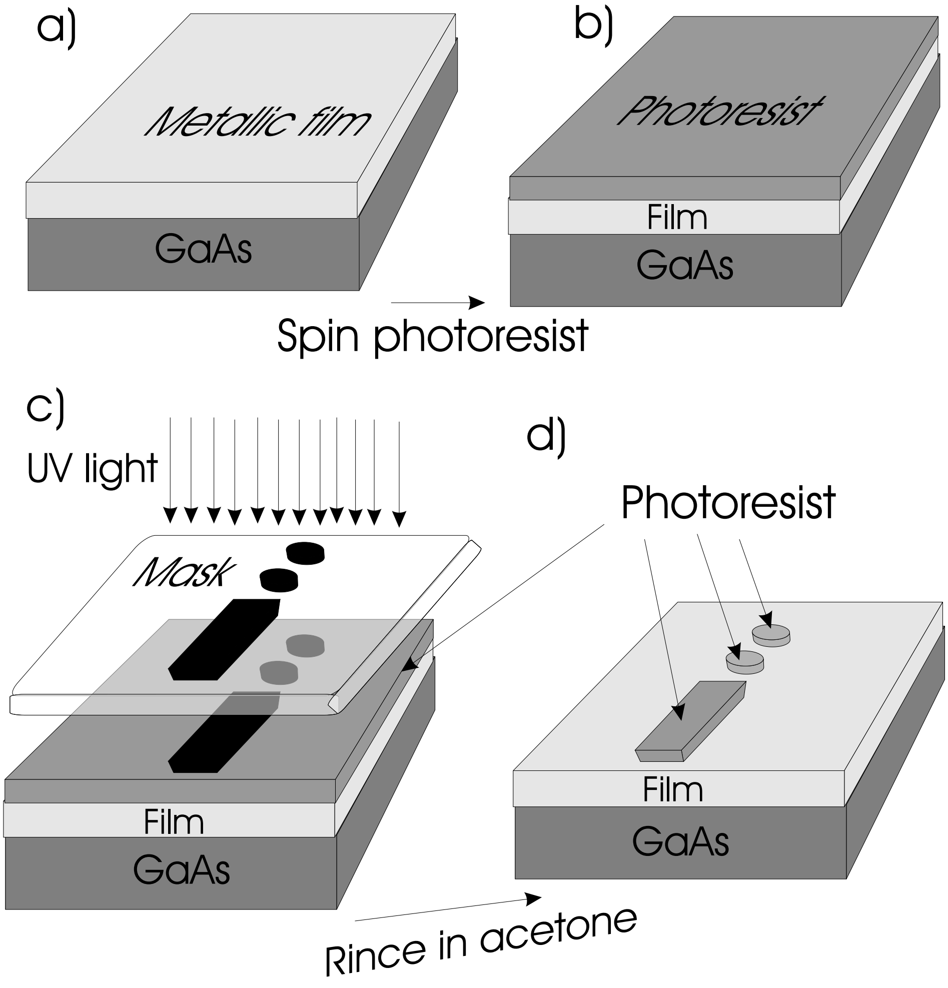

Figure A.4: Optical lithography of μm size pads defining the 20Au/12Fe/nAu/16Fe/GaAs samples for the TRMOKE measurements. (a) The epitaxial film is deposited on the GaAs substrate. (b) shows the Sample with a thick continuous layer of photoresist on top of the epitaxial film. In (c) a shadow mask defining an image of the pads is aligned with the required sample orientation. UV light illuminated the photoresist through the shadow mask affecting only the regions exposed. The photoresist becomes soluble in the developer in the regions which were exposed to UV light. (d) Shows the resulting photoresist structure after the sample was cleaned with acetone. The soluble regions of photoresist were removed. The areas of the epitaxial structure, which are needed for the TRMOKE measurements, are covered by a thick layer of photoresist.

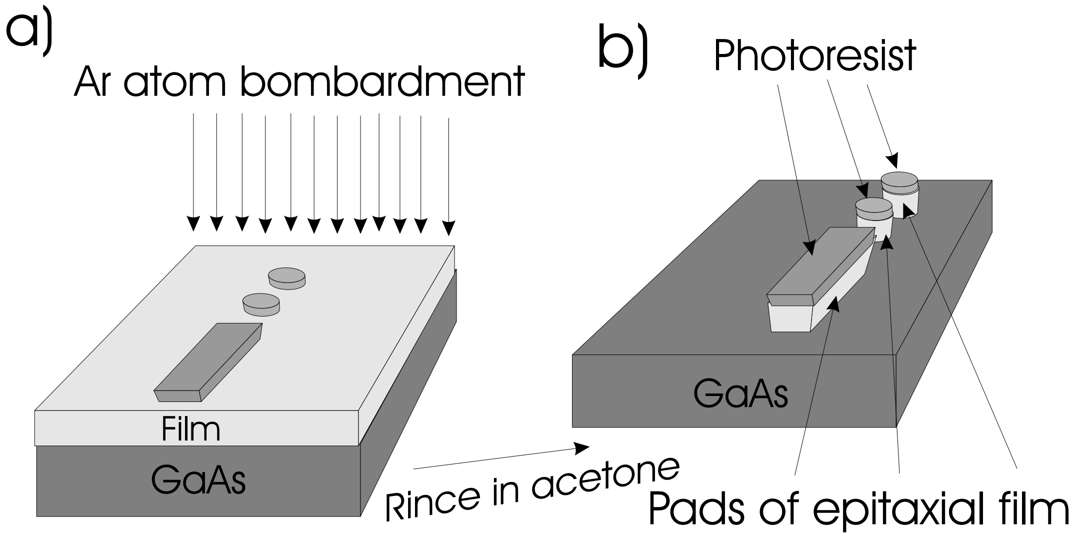

Figure A.5: (a) - The sample carrying optically defined pads was exposed to Ar ion bombardment. (b) shows the resulting pads of epitaxial film covered by a thick layer of photoresist. The regions of the epitaxial film which were exposed to Ar ion bombardment were sputtered away.

the surface. Shipley 1805 photoresist was spun on top of the wafer (cf Fig. A.6(b)) using the following spinner parameters: time - 30 s, speed - 4500 rpm. The photoresist was prebaked for 2 minutes at 90 °C. The photoresist was exposed to 20 seconds of mercury UV light through an aligned coplanar mask, see Fig. A.6(c). The mask was positioned as follows: (a) The waveguide was aligned along the [110] direction of the GaAs. (b) The central 30 μm wide conductor was located right beside the pads of the epitaxial film. The resulting pattern after developing the photoresist is shown in Fig. A.6(d).

A 200 nm Au film was evaporated across the whole wafer under an angle of 15°, see Fig. A.7(a). The angled evaporation resulted in an undercut of the Au central conductor. This is caused by the shadowing effect of the thick photoresist layer, see Fig. A.7(b). The undercut ensured that there was no electrical contact between the epitaxial pads and the coplanar waveguide. The remaining photoresist with the Au film was dissolved by putting the Sample into an acetone bath for 30 minutes. Liftoff was finalized by rinsing the Sample with acetone to ease the liftoff process on the edges of the coplanar waveguide. The resulting structure is shown in Fig. A.7(c). The 200 nm thick Au coplanar waveguide was deposited beside the pads of the epitaxial film. The epitaxial pads were accessible for the TRMOKE laser beam. The rf excitation was provided by a cw microwave signal passing through the transmission line.

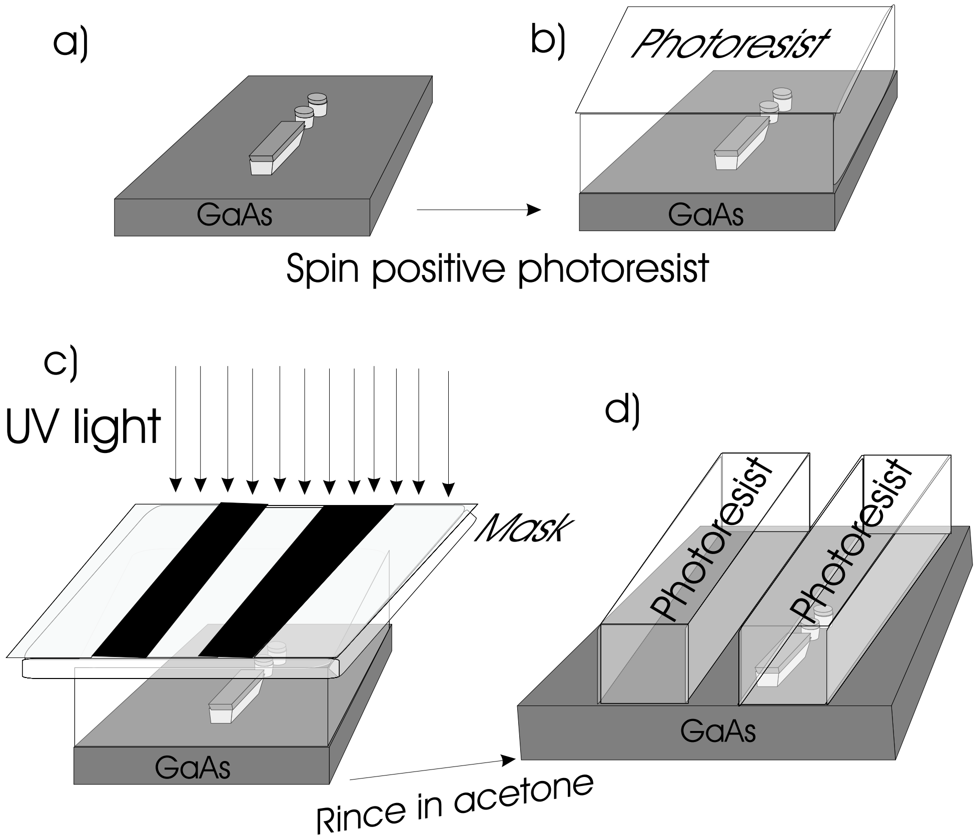

Figure A.6: Sample preparation for waveguide evaporation. In (a) the starting point is shown. The pads of the epitaxial film are left on the GaAs substrate after the dry etching. (b) shows the Sample covered by a thick continuous layer of photoresist. In (c) a shadow mask with the image of the coplanar waveguide is aligned with the required Sample orientation. The same mask was used as that shown in Fig. A.1. A magnified part of the shadow mask around the 30 μm wide central conductor is shown in (c). The mask was aligned with the waveguide axis oriented along the [110] crystallographic direction of the GaAs(001): the [110] axis of the GaAs(001) is parallel to the [110] axis of the Fe(001) films. UV light illuminated the positive photoresist through the shadow mask affecting only the regions exposed. The positive photoresist becomes soluble in the regions exposed to the UV light. (d) shows the photoresist structure after the sample is cleaned with acetone. The soluble regions of the photoresist are removed. The pads of the epitaxial structure which are needed for TRMOKE measurements are covered by a thick layer of photoresist. These epitaxial pads were located at the edge of one of the photoresist bars.

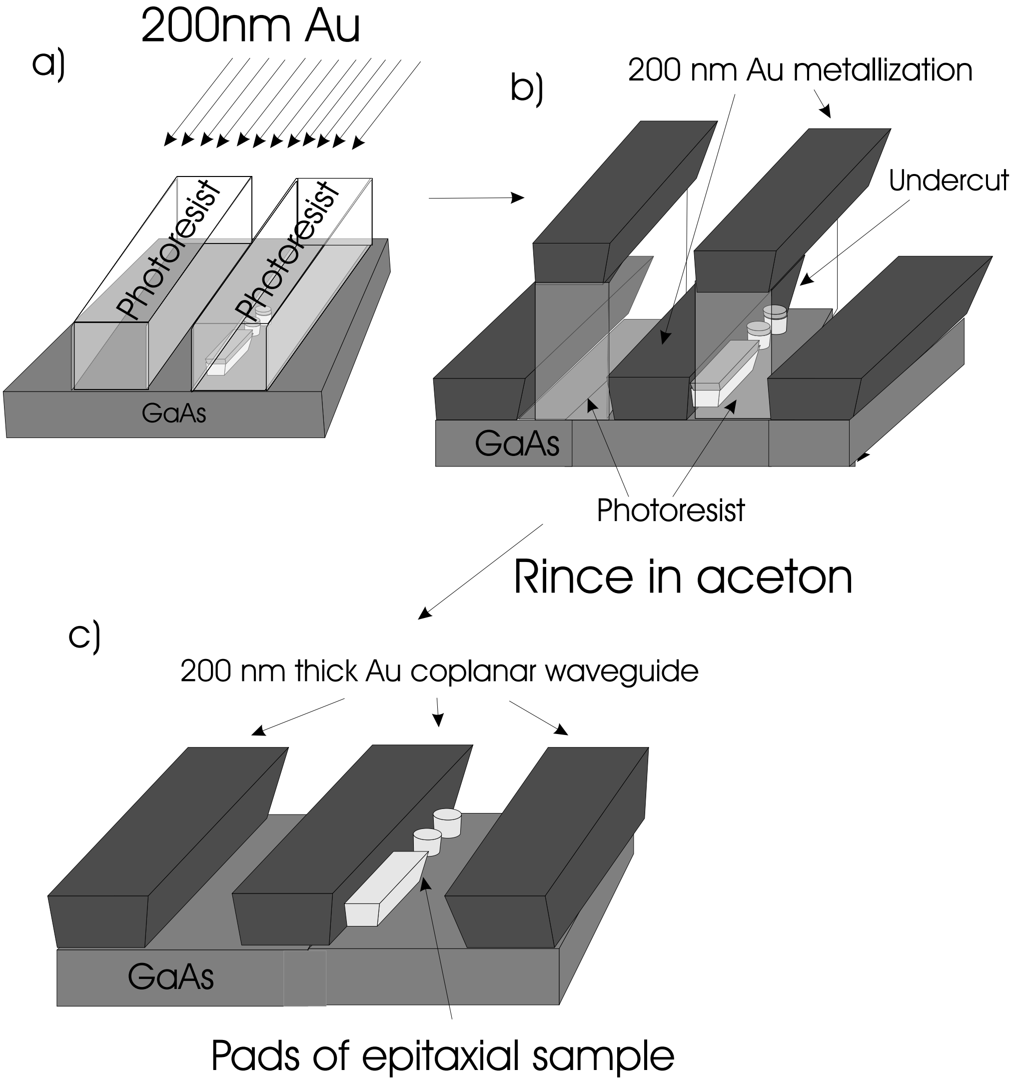

Figure A.7: (a) A 200 nm thick Au layer was evaporated on the sample carrying the photoresist bars. The evaporation was carried out under an angle to ensure electrical isolation between the waveguide and the epitaxial sample pads. (b) Shows the Sample covered by a 200 nm layer of evaporated Au. Evaporation under an angle results in an undercut of the Au central conductor. The undercut was caused by the shadowing effect due to the thick layer of the photoresist. (c) The remaining structure after applying the liftoff procedure: the Sample is put in acetone for 30 minutes and then rinsed in acetone. The photoresist is removed from the sample leaving the Au coplanar waveguide together with the specimen pads.

Appendix B

Transmission through FM/NM interface

Non-local spin dynamics in metallic multilayers was first theoretically introduced by Tserkovnyak et al. [3]. This theory is based on generalization of the Buttiker [32] theory, which derived an ac-electric current induced by the an oscillating chemical potential. In this appendix I will guide reader through the main steps of derivation of spin current created at FM/NM interface.

Brataas, Brouwer [103] and Tserkovnyak extended Buttiker theory to the spin dependent matrix current $\hat{I}^{pump}$ which is expressed in the form

$$\hat{I}^{pump}(t) = e\frac{\partial \hat{n}(l)}{\partial X}\frac{\partial X}{\partial t} , \tag{B.1}$$

where $X(t)$ is the parameter that modulates the scattering matrix $\hat{S}$, and

$$\frac{\partial \hat{n}(l)}{\partial X} = \frac{1}{4\pi i}\sum_{mn,l'}\frac{\partial \hat{S}^{\dagger}_{nm,ll'}}{\partial X}\hat{S}_{nm,ll'} + h.c \tag{B.2}$$

is the matrix emissivity into the lead l. The important point behind the current matrix $\hat{I}^{pump}(t)$ is that it incorporates both the charge I_C current and the spin flow $\vec{I}_S^{pump}$. The total current can be be expanded as a superposition of unity matrix and three spin Pauli matrices, which leads to spin independent I_C and spin dependent $\vec{I}_S^{pump}$ contributions:

$$\hat{I}^{pump}(t) = \frac{I_C}{2}\hat{1} - \hat{\vec{\sigma}}\vec{I}_S^{pump}\frac{e}{\hbar} , \tag{B.3}$$

where I_C and $\vec{I}_S^{pump}$ are the expectation values.

B.1 Diagonalization of transmission and reflection matrices.

In the laboratory system of coordinates with $\vec{M}_s$ parallel to the Z axis (see Fig. B.1), the scattering matrix $\hat{S}$ is defined in terms of transmission $\hat{t}$ and reflection $\hat{r}$ matrices, shown in Fig. B.1

$$\hat{S} = \begin{pmatrix} \hat{r} & \hat{t} \\ \hat{t} & \hat{r} \end{pmatrix}. \tag{B.4}$$

Transmission $\hat{t}$ and reflection $\hat{r}$ matrices have off diagonal components in the laboratory system of coordinates. They can be diagonalized by working in the rotating system of coordinates, where the magnetization unit vector $\vec{n} = \frac{\vec{M}}{M}$ is parallel to the z axis. Mathematically it requires the unitary transformation operator $\hat{U}$:

$$\hat{r}_{ss'} = (\hat{U}\hat{r}_U\hat{U}^{-1})_{ss'} = \hat{U}_{s\uparrow}\hat{U}^{-1}_{\uparrow s'}\hat{r}_{U,\uparrow\uparrow} + \hat{U}_{s\downarrow}\hat{U}^{-1}_{\downarrow s'}\hat{r}_{U,\downarrow\downarrow}\ , \tag{B.5}$$

where $\hat{r}_{U,ss'} = \delta_{ss'}\hat{r}_{U,ss}$ and

$$\hat{U} = \begin{pmatrix} U_{\uparrow\uparrow} & U_{\uparrow\downarrow} \\ U_{\downarrow\uparrow} & U_{\downarrow\downarrow} \end{pmatrix} = \begin{pmatrix} \cos\frac{\theta}{2}\exp^{-i\frac{\varphi}{2}} & -\sin\frac{\theta}{2}\exp^{-i\frac{\varphi}{2}} \\ \sin\frac{\theta}{2}\exp^{i\frac{\varphi}{2}} & \cos\frac{\theta}{2}\exp^{i\frac{\varphi}{2}} \end{pmatrix}\ , \tag{B.6}$$

where the off diagonal $U_{\downarrow\uparrow}$ and $U_{\uparrow\downarrow}$ elements show that the rotation of the system coordinates leads to spin mixing. As can be seen from Eq. B.5 the products $\hat{U}_{s\uparrow}\hat{U}^{-1}_{\uparrow s'}$ and $\hat{U}_{s\downarrow}\hat{U}^{-1}_{\downarrow s'}$ represent the spin projectors operators between the mixed to diagonalized state coordinates. Evaluating their explicit form allows one to express them in more compact form:

$$\hat{U}_{s\uparrow}\hat{U}^{-1}_{\uparrow s'} \equiv \hat{u}^{+} = \frac{1}{2}(\hat{1} + \hat{\vec{\sigma}}\cdot\vec{n}), \tag{B.7}$$

$$\hat{U}_{s\downarrow}\hat{U}^{-1}_{\downarrow s'} \equiv \hat{u}^{-} = \frac{1}{2}(\hat{1} - \hat{\vec{\sigma}}\cdot\vec{n})\ , \tag{B.8}$$

where $\hat{\vec{\sigma}}$ is the Pauli spin operator and $\vec{n}$ is unit vector along the magnetization direction. Using these transformations one can deduce the following equations for the transmission and reflection matrices:

$$\hat{r}^{mn} = \hat{r}^{mn}_{U,\uparrow\uparrow}\hat{u}^{+} + \hat{r}^{mn}_{U,\downarrow\downarrow}\hat{u}^{-}, \tag{B.9}$$

$$\hat{t}^{mn} = \hat{t}^{mn}_{U,\uparrow\uparrow}\hat{u}^{+} + \hat{t}^{mn}_{U,\downarrow\downarrow}\hat{u}^{-}\ , \tag{B.10}$$

where $\hat{r}^{mn}_{U,\uparrow\uparrow}$ and $\hat{t}^{mn}_{U,\uparrow\uparrow}$ are the diagonalized transmission and reflection matrices. The scattering matrix $\hat{S}$ in the new system of coordinates will have the form

$$\hat{S} = \hat{S}_{U,\uparrow\uparrow}\hat{u}^{+} + \hat{S}_{U,\downarrow\downarrow}\hat{u}^{-}\ , \tag{B.11}$$

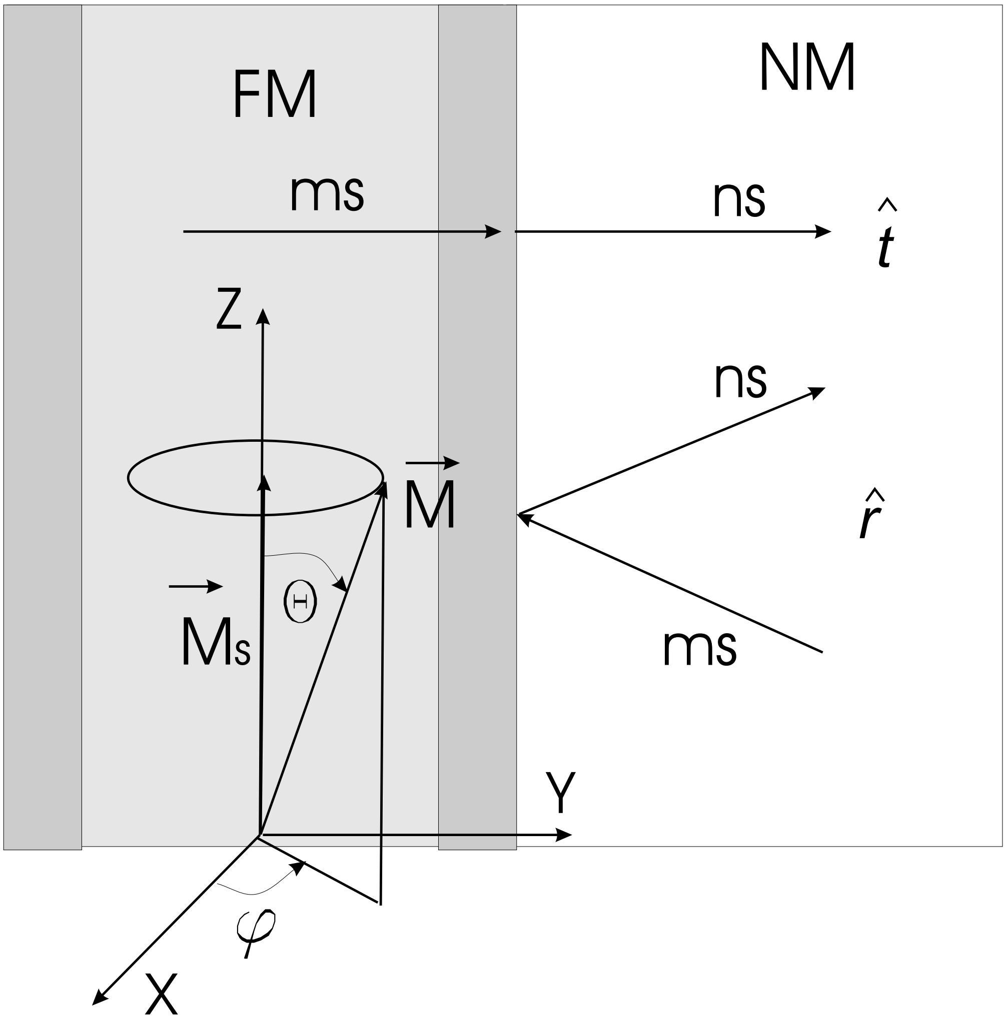

Figure B.1: Schematic cartoon showing the interface between the ferromagnet (FM) and normal metal (NM). The saturation magnetization $\vec{M}_s$ of the ferromagnet is oriented in the film plane. The angle φ corresponds to the angle between $\vec{M}$ and the X axis. The transmission and reflection matrix elements are shown for scattering without spin flip.

where

$$\hat{S}_{U,\uparrow\uparrow} = \begin{pmatrix} \hat{r}_{U,\uparrow\uparrow} & \hat{t}_{U,\uparrow\uparrow} \\ \hat{t}_{U,\uparrow\uparrow} & \hat{r}_{U,\uparrow\uparrow} \end{pmatrix} \tag{B.12}$$

and

$$\hat{S}_{U,\downarrow\downarrow} = \begin{pmatrix} \hat{r}_{U,\downarrow\downarrow} & \hat{t}_{U,\downarrow\downarrow} \\ \hat{t}_{U,\downarrow\downarrow} & \hat{r}_{U,\downarrow\downarrow} \end{pmatrix} . \tag{B.13}$$

B.2 Spin current pumped by $\vec{M}(t)$.

Following Tserkovnyak et al. the parameter $X(t)$ (see Eq. B.1) was identified with the azimuthal angle $\varphi(t)$ of $\vec{M}(t)$, see Fig. B.1. Than the current pumped into lead l is given with:

$$\hat{I}^{pump}(t) = e \frac{\partial \hat{n}(l)}{\partial \phi} \frac{\partial \phi}{\partial t} . \tag{B.14}$$

In the rotating system of coordinates the spin current $\hat{I}^{pump}(t)$ from Eq. B.14 will take the following form

$$\begin{aligned} \hat{I}^{pump}(t) = \frac{e}{4\pi i} \sum_{mn,l'} ([\hat{S}_{U,\uparrow\uparrow,nm,ll'} \frac{\partial \hat{u}^{+}}{\partial \varphi} \frac{\partial \varphi}{\partial t} + \hat{S}_{U,\downarrow\downarrow,nm,ll'} \frac{\partial \hat{u}^{-}}{\partial \varphi} \frac{\partial \varphi}{\partial t}] \\ \times [\hat{S}^{\dagger}_{U,\uparrow\uparrow,nm,ll'} \hat{u}^{+} + \hat{S}^{\dagger}_{U,\downarrow\downarrow,nm,ll'} \hat{u}^{-}] + hc) \qquad \text{(B.15)} \\ = \frac{e}{4\pi i} \sum_{mn,l'} ([\hat{S}_{U,\uparrow\uparrow,nm,l'} \hat{\dot{u}}^{+} + \hat{S}_{U,\downarrow\downarrow,nm,l'} \hat{\dot{u}}^{-}][\hat{S}^{\dagger}_{U,\uparrow\uparrow,nm,l'} \hat{u}^{+} + \hat{S}^{\dagger}_{U,\downarrow\downarrow,nm,l'} \hat{u}^{-}] \\ +[\hat{S}_{U,\uparrow\uparrow,nm,l'} \hat{u}^{+} + \hat{S}_{U,\downarrow\downarrow,nm,l'} \hat{u}^{-}][\hat{S}^{\dagger}_{U,\uparrow\uparrow,nm,l'} \hat{\dot{u}}^{+} + \hat{S}^{\dagger}_{U,\downarrow\downarrow,nm,l'} \hat{\dot{u}}^{-}]) , \qquad \text{(B.16)} \end{aligned}$$

where

$$\hat{\dot{u}}^{+} = \frac{1}{2} (\hat{\vec{\sigma}} \cdot \frac{\partial \vec{n}}{\partial t}) \tag{B.17}$$

and

$$\hat{\dot{u}}^{-} = -\frac{1}{2} (\hat{\vec{\sigma}} \cdot \frac{\partial \vec{n}}{\partial t}) . \tag{B.18}$$

Buttiker theory yields the following relations for $\hat{S}$ matrix:

$$\hat{S}^{\dagger} \hat{S} = \hat{1}, \tag{B.19}$$

$$\hat{S}^{\dagger} \hat{S}' = -\hat{S}'^{\dagger} \hat{S} , \tag{B.20}$$

where ”′” indicate derivatives with respect to the slowly varying potential. Using these identities Eq.B.15 can be rewritten

$$\begin{aligned} \hat{I}^{pump}(t) = \frac{e}{4\pi i} \sum_{mn,l'} (\hat{S}_{U,\uparrow\uparrow,nm,l'} \hat{S}^{\dagger}_{U,\uparrow\uparrow,nm,l'} [\hat{\dot{u}}^{+} \hat{u}^{+} - \hat{u}^{+} \hat{\dot{u}}^{+}] \\ + \hat{S}_{U,\downarrow\downarrow,nm,l'} \hat{S}^{\dagger}_{U,\downarrow\downarrow,nm,l'} [\hat{\dot{u}}^{-} \hat{u}^{-} - \hat{u}^{-} \hat{\dot{u}}^{-}] + \hat{S}_{U,\uparrow\uparrow,nm,l'} \hat{S}^{\dagger}_{U,\downarrow\downarrow,nm,l'} [\hat{\dot{u}}^{+} \hat{u}^{-} - \hat{u}^{+} \hat{\dot{u}}^{-}] \\ + \hat{S}_{U,\downarrow\downarrow,nm,l'} \hat{S}^{\dagger}_{U,\uparrow\uparrow,nm,l'} [\hat{\dot{u}}^{-} \hat{u}^{+} - \hat{u}^{-} \hat{\dot{u}}^{+}]) . \qquad \text{(B.21)} \end{aligned}$$

Using the identity $(\hat{\vec{\sigma}} \cdot \vec{A})(\hat{\vec{\sigma}} \cdot \vec{B}) = (\vec{A} \cdot \vec{B}) + i\hat{\vec{\sigma}}(\vec{A} \times \vec{B})$, which holds for Pauli vector matrix the explicit form of the products involving the spin projector operators $\dot{u}^+$ $\dot{u}^-$ and their derivatives in Eq.B.21 are

$$[\dot{\hat{u}}^+ \hat{u}^+ - \hat{u}^+ \dot{\hat{u}}^+] = \frac{i}{2}\hat{\vec{\sigma}}[\dot{\vec{n}} \times \vec{n}], \tag{B.22}$$

$$[\dot{\hat{u}}^- \hat{u}^- - \hat{u}^- \dot{\hat{u}}^-] = \frac{i}{2}\hat{\vec{\sigma}}[\dot{\vec{n}} \times \vec{n}], \tag{B.23}$$

$$[\dot{\hat{u}}^+ \hat{u}^- - \hat{u}^+ \dot{\hat{u}}^-] = \frac{1}{2}(\hat{\vec{\sigma}} \cdot \dot{\vec{n}}) - \frac{i}{2}\hat{\vec{\sigma}}[\dot{\vec{n}} \times \vec{n}], \tag{B.24}$$

$$[\dot{\hat{u}}^- \hat{u}^+ - \hat{u}^- \dot{\hat{u}}^+] = -\frac{1}{2}(\hat{\vec{\sigma}} \cdot \dot{\vec{n}}) - \frac{i}{2}\hat{\vec{\sigma}}[\dot{\vec{n}} \times \vec{n}] \ . \tag{B.25}$$

Inserting B.22, B.23, B.24 and B.25 into B.21 one gets

$$\begin{aligned}
\hat{I}^{pump}(t) = \frac{e}{8\pi i} \sum_{mn,l'} (&\hat{S}_{U,\uparrow\uparrow,nm,l'} \hat{S}^{\dagger}_{U,\uparrow\uparrow,nm,l'} + \hat{S}_{U,\downarrow\downarrow,nm,l'} \hat{S}^{\dagger}_{U,\downarrow\downarrow,nm,l'} \\
&- \hat{S}_{U,\uparrow\uparrow,nm,l'} \hat{S}^{\dagger}_{U,\downarrow\downarrow,nm,l'} + \hat{S}_{U,\downarrow\downarrow,nm,l'} \hat{S}^{\dagger}_{U,\uparrow\uparrow,nm,l'}) \hat{\vec{\sigma}}(\vec{n} \times \dot{\vec{n}}) \\
+ \frac{e}{8\pi i} \sum_{mn,l'} (&\hat{S}_{U,\uparrow\uparrow,nm,l'} \hat{S}^{\dagger}_{U,\downarrow\downarrow,nm,l'} - \hat{S}_{U,\downarrow\downarrow,nm,l'} \hat{S}^{\dagger}_{U,\uparrow\uparrow,nm,l'})(\hat{\vec{\sigma}} \cdot \dot{\vec{n}})
\end{aligned} \tag{B.26}$$

The expectation value of the spin current can be found as trace of the diagonalized $\hat{I}^{pump}(t)$ and yields

$$\hat{I}_S^{pump}(t) = \frac{\hbar}{4\pi} A_r \left(\vec{n} \times \frac{\partial \vec{n}}{\partial t} \right) - \frac{\hbar}{4\pi} A_i \frac{\partial \vec{n}}{\partial t} \ , \tag{B.27}$$

where the interface scattering parameters A_r and A_i are given by

$$A(r) = \frac{1}{2} \sum_{mn} (|r_{mn,U,\uparrow\uparrow} - r_{mn,U,\downarrow\downarrow}|^2 + |t_{mn,U,\uparrow\uparrow} - t_{mn,U,\downarrow\downarrow}|^2), \tag{B.28}$$

$$A(i) = Im \sum_{mn} (r_{mn,U,\uparrow\uparrow} r^*_{mn,U,\downarrow\downarrow} + t_{mn,U,\uparrow\uparrow} t^*_{mn,U,\downarrow\downarrow}) \tag{B.29}$$

It turns out that the imaginary part $A(i)$ is almost negligible due to the phase cancellation of the reflection and transmission coefficients and averaging over interface roughness.

Bibliography

[1] M.N. Baibich, J.M. Broto, A. Fert, F. Nguen Van Dau, F. Petroff, P. Eitenne, G. Creuzet, A. Friedrich, and J. Chazelas. Giant magnetoresistance of (001)Fe/(001)Cr magnetic superlattice. *Phys. Rev. Lett.*, 61:2472, 1988.

[2] G. Woltersdorf. *Spin-pumping and two-magnon scattering in magnetic multilayers.* PhD thesis, Simon Fraser University, 2004.

[3] Y. Tserkovnyak, A. Brataas, and G.E.W. Bauer. Enhanced gilbert damping in thin ferromagnetic films. *Phys. Rev. Lett.*, 88:117601, 2002.

[4] B. Heinrich, Y. Tserkovnyak, G. Woltersdorf, A. Brataas, R. Urban, and G. Bauer. Dynamic exchange coupling in magnetic bilayers. *Phys. Rev. Lett.*, 90:187601, 2003.

[5] J.R. Mac Donald. Ferromagnetic resonance and the internal field in ferromagnetic materials. *Proc. Phys. Soc. A*, 64:968, 1951.

[6] J. Lindner and M. Farle. *Magnetic Heterostructures,* ed. H. Zabel and S.D. Bader, chapter 2:Magnetic Anisotropy of Heterostructures, pages 45–66. Springer, 2008.

[7] B. Heinrich and J. F. Cochran. Ultrathin metallic magnetic films: magnetic anisotropies and exchange interaction. *Adv. Phys.*, 42:523–639, 1993.

[8] B. Heinrich, A.S. Arrot, J.F. Cochran, K.B. Urquhart, K. Myrtle, Z. Celinski, and Q.M. Zhong. Characterization and properties of ultrathin magnetic films and multilayers,. *Materials Research Society Symposium Proceedings*, 151:177, 1989.

[9] B. Heinrich, J.F. Cochran, M. Kowalevski, J. Kirschner, Z. Celinski, A.S. Arrot, and K. Myrtle. Magnetic anisotropies and exchange coupling in ultrathin fcc Co(001) structures. *Phys. Rev. B*, 44:9348, 1991.

[10] H.J.G. Draaisma and W.J.M. de Jonge. Surface and volume anisotropy from dipole-dipole interactions in ultrathin ferromagnetic films. *J. Appl. Phys.*, 64:3610, 1988.

[11] J.F. Cochran and W.J.M. Kambersky. Ferromagnetic resonance in very thin films. *J. Magn. Magn. Mater.*, 302:348, 2006.

[12] G. Wastlbauer and J.A.C. Bland. Structural and magnetic properties of ultrathin epitaxial Fe films on GaAs(001) and related semiconductor substrates. *Adv. Phys.*, 54:137–219, 2005.

[13] B. Heinrich. *Magnetic Ultrathin Film Structures III,* ed. J.A.C. Bland and B. Heinrich, chapter 5, page 143. Springer Verlag, 2004.

[14] T.L. Gilbert. A Lagrangian formulation of the gyromagnetic equation of the magnetization field. *Phys. Rev.*, 100:1243, 1955.

[15] H. Mori. Transport, collective motion, and brownian motion. *Prog. Theor. Phys.*, 33:423, 1965.

[16] H. Mori and K. Kawasaki. Theory of dynamical behaviors of ferromagnetic spins. *Prog. Theor. Phys.*, 27:529, 1962.

[17] A.G. Gurevitch. *Ferrites at Micorwave Frequencies.* New York, Consaltantys Bureau, 1963.

[18] B. Heinrich, D. Fraitova, and V. Kambersky. The influence of s-d exchange on relaxation of magnons in metals. *Phys. Stat. Sol.*, 23:501, 1967.

[19] Z. Frait and D. Fraitova. *Frontiers in Magnetism of reduced Dimension Systems, edited by P. Wigen and V. Baryachtiar and N. Lesnik.*, chapter IV, page 121. NATO-ASI, 1996.

[20] Z. Frait and H. MacFaden. Ferromagnetic resonance in metals. frequency dependence. *Phys. Rev.*, 139:1173, 1965.

[21] B. Heinrich, J. F. Cochran, and R. Baartman. Ferromagnetic resonance absorption in supermalloy at 9, 24, and 38 GHz. *Can. J. Phys.*, 55:806, 1977.

[22] S.V. Vonsovskii and J.A. Izyumov. *Fiz. Metallov i Metallovedenie*, 10:321, 1960.

[23] R. J. Elliot. Theory of the efect of spin-orbit coupling on magnetic resonance in some semiconductors. *Phys. Rev.*, 96:266, 1954.

[24] T. Valet and A. Fert. Theory of the perpendicular magnetoresistance in magnetic multilayers. *Phys. Rev. B*, 48:7099, 1993.

[25] S. Dubois, L. Piraux, J.M. George, K. Ounadjela, J.L. Duvail, and A. Fert. Evidence for a short spin diffusion length in permalloy from the giant magnetoresistance of multilayered nanowires. *Phys. Rev. B*, 60:477, 1999.

[26] L. Piraux, S. Dubois, A. Fert, and L. Belliar. The temperature dependence of the perpendicular giant magnetoresistance in Co/Cu multilayered nanowires. *Eur. J. Phys.*, B4:413, 1998.

[27] D.N. Zubarev. Double-time Green's functions in statistical physics. *Sov. Phys. Usp.*, 3:320, 1960.

[28] V. Kamberský. On ferromagnetic resonance damping in metals. *Czech. J. Phys.*, B26:1366, 1976.

[29] V. Kamberský. On the landau-lifshitz relaxation in ferromagnetic metals. *Can. J. Phys.*, 48:2906–2911, 1970.

[30] K. Baberschke. The magnetism in Ni. *Appl. Phys. A*, 62:417–427, 1996.

[31] V. Kamberský. FMR linewidth and disorder in metals. *Czech. J. Phys.*, 34:1111, 1984.

[32] M.Buettiker, H. Thomas, and A. Pretre. Current partition in multiprobe conductors in the presence of slowly oscillating external potentials. *Z. Phys.*, B94:133, 1994.

[33] M.D. Stiles and A. Zangwill. Anatomy of spin-transfer torque. *Phys. Rev. B*, 66:014407, 2002.

[34] R. Urban, G. Woltersdorf, and B. Heinrich. Gilbert damping in single and multilayer ultrathin films: role of interfaces in nonlocal spin dynamics. *Phys. Rev. Lett.*, 87(21):217204 – 4, 2001.

[35] R. Urban, B. Heinrich, and G. Woltersdorf. Semiclassical theory of spin transport in magnetic multilayers. *J. Appl. Phys.*, 93:8280, 2003.

[36] S. Mizukami, Y. Ando, and T. Miyazaki. Magnetic relaxation of normal-metal (NM)/80NiFe/NM films. *J. Magn. Magn. Mater.*, 239:42, 2002.

[37] M.V. Costache, M. Sladkov, S.M. Watts, C.H. van der Wal, and B.J. van Wees. Electrical detection of spin pumping due to the precessing magnetization of a single ferromagnet. *Phys. Rev. Lett.*, 97:216603, 2006.

[38] A. Brataas, Y. Tserkovnyak, G.E.W. Bauer, and B.I. Halperin. Spin battery operated by ferromagnetic resonance. *Phys. Rev. B*, 66:060404, 2002.

[39] E. Šimanek and B. Heinrich. Gilbert damping in magnetic multilayers. *Phys. Rev. B*, 67:144418, 2003.

[40] J. Kerr. On rotation of the plane of polarization be reflection from the pole of a magnet. *Phil. Mag.*, 3:321, 1877.

[41] E.R. Moog and S.D. Bader. Smoke signals from ferromagnettic monolayers: p(1x1) Fe/Au(100). *Superlattices and microstructures 1*, 1:543, 1981.

[42] S.D. Bader. SMOKE. *J. Magn. Magn. Mater.*, 100:440, 1991.

[43] W. Voight. *Handbuch der Electrizitat und des magnetismus 4, edited by L. Graetz*, chapter Magnetooptics, page 667. A. Barth, Leipzig, 1920.

[44] M.J. Freiser. A survey of magnetooptics effects. *IEEE Yrans. Magn.*, 4:152, 1968.

[45] J.F. Dillon. *Magnetic properties of materials edited by J. Smit*, chapter Magneto-optical properties of magnetic crystals, page 108. McGraw-Hill, New York, 1971.

[46] W. Wettling. Magneto-optics of ferrites. *J. Magn. Magn. Mater.*, 3:147, 1976.

[47] M. Faraday. On the magnetization of light and the illumination of magnetic lines of force. *Phil. Trans. Royal Soc.*, 136:1, 1846.

[48] S. Visnovsky, M. Nyvlt, V. Prosser, R. lopusnik, R. Urban, J. Ferre, G. Penissard, D. Renard, and R. Krishnan. Spin diffusion length in Py. *Phys. Rev. B*, 52:1090, 1995.

[49] S.D. Bader. Surface magneto-optic Kerr effect (SMOKE). *J. Magn. Magn. Mater.*, 200:664, 1999.

[50] G. Traeger, L. Wenzel, and A. Hubert. Computer experiments on the information depth and the figure of merit in magnetooptics. *Phys. Stat. Sol. A*, 131:201, 1992.

[51] A. Hubert and G. Traeger. Magneto-optical sensitivity functions of thin-film systems. *J. Magn. Magn. Mater.*, 124:185, 1993.

[52] J. Pommier, J.P. Jamet, J. Ferre, P. Houdy, P. Boher, and F. Pierre. Magnetic and magneto-optical properties of Tb/Fe multilayers. *J. Magn. Magn. Mater.*, 136:251, 1994.

[53] R Azzam and N. Bashara. *Ellipsometry and Polarized Light.* North-holland, Amsterdam, 1992.

[54] R. Schafer. Magneto-optical domain studies in coupled magnetic multilayers. *J. Magn. Magn. Mater.*, 148:226, 1995.

[55] J. Hamrle, J. Ferre, M. Nyvlt, and S. Visnovsky. In-depth resolution of the magneto-optical kerr effect in ferromagnetic multilayers. *Phys. Rev. B*, 66:224423, 2002.

[56] D. Briggs and M.P. Seah. *Practical surface analysis by Auger and X-ray photoelectron spectroscopy*, chapter 1, page 1. John Wiley and Sons, 1983.

[57] D. Briggs and M.P. Seah. *Practical surface analysis by Auger and X-ray photoelectron spectroscopy*, chapter 4, page 141. John Wiley and Sons, 1983.

[58] M.P. Seah and W.A. Dench. *Quantitative electron spectroscopy of surfaces: a standard data base for electron inelastic mean free paths in solids.* 1979.

[59] C.J. Powell and A. Jablonski. Evaluation of calculated and measured electron inelastic mean free paths near solid surfaces. *J. Phys. Chem.*, 28:19–62, 1999.

[60] D. Briggs and M.P. Seah. *Practical surface analysis by Auger and X-ray photoelectron spectroscopy*, chapter 5, page 181. John Wiley and Sons, 1983.

[61] D. Briggs and M.P. Seah. *Practical surface analysis by Auger and X-ray photoelectron spectroscopy*, chapter 2, page 17. John Wiley and Sons, 1983.

[62] D.W.J. Cruickshank, H.J. Juretschke, and N. Kato. *Ewald and His dynamical Theory of X-ray Diffraction.* Oxford University Press, New York, 1992.

[63] D.B. Williams and C.B. Carter. *Transmission Electron Microscopy. Volume II. Diffraction.*, chapter 12, page 196. Plenum Press, New York, 1996.

[64] Qi-Kun Xue, T. Hashizume, and T. Sakurai. Scanning tunneling microscopy study of GaAs(001) surfaces. *Applied Surface Science*, 141:244–263, 1999.

[65] I.M. van Hove, P.R. Pukite, and P.I. Cohen. The dependence of RHEED oscillations on MBE growth parameters. *J. Vac. Sci. Technol.*, B3:563–567, 1985.

[66] *OMICRON manuals. Omicron Large sample STM/AFM.* Omicron, 2001.

[67] *OMICRON manuals. SCALA control unit.* Omicron, 2001.

[68] T.L. Monchesky, A. Enders, R. Urban, K. Myrtle, B. Heinrich, X.G. Zhang, W.H. Butler, and J. Kirschner. Spin-dependent transport in Fe and Fe/Au multilayers. *Phys. Rev. B*, 71(21):214440, 2005.

[69] D.K. Biegelsen, R.D. Bringans, J.E. Northrup, and L.-E. Swartz. Surface reconstructions of GaAs(100) observed by scanning tunneling microscopy. *Phys. Rev. B*, 41(9):5701 – 6, 1990/03/15.

[70] J. Vrba. *Measurements using radiofrequencies with wavelength in cm range. In Chech*, chapter 7. Statni nakladatelstvi technicke literatury, 1958.

[71] B. Heinrich, J.F. Cochran, A.S. Arrot, S.T. Purcell, K.B. Urquhart, J.R. Dutcher, and W.F. Egelhoff. . *Appl. Phys. A*, 49:473, 1989.

[72] C. Stamm, T. Kachel, N. Pontius, R. Mitzner, T. Quast, K. Holldack, S. Khan, C. Lupulescu, E.F. Aziz, M. Wietstruk, H.A. Durr, and W. Eberhardt. Femtosecond modification of electron localization and transfer of angular momentum in nickel. *Nature materials*, 6:740–743, 2007.

[73] B.C. Choi and M. Freeman. *Ultrathin Magnetic Structures edited by J.A.C. Bland and B. Henrich.* Springer, 2005.

[74] A. Fert and P. Bruno. *Magnetic Ultrathin Film Structures II,* ed. J.A.C. Bland and B. Heinrich, chapter 2, page 82. John Wiley & Sons, 1994.

[75] S. Parkin. *Magnetic Ultrathin Film Structures II,* ed. J.A.C. Bland and B. Heinrich, chapter 2, page 148. John Wiley & Sons, 1994.

[76] M.A.M. Gijs and G.E.W. Bauer. Perpendicular giant magnetoresistance of magnetic multilayers. *Adv. Phys.*, 46:285, 1997.

[77] B. Heinrich. *Magnetic Ultrathin Film Structures II,* ed. J.A.C. Bland and B. Heinrich. Springer Verlag, 2004.

[78] M. Brockmann, M. Zölfl, S. Miethaner, and G. Bayreuther. In-plane volume and interface magnetic anisotropies in epitaxial Fe films on GaAs(001). *J. Magn. Magn. Mater.*, 198–199:384–386, 1999.

[79] J. J. Krebs, B. T. Jonker, and G. A. Prinz. Properties of Fe single-cryslat films grown on (100)GaAs by molecular-beam epitaxy. *J. Appl. Phys.*, 61:2596–2599, 1987.

[80] R. Moosbuhler, F. Bensch, M. Dumm, and G. Bayreuther. Epitaxial Fe films on GaAs(001): Does the substrate surface reconstruction affect the uniaxial magnetic anisotropy? *J. Appl. Phys.*, 91:8757–8759, 2002.

[81] A. Ionescu, M. Tselepi, D.M. Gillingham, G. Wastlbauer, S.J. Steinmuller, H.E. Beere, D.A. Ritchie, and J.A.C. Bland. Submonolayer growth of Fe on a GaAs(100)-2x6 reconstructed surface. *Phys. Rev. B*, 72(12):125404, 2005.

[82] R.A. Gordon, E.D. Crozier, D.-T. Jiang, T.L. Monchesky, and B. Heinrich. Distorted iron films on GaAs(001)-(4x6). *Phys. Rev. B*, 62(3):2151, 2000.

[83] B. Kardasz. *to be published*. PhD thesis, Simon Fraser University, 2008.

[84] R.A. Gordon and E.D. Crozier. In-plane structural anisotropy of ultrathin Fe films on GaAs(001)-4x6: X-ray absorption fine-structure spectroscopy measurements. *Phys. Rev. B*, 74:165405, 2006.

[85] R.A. Gordon, E.D. Crozier, D.T. Jiang, P.S. Budnik, T.L. Monchesky, and B. Heinrich. In situ XAFS study of Fe epitaxially grown by MBE on GaAs(001)-4x6. *Surface Science*, 581:47, 2005.

[86] B. Kardasz, J. Zukrowski, O. Mosendz, M. Przybylski, B. Heinrich, and J. Kirschner. Interface atomic structure and magnetic anisotropy in ultrathin Fe films grown by thermal deposition and pulsed laser deposition on GaAs(001). *J. Appl. Phys.*, 101:09D110, 2007.

[87] B. Heinrich and J.F. Cochran. *Handbook of Magnetism and Advanced Magnetic Materials, Edited by H. Kronmuller and S. Parkin*, volume 4, chapter Magnetic Ultrathin Films. John Wiley & Sons, 2007.

[88] B. Aktas, B. Heinrich, G. Woltersdorf, U. Urban, and et al. Magnetic anisotropies in ultrathin iron films grown on the surface-reconstructed GaAs substrate. *J. Appl. Phys.*, 102:13912, 2007.

[89] O.Mosendz, B.Kardasz, and B. Heinrich. Ferromagnetic resonance and spin momentum exchange in crystalline magnetic ultrathin films in non-collinear configuration. *J. Appl. Phys.*, 103:07B505, 2008.

[90] V.L. Safonov and H.N. Bertram. Linear stochastic magnetization dynamics and microscopic relaxation mechanisms. *J. Appl. Phys.*, 94:529, 2003.

[91] L. Berger. Emission of spin waves by a magnetic multilayer traversed by a current. *J. Appl. Phys.*, 54:9353, 1996.

[92] L. Berger. Multilayers as spin-wave emitting diodes. *J. Appl. Phys.*, 81:4880, 1997.

[93] L. Berger. Effect of interfaces on Gilbert damping and FMR linewidth in magnetic multilayers. *J. Appl. Phys.*, 90:4632, 2001.

[94] J.C. Slonczewski. Current driven excitation of magnetic multilayers. *J. Magn. Magn. Mater.*, 159:1, 1996.

[95] J.C. Slonczewski. Excitation of spin waves by an electric current. *J. Magn. Magn. Mater.*, 195:261, 1999.

[96] M. Tsoi, A.G.M. Jansen, J. Bass, W.-C. Chiang, M. Seck, V. Tsoi, and P.Wyder. Excitaion of a magnetic multilayer by an electric current. *Phys. Rev. Lett.*, 80:4281, 21998.

[97] M. Tsoi, A.G.M. Jansen, J. Bass, W.-C. Chiang, V. Tsoi, and P.Wyder. Generation and detection of phase coherent magnons. *Nature*, 406:46, 2000.

[98] J.A. Katine, F.J. Albert, R.A. Buhrman, E.B. Myers, and D.C. Ralph. Current-driven magnetization reversal and spin-wave excitations in Co/Cu/Co pillars. *Phys. Rev. Lett.*, 84:3149, 2000.

[99] F.J. Albert, J.A. Katine, R.A. Buhrman, and D.C. Ralph. Spin polarized current switching of a cobalt thin film nanomagnet. *Appl. Phys. Lett.*, 77:3809, 2000.

[100] S.I. Kiselev, J.C. Sankey, I.N. Krivorotov, N.C. Emley, R.J. Schoelkopfand R.A. Buhrman, and D.C. Ralph. Microwave oscillations of a nano-magnet driven by a spin-polarized current. *Nature*, 425:380, 2003.

[101] W.H. Rippard, M.R. Pufall, S. Kaka, S.E. Russek, and T.J. Silva. Direct-current induced dynamics in $Co_{90}Fe_{10}/Ni_{80}Fe_{20}$ point contacts. *Phys. Rev. Lett.*, 92:27201, 2004.

[102] A. Brataas, Y.V. Nazarov, and G.E.W. Bauer. Spin-transport in multi-terminal normal metal-ferromagnet systems with non-collinear magnetizations. *Euro. Phys. J. B*, 22:99, 2001.

[103] P.W. Brouwer. Scattering approach to parametric pumping. *Phys. Rev. B*, 58:R10135, 1998.

[104] M. Buttiker, H. Thomas, and A Pretre. Current partition in multiprobe conductors in the presence of slowly oscillating external potentials. *Z. Phys.*, B94:133, 1994.

[105] J. Bass and W.P. Pratt. Spin-diffusion lengths in metals and alloys, and spin-flipping at metal/metal interfaces: an experimentalists critical review. *J. Phys.: Condenced Matter*, 19:183201, 2007.

[106] J. Nibarger, R. Lopusnik, and T. Silva. Damping as a function of pulsed field amplitude and bias field in thin film Permalloy. *Appl. Phys. Lett.*, 82:2112, 2003.

[107] T. J. Klemmer, K. A. Ellis, and B. van Dover. Ferromagnetic resonance frequency of a thin Mo-permalloy film. *J. Appl. Phys.*, 87:5846, 2000.

[108] T.J. Silva, C.S. Lee, T.M. Crawford, and C.T. Rogers. Inductive measurement of ultrafast magnetization dynamics in thin-film Permalloy. *J. Appl. Phys.*, 85:7849, 1999.

[109] O.Mosendz, B.Kardasz, and B. Heinrich. Ferromagnetic resonance and spin momentum exchange in crystalline magnetic ultrathin films in non-collinear configuration. *J. Appl. Phys.*, 99:08F303, 2006.

[110] O. Mosendz, B. Kardasz, B. Heinrich, and D.S. Scmool. Spin dynamics at low microwave frequencies in crystalline fe ultrathin film double layers using co-planar transmission lines. *J. Magn. Magn. Mater.*, 300:174, 2006.

[111] G. Counil, Kim, T. Devolder, C. Chappert, K. Shigeto, and Y. Otani. Spin wave contributions to the high-frequency magnetic response of thin films obtained with inductive methods. *J. Appl. Phys.*, 95:5646, 2004.

[112] G. Woltersdorf and B. Heinrich. Two-magnon scatering in a self-assembled nanoscale network of misfit dislocations. *Phys. Rev. B*, 69:184417, 2004.

[113] P. R. Pukite, S. Batra, and P.I. Cohen. Anisotropic growth processes. *SPIE*, 796: Growth of Compound Semiconductors:22–26, 1987.

[114] P. R. Pukite, G. S. Petrich, G. J. Whaley, and P. I. Cohen. *Diffusion at Interfaces: Microscopic Concepts, edited by M. Grunze, H. J. Kreuzer and J. J.Weime*, chapter Reflection High Energy Electron Diffraction Studies of Diffusion and Cluster Formation During Molecular Beam Epitaxy, pages 30–54. Springer, 1988.

[115] M. Sparks, R. Loudon, and C. Kittel. Ferromagnetic relaxation. theory of the relaxation of the uniform precession and the degenerate spectrum in insulators at low temperatures. *Phys. Rev.*, 122:791–803, 1961.

[116] M. Sparks. *Ferromagnetic Relaxation Theory.* Mc-Graw-Hill, New York, 1966.

[117] E. Schlomann. Spin wave analysis of feromagnetic resonance in polycrystalline ferrites. *J. Phys. Chem. Solids*, 6:242–256, 1958.

[118] R. LeCraw, E.G. Spencer, and C.S. Porter. Ferromagnetic resonance linewidth in yttrium iron garnet single crystals. *Phys. Rev.*, 110:1311–1313, 1958.

[119] S. Geschwind and A.M. Clogston. Narrowing effect of dipole forces on inhomogeneousely broadened lines. *Phys. Rev.*, 108:49–53, 1957.

[120] M.J. Hurben, D.R. Franklin, and C.E. Patton. Angle dependenece of the ferromagnetic resonance linewidth in easy-axis and easy-plane single crystal hexagon ferrite disks. *J. Appl. Phys.*, 81:7458–7467, 1997.

[121] C.E. Patton, C.H. Witts, and F.B. Humphrey. Relaxation processes for ferromagnetic resonance in thin films. *J. Appl. Phys.*, 38:1358–1359, 1967.

[122] R. Arias and D. Mills. Extrinsic contribution to the ferromagnetic resonance response of ultrathin films. *Phys. Rev. B*, 60:7395, 1999.

[123] C. Kittel. *Quantum theory of solids*, chapter 4. J. Wiley and Sons, 1963.

[124] J. Lidner, L. Lenz, K. Kosubek, K. Baberschke, D. Spoddig, R. Meckenstock, J. Pelzl, Z. Frait, and D. L. Mills. Non-gilbert type damping of the magnetic relaxation in ultrathin ferromagnets. *Phys. Rev. B*, 68:060102, 2003.

[125] Y. Tserkovnyak, A. Brataas, and G.E. Bauer. Spin pumping and magnetization dynamics in metallic multilayers. *Phys. Rev. B*, 66:224403, 2002.

[126] B.Kardasz, O.Mosendz, B. Heinrich, and M.Freeman. Spin currents in Fe/Ag,Au/Fe nanostructures studied by time-resolved magneto-optical kerr effect. *J. Appl. Phys.*, 103:07C509, 2008.

[127] B. Heinrich, K. B. Urquhart, A. S. Arrott, J. F. Cochran, K. Myrtle, and S. T. Purcell. Ferromagnetic-resonance study of ultrathin bcc Fe(100) films grown epitaxially on fcc Ag(100) substrates. *Phys. Rev. Lett.*, 59:1786, 1987.

[128] O. Mosendz, G. Wolterdorf, B. Kardasz, B. Heinrich, and C.H. Back. Magnetization dynamics in the presence of pure spin currents in magnetic single and double layers in spin ballistic and diffusive regimes. *Phys. Rev. B*, submitted.

[129] S. Mizukami, Y. Ando, and T. Miyazaki. Effect of spin diffusion on gilbert damping for a very thin permalloy layer in Cu/permalloy/Cu/Pt films. *Phys. Rev. B*, 66:104413, 2002.

[130] Y. Tserkovnyak, A. Brataas, G.E. Bauer, and B.I. Halperin. Nonlocal magnetization dynamics in ferromagnetic heterostructures. *Review of Modern Physics*, 77:1375, 2005.

[131] L.D. Landau and E.M. Lifshitz. *Electrodynamics of continuous media edited by L.D. Landau and E.M. Lifshitz ; translated from the Russian by J.B. Sykes, J.S. Bell, and M.J. Kearsley.* Oxford, New York, Pergamon, 1984.

[132] J.F. Cochran and B. Heinrich. *Applications of Maxwell's Equations*, chapter 10. Simon Fraser University, 2004.

[133] *CRC Handbook of Chemistry and Physics edited by R.C. Weast, M.J. Astle and W.H. Beyer.* CRC Press, Boca raton, Florida, 1985.

[134] M.A. Ordal, L.L. Long, R.J. Bell, S.E. Bell, R.R. Bell, R.W. Alexander, and C.A. Ward. Optical properties of the metals Al, Co, Cu, Au, Fe, Pb, Ni, Pd, Pt, Ag, Ti and W in the infrared and far infrared. *Appl. Otics*, 22:1099, 1983.

[135] J.D. Jackson. *Classical electrodynamics, Third Edition.* New York: Wiley, 1988.

[136] J.F. Cochran and J.R. Dutcher. Calculation of the intensity of light scattered from magnons in thin films. *J. Magn. Magn. Mater.*, 73:299, 1988.

[137] G.S. Krinchik and V.A. Artem'ev. Magneto-optical properties of Ni, Co, and Fe in the ultraviolet visible, and infrared parts of spectrum. *Zh. Eksp. Teor. Fiz.*, 53:1901, 1967.

[138] G.S. Krinchik and V.A. Artem'ev. Magneto-optic properties of nickel, iron, and cobalt. *J. Appl. Phys.*, 39:1276, 1968.

[139] A. Hubert and R. Schafer. *Magnetic Domains. The Analysis of Magnetic Microstructures*, chapter 2. Springer, 2000.

[140] G. Woltersdorf, O. Mosendz, B. Heinrich, and C.H. Back. Magnetization dynamics due to pure spin currents. *Phys. Rev. Lett.*, 99:246603, 2007.

[141] H. Kurt, W. Chiang, C. Ritz, K. Eid, W. P. Pratt, and J. Bass. Spin-memory loss and current-perpendicular-to-plane-magnetoresistance in sputtered multilayers with Au. *J. Appl. Phys.*, 93:7918, 2003.

[142] Y. Ji, A. Hoffmann, J.S. Jiang, and S.D. Bader. Spin injection, diffusion, and detection in lateral spin-valves. *Appl. Phys. Lett.*, 85:6218, 2004.

[143] Y. Ji, A. Hoffmann, J.S. Jiang, J.E. Pearson, and S.D. Bader. Non-local spin injection in lateral spin valves. *J. Phys. D: Appl. Phys.*, 40:1280, 2007.

[144] D. Sander. The correlation between mechanism stress and magnetic properties of ultrathin films. *Reports on Progress in Physics*, 62:809, 1999.

[145] S. Chikazumi. *Physics of Magnetism*, chapter 8. John Wiley & Sons, 1964.

[146] O. Thomas, Q. Shen, P. Shieffer, N. Tournerie, and B. Lepine. Interplay between anisotropic strain relaxation and uniaxial interface magnetic anisotropy in epitaxial Fe films on (001)GaAs. *Phys. Rev. Lett.*, 90:17205, 2003.